DEPOSITION OF DILUTE AEROSOLS FROM TURBULENT GAS FLOWS IN THE PRESENCE OF ELECTRICAL FORCES

A THESIS

Presented to

The Faculty of the Graduate Division

by

William Rex Lawrence

In Partial Fulfillment

of the Requirements for the Degree

Doctor of Philosophy

in the School of Aerospace Engineering

Georgia Institute of Technology

July, 1972

In presenting the dissertation as a partial fulfillment of the requirements for an advanced degree from the Georgia Institute of Technology, I agree that the Library of the Institute shall make it available for inspection and circulation in accordance with its regulations governing materials of this type. I agree that permission to copy from, or to publish from, this dissertation may be granted by the professor under whose direction it was written, or, in his absence, by the Dean of the Graduate Division when such copying or publication is solely for scholarly purposes and does not involve potential financial gain. It is understood that any copying from, or publication of, this dissertation which involves potential financial gain will not be allowed without written permission.

_____

_____

7/25/68

DEPOSITION OF DILUTE AEROSOLS FROM TURBULENT

GAS FLOWS IN THE PRESENCE OF ELECTRICAL FORCES

Approved:

Chairman

Date approved by Chairman: 10/10/72

ACKNOWLEDGEMENTS

I would like to express my appreciation to Dr. A. Ben Huang for his guidance, advice, and cooperation during this research effort and for his constant willingness to discuss various aspects of the endeavor. Dr. D. P. Giddens and Dr. C. G. Justus, who served on the reading committee, are gratefully thanked for their encouragement and for their patient examination of the manuscript.

The numerous discussions, advice, and cooperation of fellow graduate students have contributed significantly to this effort, and it has been a pleasure to have been able to associate with them during my stay at this institution. I am also grateful for the financial assistance provided by NSF traineeship, and I would like to thank the staff of the Rich Electronic Computer Center for their valuable service.

I am grateful to my wife, Bettie, for her patience, understanding, and encouragement during my graduate work. Finally, I am especially thankful to my late uncle, Mr. Robert L. Pugh for his many years of guidance, encouragement, foresight, and unselfish sacrifice which provided the strength to embark upon this effort.

TABLE OF CONTENTS

Page

ACKNOWLEDGEMENTS ii

LIST OF TABLES v

LIST OF ILLUSTRATIONS vi

LIST OF SYMBOLS x

SUMMARY xv

Chapter

I. INTRODUCTION 1

Background and Perspective
Definition of the Problem

II. DEPOSITION IN THE ABSENCE OF ELECTRICAL FORCES AND COAGULATION EFFECTS 5

Background and Previous Efforts
Basic Concepts and Governing Equations
Discussion of Results

III. COAGULATING AEROSOL DEPOSITION IN THE ABSENCE OF ELECTRICAL FORCES 29

Turbulent Coagulation Model
Numerical Solutions
Discussion of Results

IV. AEROSOL DEPOSITION IN THE PRESENCE OF ELECTRICAL FORCES . 49

Background and Perspective
Formulation of Mathematical Model System
Axisymmetric Pipe Flow and Nondimensionalization

V. DEPOSITION WITHIN THE CONVENTIONAL ELECTROSTATIC PRECIPITATOR CONFIGURATION 84

Equilibrium Velocity Example
Nonequilibrium Diffusion Velocity Example
Comparison with Experimental Data

Chapter Page

VI. CHARGED PARTICLE CONCENTRATION DISTRIBUTION AND DEPOSITION WITHIN A LONG PIPE IN THE ABSENCE OF EXTERNAL ELECTRIC FIELD 142

Approximate Solution to Poisson's Equation
Numerical Solution Procedure
Discussion of Results

VII. ELECTROSTATIC DEPOSITION WITHIN A TWO-DIMENSIONAL CHANNEL 166

Summary of Equations
Bipolar Aerosol Deposition
Discussion of Results
Unipolar Space-Charge Induced Aerosol Deposition

VIII. DISCUSSION AND CONCLUSIONS 190

APPENDICES

A. PARTICLE FLUCTUATION VELOCITY DISTRIBUTION 195

B. ANALYTIC SOLUTIONS-NONCOAGULATING NEUTRAL AEROSOL 205

C. NUMERICAL SOLUTIONS-NONCOAGULATING NEUTRAL AEROSOL . . . 218

BIBLIOGRAPHY 221

VITA 229

LIST OF TABLES

Table Page

1. Relative Entrainment Parameter 12

LIST OF ILLUSTRATIONS

Figure		Page
1.	Deposition as a Function of Reynolds Number for Montgomery and Corn Data	20
2.	Deposition as a Function of Reynolds Number for Stavropolous Data	22
3.	Deposition as a Function of Nondimensional Relaxation Time	24
4.	Deposition as a Function of Particle Material Density for Various Radii, as Given by Analytical Solution	26
5.	Comparison of Numerical and Analytical Results for Deposition as a Function of Particle Radius	27
6.	Finite-Difference Grid System	39
7.	Number Concentration Distribution Function at Two Longitudinal Locations ($\hat{r} = 0.96$)	42
8.	Number Concentration Distribution Function at Two Longitudinal Locations ($\hat{r} = 0.0$)	43
9.	Number Concentration Radial Profiles for Three Discrete Particle Sizes	45
10.	Deposition Velocity as a Function of Particle Size Both With and Without Effect of Coagulation	46
11.	Deposition Flux as a Function of Particle Size at Two Longitudinal Locations	47
12.	Conventional Pipe-Centerline Wire Electrostatic Precipitator Configuration	85
13.	Mass Balance for a Cylindrical Element	102
14.	Total Particle Concentration Across Pipe Radius at Three Axial Locations	107
15.	Wall Concentration Distribution Function Versus Particle Radius at Three Axial Locations	108

Figure Page

16. Particle Removal Efficiency as a Function of Axial Location 110

17. Particle Radial Velocity as a Function of Radial Location at Three Axial Locations 111

18. Particulate Removal Efficiency as a Function of $\epsilon_o E_o^2/\rho_f U_{m_{z_o}}^2$ 113

19. Required Value of $\epsilon_o E_o^2/\rho_f U_{m_{z_o}}^2$ for Complete Particle Removal at Various Downstream Locations 114

20. Comparison of Turbulent Diffusion Flux with Electrical Drift Flux at Two Axial Locations 118

21. Total Particle Concentration Across the Pipe Radius at Three Axial Locations 126

22. Wall Concentration Distribution Function Versus Particle Radius at Three Axial Locations 128

23. Particulate Removal Efficiency as a Function of Axial Location 130

24. Particle Radial Velocity as a Function of Radial Location at Three Axial Locations 131

25. Particulate Removal Efficiency as a Function of $\epsilon_o E_o^2/\rho_f U_{m_{z_o}}^2$ 133

26. Effective Drift Velocity as a Function of Non-dimensional Electric-Field Parameter 135

27. Particulate Removal Efficiency as a Function of Axial Location for Inyushkin and Averbukh Data 140

28. Total Number Concentration Across Pipe Radius at Three Axial Locations ($\hat{E}_c = 1.0$) 151

29. Total Number Concentration Across Pipe Radius at Three Axial Locations ($\hat{E}_c = 2.0$) 152

30. Total Number Concentration Across Pipe Radius at Three Axial Locations ($\hat{E}_c = 3.0$) 153

Figure Page

31. Total Number Concentration Across Pipe Radius at Three Axial Locations ($\hat{E}_c = 5.0$) 154

32. Total Number Concentration Across Pipe Radius at Three Axial Locations ($\hat{E}_c = 7.0$) 155

33. Total Number Concentration Across Pipe Radius at Three Axial Locations ($\hat{E}_c = 10.0$) 156

34. Particulate Removal Efficiency as a Function of Axial Location ($a_o/R = 10^{-5}$) 158

35. Total Number Concentration Across Pipe Radius at Three Axial Locations ($\hat{E}_c = 0.1$) 159

36. Total Number Concentration Across Pipe Radius at Three Axial Locations ($\hat{E}_c = 0.3$) 160

37. Particulate Removal Efficiency as a Function of Axial Location ($a_o/R = 10^{-4}$) 161

38. Nondimensional Deposition Velocity as a Function of Axial Location for Several Values of E_c 163

39. Electric-Field Intensity as a Function of Radial Coordinate for Two Axial Locations ($a_o/R = 10^{-5}$) 165

40. Two-Dimensional Channel Flow Coordinate System 168

41. Number Concentration of Negatively-Charged Particles at Several Downstream Locations ($a_o/R = 10^{-4}$, $a_o = 10^{-3}$ cm). 178

42. Number Concentration of Negatively-Charged Particles at Several Downstream Locations ($a_o/R = 10^{-5}$, $a_o = 10^{-4}$ cm). 181

43. Number Concentration of Negatively-Charged Particles at Several Downstream Locations ($a_o/R = 10^{-5}$, $a_o = 10^{-4}$ cm). 182

44. Particulate Removal Efficiency as a Function of Precharging Downstream Distance 183

Figure Page

45. Particulate Removal Efficiency as a Function of Precharging Electric Field 184

46. Particle Number-Concentration Distribution at Two Downstream Locations ($a_o/R = 10^{-5}$, $a_o = 10^{-4}$ cm, $\hat{E}_c = 5.0$) 186

47. Wall Deposition Flux as a Function of Downstream Distance for Several Particulate Loadings 188

48. Centerplane Particle Concentration as a Function of Downstream Distance 189

49. Relative Energy and Velocity Ratio as Functions of Frequency 197

50. Particle Turbulent rms Fluctuation Velocity as a Function of Distance from Wall 204

LIST OF SYMBOLS

a	Particle radius (cm)
A	Collecting surface area (cm^2)
$A^{(q)}$	Defined by equation (4.38)
B	Defined by equation (4.39)
c	Concentration ($moles/cm^3$)
c_1	Separation of variables constant (cm^{-1})
C_D	Particle drag coefficient
d_s	Stop distance (cm)
$d^{(q)}$	Particle diameter of species (q) (cm)
D	Pipe diameter (cm)
E_i	Electric-field intensity component in i^{th} coordinate direction (volts/cm)
f	Drag-coefficient correction defined by equation (4.17)
f_r	Equivalent body-force per unit mass of fluid (dyne/gm)
$F^{(qp)}$	Time constant of velocity relaxation between species (q) and species (p) (sec^{-1})
$F_i^{(q)}$	Body force exerted on unit mass of species (q)
i	Ion current per unit length (ma/cm)
I	Rate of change of number concentration as a result of coagulation (cm^{-4} sec^{-1})
j	Ion-current density (ma/cm^2)
$J_i^{(q)}$	Diffusion flux of species (q) (gm cm^{-2} sec^{-1})
$\vec{J}$	Diffusion flux vector (gm cm^{-2} sec^{-1})
k_{12}	Collision frequency per unit volume (cm^{-3} sec^{-1})

K	Particle mobility ($cm^2\ sec^{-1}\ volt^{-1}$)
$\bar{K}$	Coefficient of particle collection (cm/sec)
K_1, K_2	Arbitrary integration functions
ℓ	Mixing length (cm)
L	Total precipitator length (cm)
m	Exponent in power-law velocity function
$m^{(q)}$	Mass of particle of species (q) (gm)
n	Number concentration distribution function ($particles/cm^4$)
$n^{(q)}$	Number concentration distribution function of species (q) ($particles/cm^4$)
N	Total number concentration ($particles/cm^3$)
N_o	Reference total number concentration ($particles/cm^3$)
N_i	Ion number density ($ions/cm^3$)
P	Pressure ($dyne/cm^2$)
$p^{(q)}$	Partial pressure of species (q) ($dyne/cm^2$)
P_m	Mixture pressure ($dyne/cm^2$)
q_i	Electric charge per ion (coul/ion)
Q	Total charge per volume of fluid ($coul/cm^3$)
r	Radial distance from centerline (cm)
r_δ	Wire radius (cm)
R	Pipe radius (cm)
Re	Reynolds number for pipe flow
Re_p	Relative Reynolds number for particle drift
S	Defined in equation (B.2)
t	Time (sec)
T	Defined in equation (B.2)

u_x, u_z	Velocity components in indicated directions (cm/sec)
u_{z_*}	Friction velocity (cm/sec)
$\vec{U}$	Velocity vector (cm/sec)
U_r, U_z	Velocity components in radial and axial directions (cm/sec)
$U_i^{(q)}$	Mean velocity component, in the i^{th} coordinate direction, of species (q) (cm/sec)
U_{m_i}	Mean velocity component, in the i^{th} coordinate direction, of mixture (cm/sec)
$U_{\Gamma_i}^{(q)}$	Velocity component, in the i^{th} coordinate direction, of coagulation-generated species (q) (cm/sec)
$\bar{\hat{U}}_{m_z}$	Spatial average of mean axial velocity component in nondimensional form
$\bar{U}_z$	Spatial average of fluid axial velocity component (cm/sec)
v_f'	Fluid turbulent rms fluctuation velocity (cm/sec)
v_p'	Particle rms fluctuation velocity (cm/sec)
V_d	Deposition velocity (cm/sec)
V	Electric potential (volts)
V_w	Electric potential at wire surface
$\bar{V}$	Fluid volume flow rate (cm^3/sec)
$V_i^{(q)}$	Diffusion velocity of species (q) in i^{th} coordinate direction (cm/sec)
w	Particle drift velocity (cm/sec)
$\vec{x}$	Spatial coordinate vector (cm)
x,y,z	Coordinate distances (cm)
$Z^{(q)}$	Charge per particle of species (q) (coul/particle)
β	$\ell^2 \lvert d\bar{U}_z/dr \rvert$ (cm^2/sec)
$\Gamma^{(q)}$	Rate of generation of species (q) per unit volume as a result of coagulation (gm cm^{-3} sec^{-1})

δ_d	$\ell + a$ (cm)
δ_D	Height of diffusion boundary layer (cm)
δ_{ji}	Kronecker delta
δ_V	Height of velocity boundary layer (cm)
$\Delta_{ji}^{(q)}$	Deformation tensor for species (q) (sec^{-1})
ϵ	Eddy diffusivity (cm^2/sec)
$\overline{\epsilon}_o$	Turbulent energy dissipation (cm^2/sec^3)
ϵ	Permittivity of particle material ($dyne/volt^2$)
ϵ_o	Permittivity of free space ($dyne/volt^2$)
ϵ_r	ϵ/ϵ_o
ζ_m	Bulk viscosity of mixture ($dyne\ sec/cm^2$)
η	Efficiency
$\theta[\ ]$	On the order of
$\theta^{(q)}$	Dilatation tensor for species (q) (sec^{-1})
$\varkappa$	Charge decay parameter
λ	Defined in equation (B.25)
μ_f	Fluid molecular viscosity ($dyne\ sec/cm^2$)
μ_m	Mixture molecular viscosity ($dyne\ sec/cm^2$)
μ_{m_2}	$\zeta_m - \frac{2}{3}\mu_m$
ν	Fluid kinematic viscosity (cm^2/sec)
ρ_f	Fluid density (gm/cm^3)
ρ_p	Aerosol material density (gm/cm^3)
ρ_m	Mixture density (gm/cm^3)
$\rho^{(q)}$	Density of species (q) (gm/cm^3)
σ_o	Geometric standard deviation of number-density distribution function

τ Stokes' relaxation time, $2 a^2 \rho_p / 9 \mu_f$ (sec)

τ_* Nondimensional Stokes' relaxation time, $\tau \mu_{z_*}{}^2 / \nu$ (see equation (2.3))

ϕ Relative entrainment parameter

Subscripts

c Charging condition

eq Equilibrium conditions

f Fluid component

i Discrete particle radius index number

j Radial coordinate index number

k Axial coordinate index number

m Mean or mixture

o Reference condition

p Particle component

r Radial component

w Wall value

x,y,z Coordinate-direction component

SUMMARY

The ability to predict quantitatively the deposition of aerosol particles onto surfaces adjacent to moving gas streams represents an important requirement for several industrial design applications. Unfortunately, the available theoretical techniques developed to date for predicting aerosol deposition fall short of this requirement. The purpose of this research effort is to develop theoretical solutions for aerosol concentration distribution and deposition flux for several flow configurations of practical interest. The effort is divided into two categories: deposition in the absence of electrical forces and deposition in the presence of electrical forces. The various analyses included herein are focused toward the turbulent flow case and include consideration of particle coagulation to the extent possible. Several analytical solutions are found which, in many cases, offer an improvement in available prediction capability; however, the major part of the effort is devoted to the development of numerical solutions for the problems of interest. Advantage is taken of the discrete-ordinate method to achieve accurate results when coagulation effects are included.

The results of the investigation might be summarized as follows:

1. Initial attention was directed toward the deposition of non-coagulating, neutral aerosols from turbulent pipe flow and from turbulent boundary layer flow. It was found that a mixing-length hypothesis provided a basis for constructing an analytical approach for conveniently predicting, with reasonable accuracy, aerosol deposition from these two

flow configurations when electrical effects are absent. Also obtained were some numerical solutions for the pipe flow case, and comparison of results predicted by the analytical solution with the numerical results and with available experimental data indicates that the mixing-length hypothesis appears to offer an advantage relative to other available approaches to predicting aerosol deposition.

2. An analysis of the influence of coagulation upon the overall deposition of neutral aerosols indicates that there is little effect upon overall mass transport for the conditions chosen for study. The versatility of the discrete-ordinate method for computationally processing the equations representing the aerosol system is clearly observed, however.

3. The approach was then extended to include problems involving significant electrical forces. The analysis was directed toward the electrostatic precipitation problem. Numerical solutions for aerosol behavior within the conventional pipe-wire precipitator indicate that the present approach is superior to the standard Deutsch formula, of use in the precipitator design field. Correlations of the numerical solutions are included for practical application.

4. The influence of turbulent diffusion was found to be small relative to overall deposition in the presence of electrical forces, although its influence upon particle concentration profiles is more significant. For configurations in which electrical-field gradients are not large, turbulent diffusion can be neglected, even with respect to particle concentration distributions.

5. Calculations were also made of space-charge deposition within

two-dimensional channel flow for representative conditions. A study of bipolarly-charged aerosol behavior within a two-dimensional channel represented the most complete application of the formulation. Results indicate a potential for further useful application of the approach developed herein.

CHAPTER I

INTRODUCTION

Background and Perspective

The ability to predict quantitatively the deposition of aerosol particles onto surfaces adjacent to moving gas streams represents an important requirement for several industrial design applications. For example, one must be able to make reasonably accurate estimates of the deposition of radioactive particles from gas flows within the ductwork associated with nuclear reactors. In addition, obtaining representative aerosol samples from these and other similar flows represents an important and often difficult task requiring some knowledge of the errors incurred by losses due to deposition. Aerosol deposition is a fundamental mechanism utilized in several air-cleaning equipment applications and is a major concern of air pollution control efforts. The variety of engineering problems associated with aerosol deposition warrants some effort to develop reliable techniques for predicting such behavior. Unfortunately, the available theoretical techniques developed to date fall short of these requirements in their reliability for accurately predicting the behavior of aerosol suspensions. The scarcity of experimental data has contributed to the uncertainty associated with the application of these theories, and consequently results given by the most applicable of these theories often can be described as only qualitatively accurate.

There appears to be two rather general subdivisions of the subject which can be identified: deposition of aerosol particles in the absence of significant electrical forces and deposition under conditions where electrical forces are at least significant, if not predominant. To the first classification, one can assign those problems associated with radioactive particle deposition, aerosol sampler losses, and several inertial particulate-fluid separation techniques, among others, whereas to the latter, one can assign the important class of problems associated with electrostatic precipitator design. Although many other examples could be cited, it is to the applications mentioned that the present effort is addressed.

Definition of the Problem

Three representative and important problems associated with aerosol deposition are those of fully-developed, incompressible turbulent pipe flow, incompressible two-dimensional turbulent boundary-layer flow on a flat plate, and incompressible two-dimensional turbulent channel flow, involving in each case suspensions of either liquid or solid particles within a gaseous medium. This set of problems involves the more basic fluid-dynamic configurations, which have, on the other hand, occurred often in design application.

There are several reasons for restricting the present effort to incompressible flow. First, flow velocities encountered in those applications of interest here are much less than sonic velocities, and hence, compressibility effects can be neglected. Note that the term incompressible is made in reference to the fluid medium and to the material

composing the aerosol particles, not to the local concentration of aerosol particles, which in fact does vary throughout the flow. Second, the assumption will be introduced later that a particle does not rebound on striking a surface, so that impact alone is sufficient to insure deposition, and that the fluid velocity is not so great as to be effective in dislodging particles from the surface by means of friction. Both elements of this assumption require relatively low flow velocities, which again precludes the necessity for including consideration of compressibility.

Consideration of the effects of turbulent flow is included in this study for several reasons. Among these are, first, that turbulent flow conditions are encountered quite often in practice and can, in fact, be regarded as the more common occurrence. Further, deposition in the absence of electrical forces and under flow conditions other than turbulent is usually of negligible proportions.

Finally, the study here includes, insofar as possible, the effects of particle coagulation as a result of interparticle collisions. The technique used to accommodate particle coagulation into the analyses represents one of the more important aspects of this research effort. The technique, known commonly as the discrete-ordinate method, represents a powerful numerical tool exploited in recent years in the study of rarefied gas dynamics. Details of this technique are given later when specific examples are considered. Although primary emphasis is placed upon obtaining results for aerosol deposition, general attention is directed also toward obtaining solutions for aerosol particle number concentration distribution throughout the flowfields of the problems

of interest.

In summary then, the purpose of this research effort is to develop theoretical solutions for aerosol concentration distribution and deposition flux for several flow configurations of practical interest. The analyses are focused toward turbulent flow and include a consideration of particle coagulation to the extent possible. Initial attention is directed toward the uncharged particle case, and the development is then extended to include electrical force effects. A review of the pertinent literature follows the same structural outline, and comparisons of the results with available experimental data are included. However, a discussion of the relevant literature is logically associated with the development of background material for each of the subdivisions and therefore is included with the latter rather than in this chapter, as is perhaps more customary.

Much of the mathematical development has been relegated to several appendices in order to provide a continuous overview of the results obtained. Nevertheless, the appendices should be considered to be an integral part of the presentation, as they contain many of the more important specific details of the development. The framework of the analyses are structured around the basic conservation equations of fluid dynamics, with such subsidiary relations and equations as are necessary to form a closed system in the mathematical sense.

CHAPTER II

DEPOSITION IN THE ABSENCE OF ELECTRICAL FORCES AND COAGULATION EFFECTS

This chapter presents the results of an analysis made of neutrally charged aerosol particle deposition from fully-developed turbulent flow, based on the mixing-length hypothesis. Consideration is devoted to two representative and important problems associated with aerosol deposition: namely, fully-developed turbulent pipe flow and two-dimensional turbulent boundary-layer flow on a flat plate.

It is the purpose of this chapter to outline an analytical approach for conveniently predicting, with reasonable accuracy, noncoaulating aerosol deposition from fully-developed turbulent pipe flow and from two-dimensional turbulent boundary-layer flow. In addition, presented also are the results of some associated detailed numerical solutions for noncoagulating aerosol concentration distributions and surface deposition characteristics for turbulent pipe flow.

Background and Previous Efforts

The mechanism for deposition from gas flows is related to the impact of suspended particles upon a bounding surface and their subsequent retention by the surface as a result of, for example, van der Waal's forces, electrostatic forces, or by the surface tension of entrained water vapor at the particle-surface interface. The nature and efficiency of these bonding forces is a complicated subject itself, as

is the influence of the interaction between the adhering particles and the adjacent moving fluid stream upon re-entrainment of the adhered particles. For particles less than about one micron in diameter and for typical engineering materials used for surfaces, it has been found that the rate of deposition upon a surface can be taken as very nearly equal to the rate at which aerosol particles reach the surface [1]. Thus, the problem resolves itself into determining the rate at which particles impact upon a surface as a result of interaction of the particles with their suspending medium and with various external forces, e.g., electrical, gravitational, etc.

It would be an exercise in futility to attempt to predict individual particle behavior with respect to deposition from a turbulent stream, and one need be concerned only with the statistical probability of deposition, consistent with the classical statistical description of turbulent flows in general. The most common avenue of approach to turbulent flow problems in the past has been one of the phenomenological theories, which have long been of value in basic fluid dynamic descriptions of turbulent flows. This chapter outlines the application of the mixing-length hypothesis of Prandtl [2] and Taylor [3] to the prediction of aerosol deposition and presents both an analytical result useful for engineering computations and a series of numerical solutions based on the mixing-length hypothesis.

Previous efforts to provide an analytical basis for predicting aerosol deposition from turbulent flows have been limited in number and have not attempted to include the effects of particle coagulation. Although these studies have been quite similar in approach, one can perhaps

distinguish three theoretical investigations which have contributed to the establishment of the basis for current thinking regarding this subject. These theories have the common basis in the time-averaged equation of continuity for isothermal systems with approximately constant component mass densities. Most neglect all terms except the diffusion term itself in the equation, and all relate the turbulent mass flux to the component concentrations by means of an equivalent Fick's "law" of diffusion for turbulent eddy transport.

As mentioned above, although no published theoretical effort has apparently been completed regarding deposition of coagulating aerosol suspensions from turbulent streams, several papers have appeared which deal with deposition of a noncoagulating aerosol. For example, one should mention the early important effort of Friedlander and Johnstone [4], who proposed the following model: Particles are diffused by eddy motion from the turbulent outer layer to within one "stop distance" of the wall. The stop distance is defined as the distance which a particle with a given initial velocity will move through a quiescent gas before coming to rest as a result of the drag force exerted on the particle by the suspending medium. At this distance from a surface, particles are supposed to have sufficient momentum to overcome the diffusive resistance near the wall and to be deposited on the surface. However, Friedlander and Johnstone based the computed stop distance on a single constant velocity, namely a root mean square normal turbulent fluctuation velocity outside the flow region near the wall. Actually one should, in principle, base the stop distance calculation on a local fluctuation velocity near the wall at the point from which deposition

by inertia is being assumed to take place. Their method involves an integral of the equivalent Fick's law for eddy diffusion, i.e., of

$$J_y = - \epsilon \frac{dc}{dy} \tag{2.1}$$

where the flux J_y is assumed constant (one-dimensional, flat plate solution) and in which values of eddy diffusivity ϵ, presumed equal to the local eddy diffusivity of the fluid, are taken from experimental data.

Davies [5] has obtained a more justifiable one-dimensional solution for the basic model proposed by Friedlander and Johnstone [4]. He proposes that particles diffuse toward the wall to within a distance which is equal to the sum of the local stop distance and the particle radius. As Friedlander and Johnstone [4], Davies [5] integrates the equivalent Fick's law for constant flux (flat plate solution) and includes a correlation for turbulent diffusivity based on several sets of experimental data, again with the assumption that particle diffusivity is equal to that of the fluid. The results are applied, however, to the cylindrical coordinate system of axisymmetric pipe flow. The author has obtained solutions for Davies formulation valid for cylindrical coordinates (not included herein) which indicate that one cannot be arbitrarily selective in applying results for the rectangular and cylindrical coordinate systems. Differences are particularly evident when the particle size-pipe radius ratio is not very small.

A method similar to those just mentioned was given by Beal [6] who attempted to include a solution valid for cylindrical coordinates. However, he assumed that the radial particle flux for pipe flow was proportional to the distance from the centerline, whereas, in fact, continuity required that the radial flux be more nearly inversely proportional to distance from the centerline. Moreover, he assumed that

> the radial velocity of the fluid close to the wall is equal to the axial velocity, and that the particle velocity toward the wall is one-half of this (to account for the velocity fluctuations being directed both toward and away from the wall).

This latter is considered an unrealistic assumption, even by Beal [6].

Several other efforts could be mentioned (see Sehmel [7], Schwendiman and Postma [8], Kneen and Strauss [9], Wells and Chamberlain [10]), but the methods used are all similar and are fundamentally based on the stop-distance concept.

An interesting and important recent effort reported by Sehmel [11] examines the influence of removing two of the assumptions made in the deposition theories just discussed, namely those regarding equality of particle and fluid diffusivities and equality of particle and fluid root-mean-square turbulent fluctuation velocities. Sehmel begins with the realization that these two assumptions may not be correct and determines what dependence these variables must have upon other parameters of the problem in order that theoretical calculations agree with experimental data. In other words, Sehmel attempts to "back calculate" particle diffusivity and rms fluctuation velocity from experimental deposition data. Also presented is a purely empirical correlation equation for the experimental deposition data he examines. Further discussion of Sehmel's

results is presented later in this chapter, and comparisons of his correlation results with present results are shown.

Basic Concepts and Governing Equations

The behavior of discrete particles in a turbulent fluid depends to a significant extent on two important parameters characterizing the flow. These are the concentration of the particles and their size relative to the scale of turbulence of the fluid, as noted by Hinze [12]. When the particle concentration is relatively large, significant coupling of the fluid-particle behavior occurs due to the mutual hydrodynamic interaction and to direct interaction resulting from interparticle collisions. The fluid-particle interaction at high particle concentration can result in significant alteration of the fluid flow and can contribute to additional damping of the turbulence. An upper limit of about one percent concentration by volume for significant interaction has been indicated by several investigators [33, p. 185]. For particles having one-micron radii, this corresponds to 10^9 particles/cm^3, and for ten-micron particles, this corresponds to about 10^6 particles/cm^3. Particle collisions may result in coagulation or, in principle, de-agglomeration. However, the probability of coagulation or agglomeration normally far exceeds that of de-agglomeration, and the effect of the latter for aerosols of interest here can be neglected. The effect of particle coagulation upon deposition is an interesting point to be demonstrated by the results of an extension of this effort in Chapter III.

An important parameter to consider is the size of the particles relative to the scale of turbulence within the flow. If the particles

are small compared with the smallest scale of turbulence and if their density is not much greater than that of the fluid, they tend to follow the detail turbulent components of the fluid. On the other hand, if the particles are large compared with the scale of turbulence, the particles tend to follow only the larger scale turbulent motions. A parameter which characterizes the scale of turbulence is the so-called mixing length hypothesized by Prandtl [2] and Taylor [3], which roughly indicates the distance within the flow over which the fluid mass approximately retains its identity*. A particle entrained within an eddy thus retains its momentum components over a distance which is on the order of the local mixing length, unless the inertia of the particle is sufficiently large to prevent its complete entrainment with the eddy. The inertia of a suspended particle has traditionally been identified with its so-called stop distance, which was defined earlier. If the initial velocity is taken to be the root-mean-square turbulent velocity component in some particular direction, then one can define an important "relative entrainment parameter" as

$$\phi = \frac{d_s}{\ell} \tag{2.2}$$

* Individual mixing lengths have been defined for momentum, heat, and mass transport. For flows for which gravitational effects or centrifugal forces do not play a role, these three lengths are of the same order of magnitude [105]. Reference is here made to the mixing length for momentum transport.

where d_s is the particle stop distance based on the rms velocity evaluated at a point and ℓ is the fluid mixing length at that point. If this ratio is much greater than unity, one can expect that the stop distance might be used to characterize the distance over which a particle can be expected to retain its initial course. However, if the relative-entrainment parameter is small, then the mixing length might be taken as the characteristic distance associated with the maintenance of the initial motion identity of the particle. It is this latter point which appears to offer an improvement in the fundamental hypotheses upon which earlier theoretical considerations were based.

For example, using $d_{s*} = \tau_* v'_{f*}$ (with τ_* given by the definition following equation (2.3) and with v'_{f*} given by equation (A.6)) and using $\ell_* \triangleq \ell u_{z*}/\upsilon$ (with ℓ given by equation (B.10) for $y_* > 5$ and by $0.378\, y_*$ for $y_* \lesssim 5$)*, one can show that for typical data such as that of Montgomery and Corn [15] the parameter ϕ is as shown in Table I.

Table 1. Relative Entrainment Parameter

$\frac{y}{R}$	ϕ
1.0	0.00041
0.1	0.00124
0.01	0.0029
0.001	0.29
0.0001	0.35

* The appropriate nondimensionalization definitions are given in Appendix B.

As y/R approaches zero, ϕ approaches $(\rho_p/\rho_f)(a/R)^2 Re^2 \gamma/544$.

Although the detailed interaction dynamics of individual particles of arbitrary size and concentration in a turbulent fluid medium is not discussed here, it is important to mention the theoretical study made by Tchen [13] on the motion of an individual small particle suspended in an isotropic turbulent fluid. On the basis of several reasonable assumptions, Tchen [13] found that, in general, for long diffusion times the coefficient of diffusion for discrete particles was equal to that of the fluid medium. Further, for short diffusion times, the difference between the two diffusion coefficients is very small for particles of unit density having diameters of the order of one micron. The assumption of equality of particle and fluid diffusivities for these types of particles is reasonable, although for much larger particles or for particles having higher material density the assumption becomes questionable. However, the problem of particle diffusivity in the nonisotropic turbulence near a wall remains unresolved, as does the question regarding particle rms turbulent fluctuation velocities.

Soo and Tien [14] investigated the effect of the wall on two-phase turbulent motion (solid particles in a gas). Their analysis indicates that the effect of the wall on particle diffusivity is secondary, although the presence of the wall affects the intensity of motion of the particles to a greater extent. Some additional discussion relative to particle response to turbulent fluctuations is presented in Appendix A.

In consideration of these results, one may reasonably retain the assumption of equality of particle and fluid diffusivities but include, at the same time, a specification of particle rms fluctuation velocity

with respect to the local fluid fluctuation velocity. The effect of the nonisotropic conditions near the wall will be included in the present analysis as a result of the following argument. Due to the induction period required for accommodation of particle velocity to that of the local fluid, one expects that the particle velocity at a given point to be related to its velocity at a point further from the wall, the change being due to relaxation of particle-fluid velocity difference during transit time between the two points. The effect can be expected to increase with increasing particle density.

An approximate differential equation for particle fluctuation velocity which is obtained in Appendix A is, in nondimensional variables,

$$\frac{dv'_{p_*}}{dy_*} = \frac{1}{\tau_*}\left(1 - \frac{v'_{f_*}}{v'_{p_*}}\right) \tag{2.3}$$

where v'_{p_*} ($\triangleq v'_p/u_{z_*}$) and v'_{f_*} ($\triangleq v'_f/u_{z_*}$) are particle and fluid rms fluctuation velocities normal to the wall at a nondimensional distance, y_*, from the wall respectively, and τ_* is the nondimensional Stokes relaxation time given by $\tau_* = \frac{1}{18}(a/R)^2(\rho_p/\rho_f)[Reu_{z_*}/\bar{u}_z]^2$. equation (2.3) which relates particle rms fluctuation velocity, fluid rms fluctuation velocity, and the Stokes relaxation time is a nonlinear differential equation. Numerical solutions to this equation as well as an asymptotic expansion for the solution valid for small τ_* are also

presented in Appendix A. Further discussion relative to the appearance of rms fluctuation velocities in equation (2.3) is presented in Appendix A.

Another fundamental assumption made in the present study is that particle concentration is sufficiently large to permit defining a statistical probability of concentration (or concentration, for brevity), but not so large that a significant effect upon the flow characteristics of the fluid medium is encountered. Thus, one can examine the time-averaged equation of continuity for an isothermal polydisperse aerosol system with constant fluid mass density

$$\frac{\partial n}{\partial t} + \vec{u} \cdot \nabla n = I - \nabla \cdot \vec{J} \qquad (2.4)$$

where $n(a, \vec{x}, t)$ is the time-averaged number concentration distribution function of particles that have radii between a and a + da; t is time; $\vec{u}$ is the particle time-averaged velocity vector; I is the rate of change of number concentration, n, as a result of coagulation; and $\vec{J}$ is the mass flux of particles of radius a. The number concentration, n, is a distribution function with respect to particle radius. Once it is determined, changes in the particle size distribution are known and hence the behavior of the system is defined. In order that a solution for n be obtained, several additional quantities must be specified. The particle mass flux $\vec{J}$ must be related to the number concentration; this has traditionally

been accomplished by means of Fick's "law" of turbulent diffusion, i.e.,

$$J = - \varepsilon \nabla n \tag{2.5}$$

in which ε is the turbulent diffusivity. Transport by molecular diffusion can be included in an analogous manner. Here the mixing-length hypothesis of Prandtl [2] and Taylor [3] is employed, which for the y-component of the mass flux can be written as

$$J_y = - \ell^2 \left| \frac{du_x}{dy} \right| \frac{dn}{dy} \tag{2.6}$$

where u_x is the x-component of the particle mean velocity vector. In the absence of external body forces (such as gravitational, electrical, etc.) acting upon the suspended particles, the mean particle axial velocity, u_x, is taken to be the same as that of the surrounding fluid. Note that the mixing length may be a function of location within the flow.

The boundary conditions imposed on the solution of equation (2.4) represent an extremely important consideration relative to the overall usefulness and accuracy of the results. With regard to predicting deposition, the most important boundary condition is that near the bounding surface upon which deposition is taking place. As previously

indicated, no particle reflection or re-entrainment from surfaces is assumed; thus, one is concerned with the particle flux toward the wall.

Previous theoretical results (e.g., Davies [5], Beal [6]) have been based on the assumption that turbulent eddies diffuse suspended particles toward regions of reduced concentration, as near an absorbing wall, until the particles reach a point located one stop distance plus the particle radius from the wall. However, calculations such as those presented earlier indicate that for typical aerosol particles in a gas such as air the local mixing length for pipe flow or flat plate flow very often exceeds the particle stop distance (based on local turbulent rms fluctuation velocity). It would thus appear that the mixing length should replace the stop distance in the above fundamental hypothesis. Therefore, the discrete particle deposition flux is given by the number concentration of that class of particles multiplied by the root-mean-square normal component of the fluctuation velocity, all evaluated at a distance from the bounding surface equal to the local mixing length plus the discrete particle radius of the class of particles of interest*.

---

* The use of rms fluctuation velocity components might be justified by the following argument. Fuchs [1, p. 262] has demonstrated the analogy between turbulent diffusion and Brownian diffusion of aerosols. From the kinetic theory of gases, one can show [104] that the flux of molecules per unit area is given by $N\bar{C}/4$ under equilibrium conditions ($\bar{C}$ is the average speed of the molecules). The rms velocity component in the x-direction is $\sqrt{\overline{C_x^2}} = \frac{1}{3}\sqrt{\overline{C^2}}$, where $\sqrt{\overline{C^2}}$ is the overall rms velocity. Further, it can be shown [104] that $\bar{C}^2 = 3\pi\overline{C^2}/8$. Hence, the flux can be shown to be given by $N\sqrt{\overline{C_x^2}} \,/\, \sqrt{3/2\pi}$. The factor $\sqrt{3/2\pi}$ in this expression is not included in the equivalent expression for aerosol flux, but in consideration of the overall expected accuracy of the approach taken here, one can reasonably neglect this factor. This approach is consistent with the previous efforts of others [4, 5, 6, 7].

This flux is equal to the local diffusion flux given by equation (2.6), i.e.,

$$\left[v_p' \, n\right]_{y=\ell+a} = \left[\ell^2 \left|\frac{du_x}{dy}\right| \frac{dn}{dy}\right]_{y=\ell+a} \tag{2.7}$$

where y is distance from the wall and v_p' is the particle rms turbulent fluctuation velocity normal to the wall which has to be determined in terms of the fluid rms fluctuation velocity from equation (2.3). This expression relates the number concentration to the gradient of the concentration at this point and constitutes the required wall boundary condition for the solution to equation (2.4). Note that the mixing length, ℓ, is obtained from the solution to $y = \ell(y) + a$.

As examples of the application of the above ideas, results of computations are included for several practical flow situations of interest, namely fully developed turbulent pipe flow and the turbulent flat plate boundary layer. Analytical expressions were found for noncoagulating aerosol deposition and are developed in Appendix B (equation (B.26) for turbulent pipe flow and equation (B.37) for turbulent boundary layer flow). Also obtained were some associated detailed numerical solutions for the noncoagulating aerosol concentration distribution and surface deposition (Appendix C). The results of analogous numerical solutions for coagulating aerosols are presented in a later chapter.

Discussion of Results

Results of some example computations based on the ideas discussed in the previous sections are presented and compared with the experimental pipe flow deposition measurements of Montgomery and Corn [15] and Stavropolous [16] in Figures 1, 2, and 3. The deposition velocity, V_d, is defined as the mass flux to the wall divided by the average particle concentration across the pipe radius. For axisymmetric pipe flow, one expects laminar flow for Reynolds numbers less than about 2300 and a transition region of intermittent turbulence for Reynolds numbers between 2300 and about 10^4 to 10^5. The distance for transition to fully-developed turbulence increases as R_e decreases. Deposition experimentally increases rapidly with R_e in this transition region; however, the approximate analytical solution is not expected to be valid in this region, and one should not in principle compare results in this region. In the region in which fully-developed turbulent flow is expected, the result predicted by the present result compares favorably with the experimental data of Montgomery and Corn (Figure 1), especially relative to the result predicted by the theories of Friedlander and Johnstone [4] and Davies [5]. These experimental results were obtained using aerosols of uranine-methylene blue in turbulent pipe flows. The reader is referred to the original papers for discussion relative to the experimental procedures employed. It is significant to note that Montgomery and Corn [15] found that electrical changes present on aerosol particles had a large effect on their initial data, and they subsequently took extra precautions to insure charge equilibrium in their later measurements. One notes in Figure 1 that the deposition result predicted by Davies' theory, which

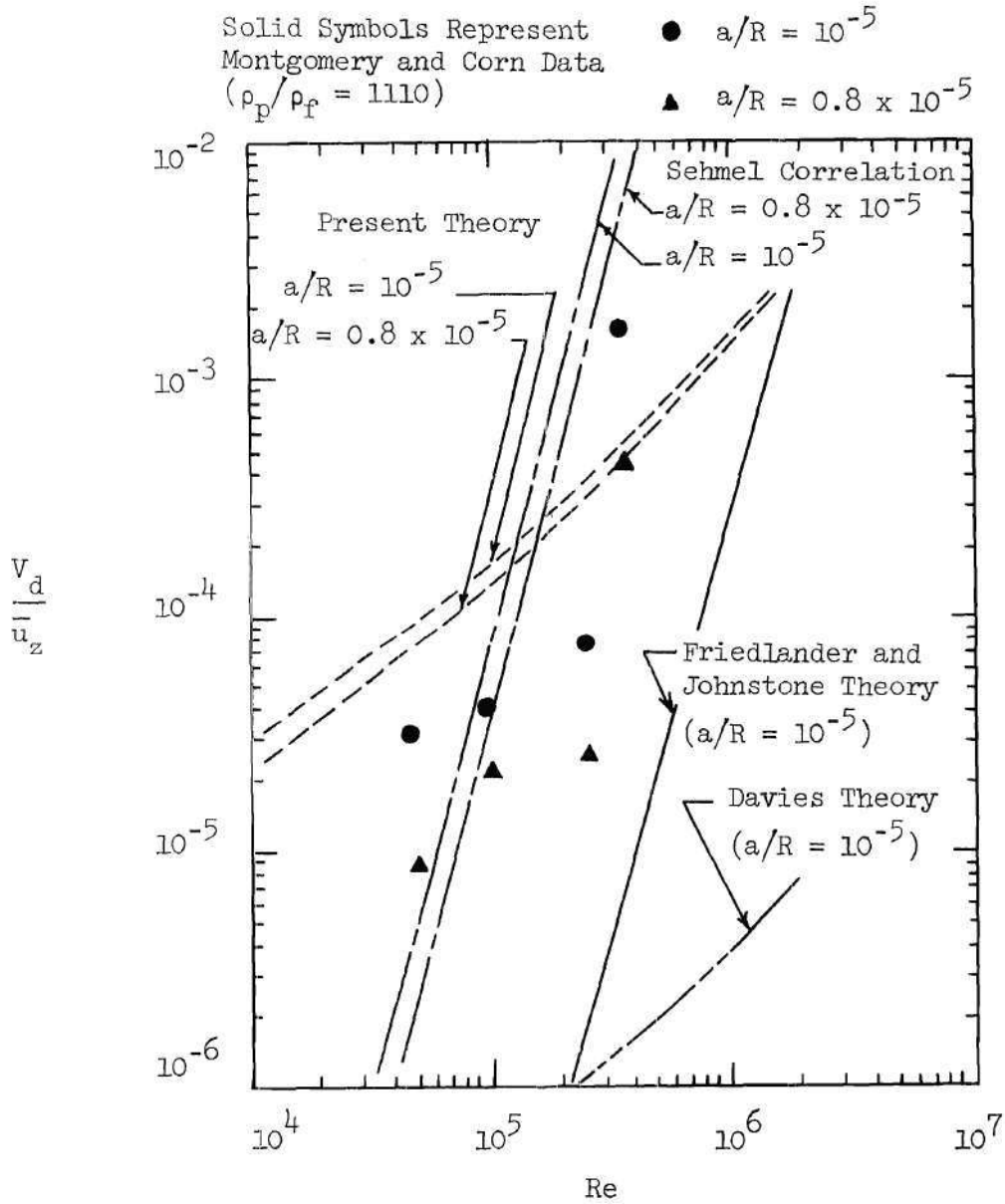

Figure 1. Deposition as a Function of Reynolds Number for Montgomery and Corn Data

one would expect to be superior to that of Friedlander and Johnstone, is actually in poorer agreement with the data at higher Reynolds numbers than is the latter theory. At even higher Reynolds numbers, significant re-entrainment of deposited particles can be expected and no comparison is attempted. At R_e approximately equal to 10^5, one could expect more-or-less optimum conditions for comparison of experimental and present theoretical results. Also shown in Figure 1 is the deposition rate obtained by extending the empirical correlation formula of Sehmel [11] to the higher Reynolds number range of the Montgomery and Corn data. One notes that although the Montgomery and Corn data appear consistent with the Sehmel correlation at lower Reynolds numbers, their high Reynolds number data indicate a deposition rate significantly lower than would be predicted by extension of the lower Reynolds number trend.

This effect can be seen more dramatically in the data shown in Figure 2 of Stravopolous [16], who presents deposition data for lycopodium powder (particle diameter = 30 μ). These data were employed by Sehmel in his empirical correlation, but one notes again the difference between high and low Reynolds number deposition rates not exhibited in the correlation. It is important to note that Stravopolous and Montgomery and Corn took special precautions to insure that particle re-entrainment was not a significant factor. Here there is closer agreement between the theoretical prediction of Friedlander and Johnstone and that of the present analysis than exhibited for the Montgomery and Corn data. The reason for this closer agreement can be discerned by examining the results obtained for particle rms fluctuation velocity v'_{p_*} in Appendix A. Recall that Friedlander and Johnstone assumed that v'_{p_*} was constant near the

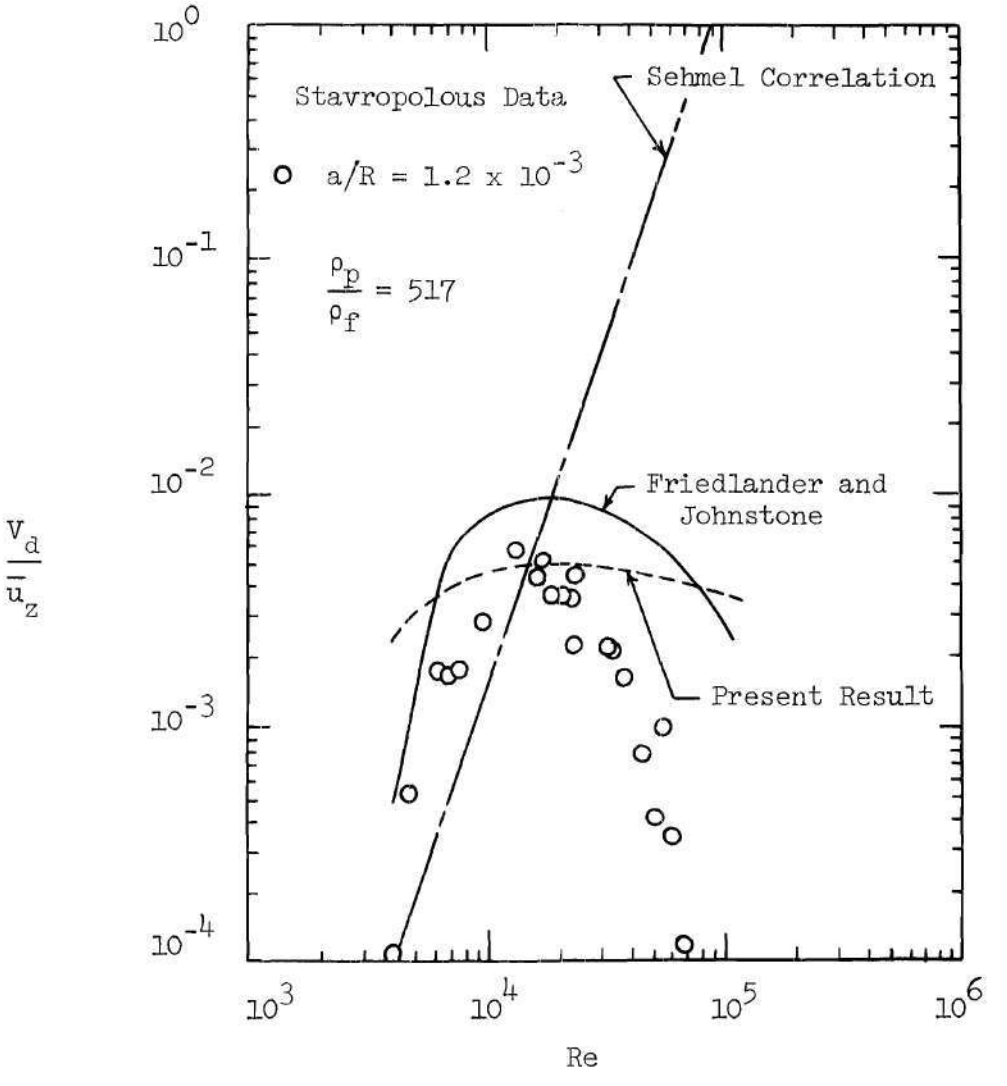

Figure 2. Deposition as a Function of Reynolds Number for Stavropolous Data

wall and equal to 0.9 times the fluid fluctuation velocity in the central core. The solutions for v'_{p_*} given in Appendix A indicate that as the particle relaxation time τ_* becomes larger, v'_{p_*} tends to approach one, its presumed value in the central core. Thus for large τ_*, i.e., large particle radius, material density, or flow Reynolds number, the Friedlander and Johnstone estimate for v'_{p_*} is not unreasonable. On the other hand, as τ_* becomes small, v'_{p_*} approaches v'_{f_*} and the Friedlander and Johnstone estimate becomes unusable.

This point is illustrated in Figure 3, in which V_{d_*} $(= V_d/u_{z_*})$ is plotted as a function of particle nondimensional relaxation time with parametric dependence upon flow Reynolds number. Although neither the present theoretical prediction nor the empirical correlation of Sehmel in principle exhibit strict functional dependence for this type of graphical presentation, they are shown for comparison with the experimental data of Stavropolous and Montgomery and Corn and the theoretical prediction of Friedlander and Johnstone. One notes the relative independence of τ_* which the deposition rate predictions of Friedlander and Johnstone and of the present theory indicate for τ_* greater than about 20, consistent with the result that v'_{p_*} approaches one for large τ_*. This independence is not present in the empirical correlation, which in addition indicates deposition rates much too high at the higher flow Reynolds number of 2×10^6.

In summary, then, one notes that although a significant quantity of data exist for Re less than about 10^4 to quantitatively define deposition in this flow regime, the limited amount of experimental data which exist at higher Reynolds numbers indicate that extrapolations of

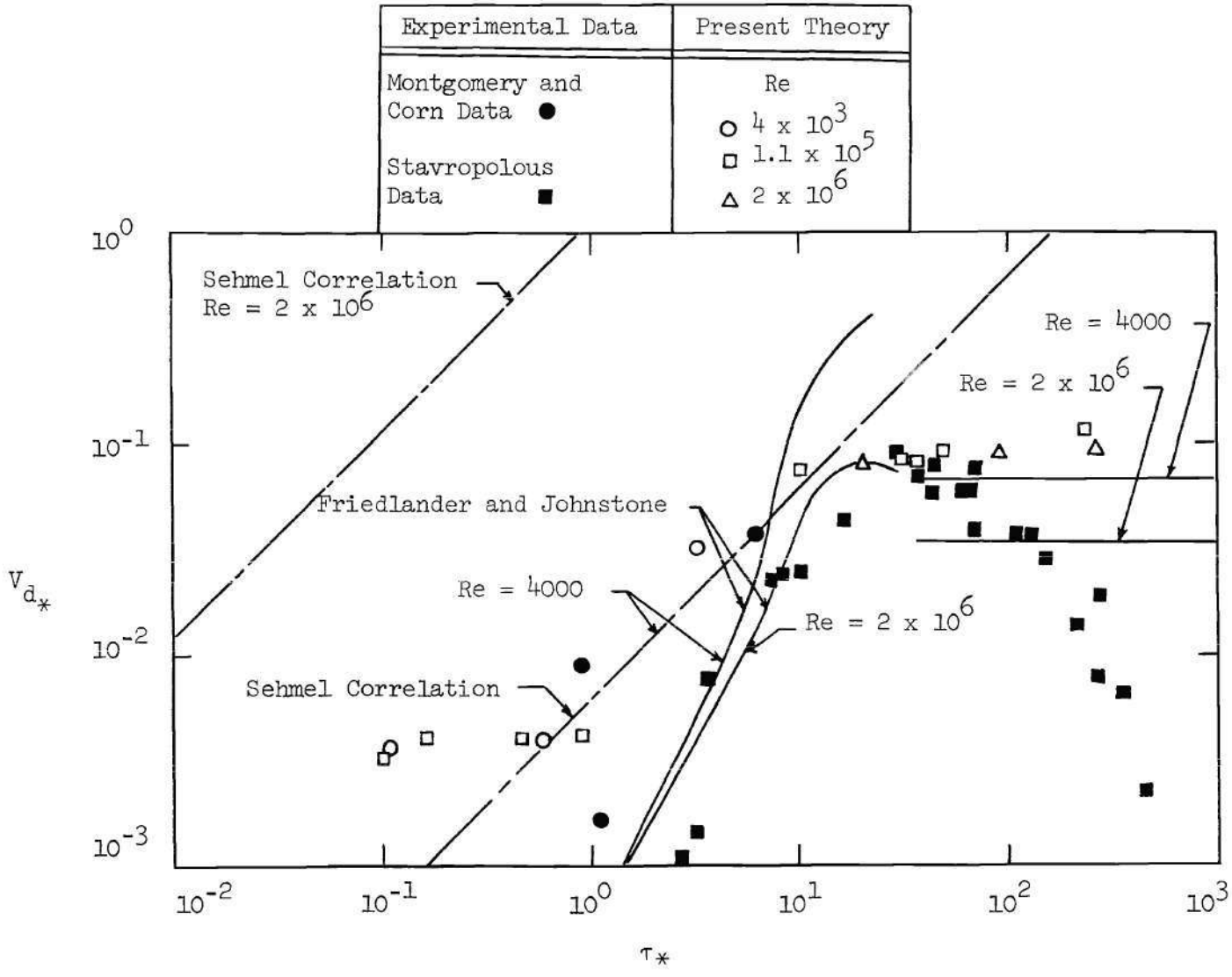

Figure 3. Deposition as a Function of Nondimensional Relaxation Time

lower Re data are not valid. There exists a need for additional data in this flow regime both to indicate more clearly this basic difference in deposition behavior and to define the limits of validity of the present results.

Figure 4 presents the deposition as a function of particle material density, as computed for turbulent pipe flow from equation (B.26) of Appendix B.

The numerical solution for deposition velocity as obtained from equation (C.2) is shown in Figure 5, which presents deposition velocity as a function of particle radius for Re = 10^5. For illustrative purposes, computations were made for a noncoagulating, polydisperse aerosol with $\rho_p/\rho_f = 1110$ and $a_o/R = 10^{-5}$. The centerline number concentration distribution was taken to be log-normal with respect to particle radius, i.e.,

$$\hat{n}_i(\hat{a}) = \frac{\exp\left[-(\ln \hat{a})^2/2\sigma_o^2\right]}{\sqrt{2\pi}\,\sigma_o \exp(\sigma_o^2/2)}$$

where σ_o is the geometric standard deviation, taken to be 0.10 here.

Also shown in Figure 5 is the deposition velocity as predicted by the approximate analytical solution. The analytical result is consistently somewhat less than the numerical solution, but the difference is definitely less than the scatter in experimental data. Thus, the analytical result gives a useful and reasonably faithful representation

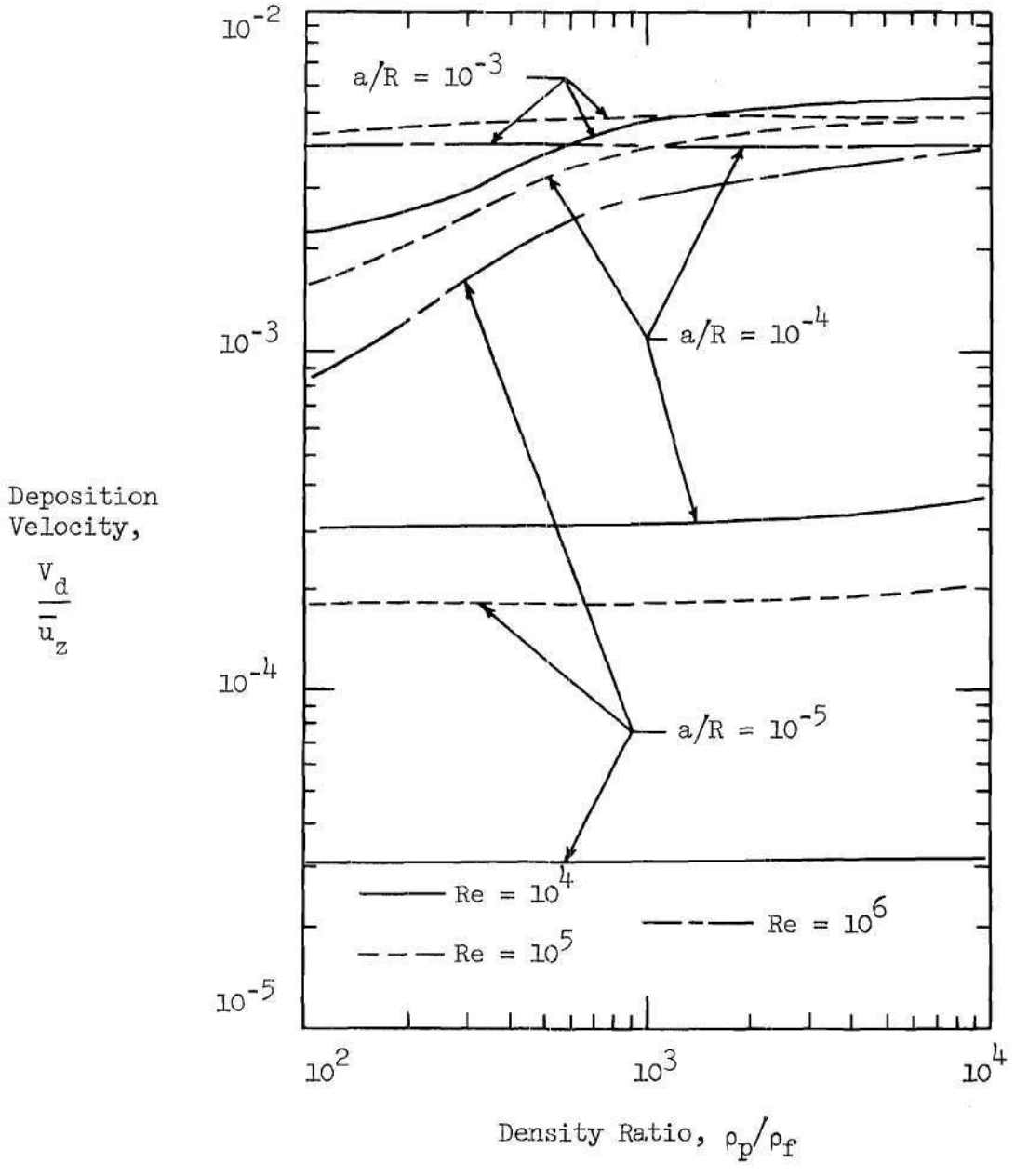

Figure 4. Deposition as Function of Particle Material Density for Various Radii, as Given by Analytical Solution

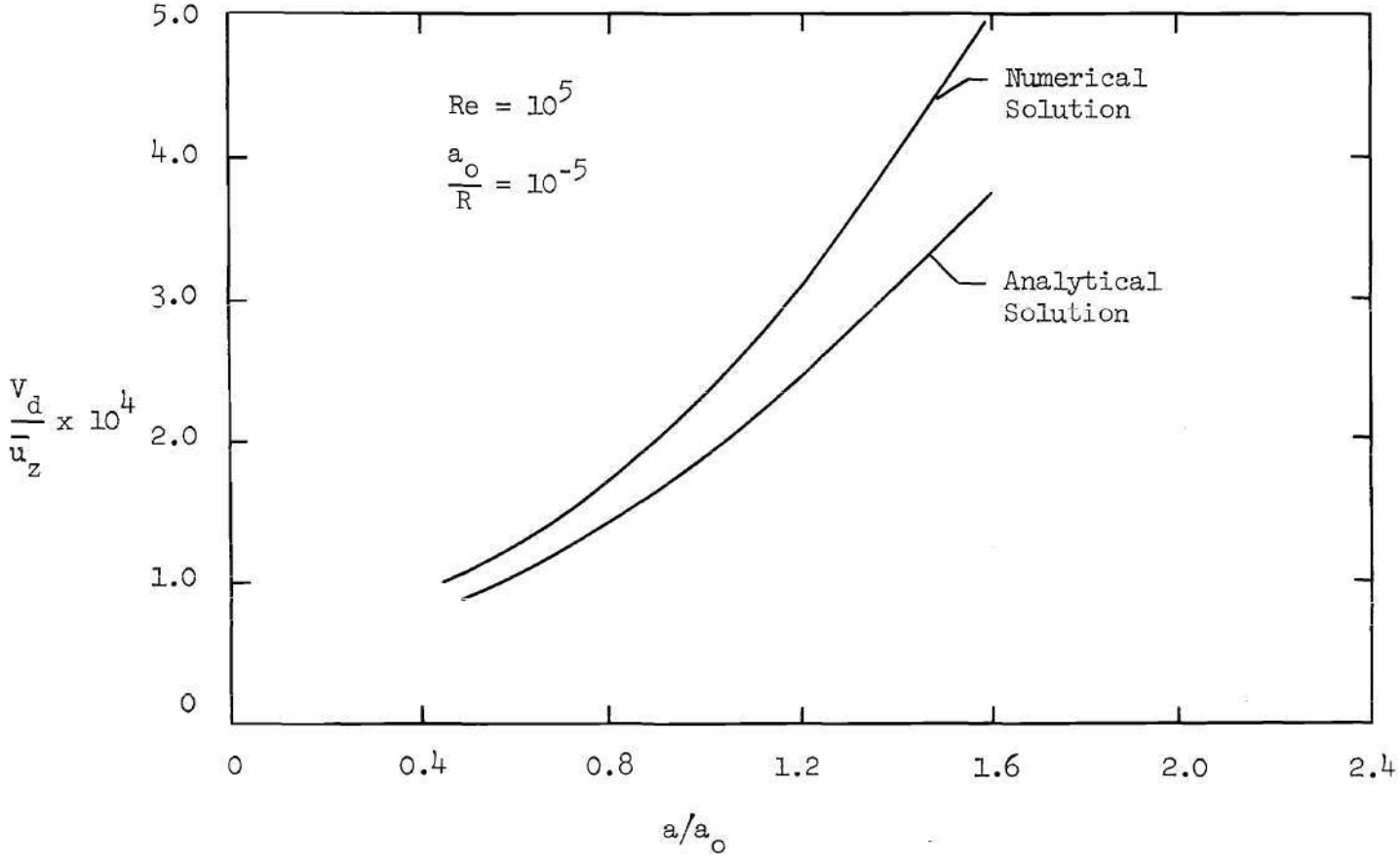

Figure 5. Comparison of Numerical and Analytical Results for Deposition as a Function of Particle Radius

of the numerical solution for noncoagulating aerosol deposition. The question to be resolved, however, is how significant can the effects of particle coagulation be on particle deposition? This question is the subject of a later chapter, which examines numerical solutions for coagulating, polydisperse aerosol deposition.

On the basis of the results of this portion of the study several remarks can be made.

1. The application of the mixing-length hypothesis for aerosol deposition from turbulent flows has made available analytical expressions for deposition velocities, i.e., equation (B.26) for axisymmetric pipe flow and equation (B.37) for boundary-layer flow.

2. Comparison of results predicted by these expressions with the results of some detailed numerical solutions and with available experimental data indicates that the mixing-length hypothesis appears to contribute improvement in available theoretical prediction capability in the fully-developed turbulent flow regime.

3. Although a significant quantity of data exists for Re less than about 10^4, the limited amount of experimental data which exist at higher Reynolds numbers indicate that extrapolations of lower Re data are not valid. There exists a need for additional data in this flow regime both to more clearly indicate this basic difference in deposition behavior and to define the limits of validity of the present results.

CHAPTER III

COAGULATING AEROSOL DEPOSITION IN THE ABSENCE OF ELECTRICAL FORCES

This chapter presents an extension of the results of Chapter II to include numerical solutions for coagulating liquid aerosol concentration distributions and surface deposition characteristics for turbulent pipe flow. Chapter II outlined an analytical approach for conveniently predicting, with reasonable accuracy, noncoagulating aerosol deposition from fully developed turbulent pipe flow and from two-dimensional turbulent boundary-layer flow. In addition, presented were results of some associated numerical solutions for the noncoagulating case. The question left unresolved by those results was how significant can the effects of particle coagulation be on particle deposition? This problem represents the basis for the present chapter.

The time-averaged equation of continuity for an isothermal, aerosol system with constant fluid mass density can be written as equation (2.4), wherein $n(a,\vec{x},t)$ is the time-averaged number concentration distribution function of particles of radius a; t is time; $\vec{u}$ is the particle time-averaged velocity vector; I is the rate of change of number concentration, n, as a result of coagulation; and $\vec{J}$ is the mass flux of particles of radius a. As in Chapter II, the mixing-length hypothesis is employed and the following additional relations are adopted:

$$u_z = u_{z_o} \left(1 - \frac{r}{R}\right)^{1/m} \tag{3.1}$$

and $$\ell \cong 0.14\ R \sqrt{y/R},\ \text{for}\ 0 \leq y \leq R. \tag{3.2}$$

An expression for the coagulation term, I, of equation (2.4) is developed in the following section. The development in Chapter II regarding the wall boundary condition resulting from the mixing-length hypothesis is followed herein, i.e., equation (2.7) is again used. As discussed in Chapter II this expression relates the number concentration and the gradient of the concentration at this point and constitutes the required wall boundary condition for the solution to equation (2.4).

Turbulent Coagulation Model

The rate of coagulation of particles is based on the assumption that all inter-particle collisions result in coagulation of the particles into a single spherical particle whose volume is the sum of the volumes of the two colliding particles. Only binary collisions are considered, and de-agglomeration is assumed non-existent. Thus, one must determine the collision rate between particles. In the absence of electrical charges on individual particles, several collision mechanisms can be identified. Among these are Brownian motion, velocity-gradient induced collisions, and turbulence induced collisions. Brownian motion

is a result of particle collisions with gas molecules, which are in constant thermal motion. Velocity-gradient coagulation occurs as a result of two particles moving along pathlines with different velocities. If the distance between pathlines is less than the sum of the radii of the two particles, then a collision will occur.

There are two mechanisms for collisions involving particles suspended in a turbulent medium. The first is due to spatial variations in fluctuation velocities within the medium, whereas the second is due to turbulent induced accelerations of partially entrained particles. In regard to the latter instance, the response of individual particles will depend on their masses and sizes, and hence, a mechanism for collision of different size particles is generated. It is this latter mechanism which is taken to be the predominant one for the present study. According to Saffman and Turner [17], the number of collisions experienced by particles of radius a_1 to $a_1 + da_1$ with particles of radius a_2 to $a_2 + da_2$ per unit time and volume for this second turbulent mechanism is given by

$$K_{12} = \pi \frac{\rho_p}{\rho_f} \frac{\bar{\epsilon}_o^{3/4}}{\nu^{5/4}} (a_1 + a_2)^2 (a_1^2 - a_2^2)\, n(a_1) n(a_2) da_1 da_2 \qquad (3.3)$$

where ρ_p is the density of the aerosol particles, $\bar{\epsilon}_o$ is the rate of energy dissipation occurring in the flow per unit time and volume (the expression for pipe flow is given in equation (3.8), and ν is the kinematic viscosity

of the medium. A particle of class a_1 is removed upon each collision involving one of these particles, and a particle of class a_1 is generated by each collision involving two particles whose cumulative volume is equal to $4\pi a_1^3/3$. Thus, there is both a gain term and a loss term in the coagulation term, I, of equation (2.4). Considering all collisions, then one can write the net change in the number concentration of class a_1 as a result of coagulation as

$$I = \pi \frac{\rho_p}{\rho_f} \frac{\bar{\epsilon}_o^{3/4}}{\nu^{5/4}} \left[- \int_{a_z=0}^{\infty} (a_1 + a_2)^2 \left| a_1^2 - a_z^2 \right| n(a_1)\, n(a_2)\, da_2 + \right. \tag{3.4}$$

$$\left. \frac{1}{2} \int_{a_z=0}^{a_1} (a' + a_2)^2 \left| a'^2 - a_z^2 \right| n(a')\, n(a_2)\, \frac{a_1^2}{a'^2}\, da_2 \right\}$$

where $a' = (a_1^3 - a_2^3)^{1/3}$. The gain term is obtained by considering the total collision rate involving particles whose cumulative volume is that of a particle having radius a_1. The energy dissipation is a function of the particular flow of interest and is given later when specific examples are considered.

Numerical Solutions

The governing equation to be solved is equation (2.4) simplified for steady-state, axisymmetric pipe flow conditions, with the particle

mass flux given by equation (2.6) and the coagulation term replaced by equation (3.4). The dependent function, $n(a, \vec{x})$ is a function of three variables; namely particle radius, a; and spatial coordinates r and z. However, the dependence with respect to a appears explicitly only in the coagulation integrals of equation (3.4). The governing equation lends itself to numerical solution by the so-called discrete-ordinate method which has been used extensively and successfully to solve the integrodifferential equations of the theory of radiative transfer, Chandrasekhar [18], and in the study of nonequilibrium rarefied gas dynamics, Giddens [19], Huang and Hartley [20], [21]. This technique consists of replacing the integration over particle-radius space of the number concentration distribution function in the continuity equation by an appropriate quadrature. This requires approximating the particle-radius dependence of the number concentration by a set of functions, each evaluated at selected discrete points in particle-radius space. The number of discrete points used reflects the degree of approximation desired. The problem is transformed into finding a solution for a system of coupled, partial differential equations in a set of functions which are continuous in spatial dependence but are point-functions in particle-radius space.

Define nondimensional variables as follows:

$$\hat{r} = r/R \ , \qquad \hat{n} = n\, a_o/N_o \ , \qquad \hat{a} = a/a_o;$$

$$\hat{z} = z/R \ , \qquad \hat{U}_z = U_z/U_{z_o} \ , \qquad (U_{z_o} = U_z(r = 0));$$

where $\int_{a=0}^{\infty} n_o \, da = N_o$ and n_o is the centerline number concentration distribution function at $\hat{z} = 0$. Now using equations (2.6), (3.1), and (3.2) in equation (2.4) one can write the equation to be solved in nondimensional form as

$$\frac{u_{z_o} N_o}{a_o R} (1 - \hat{r})^{1/m} \frac{\partial \hat{n}}{\partial \hat{z}} = \frac{0.0196 \, u_{z_o}}{m} \left(\frac{N_o}{a_o R}\right)(1 - \hat{r})^{1/m} + \tag{3.5}$$

$$\left\{ \frac{\partial^2 \hat{n}}{\partial \hat{r}^2} + \left[\frac{1}{\hat{r}} - \frac{1}{m(1-\hat{r})}\right] \frac{\partial \hat{n}}{\partial \hat{r}} \right\} + I$$

The coagulation term becomes

$$I = \pi \frac{\rho_p}{\rho_f} \frac{\bar{\varepsilon}_o^{3/4}}{\nu^{5/4}} a_o^3 N_o^2 \left\{ - \int_{\hat{a}_z=0}^{\infty} K(\hat{a}, \hat{a}_2) \, d\hat{a}_2 + \right. \tag{3.6}$$

$$\left. \tfrac{1}{2} \int_{\hat{a}_z=0}^{\hat{a}} K(\hat{a}', \hat{a}_2) \left(\frac{\hat{a}}{\hat{a}'} \right)^2 d\hat{a}_2 \right\}$$

where, for example,

$$K(\hat{a}, \hat{a}_2) = (\hat{a} + \hat{a}_2)^2 \, |\hat{a}^2 - \hat{a}_2{}^2| \, \hat{n}(\hat{a}) \, \hat{n}(\hat{a}_2) \tag{3.7}$$

and again $\hat{a}' = (\hat{a}^3 - \hat{a}_2{}^3)^{1/3}$.

The rate of energy dissipation, $\bar{\epsilon}_o$, can be represented by the expression [46]

$$\epsilon_o = \ell^2 \left|\frac{du_z}{dr}\right|^3 \tag{3.8}$$

which closely approximates the experimental results obtained by Laufer [22]. Thus, the equation to be solved can be written as

$$\frac{\partial \hat{n}}{\partial \hat{z}} = \frac{0.0196}{m} \left\{ \frac{\partial^2 \hat{n}}{\partial \hat{r}^2} + \left[\frac{1}{\hat{r}} - \frac{1}{m(1-\hat{r})} \right] \frac{\partial \hat{n}}{\partial \hat{r}} \right\} + \tag{3.9}$$

$$P(\hat{r}) \left\{ -\int_{\hat{a}_2=0}^{\infty} K(\hat{a}, \hat{a}_2) \, d\hat{a}_2 + \tfrac{1}{2} \int_{\hat{a}_2=0}^{\hat{a}} K(\hat{a}', \hat{a}_2) \left(\frac{\hat{a}}{\hat{a}'} \right)^2 d\hat{a}_2 \right\}$$

where

$$P(\hat{r}) = \frac{\pi}{2^{5/4}} \frac{\rho_p}{\rho_f} \frac{1}{\bar{\hat{u}}_z^{5/4}} \frac{Re^{5/4}}{(1-\hat{r})^{1/m}} \left(\frac{a_o}{R} \right) (a_o^3 N_o) \left(\frac{\ell}{R} \right)^{3/2} \left| \frac{d\hat{u}_z}{d\hat{r}} \right|^{9/4} \quad (3.10)$$

and

$$\frac{\ell}{R} = 0.14 \sqrt{1 - \hat{r}} \quad (3.11)$$

$$\hat{u}_z = (1 - \hat{r})^{1/m} \quad (3.12)$$

The number concentration distribution is discretized with respect to particle radius, and thus equation (3.9) becomes

$$\frac{\partial \hat{n}_i}{\partial \hat{z}} = \frac{0.0196}{m} \left\{ \frac{\partial^2 \hat{n}_i}{\partial \hat{r}^2} + \left[\frac{1}{\hat{r}} - \frac{1}{m(1-\hat{r})} \right] \frac{\partial \hat{n}_i}{\partial \hat{r}} \right\} + \quad (3.13)$$

$$T_i(\hat{z}, \hat{r}), \; i = 1, 2, \ldots$$

where $\hat{n}_i$ represents $\hat{n}(a_i)$ and $T_i(\hat{z}, \hat{r})$ is the coagulation term of equation (3.9) evaluated for $\hat{a} = \hat{a}_i$. The solution to this system of equations is approximated by the solution to an associated set of finite-difference equations obtained from equation (3.13). The region of

physical space is covered with a set of discrete points aligned along the radial and axial coordinate directions, as illustrated in Figure 6. The derivatives appearing in equation (3.13) are replaced by the following finite-difference approximations:

$$\frac{\partial \hat{n}_i}{\partial \hat{r}} \cong \frac{1}{2(\Delta \hat{r})} \left[\hat{n}_{i,j+1,k} - \hat{n}_{i,j+1,k} \right] \tag{3.14}$$

$$\frac{\partial^2 \hat{n}_i}{\partial \hat{r}^2} \cong \frac{1}{(\Delta \hat{r})^2} \left[\hat{n}_{i,j+1,k} - 2\hat{n}_{i,j,k} + \hat{n}_{i,j-1,k} \right] \tag{3.15}$$

$$\frac{\partial \hat{n}_i}{\partial \hat{z}} \cong \frac{1}{(\Delta \hat{z})} \left[\hat{n}_{i,j,k+1} - n_{i,j,k} \right] \tag{3.16}$$

Note that the radial derivatives are replaced by central differences, whereas, the axial derivative is replaced by a simple forward-difference approximation. equation (3.13) becomes

$$\hat{n}_{i,j,k+1} = \hat{n}_{i,j,k} + \frac{0.0196}{m} \frac{\Delta \hat{z}}{(\Delta \hat{r})^2} \left\{ \left[1 + \frac{\Delta \hat{r}}{2} \left(\frac{1}{\hat{r}} - \frac{1}{m(1-\hat{r})} \right) \right] \hat{n}_{i,j+1,k} \right. \tag{3.17}$$

(Equation Continued)

$$2\hat{n}_{i,j,k} - \left[\frac{\Delta\hat{r}}{2}\left(\frac{1}{\hat{r}} - \frac{1}{m(1-\hat{r})}\right) - 1\right]\hat{n}_{i,j-1,k}\Big\} - (\Delta\hat{z})\,T_{i,j,k}$$

Thus, an explicit calculation algorithm is generated, and one can "march" the solution downstream from an initial axial position at which the number concentration is known. The boundary condition at the pipe centerline is $\left(\frac{\partial\hat{n}_i}{\partial\hat{r}}\right)_{\hat{r}=0} = 0$, and the boundary condition near the wall is given by equation (2.7).

There is an apparent difficulty in the computation at $\hat{r} = 0$, since one notes the term $\frac{1}{\hat{r}}\frac{\partial n}{\partial r}$ in equation (3.5). However, this is eliminated by noting that the symmetry requirement at $\hat{r} = 0$ gives $\frac{\partial\hat{n}}{\partial\hat{r}} = 0$. Thus, L'Hospital's rule gives

$$\lim_{\hat{r}\to 0}\frac{1}{\hat{r}}\frac{\partial\hat{n}}{\partial\hat{r}} = \lim_{\hat{r}\to 0}\frac{\partial^2\hat{n}}{\partial\hat{r}^2} \tag{3.18}$$

Thus, at $\hat{r} = 0$, equation (3.5) is replaced by

$$\frac{u_{z_o} N_o}{a_o R}(1-\hat{r})^{1/m}\frac{\partial\hat{n}}{\partial\hat{z}} = \frac{0.0196\,u_{z_o}}{m}\left(\frac{N_o}{a_o R}\right)(1-\hat{r})^{1/m}\left[2\frac{\partial^2\hat{n}}{\partial\hat{r}^2}\right] + I \tag{3.19}$$

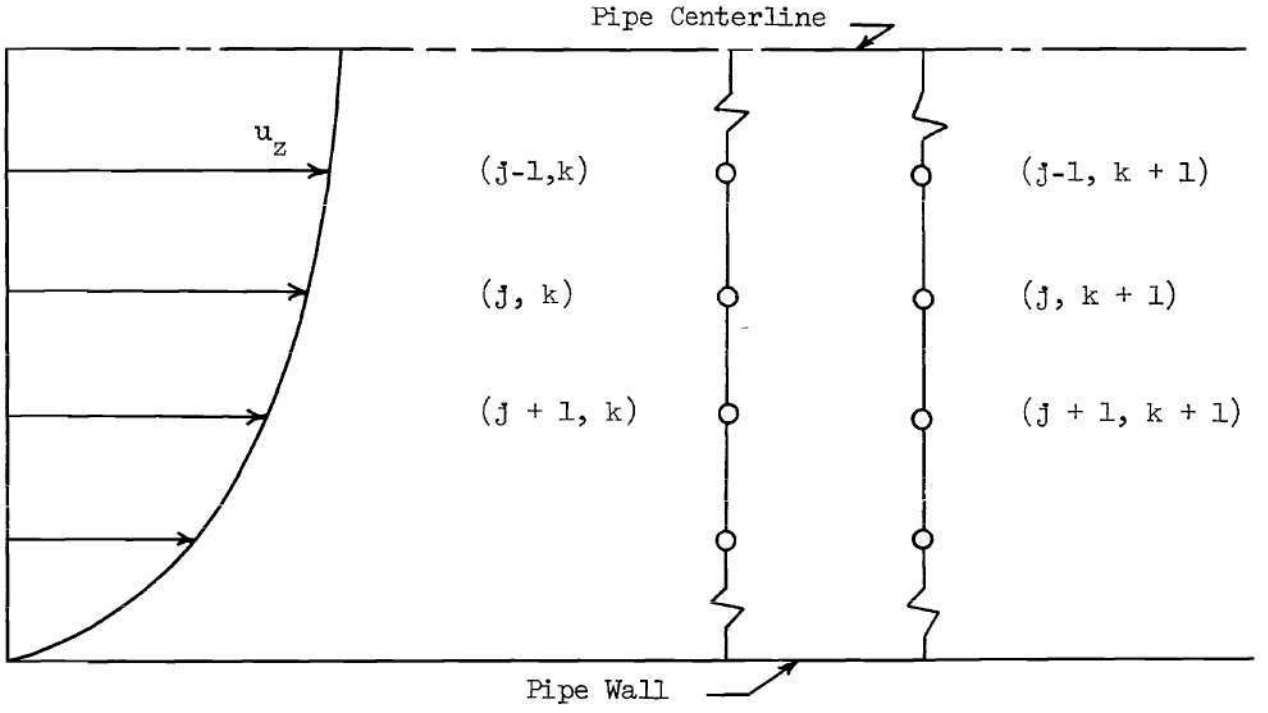

Figure 6. Finite-Difference Grid System

The finite-difference formulation for $\hat{r} = 0$ is modified accordingly.

Discussion of Results

The following parameters were chosen for illustrative computations.

$$Re = 10^5, \qquad a_o = 10^{-4} \text{ cm},$$

$$\rho_p/\rho_f = 1110, \qquad a_o/R = 10^{-5},$$

$$N_o = 10^6 \text{ cm}^{-3}$$

Although the value of N_o chosen is rather high for typical concentrations produced by spinning-disc aerosol generators, it was noted that it appears only in the coagulation integrals. Since the most significant effect which coagulation could produce was the subject of the investigation, a somewhat high value of N_o was desirable.

The solution, obtained from equation (3.17) was begun at an axial position at which the aerosol number concentration was taken to be uniform with respect to radial position and log-normal with respect to particle radius, i.e.,

$$\hat{n}_i(\hat{a}) = \frac{\exp\left[-(\ln \hat{a})^2/2\sigma_o^2\right]}{\sqrt{2\pi}\,\sigma_o \exp\left(\sigma_o^2/2\right)} \tag{3.20}$$

where σ_o is the geometric standard deviation. The solution was obtained from $\hat{z} = 0$ to $\hat{z} = 4.27$ with $\Delta\hat{z} = 0.07$. Particle number concentrations for discrete radii from $\hat{a} = 0.5$ to $\hat{a} = 1.48$ with $\Delta\hat{a} = 0.02$ were obtained at each axial location, and discrete deposition velocities were computed. Since the number concentrations vary with particle radius, the deposition velocities were converted to deposition fluxes by multiplying each deposition velocity by the respective relative centerline number concentration.

Figure 7 presents the concentration distribution as a function of particle radius near the wall ($\hat{r} = 0.96$) at two longitudinal locations ($\hat{z} = 0$ and 4.27). One expects that coagulation reduces concentrations near the peak and increases concentrations most rapidly for particles whose volumes are twice those of the initially maximum concentration. Deposition, of course, reduces the concentration of all particles. It is apparent that effect of coagulation outweighs deposition for the larger particles, as their concentration increases in the downstream direction.

Figure 8 presents equivalent results for particles at the pipe centerline. The effect upon centerline concentration distribution is barely discernable, even at $\hat{z} = 4.27$. The marked effect of coagulation near the wall is apparently due to the low mean velocity there and the consequent long coagulation time relative to that for particles near the higher velocity centerline region. It is interesting to note that the radial concentration distribution of the larger particles may thus increase as one proceeds from the centerline toward the wall, although it will drop very close to the wall as a result of deposition. Thus,

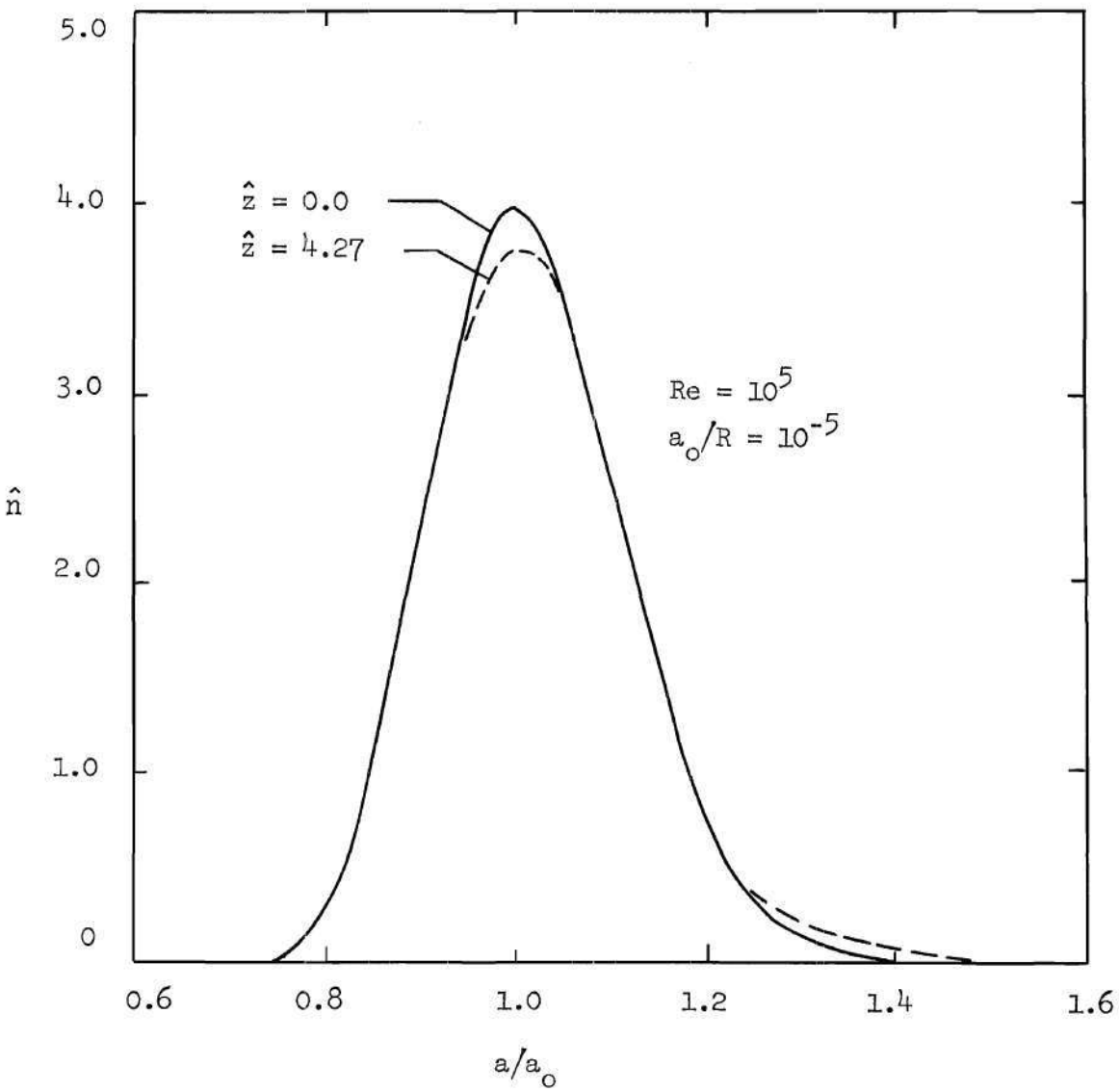

Figure 7. Number Concentration Distribution Function at Two Longitudinal Locations ($\hat{r}$ = 0.96)

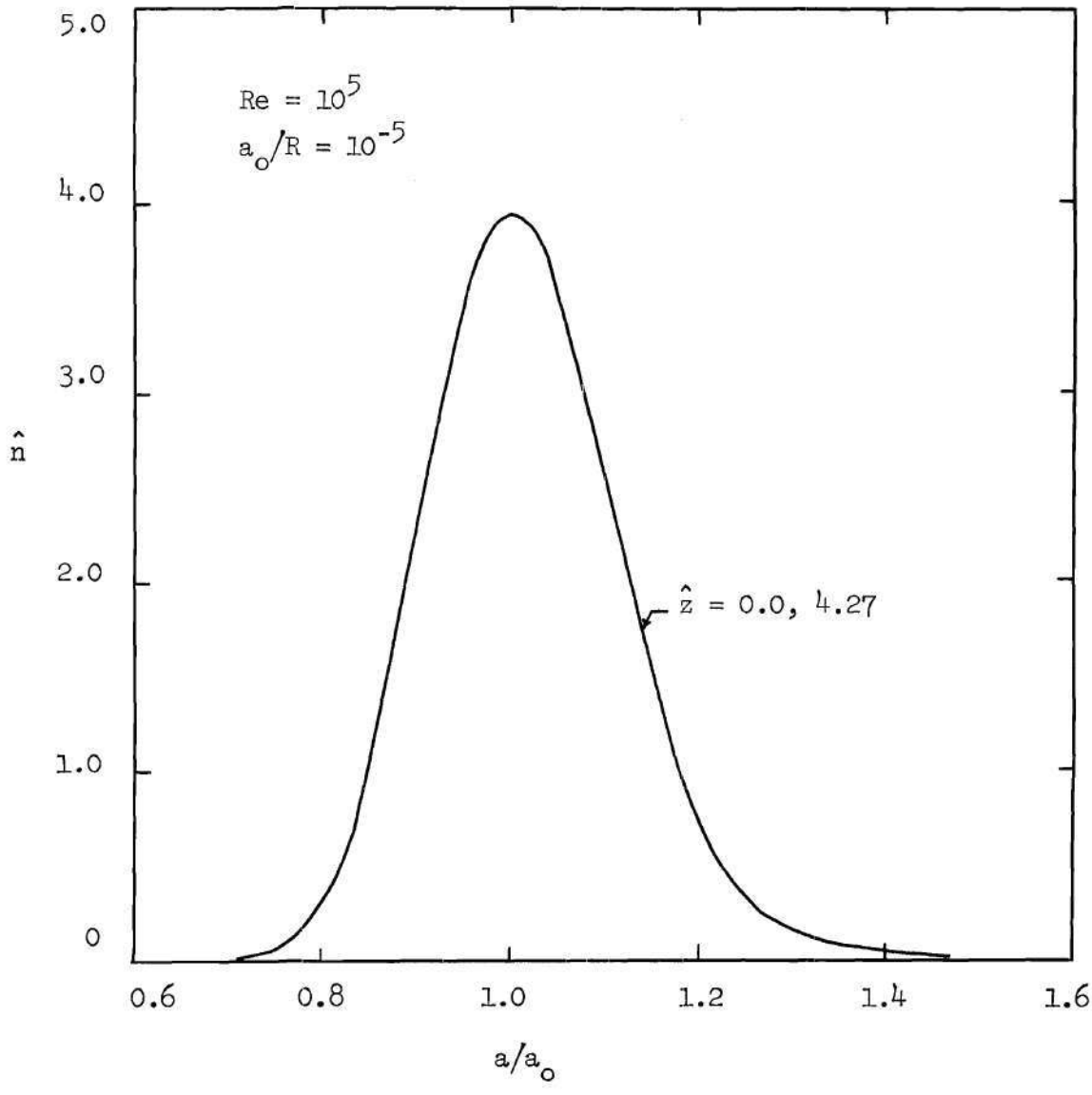

Figure 8. Number Concentration Distribution Function at Two Longitudinal Locations ($\hat{r}$ = 0.0)

for these particles, there is a simultaneous diffusion both toward the centerline and toward the wall, with maximum concentration occurring somewhere in between them.

Figure 9 presents several radial concentration profiles at $\hat{z} = 4.27$. It is apparent that the assumption made earlier with regard to the small relative change in concentration across the pipe radius is quite reasonable for particle sizes near that at peak concentration $\left(\frac{a}{a_o} = 1.0 \right)$.

Figure 10 presents deposition velocity as function of particle size both with and without effect of coagulation. As expected, the effect of coagulation is large for the larger particles; however, since the deposition flux is defined as $V_{d_i} \bar{n}_i / \bar{u}_z$, and since the average concentration of the larger particles is small, the net flux to the wall for the larger particles is still very small (this is indicated in Figure 11).

Figure 11 presents the deposition flux at two axial locations, $\hat{z} = 0.07$ and $\hat{z} = 4.27$. The net deposition velocity, obtained by integrating the flux with respect to particle radius, is seen to decrease as one proceeds downstream. Also shown in Figure 11 is the deposition flux which would be predicted by the analytical solution, equation (B.26), for the same centerline number concentration distribution. The agreement is good, considering that the effects of coagulation were neglected in obtaining equation (B.26).

On the basis of the results presented in this chapter, several remarks can be made.

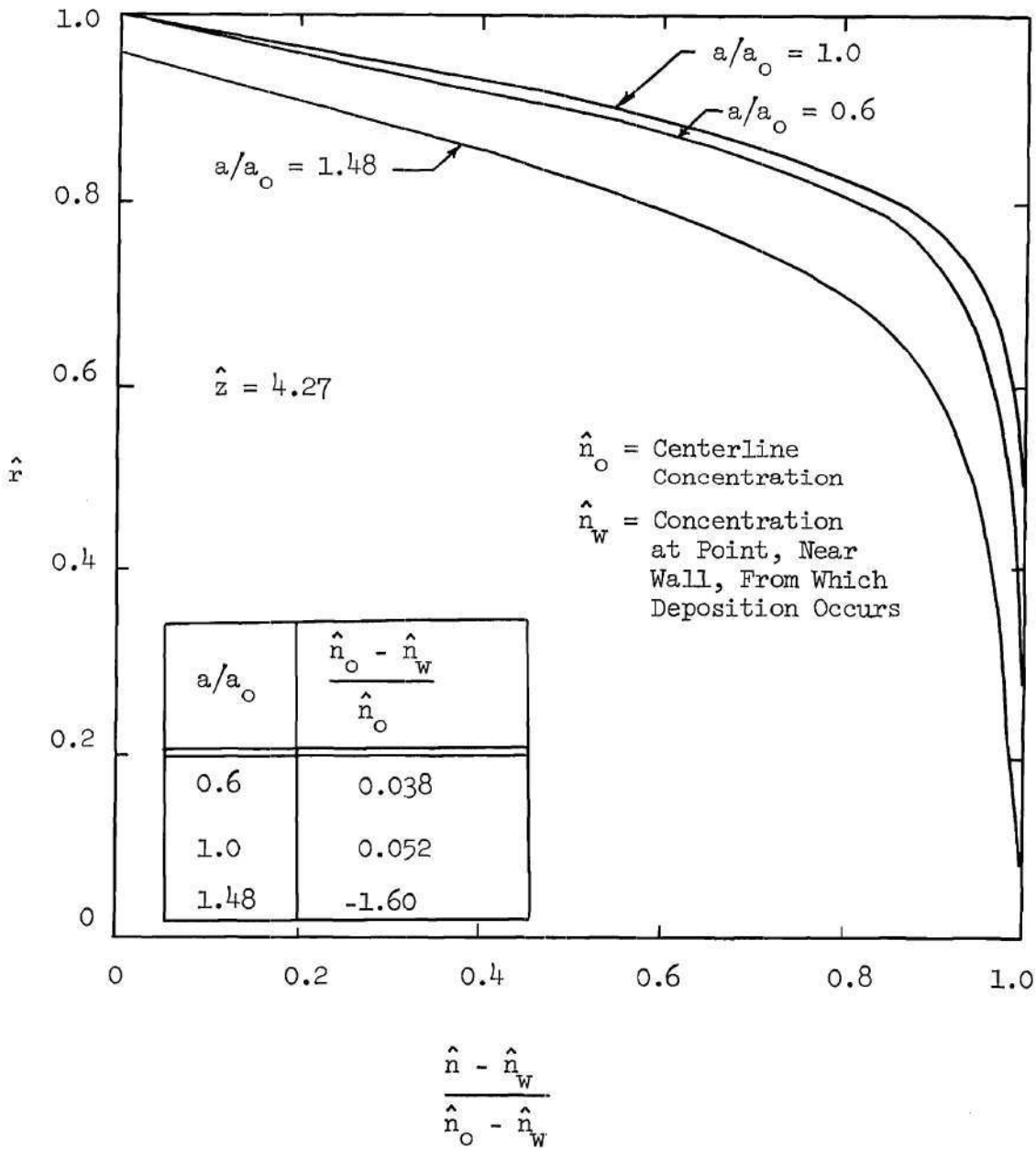

a/a_o	$\frac{\hat{n}_o - \hat{n}_w}{\hat{n}_o}$
0.6	0.038
1.0	0.052
1.48	-1.60

Figure 9. Number Concentration Radial Profiles for Three Discrete Particle Sizes

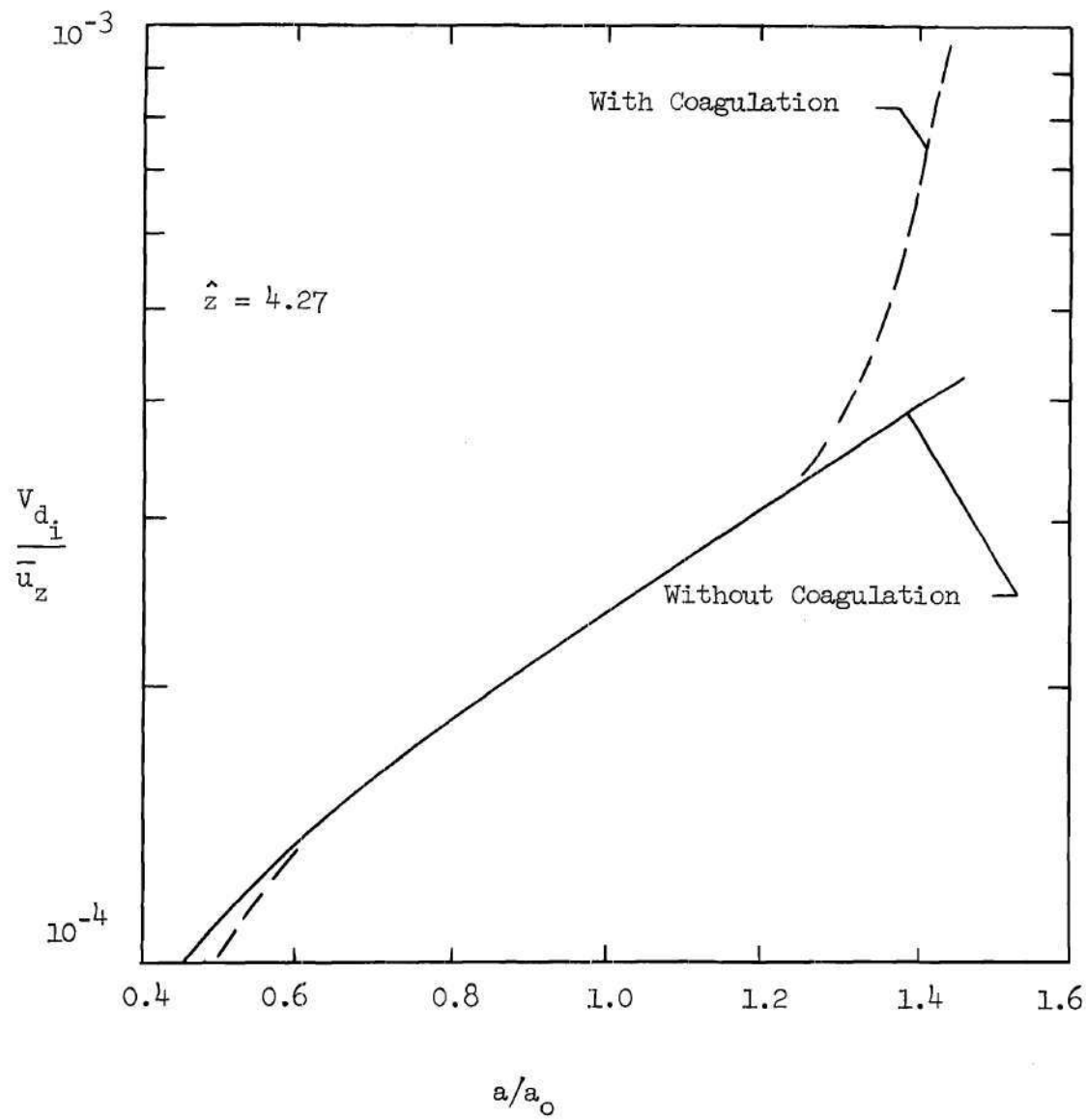

Figure 10. Deposition Velocity as a Function of Particle Size Both With and Without Effect of Coagulation

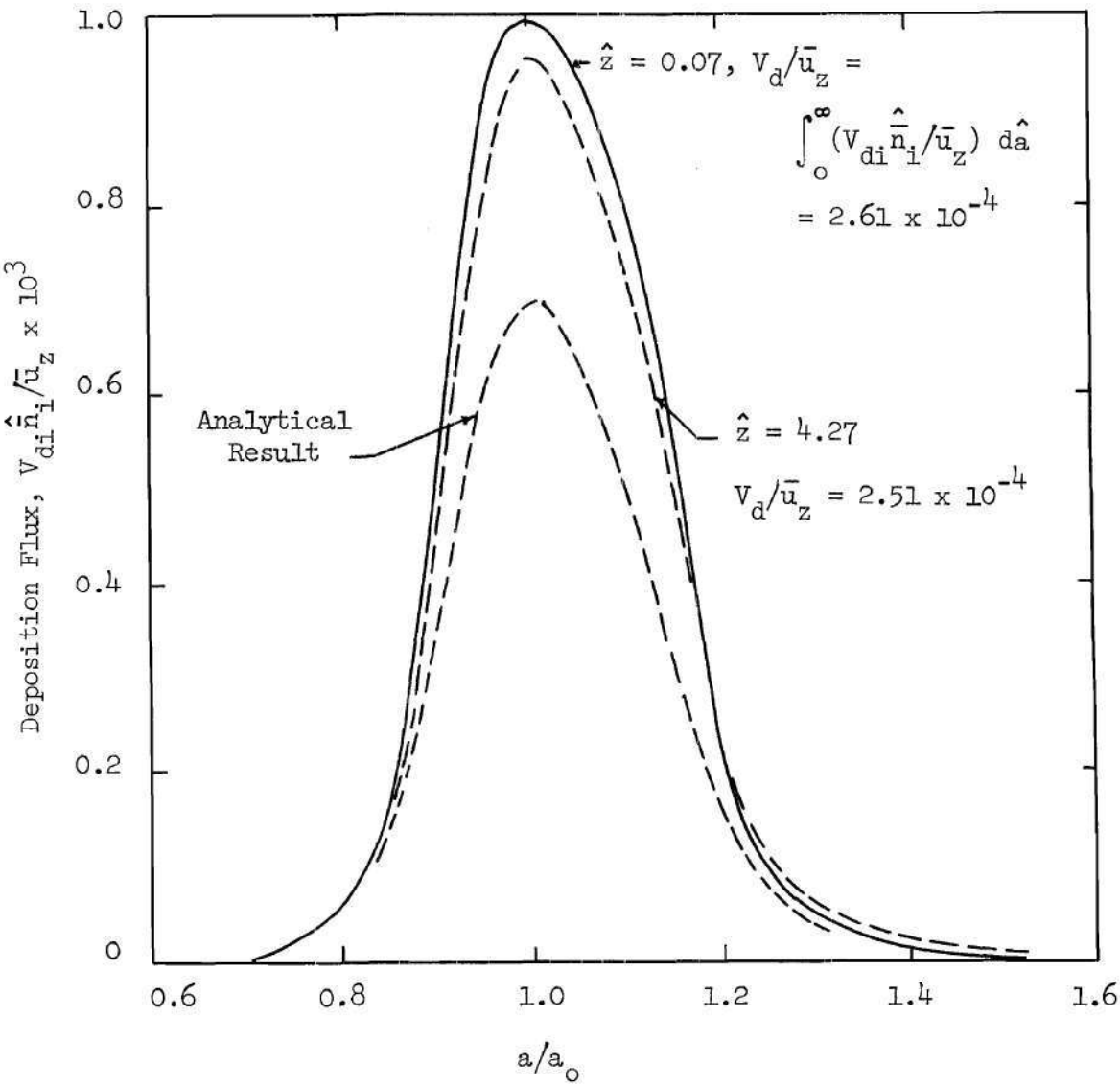

Figure 11. Deposition Flux as a Function of Particle Size at Two Longitudinal Locations

1. Comparison of results obtained for coagulating and noncoagulating aerosols indicates that for the representative cases considered there is little influence upon total deposition as a result of coagulation. However, the influence of coagulation upon the flow dynamics and deposition of aerosols in the presence of electrical forces remains as an important unknown.

2. The lack of experimental data with which to compare results of this effort indicates that such data are needed to provide a foundation for establishing some degree of confidence when attempting to deal with problems involving deposition of coagulating aerosols.

CHAPTER IV

AEROSOL DEPOSITION IN THE PRESENCE OF ELECTRICAL FORCES

This chapter presents an introduction to the problem of predicting aerosol deposition behavior in the presence of significant electrical forces, including some discussion of the current importance associated with being able to describe this phenomenon theoretically and a formulation of the equations which hopefully model to an acceptable degree the physics embodied within this deposition problem. After a review of background material, including an examination of the salient elements of the relevant literature devoted to this topic, consideration is directed toward identifying those important physical aspects of the problem which require realistic modeling and to those assumptions which are incorporated into the analysis to keep the mathematical development at least tractable.

Background and Perspective

The analysis presented in the previous chapters has excluded the effects of electrical forces for the sake of relative simplicity. However, electrical forces arising from electrostatic charges are almost always present in fluid-particle systems, and, quite often, are responsible for a preponderant influence on the mass transport processes in such systems. Sometimes this influence is intentional from the design viewpoint, as in such important applications as electrostatic precipitation, xerography, and colloidal propulsion, among others. At other times,

electrostatic charges are the result of natural phenomena and influence such important behavior as cloud droplet formation and deposition of atmospheric dusts.

The emphasis here is, by choice, focused toward the electrostatic precipitation problem both for its importance from an environmental standpoint and because the flow geometries encountered in the electrostatic precipitation design problem are akin to those of traditional interest to the fluid dynamicist, e.g., turbulent pipe flow and turublent boundary-layer flow.

Since about 1908, the electrostatic precipitator has provided an important solution to many gas-cleaning problems. In spite of many improvements, achieved primarily by cut-and-try techniques, the basic system has remained essentially unchanged since its inception. Although the initial work, dating from as early as 1824, was essentially empirical in approach, some effort directed toward a fundamental understanding of the physical aspects involved in the process began about 1920 and has continued on a generally increasing scale since that time, particularly since the 1950's. Today, the technology available to the electrostatic-precipitator designer and builder can be described as moderately well understood with respect to the traditional system. Unfortunately, it appears that the empiricism still required in the design and development phase of industrial electrostatic precipitator systems has provided a constraint on the capability to implement significant new design ventures without an investment in prototype plant developments. There exists a need for reliable analytical prediction techniques in order that novel approaches may be evaluated for effectiveness. A brief

overview of the theoretical techniques available may be useful in illustrating this point.

In any electrostatic precipitation or electro-deposition process, suspended particles within the gas to be cleaned are inititally electrically charged and are subsequently removed or "stripped" from the gas by means of some combination of inertial and electrical forces developed upon the particles, which are deposited as a result upon a surface bounding the gas. Particle charging is almost universally accomplished by means of corona-discharge techniques, and an electric-field provides the necessary separating forces for particle removal. The gas flows encountered in industrial gas-cleaning operations are usually turbulent, and therefore one is concerned with predicting the behavior of charged particles suspended within a turbulent gas flow and subjected to the influence of an external electric field. Several efforts which are documented in the literature have been devoted to developing an understanding of this problem.

Deutsch [23] presented, in 1922, a theoretical formula for electrostatic-precipitator efficiency of the form

$$\eta = 1 - e^{-Aw/\bar{V}} \tag{4.1}$$

where $$\eta = \frac{\text{weight of particles collected}}{\text{weight of particles entering}}$$

A = collecting surface area (cm^2)

$\overline{V}$ = gas volume flow rate (cm^3/sec)

w = particle "migration" velocity (cm/sec)

Although the Deutsch formula was derived on the basis of several somewhat arbitrary assumptions, its relative accuracy and ease of application have resulted in its being the basis of most precipitator design, perhaps with an empirically obtained effective migration or drift velocity inserted to improve agreement with experimental data.

White [24] obtained equations for particle collection efficiency, including the cases of steady and pulsating voltages, uniform and non-uniform particle size distributions, and pipe and duct precipitators. Collection is assumed to occur if a particle, as a matter of statistical probability happens to drift within a certain capture distance of the wall. This probability of being within a certain area is taken to be proportional to the ratio of this area to the cross-sectional area of the pipe or duct. Thus, turbulence in the precipitator is taken to be a mechanism for complete mixing which, in turn, yields a uniform particle concentration across any section of the duct. This latter assumption has been invalidated by the mass of experimental data available, which indicate quite important radial or transverse particle

concentration gradients. White's results yield the Deutsch equation, although derived on a different basis; however, White recognized the discrepancy between his results and experimental data and recommended the use of the Deutsch equation with modified values of w determined from actual field experience.

Friedlander [25] recognized the necessity of including the effect of eddy diffusion in the analysis and obtained an approximate solution to the continuity equation with the particle concentration assumed zero at the wall. He obtained an efficiency equation similar to the Deutsch equation but having a correction term, depending on the wall friction, appearing in the exponential term. The result again involves the yet-to-be determined effective drift velocity, which requires experimental determination.

Williams and Jackson [26] obtained results for the theoretical efficiency of an electrostatic precipitator by considering the effect of radial eddy diffusion of particles but otherwise retaining all the other assumptions made by Deutsch, i.e.,

(i) at the inlet to the precipitator the particle concentration is spatially uniform across the section,

(ii) all particles have the same drift velocity, which is attained instanteously upon entering the precipitator.

(iii) the drift velocity is spatially invariant and is independent of particle concentration,

(iv) all particles reaching a wall adhere to it.

Williams and Jackson obtain a numerical solution to the time-averaged continuity equation for particle concentration,

$$w \frac{\partial C}{\partial x} + v \frac{\partial C}{\partial y} = \frac{\partial}{\partial x} \left(D \frac{\partial C}{\partial x} \right) \qquad (4.2)$$

where w is the electrically induced drift velocity of the particles, and D is their eddy diffusivity. The y-coordinate direction is along the primary flow direction within the electrostatic precipitator. The boundary conditions imposed by Williams and Jackson are

$$C = C_o \quad \text{at} \quad y = 0,$$

$$D\partial C/\partial x - wC = 0 \quad \text{at} \quad x = 0,$$

and $$\partial C/\partial x = 0 \quad \text{at} \quad x = b \text{ (at the wall)},$$

where the latter condition is imposed to be compatible with their assumption that D decreases discontinuously to zero at the wall [26]. They replace the x-derivatives by finite-difference approximations and obtain a system of ordinary differential equations in the y-direction. The system is solved by a Runge-Kutta method programmed for digital computer computation. Their result is again dependent upon an empirically derived drift velocity, and they obtain concentration profiles which result in turbulent diffusion away from the deposition wall, a result directly

contrary to Friedlander's model [25].

Inyushkin and Averbukh [27] attempt to incorporate into the basic Deutsch equation a term to account for the effect of turbulence on deposition. They cite an expression for particle deposition from a turbulent gas stream in the absence of electrical forces, of the form

$$\eta = 1 - e^{-A\overline{K}/\overline{V}} , \tag{4.3}$$

where $\overline{K}$ is a coefficient of particle collection, so called, which is a function of Reynolds number. Combining this equation with equation (4.10) with the assumption of additivity of effects, they obtain

$$\eta = 1 - e^{-A(w+\overline{K})/\overline{V}} \tag{4.4}$$

Cooperman [28] proposed a model of the precipitation process based on the coextensive mechanisms of turbulent diffusion, electrostatic migration, and particle re-entrainment from the wall. As does Friedlander [25], Cooperman takes the particle concentration to be zero at the wall under conditions of zero re-entrainment. Re-entrainment is accounted for by a probability of re-entrainment, but it is required that this parameter be obtained empirically. Cooperman does not present numerical solutions to the proposed model, however.

Robinson [29] attempts to obtain a modification to the Deutsch efficiency equation to account for the effects of particle re-entrainment and nonuniformity of particle concentration across the precipitator cross section. His approach represents an effort to retain the simplicity of the original Deutsch relation, yet to meet, in some measure, some of the more serious objections to the old theory. Similar assumptions are made relative to those of Inyushkin and Averbukh [27] with respect to turbulent diffusion and inertial penetration of the diffusivity "barrier" at the wall. As do Williams and Jackson [26] , Robinson [29] takes the diffusive particle transport to be zero at the wall and accounts for particle re-entrainment in terms of two particle fractions, one having a given nonzero probability of permanent deposition and the other having a zero probability. Because of re-entrainment, the particle net deposition is not an exponentially decreasing function of precipitator size, as in the Deutsch relation, although the flux toward the wall does remain exponential. Robinson points out, however, that it remains to be seen whether or not his approach will ultimately lead to useful prediction and design equations.

In a later paper, Robinson [30] notes that under electrical and fluid flow conditions similar to those that often occur in practice, the effect of the electrical wind, so called, appears to make a significant contribution to transverse gas flow, and he suggests that this effect should be considered in any analysis of precipitator performance. However, during the colloquium on electrostatic precipitation held in 1965, it was noted [31] that significant electric wind effects are observed only at ionization-current densities far above those values

normally encountered in practice. It was concluded that the influence of electric wind on overall separation efficiency can be neglected.

A somewhat different electrostatic precipitator design configuration was evaluated theoretically by Collier, et. al. [32], who applied electrogasdynamic principles to obtain approximate deposition results due solely to space-charge mutual repulsion of particles suspended in a very low speed flow within the collector section. They obtained an approximate solution to Poisson's equation for the space-charge field with the assumption that particle concentration is a spatial function of flow-stream coordinate only. Also presented are simplified analyses of ionization and particle charging performance of their precipitator. The importance of the work lies in the fact that it represents some effort to apply the basic concepts of electrogasdynamics to an electrostatic precipitator device which differs in basic design from the classical design introduced in 1908.

It would appear that with the exception of this latter effort, the theoretical prediction and design developments available to the precipitator designer are limited in application to the traditional design and in fact provide little basis for evaluating new design concepts. The assumptions and conclusions derived from these efforts are often contradictory, so that some clarification of physical behavior is needed with respect to electrogasdynamic applications.

Several example computations involving electrogasdynamics of particle suspensions are given by Soo [33]. Sufficient approximation was introduced into his analyses to permit analytical solutions for particle concentration to be found. Although results were obtained for

only the simplest of problems and are, in effect, restrained from generalization by the solution technique, the results are nevertheless interesting and provide further evidence of the potential offered by a numerical approach to a general formulation.

Formulation of Mathematical Model System

The approach taken here extends the earlier formulation of the fluid-particle system as a continuum with additional consideration of the momentum equations, Poisson's equation, and pertinent transport properties. As before, account is made for the distribution in the size of particles in the formulation by considering that particles of different sizes constitute different components of a continuum mixture. Those comments made earlier with respect to particulate phase concentration limits also apply here. The electric field intensity is taken to be governed by Poisson's equation of electromagnetic theory. However, specific reference to its solution is deferred until particular flow examples are considered, since, in the present formulation, this solution is based on simplifying assumptions indigenous to the particular example.

The formulation developed here is specifically oriented toward a reasonably accurate description of electrostatic deposition of charged aerosol particles within a variety of precipitator configurations. However, there are many aspects of current precipitator design and performance which, if included within the theoretical development, would hopelessly complicate the analysis and probably preclude the structuring of a useful solution, upon which the additional consideration of these

subsidiary aspects would seek to improve. Two important items of this type involve electrode sparkover and voltage waveform effects [34].

An attempt to include the effects of time-dependent voltage within the analysis would introudce another independent variable, time, into the problem. Formulation of the general unsteady problem represents a rather involved impediment to solution, especially with respect to computer storage requirements necessary to march an entire flowfield solution stepwise from t = 0. Perhaps a better approach is to solve the steady problem for voltages taken as root-mean-square voltages computed in the usual way from the time-dependent waveform. The steady-state solution might then be taken to represent the time-averaged solution of the equivalent unsteady problem in some cases.

Equations of Momentum and Continuity

The more common formulation of conservation equations for mixtures refers to the motion of the center of mass of the system, with individual component velocities identified with a diffusion flux through the mixture. It has been found [33] that when dealing with fluid-particle systems, it is often expedient and advantageous to consider the individual component velocities directly. The latter approach is followed here, and in order that the results be easily adapted to computations for physical systems, quantities readily identified with measurable properties are retained in favor of less easily measurable quantities.

The equations of momentum for species q = 1, 2, . . . , ν can be written with the conventional summation notation as [33]

$$\rho^{(q)} \frac{dU_i^{(q)}}{dt^{(q)}} = \frac{\partial}{\partial x_j}\left[- P^{(q)} \delta_{ji} + \mu_m{}^{(q)} \Delta_{ji}{}^{(q)} + \mu_{m2}\theta^{(q)}\delta_{ji}\right] + \quad (4.5)$$

$$\rho^{(q)} F_i{}^{(q)} - (U_i{}^{(q)} - U_{\Gamma_i}{}^{(q)}) \Gamma^{(q)} S(\Gamma^{(q)}) +$$

$$\rho^{(q)} \sum_{(p)} F^{(qp)} (U_i{}^{(p)} - U_i{}^{(q)})$$

where

$\rho^{(q)}$ is the density of species (q),

$U_i{}^{(q)}$ is the mean velocity component in the i^{th} coordinate direction of species (q),

$$\frac{d}{dt^{(q)}} = \frac{\partial}{\partial t} + U_j{}^{(q)} \frac{\partial}{\partial x_j}$$

$P^{(q)}$ is the static partial pressure of species (q),

$\mu_m \Delta_{ji}{}^{(q)}$ and $\mu_{m2}\theta^{(q)}\delta_{ji}$ are viscous transport terms, neglected here,

$F_i{}^{(q)}$ is the body force acting on unit mass of species (q),

$\Gamma^{(q)}$ is the rate of generation of species (q) per unit volume,

$U_{\Gamma_i}^{(q)}$ is the velocity component in the i^{th} coordinate direction of the generated species (q) material, and

$F^{(qp)}$ is the time constant of velocity relaxation due to the interaction between species (q) and the other species (p) of the mixture. Note that

$$\sum_{(q)} \rho^{(q)} \sum_{(p)} F^{(qp)} \left(U_i^{(p)} - U_i^{(q)}\right) = 0$$

The term S(x) is the unit-step function,

$$S(x) = \begin{matrix} 0 & \text{if} & x < 0 \\ 1 & \text{if} & x \geq 0, \end{matrix}$$

so that if $\Gamma^{(q)}$ is negative, the term

$$\left(U_i^{(q)} - U_{\Gamma_i}^{(q)}\right) \Gamma^{(q)} S\left(\Gamma^{(q)}\right)$$

in equation (4.5) is omitted.

The source term accounts for the fact that the generated species is not, in general, at velocity $U_i^{(q)}$. For the present study, this source is taken to be solely that of particle coagulation, and therefore there is no contribution to the momentum equation by those particles lost by coagulation.

The specific assumptions which have been made in obtaining equation (4.5) are given by Soo [33] and are not repeated here. Although the viscous transport terms are presented for a Newtonian behavior, these terms are negelcted at the outset. An advanced treatment would not only retain these terms but would account also for the non-Newtonian nature of the particle behavior. It should be noted that the effect of mutual interaction among species is modelled by a relaxation term proportional to the velocity difference between species.

The density of the mixture is given by

$$\rho_m = \sum_{(q)} \rho^{(q)} \tag{4.6}$$

and the i^{th} component of the mixture velocity is

$$\rho_m U_{m_i} = \sum_{(q)} \rho^{(q)} U_i^{(q)} \tag{4.7}$$

The static pressure is given by

$$P_m = \sum_{(q)} p^{(q)} \tag{4.8}$$

For application to the study of a relatively dilute aerosol system, species q = 1, 2, . . . , ν - 1 are considered to be the particle suspension components, with each discrete particle size being considered a distinct species. Species (q) = (ν) is taken to be the suspending fluid medium. Further, the term in equation (4.5) involving the mutual interaction term, $F^{(qp)}$, is simplified by noting that for dilute suspensions, the force exerted on species (q) as a result of interaction with other species is primarily a result of the velocity difference,

$$(U_i^{(\nu)} - U_i^{(q)})$$

between species (q) and the suspending medium. Thus, terms in the summation involving mutual interaction among the suspended particles are neglected. The influence due to these latter interactions is taken to be given solely by the source term involving $\Gamma^{(q)}$.

For the present study, the external body forces exerted upon

components of the mixture are restricted to electric-field forces. The electric force acting on a charged particle is $Z^{(q)}\vec{E}$, where $Z^{(q)}$ is the charge per particle of species (q) at a given point in physical space and $\vec{E}$ is the electric field intensity vector at that point. Thus, the electric force acting on unit mass of species (q) is

$$F_i^{(q)} = \frac{1}{m^{(q)}} Z^{(q)} E_i \tag{4.9}$$

where $m^{(q)}$ is the mass per particle of species (q).

The electric field satisfies Poisson's equation, i.e.,

$$\nabla \cdot \vec{E} = \sum_{(q)} (\rho^{(q)} Z^{(q)}/m^{(q)} \epsilon_o) \tag{4.10}$$

where ϵ_o is the permittivity of free space. The electric field is also related to a scalar potential function, the so-called electric potential, under steady-state conditions by

$$\vec{E} = - \nabla V \tag{4.11}$$

Thus, from equations (4.10) and (4.11), one has

$$\nabla^2 V = - \sum_{(q)} \left(\rho^{(q)} \, Z^{(q)} / m^{(q)} \, \varepsilon_o \right) \tag{4.12}$$

The time constant of velocity relaxation, $F^{(qp)}$, is obtained from a consideration of the drag coefficient of a single particle. This is expected to be reasonably valid for dilute suspensions, although for relatively dense suspensions consideration should be devoted to the drag of a cloud of particles, since mutual interaction may result in an accumulative behavior quite different from what might be predicted based on a summation of isolated individual particle transport effects. With the Stokes' form of the drag coefficient relationship, the time constant can be written as [1]

$$F^{(qf)} = \frac{18 \, \mu_f}{\rho_p (d^{(q)})^2} \tag{4.13}$$

Equation (4.5) can therefore be written as

$$\rho^{(q)} \frac{dU_i^{(q)}}{dt^{(q)}} = - \frac{\partial P^{(q)}}{\partial x_i} + \frac{\rho^{(q)}}{m^{(q)}} Z^{(q)} \, E_i - \tag{4.14}$$

(equation cont.)

$$(U_i^{(q)} - U_{\Gamma_i}^{(q)})\, \Gamma^{(q)}\, S(\Gamma^{(q)}) +$$

$$\rho^{(q)}\, \frac{18\, \mu_f}{\rho_p (d^{(q)})^2}\, (U_i^{(f)} - U_i^{(q)})$$

The result just obtained for the time constant of velocity relaxation is based on a drag coefficient relationship which is approximately valid within the Stokes' flow regime. If a relative Reynolds number is defined as

$$Re_p = \frac{\rho_f (\Delta V)\, d^{(q)}}{\mu_f} \tag{4.15}$$

then the previous result remains valid whenever $Re_p \leq 1$. However, when Re_p is greater than one, experimental drag data for spheres indicate considerable deviation from Stokes' value as Re_p increases, with the drag coefficient becoming approximately constant in the range $700 \leq Re_p \leq 10{,}000$ [35].

An empirical correction to Stokes' drag formula which extends its validity to $Re_p \approx 700$ has been obtained [36] and can be expressed as

$$C_D = 24\ f/Re_p \tag{4.16}$$

where

$$f = (28\ Re_p^{-0.85} + 0.48)/(24\ Re_p^{-1.0}) \tag{4.17}$$

Therefore, for $Re_p \geq 1$, the last term on the right hand side of equation (4.14) is to be multiplied by f as obtained from equation (4.17).

The equations of species continuity are

$$\frac{\partial \rho^{(q)}}{dt} + \frac{\partial}{\partial x_i}\left(\rho^{(q)}\ U_i^{(q)}\right) = \Gamma^{(q)} \tag{4.18}$$

for $q = 1, 2, \ldots, \nu$. One can define the diffusion flux as

$$J_i^{(q)} = \rho^{(q)}\left(U_i^{(q)} - U_{m_i}\right) \tag{4.19}$$

and the diffusion velocity as

$$V_i^{(q)} = U_i^{(q)} - U_{m_i} \tag{4.20}$$

Thus,

$$V_i^{(q)} = J_i^{(q)} / \rho^{(q)}$$

If one specifies the fluid velocity distribution and fluid density, then $U_i^{(f)}$ and $\rho^{(f)}$ are known. One is left with $(4\nu - 1)$ unknowns; namely,

$\rho^{(q)}$ $\quad q = 1, 2, \ldots, \nu - 1$

$U_i^{(q)}$ $\quad i = 1, 2, 3;\ q = 1, 2, \ldots, \nu - 1$

E_i $\quad i = 1, 2, 3$

at each point within the flowfield of interest. The equations to be

solved are equations (4.12), (4.14), and (4.18). For steady flow, equations (4.14) and (4.18) are parabolic, whereas equation (4.12), written in terms of the electric potential, is elliptic. The system of equations is coupled, so that the overall problem is elliptic in character unless the elliptic Poisson's equation can be decoupled, so to speak, from the momentum and continuity equations by appropriate approximations. This latter approach is followed here and is the subject of later discussion.

Rather than consider a finite set of discrete particle sizes one can alternately consider an essentially continuous density distribution function with respect to particle radius, a. As before, let the density of particles of type (q) having radii between a and a + da be

$$\rho^{(q)} = m^{(q)}\, n^{(q)}\, da \tag{4.21}$$

where

$$m^{(q)} = \frac{4\pi}{3}\left(\frac{d^{(q)}}{2}\right)$$

and $n^{(q)}$ is a number concentration distribution function, evaluated

at particle radius a. Thus, equations (4.12) and (4.14) become

$$\nabla^2 V = - \int_{a=o}^{\infty} \frac{n^{(q)}}{\epsilon_o} Z^{(q)} \, da \tag{4.22}$$

and

$$n^{(q)} U_j^{(q)} \frac{\partial U_i^{(q)}}{\partial x_j} = \frac{n^{(q)}}{m^{(q)}} Z^{(q)} E_i - (U_i^{(q)} - U_{I_i}^{(q)}) I^{(q)} S(I^{(q)}) +$$

$$n^{(q)} \frac{18 \mu_f f}{\rho_p (d^{(q)})^2} (U_i^{(f)} - U_i^{(q)}) \tag{4.23}$$

where $I^{(q)}$ is the source term for $n^{(q)}$ corresponding to $\Gamma^{(q)}$ for $\rho^{(q)}$. Note that the correction term, f, has been included with the Stokes' drag term and that the partial pressure contribution of the suspended particles has been neglected, as can be done for dilute systems. Finally, equation (4.18) likewise becomes

$$\frac{\partial}{\partial x_i} (n^{(q)} U_i^{(q)}) = I^{(q)} \tag{4.24}$$

It is important to note that several aspects of the physical behavior of a particulate system can be envisioned which are not modelled by the present formulation. Perhaps one of the more important involves the presumed nature of the fluid-particle interaction, which leads to the velocity relaxation parameter. This problem is discussed by Soo [33], and his analysis indicated that outside the Stokes'-Law range, the drag coefficient of the particles depends on their concentration in addition to the relative Reynolds number. The influence of the particulate load and electrostatic ion drift upon the flow characteristics of the suspending medium is discussed elsewhere [58, 62, 67] and is not inclued in the present analysis.

Particle Charge

Experimental evidence obtained from numerous studies indicates that most natural and man-made aerosols carry electric charges. The magnitude of the charge carried of course depends on a combination of factors, including method of aerosol formation, temperature, humidity, and electrical environment, but electrically neutral aerosols are, in fact, the exception rather than the rule. However, naturally occurring charges are usually bipolar and of such low magnitude as to be inadequate for practical gas-cleaning operations. Economic considerations dictate that for those applications considered here, additional particle charging must be effected by the design application itself. For example, electrostatic precipitator designs employing a corona discharge result in particle charging as a result of the ionized gaseous environment generated within the primary precipitation section. Other

applications can be envisioned which require particle charging prior to entrance into a primary operations stage having no corona discharge field. In such cases, particle charging could be achieved by a corona discharge in the upstream charging section.

Two distinct particle-charging mechanisms can be identified when aerosol particles are located within an environment composed of free ions and an electric field. The more important involves ion attachment in the electric field and is usually referred to as field charging. Another charging process results from the random thermal motion of the ions and is influenced to a much lesser degree by the external electric field. This latter process is usually referred to as diffusion charging and in practice tends to be important for particles smaller than about 0.2 microns in diameter. Field charging predominates for particles larger than about 0.5 microns [34]. Derivations of the equations for each of these charging processes are not reproduced here, as they are readily available elsewhere [34]. The applications of interest in the present study are those for which the field charging mechanism predominates, and therefore the charging relations for this mechanism are the subject of discussion here.

Two important parameters which need to be considered are the equilibrium charge per particle and the time required to achieve this charge. The equilibrium charge per particle attained with an applied electric field of intensity normally encountered in an electrostatic precipitator can be shown to be [34]

$$Z^{(q)} = 4\pi \epsilon_o E_c a^2 \left(1 + 2 \frac{\epsilon_r - 1}{\epsilon_r + 2}\right) \qquad (4.25)$$

where $\epsilon_r = \epsilon/\epsilon_o$, and ϵ is the permittivity of the particle material. E_c is the charging electric field intensity at the point of consideration. Typical charges vary from a few hundred for one-micron particles to as high as 10^6 electronic charges for a ten-micron particle in a fairly strong corona-discharge field. If the time required to achieve this equilibrium charge is comparable to the particle residence time within the flowfield of interest, then an additional charging rate equation must be added to the system of equations assembled to model the flow behavior. However, computations [34] indicate that for typical precipitator design applications, the charging time can be considered insignificant with respect to residence times, so that charging can be considered effectively instantaneous. For applications where much higher flow velocities are encountered, this simplification may be untenable. For example, the time constant of charging ranges from about 10^{-1} to 10^{-4} seconds, but charging ordinarily may be considered reasonably complete in about 10^{-2} seconds. This latter value would indicate that particle charging in a precipitator at gas velocities of five to ten feet per second is completed in the first few inches of the flow path in the corona field.

Axisymmetric Pipe Flow and Nondimensionalization

The first examples to be considered involve axisymmetric pipe

flow, and therefore the formulation developed previously is now specialized for this flow geometry and appropriate nondimensionalization is introduced. Equation (4.22) can be written in terms of the electric field intensity as

$$\frac{1}{r}\frac{\partial}{\partial r}(rE_r) + \frac{\partial E_z}{\partial z} = \int_{a=o}^{\infty} \frac{n^{(q)}}{\epsilon_o} Z^{(q)}\, da \qquad (4.26)$$

where r and z are the radial and longitudinal coordinate directions, respectively. The radial momentum equation can be obtained from equation (4.23) as

$$n^{(q)}\left[U_r^{(q)}\frac{\partial U_r^{(q)}}{\partial r} + U_z^{(q)}\frac{\partial U_r^{(q)}}{\partial z}\right] = \frac{n^{(q)}}{m^{(q)}} Z^{(q)} E_r - \qquad (4.27)$$

$$(U_r^{(q)} - U_{I_r}^{(q)})\, I^{(q)}\, S(I^{(q)}) + n^{(q)}\frac{18\mu_f f}{\rho_p (d^{(q)})^2}(U_r^{(f)} - U_r^{(q)})$$

and the longitudinal momentum equation likewise can be written

$$n^{(q)}\left[U_r^{(q)}\frac{\partial U_z^{(q)}}{\partial r} + U_z^{(q)}\frac{\partial U_z^{(q)}}{\partial z}\right] = \frac{n^{(q)}}{m^{(q)}} Z^{(q)} E_z - \qquad (4.28)$$

(Equation continued)

$$(U_z^{(q)} - U_{I_z}^{(q)})\, I^{(q)}\, S(I^{(q)}) + n^{(q)} \frac{18\mu_f f}{\rho_p (d^{(q)})^2} (U_z^{(f)} - U_z^{(q)}$$

Recall that in each of these equations, one can substitute the relation, obtained from equation (4.20),

$$U_i^{(q)} = U_{m_i} + V_i^{(q)}$$

In addition, for this flow geometry

$$U_r^{(q)} \cong V_r^{(q)}$$

since

$$U_{m_r} \cong 0$$

(this latter result can be modified by secondary flow components due

to the so-called electric wind if the electric field intensities are quite large). If coagulation is neglected, one can write the equations to be solved as

$$\frac{1}{r}\frac{\partial}{\partial r}(rE_r) + \frac{\partial E_z}{\partial z} = \int_{a=o}^{\infty} \frac{n^{(q)}}{\epsilon_o} Z^{(q)}\, da \qquad (4.29)$$

$$V_r^{(q)} \frac{\partial V_r^{(q)}}{\partial r} + (U_{m_z} + V_z^{(q)}) \frac{\partial V_r^{(q)}}{\partial z} = \frac{1}{m^{(q)}} Z^{(q)} E_r - \qquad (4.30)$$

$$\frac{18\,\mu_f f}{\rho_p (d^{(q)})^2} V_r^{(q)}$$

$$V_r^{(q)} \frac{\partial (U_{m_z} + V_z^{(q)})}{\partial r} + (U_{m_z} + V_z^{(q)}) \frac{\partial (U_{m_z} + V_z^{(q)})}{\partial z} = \qquad (4.31)$$

$$\frac{1}{m^{(q)}} Z^{(q)} E_z - \frac{18\,\mu_f f}{\rho_p (d^{(q)})^2} V_z^{(q)}$$

and

$$\frac{1}{r}\frac{\partial}{\partial r}\left[rn^{(q)}\,V_r^{(q)}\right] + \frac{\partial}{\partial z}\left[n^{(q)}(U_{m_z} + V_z^{(q)})\right] = 0 \qquad (4.32)$$

In these equations, the diffusion velocity components for the host fluid have been neglected, i.e.,

$$V_r^{(f)} \cong 0 \quad \text{and} \quad V_z^{(f)} \cong 0$$

Preparatory to constructing a numerical algorithm for this system, it is advantageous to transform the system into an appropriate nondimensional form. Accordingly, the following nondimensional variables are defined:

$$\hat{r} = r/R, \quad \hat{z} = z/R, \quad \hat{n}^{(q)} = n^{(q)}\,a_o/N_o,$$

$$\hat{U}_r^{(q)} = U_r^{(q)}/U_{m_{z_o}}, \quad \hat{U}_z^{(q)} = U_z^{(q)}/U_{m_{z_o}},$$

(Equation continued)

$$\hat{V}_r^{(q)} = V_r^{(q)}/U_{m_{Z_o}}, \quad \hat{V}_z^{(q)} = V_z^{(q)}/U_{m_{Z_o}},$$

$$\hat{U}_{m_Z} = U_{m_Z}/U_{m_{Z_o}}, \quad \hat{Z}^{(q)} = Z^{(q)}/\left(\frac{\epsilon_o E_o}{N_o R}\right),$$

$$\hat{E}_r = E_r/E_o, \quad \hat{E}_z = E_z/E_o, \quad \hat{a} = a/a_o \tag{4.33}$$

The quantities E_o, N_o, and R are reference quantities which are, at this point, arbitrary. In terms of these nondimensional variables, equations (4.29), (4.30), (4.31), and (4.32) become

$$\frac{1}{\hat{r}}\frac{\partial}{\partial \hat{r}}(\hat{r}\hat{E}_r) + \frac{\partial \hat{E}_z}{\partial \hat{z}} = \int_{a=o}^{\infty} \hat{n}^{(q)}\, \hat{Z}^{(q)}\, d\hat{a} \tag{4.34}$$

$$\hat{V}_r^{(q)}\frac{\partial \hat{V}_r^{(q)}}{\partial \hat{r}} + (\hat{U}_{m_Z} + \hat{V}_z^{(q)})\frac{\partial \hat{V}_r^{(q)}}{\partial \hat{z}} = A^{(q)}\, \hat{Z}^{(q)}\, \hat{E}_r - \tag{4.35}$$

$$B\left(\frac{R}{a_o}\right)^2 \hat{a}^{-2}\, \hat{V}_r^{(q)}$$

$$\hat{V}_r^{(q)} \frac{\partial(\hat{U}_{m_z} + \hat{V}_z^{(q)})}{\partial \hat{r}} + (\hat{U}_{m_z} + \hat{V}_z^{(q)}) \frac{\partial(\hat{U}_{m_z} + \hat{V}_z^{(q)})}{\partial \hat{r}} = \tag{4.36}$$

$$A^{(q)} Z^{(q)} \hat{E}_z - B \left(\frac{R}{a_o} \right)^2 \hat{a}^{-2} \hat{V}_z^{(q)}$$

and

$$\frac{1}{\hat{r}} \frac{\partial}{\partial \hat{r}} \left[\hat{r} \hat{n}^{(q)} \hat{V}_r^{(q)} \right] + \frac{\partial}{\partial \hat{z}} \left[\hat{n}^{(q)} (\hat{U}_{m_z} + \hat{V}_z^{(q)}) \right] = 0 \tag{4.37}$$

where

$$A^{(q)} = \epsilon_o E_o^2 / (N_o m^{(q)} U_{m_{z_o}}^2) \tag{4.38}$$

$$B = \frac{9 \mu_f f}{2 \rho_p U_{m_{z_o}} R} \tag{4.39}$$

Equilibrium Velocity and Equilibration Distance

Before proceeding to particular computational examples, it is useful first to consider the distance required for equilibration of particle velocity resulting from the opposing forces of an electric field and fluid-particle viscous drag. Proper inplementation of a stable and useful numerical solution algorithm depends upon knowing the ratio of numerical step size to this equilibration distance, and a definite simplification in the computational effort results when this ratio is much greater than one.

Although the definition of an appropriate local equilibrium velocity is straightforward, an equivalent equilibration distance definition requires some care and is to an extent a matter of choice. The equilibrium velocity defined here is a local equilibrium velocity but is taken to be the asymptotic velocity to which the particle would approach in a infinite, uniform fluid medium under the influence of an electric field intensity and fluid-dynamic conditions identical to those at the point of interest in the actual flowfield. For example, examination of equation (4.35) indicates that the above defined equilibrium velocity, for the radial direction, is achieved when the left hand side of this equation becomes zero. Thus, by equating the right hand side of equation (4.35) to zero also, one obtaines the equilibrium radial velocity as

$$\left[\hat{V}_r(q)\right]_{eq} = \frac{A(q)\hat{Z}(q)\hat{E}_r}{B(R/a_o)^2\,\hat{a}^{-2}} \qquad (4.40)$$

However, the distance required to achieve some fraction of this equilibrium velocity, again in an infinite medium, is also of interest. Therefore, consider the axial variation of the radial particle velocity, with zero initial velocity conditions imposed at $\hat{z} = 0$. Equation (4.35) yields

$$\frac{\partial \hat{V}_r^{(q)}}{\partial \hat{z}} = \frac{A^{(q)}\hat{Z}^{(q)}\hat{E}_r - \hat{V}_r^{(q)}[B(R/a_o)^2 \hat{a}^{-2}]}{\hat{U}_{m_z} + \hat{V}_z^{(q)}} \tag{4.41}$$

since $\partial \hat{V}_r^{(q)}/\partial \hat{r}$ is zero for the conditions specified. If

$$|\hat{V}_z^{(q)}| \ll |\hat{U}_{m_z}|$$

equation (4.41) can be solved for $\hat{V}_r^{(q)}$ to yield

$$\hat{V}_r^{(q)} = \frac{A^{(q)}\hat{Z}^{(q)}\hat{E}_r}{B(R/a_o)^2 \hat{a}^{-2}} \left[1 - e^{-\frac{B}{\hat{U}_{m_z}} \left(\frac{R}{a_o}\right)^2 \hat{a}^{-2}\hat{z}}\right] \tag{4.42}$$

since only $\hat{V}_r^{(q)}$ and $\hat{z}$ are presumed variable for the present analysis. Note that equation (4.42) recovers the equilibrium velocity given by equation (4.40) in the limit as $\hat{z} \to \infty$. However, equation (4.42) also

indicates the distance required for the velocity to approach this equilibrium value.

The equilibrium distance will here be defined as that axial distance required for

$$\hat{V}_r^{(q)} = 0.98 \left[\hat{V}_r^{(q)}\right]_{eq}$$

that is, for the velocity to reach 98 percent of its equilibrium value. Thus,

$$\hat{z}_{eq} = 4\hat{U}_{m_z} / \left[B \left(\frac{R}{a_o} \right)^2 \hat{a} - 2\right] \tag{4.43}$$

or

$$\hat{z}_{eq} = \frac{4}{9} \hat{U}_{m_z} \, Re \left(\frac{\rho_p}{\rho_f} \right)\left(\frac{a_o}{R} \right)^2 \hat{a}^2 \tag{4.44}$$

since

$$B = 9(\rho_f/\rho_p)/Re$$

Recall, however, that within the actual flowfield, there exist point-to-point variations in flow conditions, so that care must be exercised when attempting to relate this equilibration distance to the actual flowfield geometry. Nevertheless, the ratio of this distance to numerical step size is an important quantity to condiser when constructing numerical solution algorithms, as will be noted in the next chapter.

CHAPTER V

DEPOSITION WITHIN THE CONVENTIONAL ELECTROSTATIC PRECIPITATOR CONFIGURATION

Equilibrium Diffusion Velocity Example

As a first example, computations were made with respect to the conventional pipe with centerline-wire configuration typical of many electrostatic precipitator installations (Figure 12). This configuration has been the subject of much of the effort related to theoretical prediction of deposition, and, in addition, there exists some laboratory data with which to compare theoretical results. It therefore represents a useful flow geometry with which to examine the relative accuracy and utility of the method proposed here.

As calculations later show, by restricting the particulate loading to relatively small particles, explicit numerical solution of the particle radial and axial momentum equations can be eliminated. This accrues from the fact that the ratio of particle velocity relaxation distance to the chosen finite-difference step size is much less than one, and therefore particulate diffusion velocities for these smaller particles are essentially at local equilibrium values.

Summary of Equations to be Solved

Computations are made for aerosol particle concentration distributions and wall deposition downstream from the point $\hat{z} = 0$, at which the particulate loading can be described as log-normal with

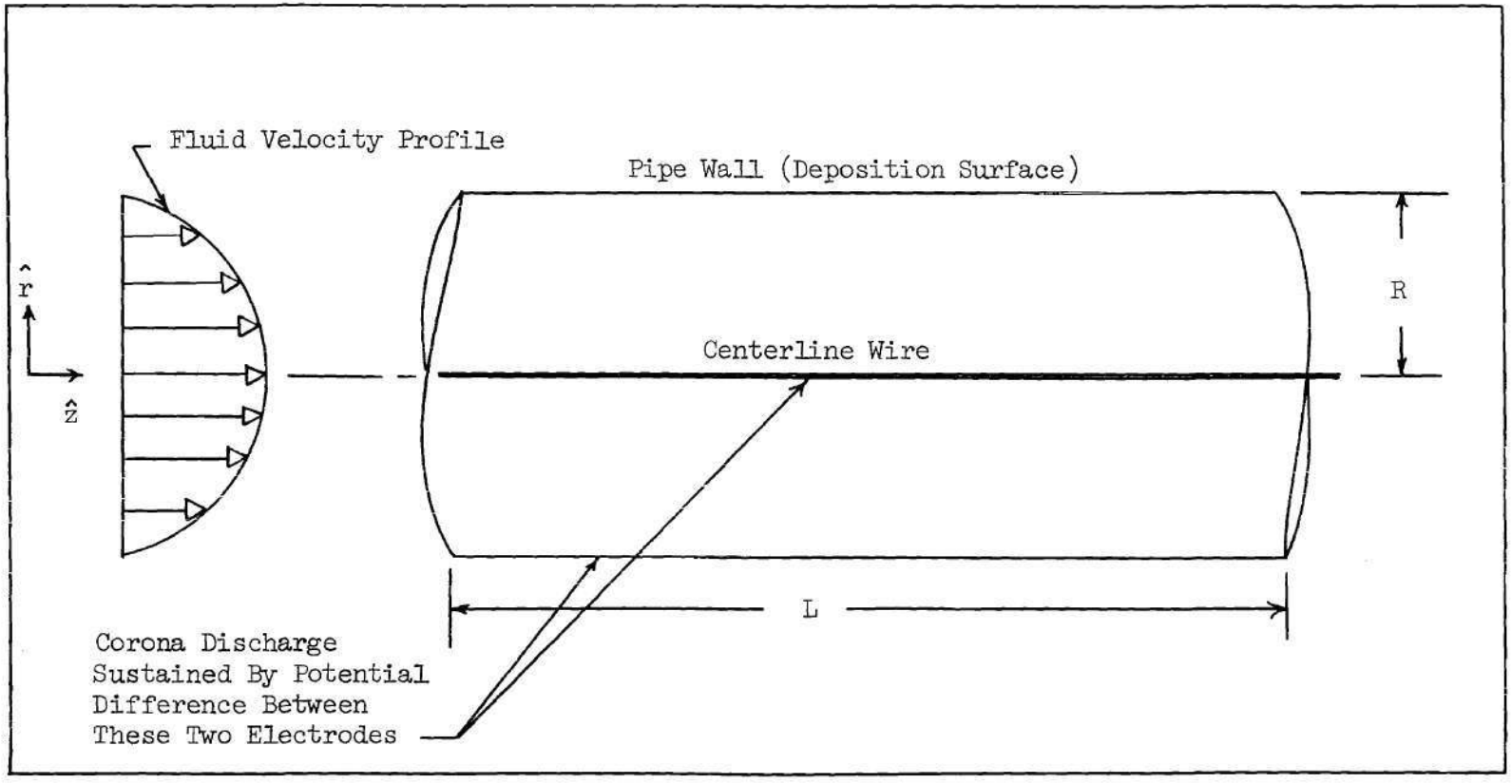

Figure 12. Conventional Pipe-Centerline Wire Electrostatic Precipitator Configuration

respect to particle radius and uniformly distributed across the pipe cross section. The electrical field is provided by a potential difference between an axial, centerline wire and the pipe wall but is modified by the space charge of the particulate cloud and ion current in accord with Poisson's equation. The field intensity is assumed sufficient to insure corona discharge near the centerline wire. A unipolar aerosol electrical charge is presumed to exist at $\hat{z} = 0$, with individual particle charge at the equilibrium value corresponding to the local electric field. As the particles proceed downstream, their charges vary since ions are free to attach or detach themselves and move with relatively high mobility through the ionized gas generated by the corona discharge.

For simplicity, the gas flow supporting the particulate load is taken to be fully developed turbulent flow and uninfluenced by the aerosol dynamics or by the ion drift. The applicable equations are Poisson's equation, equation (4.34),

$$\frac{1}{\hat{r}} \frac{\partial}{\partial \hat{r}} (\hat{r}\hat{E}_r) + \frac{\partial \hat{E}_z}{\partial \hat{z}} = \int_{a=o}^{\infty} \hat{n}(q)\, \hat{Z}(q)\, d\hat{a} \qquad (5.1)$$

with the particle charge, $\hat{Z}(q)$, given by equation (4.25); the continuity equation (4.37),

$$\frac{1}{\hat{r}} \frac{\partial}{\partial \hat{r}} \left[\hat{r}\, \hat{n}^{(q)}\, \hat{V}_r^{(q)} \right] + \frac{\partial}{\partial \hat{z}} \left[\hat{n}^{(q)} \left(\hat{U}_{m_z} + \hat{V}_z^{(q)} \right) \right] = 0 \qquad (5.2)$$

and the radial and axial momentum equations, equations (4.35) and (4.36), respectively. Coagulation may be neglected for the present model since the aerosol particles sustain a unipolar charge throughout the flow-field [1]. At this point, one could apply the traditional Reynolds' procedure for turbulent flow and express the basic equations in terms of time mean values and fluctuations [12]. The procedure can be expected to result in additional transport and dissipation terms in the equations. These additional Reynolds' terms are omitted in the development here initially but are modelled later by expressions of the form given in equation (5.36).

It should be noted that, in principle, the electric field intensity is influenced by the corona current, so that the right-hand side of Poisson's equation, equation (5.1), contains a term corresponding to the free-ion charge contribution to the overall space charge. However, it is known from practice that the corona current is reduced almost to zero in the presence of the particulate load, even for relatively high precipitator voltages [34], as can be expected in consideration of the relatively high mobility and particle attachment rate of the gaseous ions. Hence, it is reasonable to include only the space-charge contribution of the aerosol particles when considering Poisson's equation.

Parameters for Example Computation

The following parameters were chosen for initial computations and are similar to those selected for the previous uncharged aerosol deposition cases considered:

$$Re = 10^5, \qquad L/R = 35, \qquad a_o/R = 10^{-5},$$

$$a_o = 10^{-4} \text{ cm}, \qquad \rho_p/\rho_f = 1110, \qquad N_o = 10^6 \text{ cm}^{-3}$$

The particles have an initial distribution with respect to radius centered at one micron and distributed log-normally with geometric standard deviation 0.10, i.e.,

$$n_{z=0}(a) = \frac{\exp\left[-(\ln \hat{a})^2/(2\sigma_o^2)\right]}{\sqrt{2\pi}\,\sigma_o \exp(\sigma_o^2/2)} \tag{5.3}$$

as before. A nondimensional parameter which appears in the computations is $\epsilon_o E_o^2/(\rho_f U_{m_{z_o}}^2)$ and is assigned the typical value 0.011 initially, which corresponds to $E_o = 4$ kv/cm.

The nondimensional velocity equilibration distance is given by equation (4.44). As before, putting $\hat{U}_{m_z} = (1-\hat{r})^{1/m}$ for pipe flow

results in $\hat{z}_{eq}$ varying from zero at the pipe wall to a value

$$[\hat{z}_{eq}] = 0.00493\ \hat{a}^2$$

at the centerline. Since $\hat{a} = O[1]$, then $\hat{z}_{eq}$ is less than about 0.005 throughout the flowfield and is much less than this quantity within most of the region of interest. A numerical computation step size in the $\hat{z}$ direction of 0.07 represents a useful compromise between the limitations imposed by computational stability, on the one hand, and cumulative numerical truncation error, on the other. Hence, for this example, the ratio of velocity equilibration distance to numerical step size in the axial, solution-marching direction is much less than one everywhere in the flow-field, and therefore particle velocities can be assigned their local equilibrium values without loss of accuracy. Thus, radial and axial particle velocities are obtained as in equation (4.40), i.e.,

$$\hat{V}_r^{(q)} = \frac{A^{(q)}\ \hat{Z}^{(q)}\ \hat{E}_r}{B(R/a_o)^2\ \hat{a}^{-2}} \tag{5.4}$$

and

$$\hat{V}_z^{(q)} = \frac{A^{(q)}\ \hat{Z}^{(q)}\ \hat{E}_z}{B(R/a_o)^2\ \hat{a}^{-2}} \tag{5.5}$$

where, as can be shown,

$$A^{(q)}\ \hat{Z}^{(q)} = 3\left(1 + 2\,\frac{\epsilon_r - 1}{\epsilon_r + 2}\right)\frac{\rho_f}{\rho_p}\left(\frac{\epsilon_o E_o^2}{\rho_f U_{m_{z_o}}^2}\right)\frac{\hat{E}}{(a_o/R)\ \hat{a}} \tag{5.6}$$

$$\hat{E} = \left[\ \hat{E}_r^{\,2} + \hat{E}_z^{\,2}\ \right]^{\frac{1}{2}} \tag{5.7}$$

$$B = 9\left(\frac{\rho_f}{\rho_p}\right)\frac{1}{Re} \tag{5.8}$$

For aerosol particles composed of conducting material, $\epsilon_r \to \infty$ and $(\epsilon_r - 1)/(\epsilon_r + 2) \to 1$ in equation (5.6). The particles considered here are presumed conductive, although computations for dielectric particles are no more complex.

The equations to be used are therefore equations (5.1), (5.2), (5.4), and (5.5) along with subsidiary equations (5.3), (5.6), (5.7), and (5.8), among others. Boundary conditions are required for the

particle number concentration and electric potential, from which the electric field components are obtainable. At the centerline, symmetry considerations would imply that the radial derivative of the particle number concentration vanish, i.e.,

$$\left[\frac{\partial \hat{n}^{(q)}}{\partial \hat{r}}\right]_{\hat{r}=0} = 0, \quad q = 1, 2, \ldots, \nu - 1 \tag{5.9}$$

The boundary condition on the concentration near the wall is much less obvious. The computations for noncharged particles presented in previous chapters are based on a wall boundary condition for particle concentration obtained by equating turbulent diffusion flux to the inertial deposition flux at an appropriate distance from the wall, i.e., by equation (2.7) of Chapter II. However, the mixing length deposition concept upon which this boundary condition is based does not enter into the present formulation, so that this previous result is not used here.

Three alternative approaches have been adopted in the literature. In some studies, e.g. that by Copperman [28], the particle concentration is presumed to drop to zero at a precipitation surface. The argument is based on the assumption that, for zero particle re-entrainment, the wall is a perfect collector and therefore, according to the argument, the particle concentration is zero at the surface. However, one can easily visualize a circumstance involving a uniform concentration of

particles flowing toward a collecting wall and being captured, without the concentration falling to zero at the wall. In fact, in the true physical case, perfect collection at a wall implies an unsteady buildup of material onto the surface, so that a condition involving zero particle concentration immediately adjacent to this surface is actually somewhat difficult to justify.

An alternate approach [29] assumes that the wall concentration is some constant fraction of the mean concentration at each cross section. However, this constant fraction results in the introduction of an additional unknown parameter into the analysis and must be determined from experiment.

A third, more common, alternative is to assume that the radial derivative of the particle concentration vanishes at the wall. This is the so-called "Danckwerts" boundary condition, originally applied by Danckwerts [37] to the steady-state flow of a reactant through a packed tubular reaction vessel. Danckwerts' original argument was based on an intuitive resolution of an apparent indeterminacy in his mathematical development which arose if that boundary condition were not adopted. Later, Pearson [38] obtained a more rigorous mathematical justification for the Danckwerts boundary condition when the turbulent coefficient of diffusion is assumed to decrease discontinuously to zero at a wall. The boundary condition in the true physical situation in which the diffusivity decreases rapidly, but not discontinuously, to zero is probably different from the Danckwerts condition, but experimental evidence [39, 31] indicates that the true condition is probably not very different from this idealization.

One might possibly identify a fourth approach as the technique in which the wall concentration is merely specified beforehand [33]. The problem of course, is that the wall concentration is unknown beforehand, in general, so that the method is basically semi-empirical in practical application.

Of the possible conditions to apply, the Danckwerts boundary condition appears to be the more justifiable and is adopted here. However, the present state of the problem is clearly unresolved, and additional effort directed toward determining the proper condition is needed.

Poisson's equation written in terms of the electric potential is of the classical elliptic type, so that, in principle, one would need to specify boundary conditions for the potential everywhere on the closed surface bounding the field of interest. However, the necessity for including Poisson's equation, as such, within the numerical solution procedure is avoided here by initially determining an approximate solution of Poisson's equation which satisfies the desired boundary conditions for the potential. This approximate solution is employed where necessary to evaluate the electric field intensity; however, this solution is not completely uncoupled from the numerical procedure since the local particle concentration is required at each evaluation, and this latter quantity must evolve from the computations as they proceed. This solution is the subject of the next section.

Approximate Solution to Poisson's Equation

Poisson's equation written in terms of the electric intensity is

$$\frac{1}{\hat{r}} \frac{\partial}{\partial \hat{r}} (\hat{r}\hat{E}_r) + \frac{\partial \hat{E}_z}{\partial \hat{z}} = \int_{\hat{a}=0}^{\infty} \hat{n}(q)\ \hat{Z}(q)\ d\hat{a} \tag{5.10}$$

Define $Q(\hat{z}, \hat{r})$ by

$$Q(\hat{z}, \hat{r}) = \int_{\hat{a}=0}^{\infty} \hat{n}(q)\ \hat{Z}(q)\ d\hat{a} \tag{5.11}$$

Now, for the pipe-wire configuration having a relatively strong radial electric field intensity, one expects that

$$\frac{\partial \hat{E}_z}{\partial \hat{z}} << \frac{1}{\hat{r}} \frac{\partial}{\partial \hat{r}} (\hat{r}\hat{E}_r) \tag{5.12}$$

that is, the axial derivative is much less than the corresponding radial term. Thus, the equation to be solved can be simplified to

$$\frac{1}{\hat{r}} \frac{\partial}{\partial \hat{r}} (\hat{r}\hat{E}_r) = Q(\hat{z}, \hat{r}) \tag{5.13}$$

Multiply equation (5.13) by $\hat{r}$ and integrate both sides indefinitely with respect to $\hat{r}$ to obtain

$$\hat{r}\hat{E}_r = \int \hat{r}\, Q(\hat{z}, \hat{r})\, d\hat{r} + K_1(\hat{Z}) \tag{5.14}$$

As is shown later, the numerical solution does not provide useful results near the centerline wire of the present configuration, and an approximate solution to an overall mass-conservation equation is developed for this region. This circumstance is brought about by the near singularity in the electric field intensity and radial velocity near the centerline. Therefore, equation (5.14) is expected to be employed only for values of $\hat{r}$ not very close to zero. Within this outer region of interest, it can be shown by computation (presented later) that Q is primarily a function of $\hat{z}$. Thus, one can write equation (5.14) approximately as

$$\hat{r}\hat{E}_r = \tfrac{1}{2}\hat{r}^2\, Q(\hat{z}) + K_1(\hat{z}) \tag{5.15}$$

Therefore, the radial electric field component is

$$\hat{E}_r = \tfrac{1}{2}\hat{r}\, Q(\hat{z}) + \frac{K_1(\hat{z})}{\hat{r}} \tag{5.16}$$

Now, $\hat{E}_r$ is related to the electric potential as

$$\hat{E}_r = - \frac{\partial \hat{V}}{\partial \hat{r}} \tag{5.17}$$

where $\hat{V}$ is here defined by

$$\hat{V} = V/(RE_o) \tag{5.18}$$

Thus, equation (5.16) gives

$$\frac{\partial V}{\partial \hat{r}} = - \tfrac{1}{2} \hat{r} \, Q(\hat{z}) - \frac{K_1(\hat{z})}{\hat{r}}$$

Integrating this yields

$$\hat{V} = - \tfrac{1}{4} \hat{r}^2 \, Q(\hat{z}) - K_1(\hat{z}) \ln \hat{r} + K_2(\hat{z}) \tag{5.19}$$

Since $\hat{E}_z = - \partial\hat{V}/\partial\hat{z}$, then

$$\hat{E}_z = \tfrac{1}{4}\,\hat{r}^2\,\frac{dQ}{dz} + (\ln\,\hat{r})\,\frac{dK_1}{d\hat{z}} - \frac{dK_2}{d\hat{z}} \qquad (5.20)$$

Both the wire and the pipe wall are equipotential surfaces, so $\hat{V}$ will be constant along both. The potential is arbitrarily set equal to zero along the pipe wall, $\hat{r} = 1$. This boundary condition implies that

$$K_2(\hat{z}) = \tfrac{1}{4}\,Q(\hat{z}) \qquad (5.21)$$

At the wire surface, $\hat{r} = \hat{r}_\delta$, one can put $\hat{V} = \hat{V}_w$, so that equation (5.19) gives

$$K_1(\hat{z}) = \left[Q(\hat{z})\left(\frac{1-\hat{r}_\delta^{\,2}}{4}\right) - \hat{V}_w\right] / \ln\,\hat{r}_\delta \qquad (5.22)$$

Combining equations (5.21) and (5.22) with equations (5.16) and (5.20) gives

$$\hat{E}_r = \tfrac{1}{2}\hat{r}\, Q(\hat{z}) + \frac{Q(\hat{z})\left(\frac{1-\hat{r}_\delta^{\,2}}{4}\right) - \hat{V}_w}{\hat{r}\ln\hat{r}_\delta} \tag{5.23}$$

and

$$\hat{E}_z = \tfrac{1}{4}\frac{dQ}{d\hat{z}}\left[\frac{\ln\hat{r}}{\ln\hat{r}_\delta}(1-\hat{r}_\delta^{\,2}) - (1-\hat{r}^2)\right] \tag{5.24}$$

With this approach, one is still free to specify $\hat{V}_w$. Equations (5.23) and (5.24) are the desired relations for the electric field components. Note that $Q(\hat{z})$ is obtainable from the numerical solution for $\hat{n}^{(q)}$ at each cross section by an appropriate quadrature. For the present calculations, $Q(\hat{z})$ is taken to be the average over the cross-sectional area, i.e.,

$$Q(\hat{z}) = \frac{1}{A}\int Q(\hat{z}, \hat{r})\, dA$$

Thus, with $dA = 2\pi\,\hat{r}\,d\hat{r}$, this becomes

$$Q(\hat{z}) = \frac{1}{\pi}\int_{\hat{r}=\hat{r}_\delta}^{1}\left[\int_{\hat{a}=0}^{\infty} \hat{n}^{(q)}\,\hat{Z}^{(q)}\,d\hat{a}\right] 2\pi\,\hat{r}\,d\hat{r} \qquad (5.25)$$

For computational purposes, $\hat{E}_r$ is put equal to one at $\hat{z} = 0$ and $\hat{r} = 1$, although other values would also be appropriate. A typical wire radius, r_δ, of 0.02 in. is used.

Numerical Solution Procedure

The continuity equation, equation (5.2), can be written in expanded form and solved for $\partial\hat{n}^{(q)}/\partial\hat{z}$ to obtain

$$\frac{\partial\hat{n}^{(q)}}{\partial\hat{z}} = -\frac{\dfrac{\hat{n}^{(q)}}{\hat{r}}\hat{V}_r^{(q)} + \hat{V}_r^{(q)}\dfrac{\partial\hat{n}^{(q)}}{\partial\hat{r}} + \hat{n}^{(q)}\left[\dfrac{\partial\hat{V}_r^{(q)}}{\partial\hat{r}} + \dfrac{\partial\hat{V}_z^{(q)}}{\partial\hat{z}}\right]}{\hat{U}_{m_z} + \hat{V}_z^{(q)}} \qquad (5.26)$$

For the present example, it is expected that $\hat{V}_z^{(q)}$ is much less than $\hat{V}_r^{(q)}$ since $\hat{E}_z$ is much less than $\hat{E}_r$. Further, it can also be expected that $\hat{V}_z^{(q)} \ll \hat{U}_{m_z}$ and that $\partial\hat{V}_z^{(q)}/\partial\hat{z}$ can be neglected with respect to $\partial\hat{V}_r^{(q)}/\partial\hat{r}$. Hence, equation (5.26) can be written as

$$\frac{\partial\hat{n}^{(q)}}{\partial\hat{z}} = -\frac{1}{\hat{U}_{m_z}}\left[\hat{V}_r^{(q)}\left(\frac{\hat{n}^{(q)}}{\hat{r}} + \frac{\partial\hat{n}^{(q)}}{\partial\hat{r}}\right) + \hat{n}^{(q)}\frac{\partial\hat{V}_r^{(q)}}{\partial\hat{r}}\right] \qquad (5.27)$$

As was observed in Chapter II for the uncharged particle deposition results, there is here also an apparent singularity at $\hat{r} = 0$ since $\hat{V}_r^{(q)}$ is zero at $\hat{r} = 0$ in order to preserve symmetry. As before, however, L'Hospital's rule can be employed to indicate that

$$\lim_{\hat{r} \to o} \frac{\hat{V}_r^{(q)}}{\hat{r}} = \lim_{\hat{r} \to o} \frac{\partial \hat{V}_r^{(q)}}{\partial \hat{r}} \tag{5.28}$$

Noting also that

$$\frac{\partial \hat{n}^{(q)}}{\partial \hat{r}} = 0$$

at $\hat{r} = 0$, one can write equation (5.27) for $\hat{r} = 0$ in the form

$$\frac{\partial \hat{n}^{(q)}}{\partial \hat{r}} = - \frac{1}{\hat{U}_{m_z}} \left[2 \hat{n}^{(q)} \frac{\partial \hat{V}_r^{(q)}}{\partial \hat{r}} \right] , \quad \hat{r} = 0 \tag{5.29}$$

However, preliminary computations indicated that the numerical procedure outlined is not useful near $\hat{r} = 0$, as noted earlier, so that

an alternate procedure was required near the centerline. This might be anticipated on the basis of the indicated singularity of $\hat{E}_r$, and hence of $\hat{V}_r^{(q)}$, as $\hat{r}$ approaches zero. Nevertheless, it is useful to note here the alternative form of the continuity equation, which will in fact become useful in a later example.

As an alternative to the continuity equation valid for $\hat{r} = 0$, equation (5.29), consider a mass balance for a cylindrical element of radius $\hat{r}_2$ where $\hat{r}_\delta < \hat{r}_2 < 1$, as illustrated in Figure 13. Continuity of mass flow implies that, approximately,

$$\pi \hat{r}_2^{\,2}\, \hat{n}^{(q)}\, \hat{U}_{m_z} \cong \pi \hat{r}_2^{\,2}\, (\hat{n}^{(q)} + d\hat{n}^{(q)})\, \hat{U}_{m_z} +$$

$$2\pi \hat{r}_2\, (d\hat{z}) \left(\hat{n}^{(q)} + \frac{d\hat{n}^{(q)}}{2}\right) \left(\hat{V}_r^{(q)} + \frac{d\hat{V}_r^{(q)}}{2}\right)$$

which becomes

$$\frac{d\hat{n}^{(q)}}{d\hat{z}} \simeq - \frac{2}{\hat{r}_2\, \hat{U}_{m_z}} \left[\hat{n}^{(q)}\, \hat{V}_r^{(q)}\right]_{\hat{r} = \hat{r}_2} \tag{5.30}$$

This equation can be used to compute the axial variation of the average

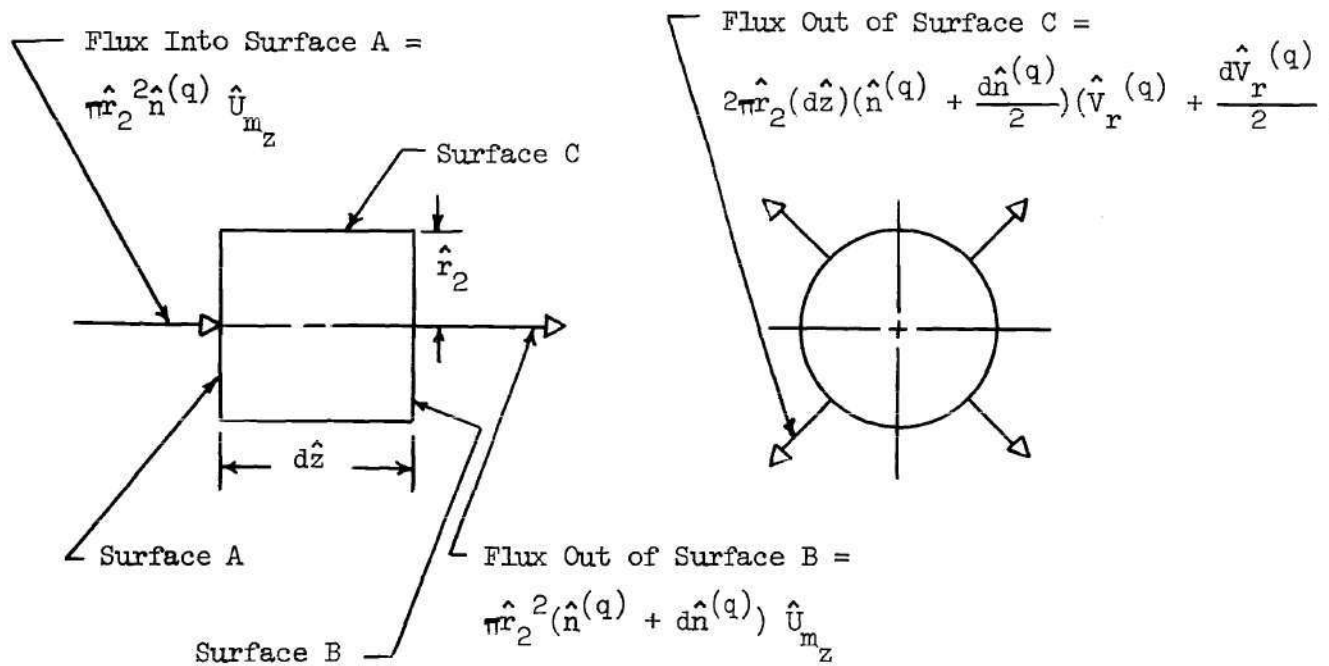

Figure 13. Mass Balance For a Cylindrical Element

number concentration within the cylindrical element. For purposes of the present computation, $\hat{r}_2$ is put equal to 0.2.

The numerical computation procedure is analogous to that outlined previously in Chapter III. Radial derivatives are replaced by central-difference approximations, whereas axial derivatives are replaced by simple forward-difference approximations, as illustrated by equations (3.14) and (3.16) of Chapter III. For example, equation (5.27) becomes

$$\hat{n}_{i,j,k+1} = \hat{n}_{i,j,k} - \frac{\Delta\hat{z}}{\Delta\hat{r}} \frac{1}{\hat{U}_{m_z}} \left\{ \hat{V}_{r_{i,j,k}} \left[\Delta\hat{r} \frac{\hat{n}_{i,j,k}}{\hat{r}} + \right. \right. \tag{5.31}$$

$$\left. \frac{\hat{n}_{i,j+1,k} - \hat{n}_{i,j-1,k}}{2} \right] + \tfrac{1}{2} \hat{n}_{i,j,k} \left[\hat{V}_{r_{i,j+1,k}} - \right.$$

$$\left. \left. \hat{V}_{r_{i,j-1,k}} \right] \right\}$$

where subscripts i, j, and k represent discrete particle radius index number, radial coordinate index number, and axial coordinate index number, respectively, as before. Thus, again, an explicit calculation algorithm is generated, and one can march the solution downstream from $\hat{z} = 0$. As before, $\Delta\hat{r}$ is put equal to 0.04.

The elemental mass flux to the wall is given by the integral

$$\int_{a=o}^{\infty} \left[n(q)\, m(q)\, V_r(q) \right]_{wall} (2\pi R\, dz)\, da$$

or, in nondimensional form

$$\rho_p N_o \frac{8}{3} \pi^2 a_o^3 U_{m_{z_o}} R^2 \int_{\hat{a}=o}^{\infty} \left[\hat{n}(q)\, \hat{a}^3\, \hat{V}_r(q) \right]_{wall} d\hat{z}\, d\hat{a} \qquad (5.32)$$

The mass flux per unit length of the flow is, in nondimensional form,

$$\rho_p N_o \frac{8}{3} \pi^2 a_o^3 U_{m_{z_o}} R \int_{a=o}^{\infty} \left[\hat{n}(q)\, \hat{a}^3\, \hat{V}_r(q) \right] d\hat{a} \qquad (5.33)$$

The efficiency at $\hat{z}$ is defined as the total mass flux to the wall from $\hat{z} = 0$ to $\hat{z} = \hat{z}$ divided by the input particulate mass flux into the pipe at $\hat{z} = 0$. An efficiency of one therefore represents total removal of the particulate loading. The input particulate mass flux is given by the expression

$$\int_{r=r_\delta}^{R} \left\{ \int_{a=o}^{\infty} n_{z=o}^{(q)} \left(\rho_p \frac{4}{3} \pi a^3\right) da \right\} U_{m_z} 2\pi r \, dr$$

or, in nondimensional form,

$$\rho_p N_o \frac{8}{3} \pi^2 a_o^3 U_{m_{z_o}} R^2 \int_{\hat{r}=\hat{r}_\delta}^{1} \left[\int_{\hat{a}=o}^{\infty} \hat{n}_{\hat{z}=o}^{(q)} \hat{a}^3 \, d\hat{a} \right] \hat{U}_{m_z} \hat{r} \, d\hat{r} \qquad (5.34)$$

Therefore, the efficiency is

$$\eta = \frac{\rho_p N_o \frac{8\pi^2}{3} a_o^3 U_{m_{z_o}} R^2 \int_{\hat{z}=o}^{\hat{z}} \int_{\hat{a}=o}^{\infty} \left[\hat{\eta}^{(q)} \hat{a}^3 \hat{V}_r^{(q)} \right]_{wall} d\hat{z} \, d\hat{a}}{\rho_p N_o \frac{8\pi^2}{3} a_o^3 U_{m_{z_o}} R^2 \int_{\hat{r}=\hat{r}_\delta}^{1} \int_{\hat{a}=o}^{\infty} \left[\hat{\eta}_{\hat{z}=o}^{(q)} \hat{a}^3 \, d\hat{a} \right] \hat{U}_{m_z} \hat{r} \, d\hat{r}}$$

or

$$\eta = \frac{\int_{\hat{z}=0}^{\hat{z}} \int_{\hat{a}=0}^{\infty} \left[\hat{\eta}^{(q)} \hat{a}^3 \hat{V}_r^{(q)} \right]_{wall} d\hat{z}\, d\hat{a}}{\int_{\hat{r}=\hat{r}_\delta}^{1} \int_{\hat{a}=0}^{\infty} \left[\hat{r}^{(q)}_{\hat{z}=0} \hat{a}^3 d\hat{a} \right] \hat{U}_{m_z} \hat{r}\, d\hat{r}} \qquad (5.35)$$

Note that the denominator of this expression can be explicitly evaluated by using equation (5.3) and $\hat{U}_{m_z} = (1-\hat{r})^{1/m}$.

Discussion of Results

Graphical illustrations of some of the results for this example are shown in Figures 14 through 22. Figure 14 presents concentration profiles for total particle concentration, $\hat{N} = \int_0^\infty \hat{n}^{(q)}\, d\hat{a}$, across the pipe radius at $\hat{z}$ = 4.27, 9.17 and 34.37. It can be seen that the particle concentration decreases quite rapidly near the centerline, consistent with the large electric field and radial particle velocity in this region. Also shown in Figure 14 are the concentration profiles obtained when turbulent diffusion effects are considered. These latter results are discussed later.

The behavior of individual particle wall concentration distribution functions at three axial locations is illustrated in Figure 15, which presents $\hat{n}^{(q)}_{wall}$ as a function of particle radius, $\hat{a}$, at z = 0, 9.87 and 34.37. The reduction in particle concentration is relatively uniform with respect to particle radius. The numerical solutions for concentration distribution functions are quite smooth and consistent, indicating no evidence of numerical instability.

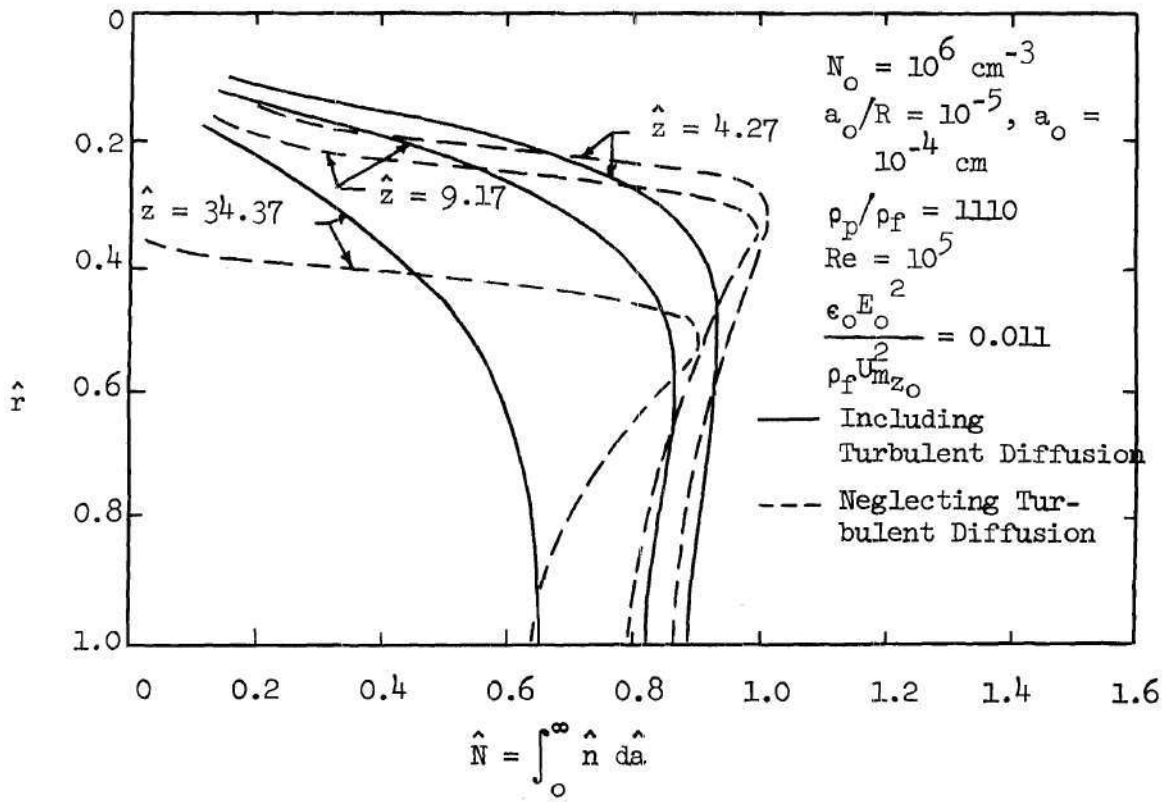

Figure 14. Total Particle Concentration Across Pipe Radius at Three Axial Locations

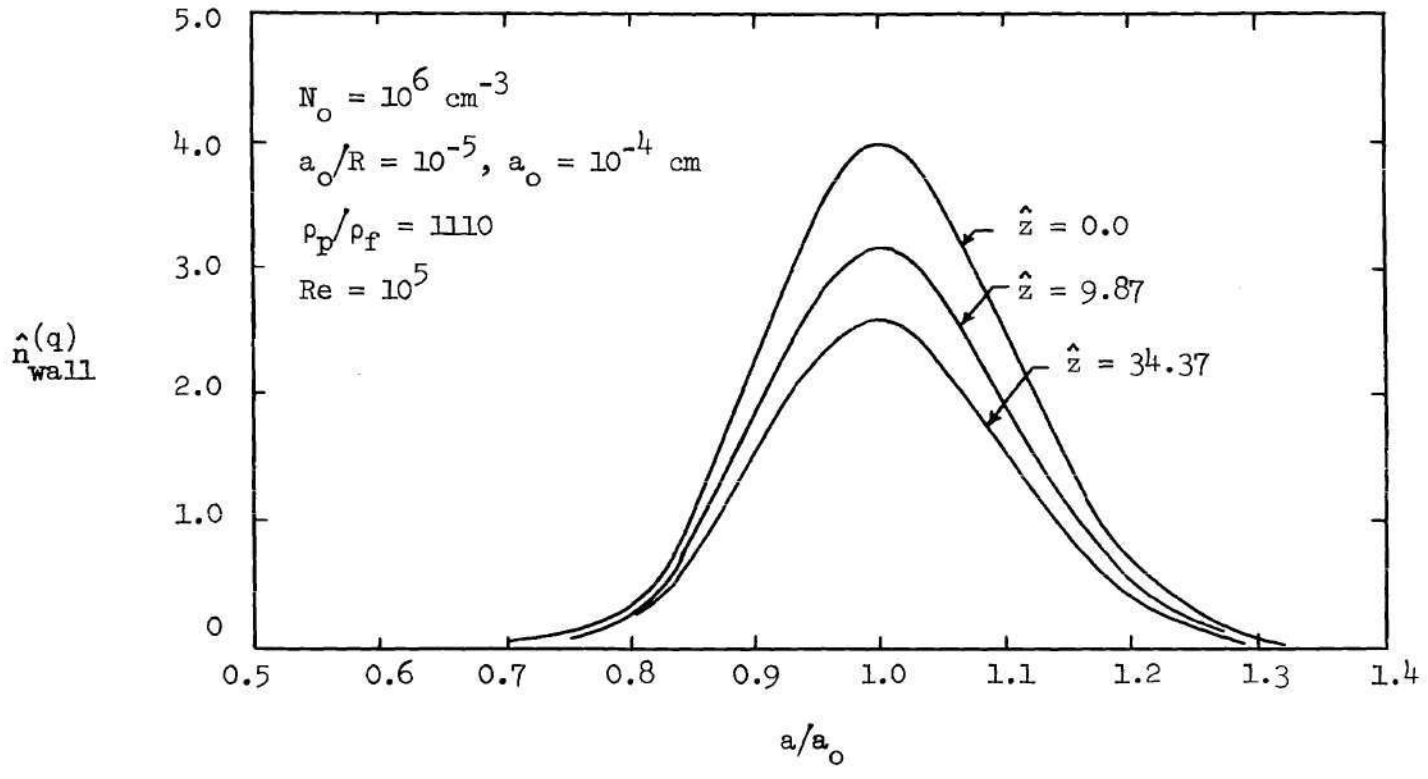

Figure 15. Wall Concentration Distribution Function Versus Particle Radius at Three Axial Locations

The removal efficiency, as obtained using equation (5.35), is shown in Figure 16 and compared with theoretical efficiency predictions obtained from the Deutsch formula. For this example, the numerical results for particulate removal efficiency indicate that the Deutsch formula predictions are quite reasonable for these conditions, at least as far downstream as $\hat{z} = 30$, where some difference is noted.

Figure 17 presents the particle radial velocity distribution across the pipe radius at z = 0, 4.27 and 34.37. Since the diffusion velocity at each point in this example is proportional to the local electric field intensity, one can also visualize the figure as representing the electric field variation across the pipe radius. One notes that the velocity varies only slightly with radius for $\hat{r}$ greater than about 0.4, compared to its variation for $\hat{r}$ less than 0.4. The only significant variation with axial location occurs near the wall, and the results indicate that the reduction in total charge and its associated self-repulsion effect results in a reduction in particle radial velocities near the wall as the flow proceeds downstream.

The computational results discussed thus far in this chapter were obtained for

$$\epsilon_o E_o^2 / (\rho_f U_{m_{z_o}}^2) = 0.001$$

This quantity essentially involves the ratio of electrical force to

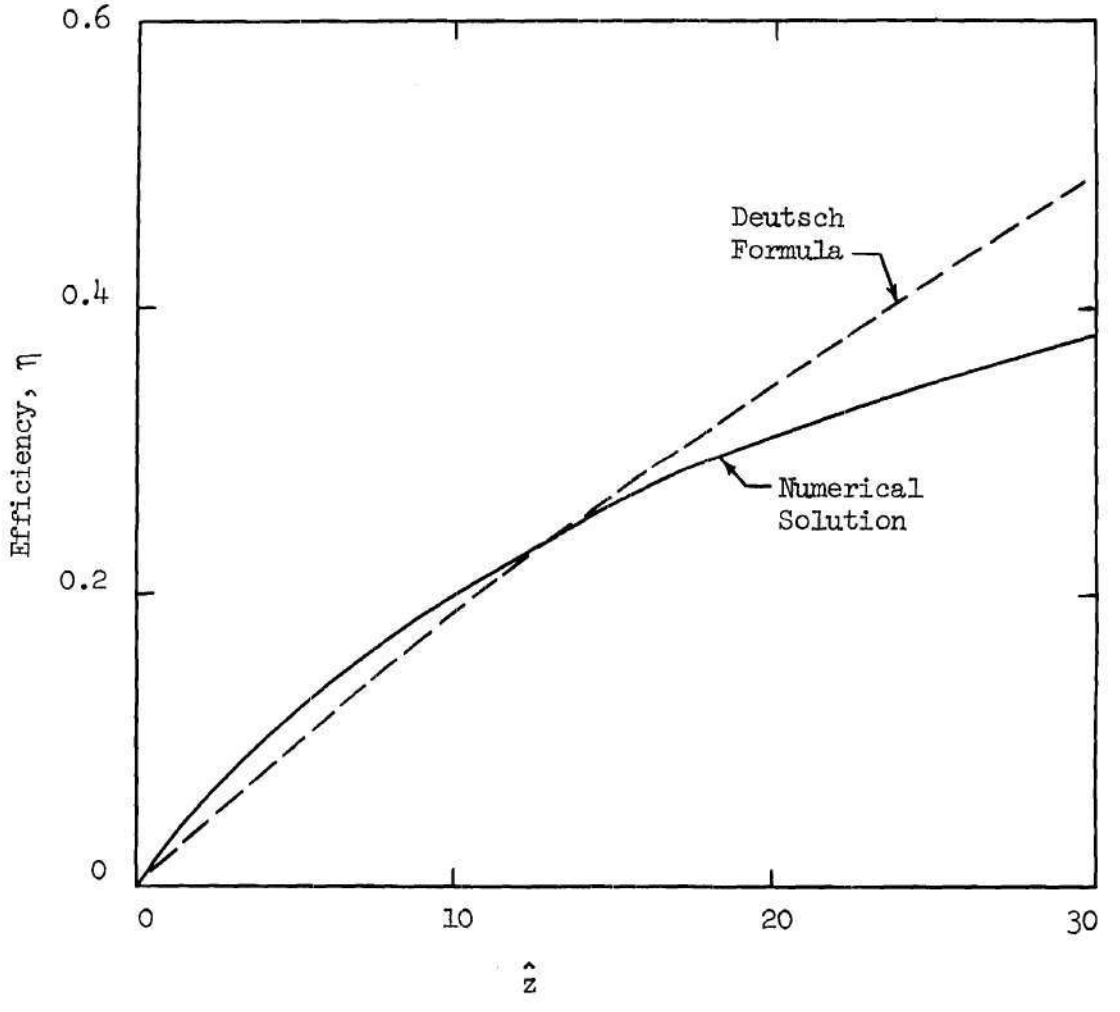

Figure 16. Particle Removal Efficiency as a Function of Axial Location

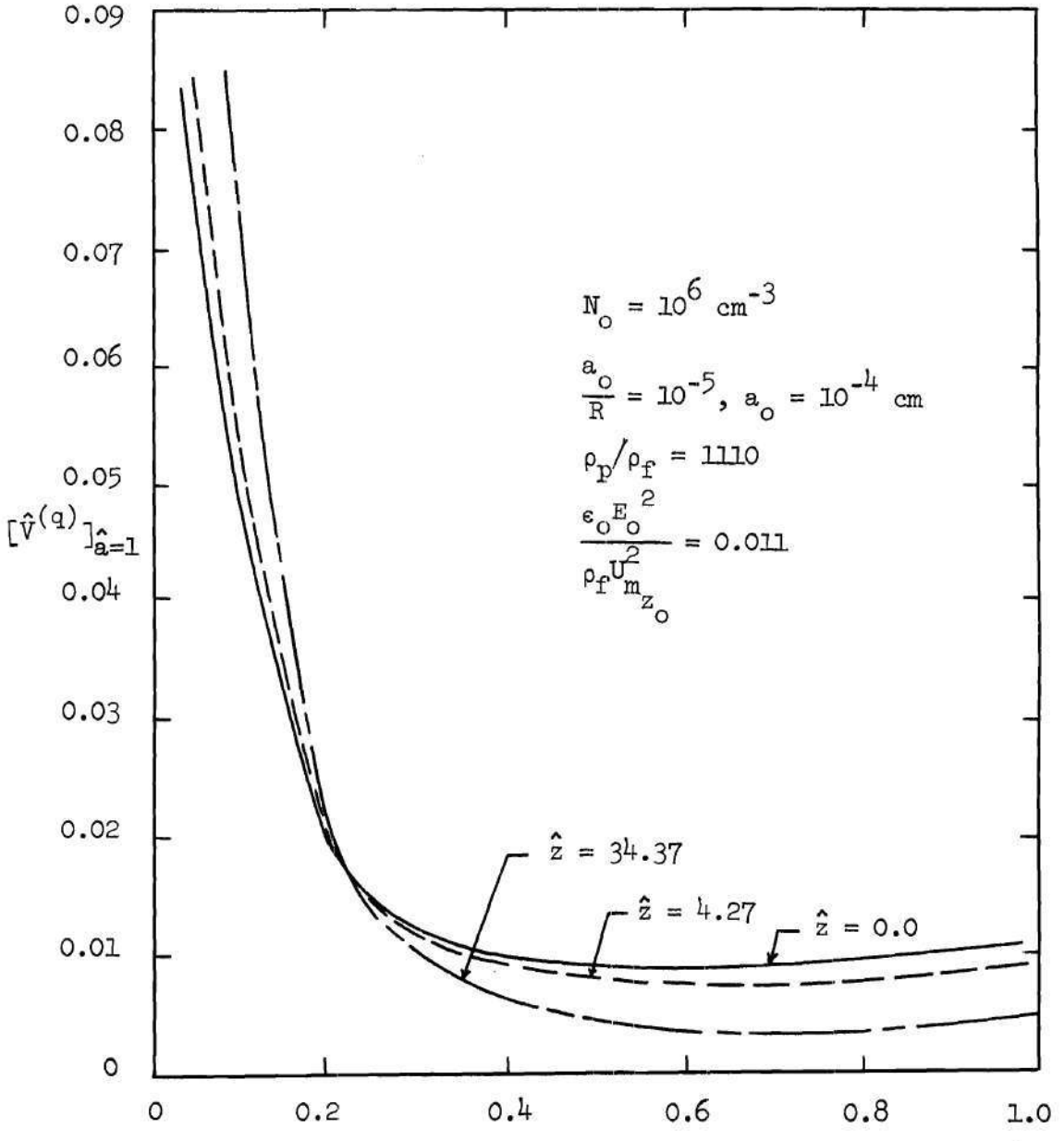

Figure 17. Particle Radial Velocity as a Function of Radial Location at Three Axial Locations

inertia force, and it therefore represents an important design parameter which requires some study relative to its influence upon the flow dynamics, e.g., upon the particulate-removal efficiency at any given downstream location. Accordingly, the previously discussed numerical solution procedure was repeated for sufficient values of $\epsilon_o E_o^2/(\rho_f U^2_{m_{z_o}})$ between 0.00011 and 0.880 to adequately define its influence upon particulate-removal efficiency from $\hat{z} = 0$ to $\hat{z} = 30$. Results are presented in Figure 18 for $\hat{z} = 5, 10, 20, 30$. As can be seen, the efficiency is relatively insensitive to $\epsilon_o E_o^2/(\rho_f U^2_{m_{z_o}})$ for efficiencies less than about 20 percent but varies considerably with increasing $\epsilon_o E_o^2/(\rho_f U^2_{m_{z_o}})$ for efficiences greater than about 20 percent. Further, there exists apparent upper limits for $\epsilon_o E_o^2/(\rho_f U^2_{m_{z_o}})$ at which particulate removal efficiency is essentially 100 percent at various values of $\hat{z}$. This is further illustrated in Figure 19, which presents $\epsilon_o E_o^2/(\rho_f U^2_{m_{z_o}})$ as a function of downstream distance, $\hat{z}$, at which particulate removal efficiency is essentially complete. It can be seen that, for the conditions chosen, there appears to be little advantage in extending the precipitation section beyond $\hat{z} = 30$, since the required value of $\epsilon_o E_o^2/(\rho_f U^2_{m_{z_o}})$ remains relatively stationary for $\hat{z}$ greater than about 30. Further analysis of these additional computational examples indicates that the discussion and conclusions with respect to the $\epsilon_o E_o^2/(\rho_p U^2_{m_{z_o}}) = 0.011$ case, examined earlier in some detail, remain valid for the other examined values of this latter parameter.

It is useful to examine the assumption that the turbulent

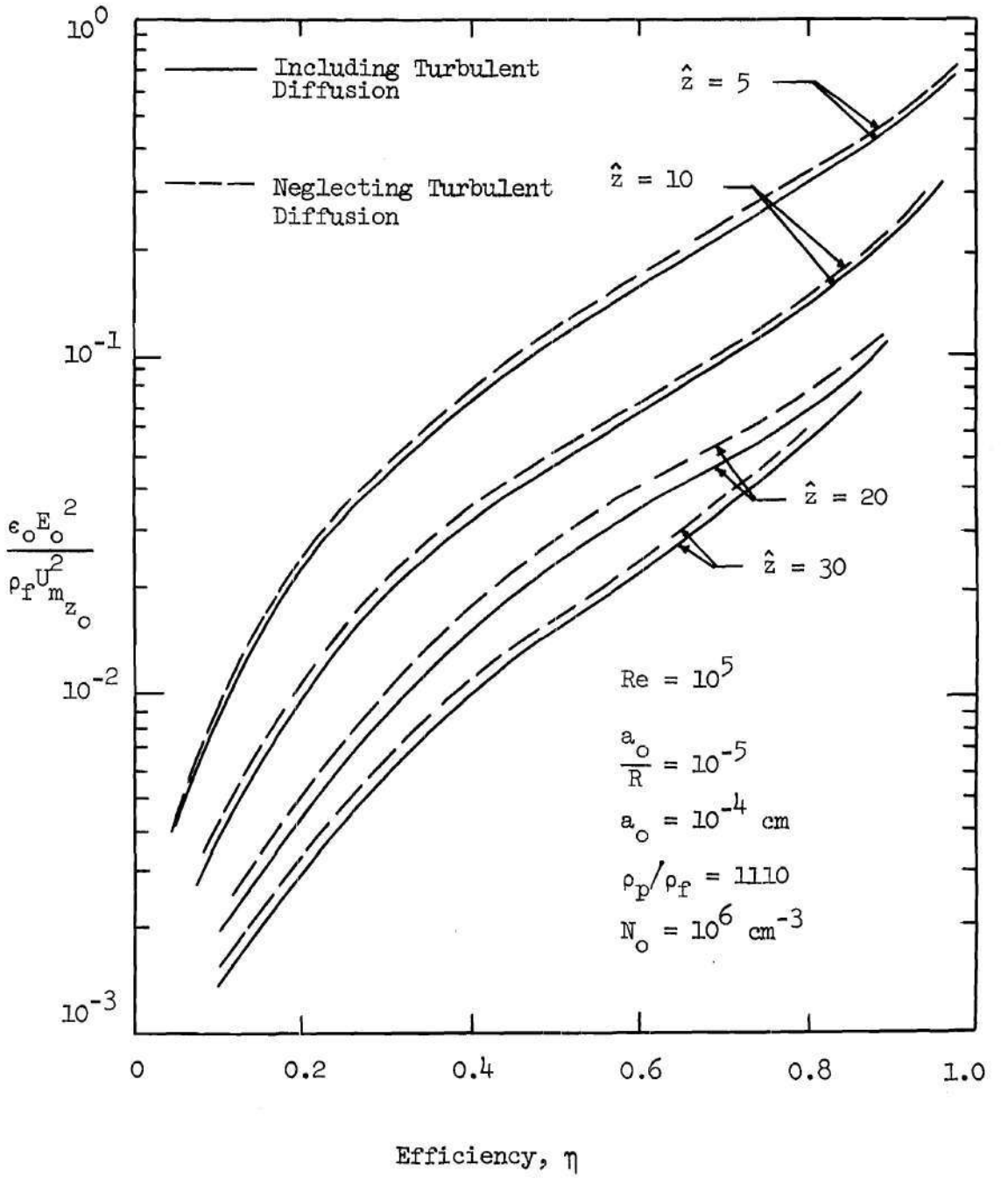

Figure 18. Particulate Removal Efficiency as a Function of $\epsilon_o E_o^2/\rho_f U_{m_{z_o}}^2$

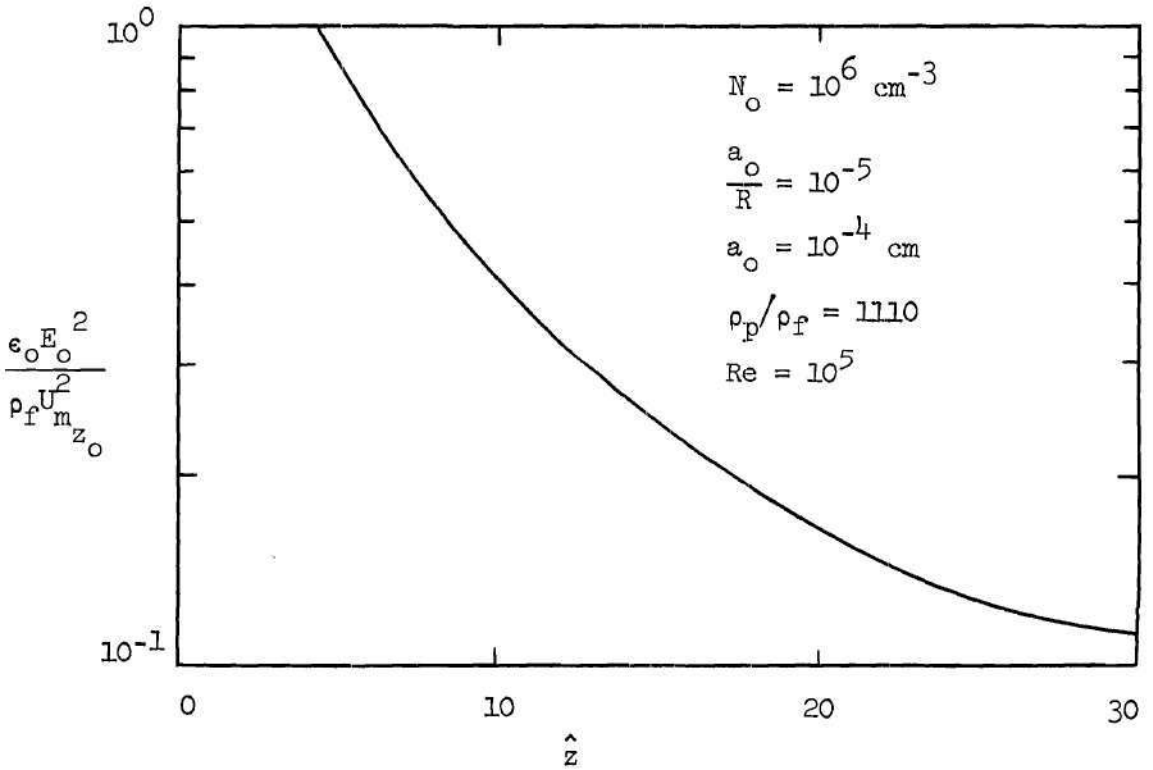

Figure 19. Required Value of $\epsilon_o E_o^2/\rho_f U_{m_{z_o}}^2$ for Complete Particle Removal at Various Downstream Locations

diffusion flux is negligible with respect to the particle flux due to electric drift. Using equation (2.6), one can express the turbulent diffusion flux, within the framework of the present analysis, as

$$\hat{J}_r = \hat{\ell}^2 \left| \frac{d\hat{U}_{m_z}}{d\hat{r}} \right| \frac{d\hat{N}}{d\hat{r}} \tag{5.36}$$

The corresponding flux due to electrical drift is given by

$$\int_{\hat{a}=o}^{\infty} \hat{n}^{(q)} \hat{V}_r^{(q)} \, d\hat{a} \cong \hat{N} \left[\hat{V}_r^{(q)}\right]_{\hat{a}=1} \tag{5.37}$$

Numerical solutions were obtained for the indicated conditions of the current example, including consideration of the additional mass transport due to turbulent diffusion flux, and compared with corresponding results obtained when turbulent diffusion was neglected.

The modification to the numerical computation procedure to account for turbulent diffusion for the present example involves the addition of a term to the diffusion velocity expression, i.e.,

$$\hat{V}_r^{(q)} = \left[\hat{V}_r^{(q)}\right]_{\substack{\text{electrical} \\ \text{drift}}} + \left[\hat{V}_r^{(q)}\right]_{\substack{\text{turbulent} \\ \text{diffusion}}} \tag{5.38}$$

where the first term on the right-hand side represents the previous equilibrium diffusion velocity resulting from electrical forces and, as earlier,

$$\left[\hat{V}_r^{(q)}\right]_{\substack{\text{turbulent}\\ \text{diffusion}}} = -\frac{\hat{\ell}^2}{\hat{n}^{(q)}}\left|\frac{d\hat{U}_{m_z}}{d\hat{r}}\right|\frac{d\hat{n}^{(q)}}{d\hat{r}} \tag{5.39}$$

Figure 14, considered earlier, presents a comparison of number-concentration profiles obtained at three axial locations (it is interesting to note that the inclusion of turbulent diffusion into the computations approximately doubled the required computation time). One notes from Figure 14, as expected, a general "smoothing" of the profiles, with the inward flux near the centerline tending to retard the decrease in number concentration in this region and the outward flux nearer the wall tending to transport additional material to this outer region. The concentration increase due to diffusional transport near the wall is seen to be relatively small, and since the diffusion velocity remains approximately the same as without turbulent diffusion (recall the Danckwerts' wall-boundary condition imposed on the problem), then one can anticipate both a small increase in mass flux to the wall as a result of diffusion and a corresponding increase in particulate removal efficiency at any given location. These diffusional processes tend to smooth out the concentration gradients and, according to the Deutsch theory, are presumed to result in a completely uniform

concentration profile throughout the precipitation section. This latter is, however, at variance with the present results and with experimental observations of precipitator performance, which indicate concentration profiles very similar to those of Figure 14.

A comparison of the relative magnitudes of the turbulent diffusion flux and the electrical-drift flux is shown in Figure 20 for conditions of the initial example of this chapter. Note that the diffusion flux is, in fact, relatively small with respect to electrical drift except for a narrow region where, as indicated in Figure 14, there exists a significant number-concentration gradient. There, the gradient is such that diffusion tends to transport particles toward the centerline, whereas, nearer the wall, there exists a much smaller diffusion flux outward toward the wall for $\hat{z}$ less than about 10. Figure 18, also examined earlier, presents a comparison of results for efficiency as a function of $\epsilon_o E_o^2/(\rho_f U_{m_{z_o}}^2)$ at $\hat{z} = 0$, 10, 20, and 30. As expected, turbulent diffusion increases the efficiency at any given location.

Nonequilibrium Diffusion Velocity Example

The previous computational examples were based on a particle most probable radius of one micron, and the results indicated that the particle diffusion velocities remain essentially at their equilibrium values throughout the flowfield. As can be seen from equation (4.44), larger values of a_o/R would result in increased velocity equilibration distances, and when the equilibration distances are no longer negligible with respect to the numerical step size, particle diffusion

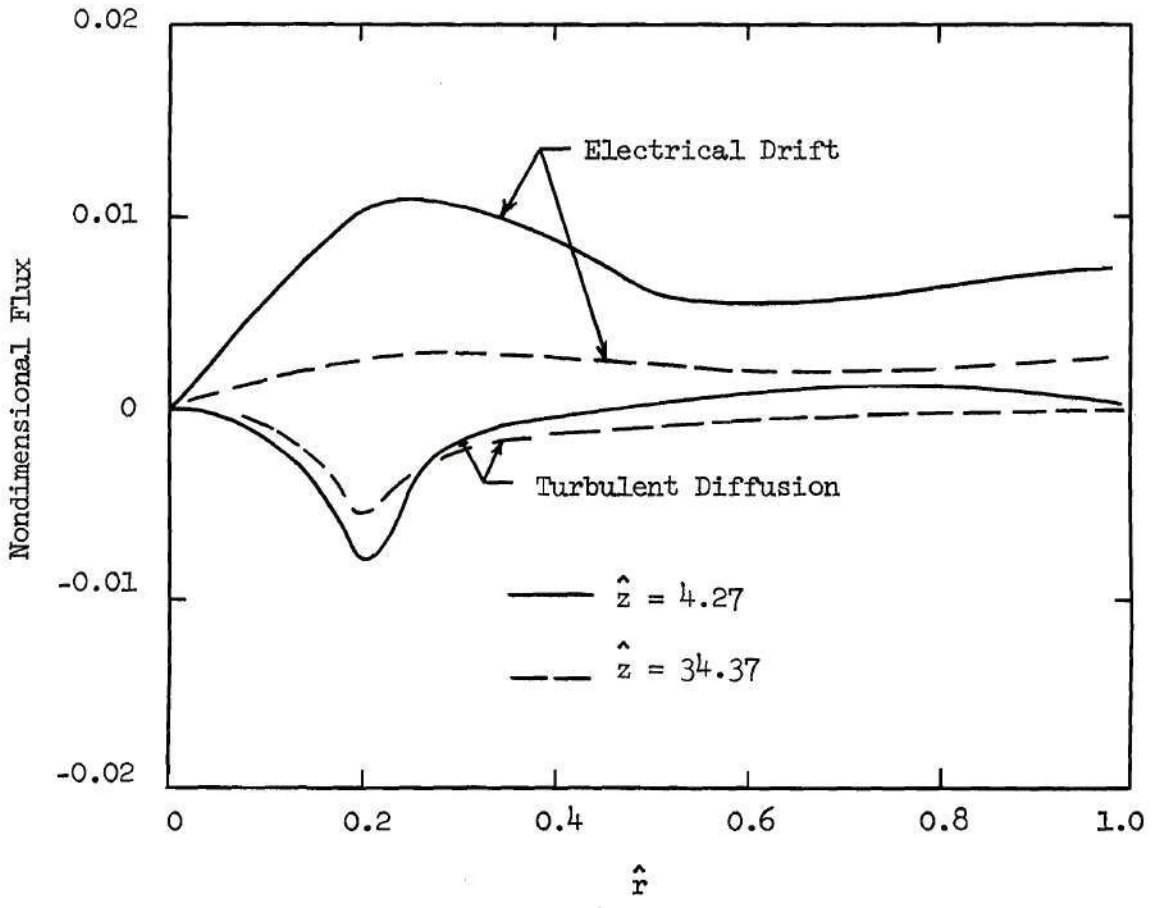

Figure 20. Comparison of Turbulent Diffusion Flux with Electrical Drift Flux at Two Axial Locations

velocities can no longer be expected to ramain at their local equilibrium values.

In order to determine the effect of nonequilibrium particle velocities on the results of interest, the equilibrium velocity example of the previous sections was modified to represent a particulate loading having a most probable radius of ten microns, i.e., $a_o/R = 10^{-4}$ and $a_o = 10^{-3}$ cm. However, for the same external electric field as considered for the basic example of the previous sections, one notes that the particulate charge, $\hat{Z}^{(q)}$, given by equation (4.25) will increase by a factor of 100 when a_o/R is increased by a factor of ten. The total electric charge presented at the inlet, $\hat{z} = 0$, for the same total number of particles would increase by a factor of 100, and this condition would result in additional, undesired effects upon the system deposition and behavior. Therefore, the quantity N_o is taken to be 10^{-4} cm^{-3}, so that the product $N_o(a_o/R)^2$ in the expression for $\hat{Z}^{(q)}$ is the same as for the previous example. Under this condition, then, the total electric charge presented at the inlet is the same for this larger particle example as for the previous, smaller particle example. With the exception of these modifications, the parameters of the two examples remain the same. Experimental evidence indicates that precipitator efficiency is essentially independent of inlet particle concentration [24].

Computations of particle equilibration distance as given by equation (4.44) indicate that $\hat{z}_{eq}$ varies from zero at the pipe wall to a value $[\hat{z}_{eq}]_{\hat{r}=0} = 0.493\ \hat{a}^2$ at the centerline. These values of $\hat{z}_{eq}$ are, in fact, greater than before by a factor of 100 and, near the

centerline, are larger than the streamwise numerical step size. Therefore, within a portion of the flowfield near the centerline, it is no longer appropriate to assume that the particle diffusion velocities are near equilibrium, although near the wall, this is still permissible. Since the mean velocity is assumed to approach zero at a solid surface in this continuum approximation, equation (4.44) indicates that $\hat{z}_{eq}$ will always approach zero near a wall. Therefore, a boundary condition on diffusion velocities is defined by the equilibrium condition at the wall.

Other appropriate boundary conditions for diffusion velocities are provided by physical considerations at the pipe centerline. Symmetry conditions at the centerline indicate that the radial derivative of the axial velocity vanish at $\hat{r} = 0$. As before, however, it can be shown that the radial velocity increases without bound as one approaches the centerline, as would be expected from the electric-field variation, but must be zero at the centerline itself (discounting the presence of the centerline wire). This discontinuous behavior is again a source of numerical computational difficulties, and therefore the centerline computation approximation of the previous example is again here adopted.

Numerical Solution Procedure

The numerical solution technique for this example is essentially the same as that developed for the previous example, with the exception of the approach taken to account for the nonequilibrium nature of the particle diffusion velocity. Computations indicate that the region near the wall within which diffusion velocities can be assumed in local equilibrium, combined with the region near the centerline for which

a modified solution procedure is necessary actually comprise a rather significant portion of the flowfield. Therefore, only a rather confined region need be the subject of some nonequilibrium-velocity considerations.

One could formulate a solution technique which incorporates the momentum equations, equations (4.35) and (4.36), into the algorithm. Since the region within which this would be necessary is rather small and the degree of nonequilibrium is not large for this example, it was decided at the outset not to involve the additional complexity associated with including the momentum equations, but rather to explore the possibility for implementing a simpler relaxation model for the diffusion velocity behavior. Simultaneous solution of the momentum equations and the continuity equation is deferred until later examples are considered.

Before attempting to structure an appropriate relaxation model for velocity relaxation, it may be constructive to examine certain aspects of the momentum equation itself. Consider the radial momentum equation, equation (4.35). Solving this equation for $\partial \hat{V}_r^{(q)}/\partial \hat{z}$ and using equation (5.4) for $(\hat{V}_r^{(q)})_{eq}$ yields

$$\frac{\partial \hat{V}_r^{(q)}}{\partial \hat{z}} = \frac{1}{\hat{U}_{m_z}} \left\{ \frac{B}{\left(\frac{a_o}{R}\right)^2 \hat{a}^2} \left[(\hat{V}_r^{(q)})_{eq} - \hat{V}_r^{(q)} \right] - \hat{V}_r^{(q)} \frac{\partial \hat{V}_r^{(q)}}{\partial \hat{r}} \right\} \quad (5.40)$$

Since $\hat{z}_{eq} = 4\, \hat{U}_{m_z} (a_o/R)^2\, \hat{a}^2/B$ by definition, then equation (5.40) can

be written as

$$\frac{\partial \hat{V}_r^{(q)}}{\partial \hat{z}} = \frac{1}{\hat{U}_{m_z}} \left\{ \frac{4\hat{U}_{m_z}}{\hat{z}_{eq}} \left[(\hat{V}_r^{(q)})_{eq} - \hat{V}_r^{(q)} \right] - \hat{V}_r^{(q)} \frac{\partial \hat{V}_r^{(q)}}{\partial \hat{r}} \right\} \quad (5.41)$$

or

$$\hat{U}_{m_z} \frac{\partial \hat{V}_r^{(q)}}{\partial \hat{z}} + \hat{V}_r^{(q)} \frac{\partial \hat{V}_r^{(q)}}{\partial \hat{r}} = \frac{4\hat{U}_{m_z}}{\hat{z}_{eq}} \left[(\hat{V}_r^{(q)})_{eq} - \hat{V}_r^{(q)} \right] \quad (5.42)$$

Substituting $d\hat{V}_r^{(q)}/dt^{(q)}$ for the left-hand side of equation (5.42) yields

$$\frac{d\hat{V}_r^{(q)}}{dt^{(q)}} = \frac{4\,\hat{U}_{m_z}}{\hat{z}_{eq}} \left[(\hat{V}_r^{(q)})_{eq} - \hat{V}_r^{(q)} \right] \quad (5.43)$$

Thus, the momentum equation can be written in a relaxation form, with a relaxation time here obtained as $(4\,\hat{U}_{m_z}/\hat{z}_{eq})^{-1}$. Since $\hat{U}_{m_z}$ is expected to be much greater than $\hat{V}_r^{(q)}$, the left-hand side of equation (5.43) can

be effectively replaced by $\hat{U}_{m_z} \partial \hat{V}_r^{(q)}/\partial\hat{z}$. Finally, formulating the resulting equation in finite-difference form yields (in backward-difference form)

$$\hat{U}_{m_z}\left[\frac{(\hat{V}_r^{(q)})_{\hat{z}} - (\hat{V}_r^{(q)})_{\hat{z}-\Delta\hat{z}}}{\Delta\hat{z}}\right] = \frac{4\hat{U}_{m_z}}{\hat{z}_{eq}}\left[(\hat{V}_r^{(q)})_{eq} - \hat{V}_r^{(q)}\right]_{\hat{z}-\Delta\hat{z}} \quad (5.44)$$

for a simple Euler scheme. This can be written in the form

$$[\hat{V}_r^{(q)}]_{\hat{z}} = \left\{[\hat{V}_r^{(q)}]_{\hat{z}-\Delta\hat{z}} - [(\hat{V}_r^{(q)})_{eq}]_{\hat{z}-\Delta\hat{z}}\right\}\left(-\frac{4\Delta\hat{z}}{\hat{z}_{eq}}\right) + (\hat{V}_r^{(q)})_{\hat{z}-\Delta\hat{z}} \quad (5.45)$$

or

$$[\hat{V}_r^{(q)}]_{\hat{z}} = \left\{[\hat{V}_r^{(q)}]_{\hat{z}-\Delta\hat{z}} - [(\hat{V}_r^{(q)})_{eq}]_{\hat{z}-\Delta\hat{z}}\right\}\left(1 - \frac{4\Delta\hat{z}}{\hat{z}_{eq}}\right) + [(\hat{V}_r^{(q)})_{eq}]_{\hat{z}-\Delta\hat{z}} \quad (5.46)$$

Now, the model equation, equation (5.46), yields the desired result only for relatively small values of $\Delta\hat{z}/\hat{z}_{eq}$. That is, one expects that when $\Delta\hat{z}/\hat{z}_{eq}$ approaches zero, $\hat{V}_r^{(q)}$ remains constant. Equation (5.46)

implies that

$$[\hat{V}_r^{(q)}]_{\hat{z}} = [\hat{V}_r^{(q)}]_{\hat{z}-\Delta\hat{z}}$$

when $\Delta\hat{z}/\hat{z}_{eq} = 0$, as desired. On the other hand, as $\Delta\hat{z}/\hat{z}_{eq}$ increases, one expects that

$$[\hat{V}_r^{(q)}]_{\hat{z}} \rightarrow [\hat{V}_r^{(q)}{}_{eq}]_{\hat{z}}$$

but equation (5.46) does not indicate this desired limiting behavior. The difficulty is generated by the finite-difference form; however, a reasonable relaxation model can be obtained from these previous considerations by noting that the solution to equation (5.43) is exponential in character. On this basis, the following model is proposed:

$$[\hat{V}_r^{(q)}]_{\hat{z}} - [(\hat{V}_r^{(q)})_{eq}]_{\hat{z}-\Delta\hat{z}} = [\hat{V}_r^{(q)} - (\hat{V}_r^{(q)})_{eq}]_{\hat{z}-\Delta\hat{z}}\, e^{-\frac{4\Delta\hat{z}}{\hat{z}_{eq}}} + \tag{5.47}$$

$$\left\{[(\hat{V}_r^{(q)})_{eq}]_{\hat{z}} - [(\hat{V}_r^{(q)})_{eq}]_{\hat{z}-\Delta\hat{z}}\right\} S\left(\frac{\Delta\hat{z}}{\hat{z}_{eq}} - 1\right)$$

where S (x) is the unit step function, i.e.,

$$S(x) = \begin{matrix} 0 \text{ if } x < 0 \\ 1 \text{ if } x \geq 0 \end{matrix}$$

Examination of the model behavior exhibited by equation (5.47) indicates that

$$[\hat{V}_r^{(q)}]_{\hat{z}} \rightarrow [\hat{V}_r^{(q)}]_{\hat{z}-\Delta\hat{z}}$$

as $\Delta\hat{z}/\hat{z}_{eq} \rightarrow 0$, as desired, and that

$$[\hat{V}_r^{(q)}]_{\hat{z}} \rightarrow [(\hat{V}_r^{(q)})_{eq}]_{\hat{z}}$$

as $\Delta\hat{z}/\hat{z}_{eq} \rightarrow \infty$, also as desired. In addition, the model indicates that $\hat{V}_r^{(q)}$ relaxes toward $(\hat{V}_r^{(q)})_{eq}$ with a relaxation distance $\hat{z}_{eq}/4$ when $\Delta\hat{z} \lesssim \hat{z}_{eq}$, again as desired. Therefore, equation (5.47) represents a useful velocity relaxation model for this example.

Discussion of Results

Figure 21 illustrates concentration profiles for total particle

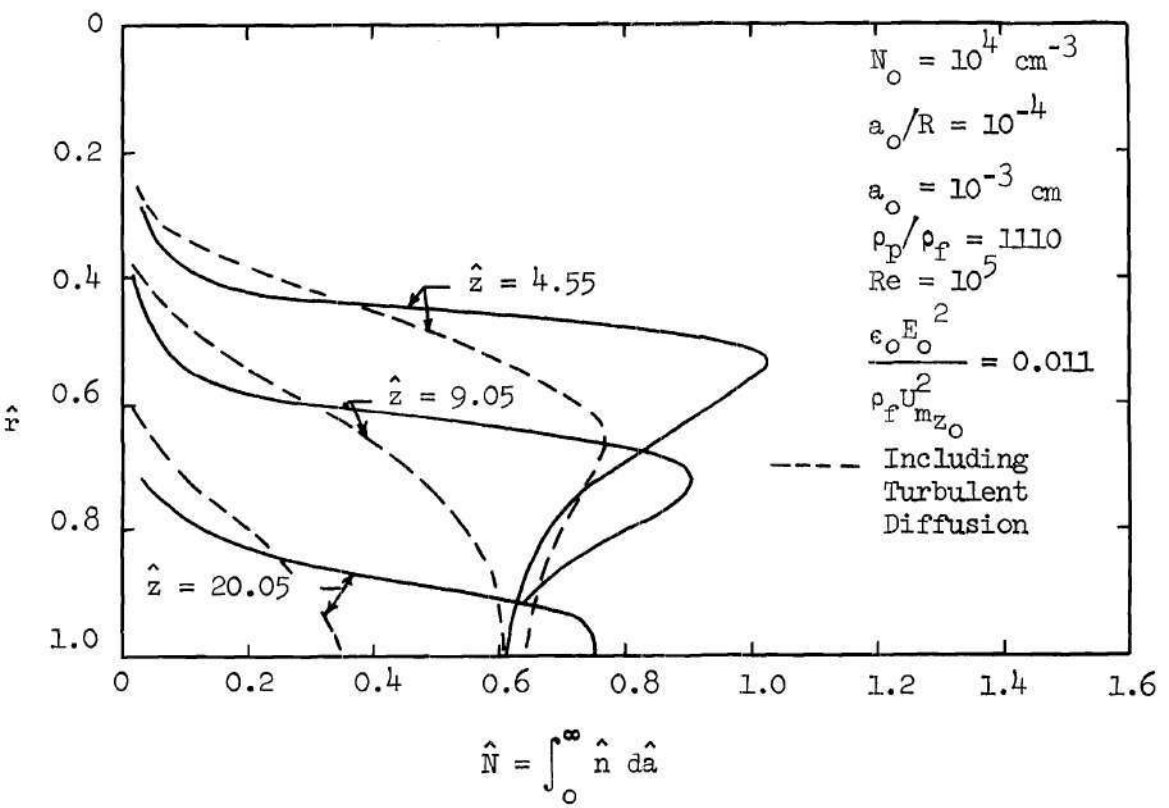

Figure 21. Total Particle Concentration Across the Pipe Radius at Three Axial Locations

concentration, $\hat{N}$, across the pipe radius at $\hat{z} = 4.55$, 9.05, and 20.05. Comparing these profiles with those obtained for the previous example indicates similar behavior, with the particle concentration near the centerline being reduced to zero rather quickly and with this region extending further toward the wall as the flow proceeds downstream. Note that for the larger particles, the reduction in total concentration is greater at any given axial location. The peaking tendency indicated in the profiles when turbulent diffusion is neglected is more pronounced here, and as the peak moves toward the wall, the wall concentration actually increases as the flow proceeds downstream. However, when turbulent diffusion effects are considered, the peaking tendency is essentially removed. The concentration at the wall, on the other hand, is not significantly affected by diffusion until $\hat{z}$ becomes greater than about 10.

The peaking effect observed when turbulent diffusion is neglected is illustrated also in Figure 22, which represents individual particle wall concentration distribution functions at three axial locations. Although the reduction in wall concentration which occurs from $\hat{z} = 0$ to $\hat{z} = 9.05$ is similar to that illustrated in Figure 15 for smaller particles, although more pronounced, the behavior as the flow proceeds to $\hat{z} = 20.05$ is quite different. Consistent with the movement of the peak in concentration toward the wall, as illustrated in Figure 21, the particle distribution function at the wall tends to increase. This increase is more pronounced for particle radii below $\hat{a} = 1.1$, but the higher deposition flux for larger particles outweighs this effect, and their concentration is less at $\hat{z} = 20.05$ than at $\hat{z} = 9.05$.

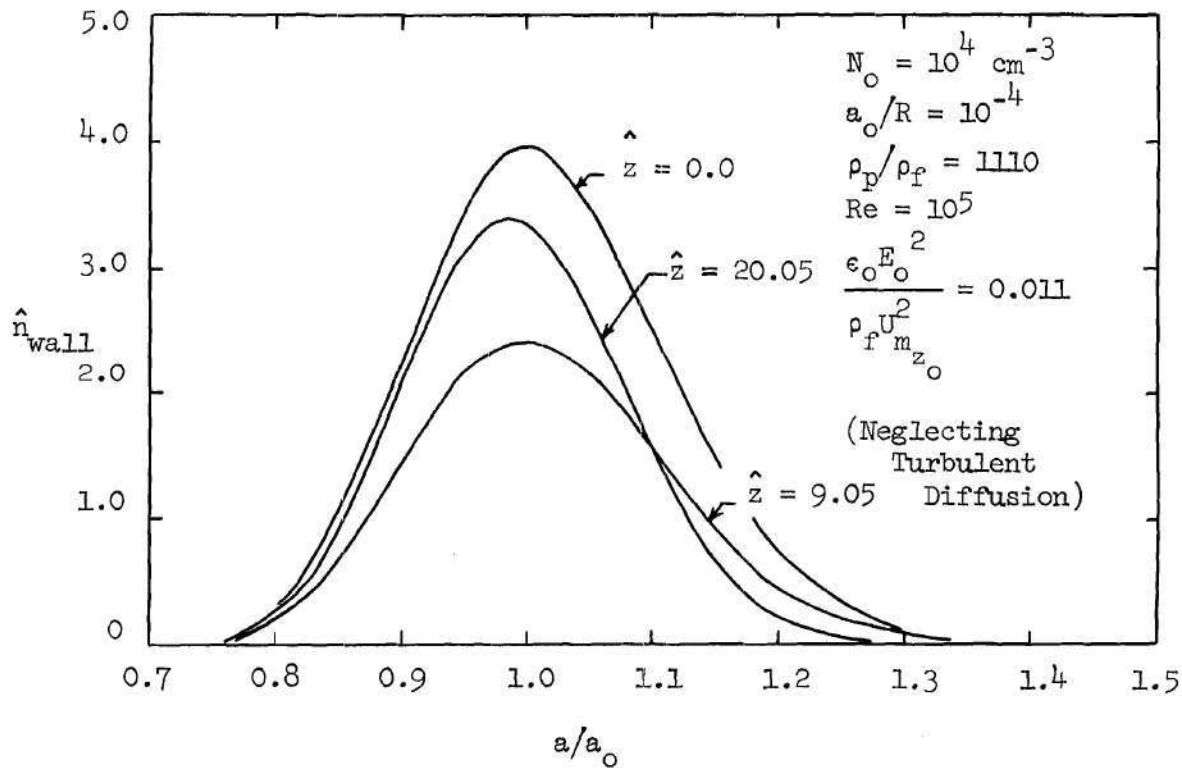

Figure 22. Wall Concentration Distribution Function Versus Particle Radius at Three Axial Locations

When turbulent diffusion effects are included, the concentration distributions decrease consistently, as would be expected from previous results discussed.

The particle removal efficiency is shown in Figure 23, in which also are shown some numerical solutions for efficiency corresponding to $\rho_p/\rho_f = 500$ (fly ash) and $\rho_p/\rho_f = 8820$ (lead), in addition to that for $\rho_p/\rho_f = 1100$ considered heretofore. Although the previous example for smaller particles indicated close agreement between the numerical solution and the Deutsch formula, the numerical solution for removal efficiency for this larger particle example indicates considerable difference between the two results. The Deutsch formula yields an efficiency much too high at any given axial location, although the asymptotic limit for both results is, of course, one. Note that deposition increases as anticipated when turbulent diffusion effects are included in the numerical solution.

Figure 24 presents the particle radial velocity across the pipe radius at $\hat{z} = 0$, 4.05, and 34.55. Also shown are the equilibrium velocity profiles at $\hat{z} = 4.05$ and 34.55. Note that, as expected, the actual velocity profiles differ only slightly from the equilibrium profiles, with the greatest difference being in the region near the centerline, where the particle concentration has been reduced almost to zero. It is also interesting to note that, although the particle radial velocity has been taken as zero for all $\hat{r}$ at $\hat{z} = 0$, it achieves a near equilibrium value rather quickly and remains near equilibrium throughout the flow.

Figure 25 illustrates the influence of the parameter

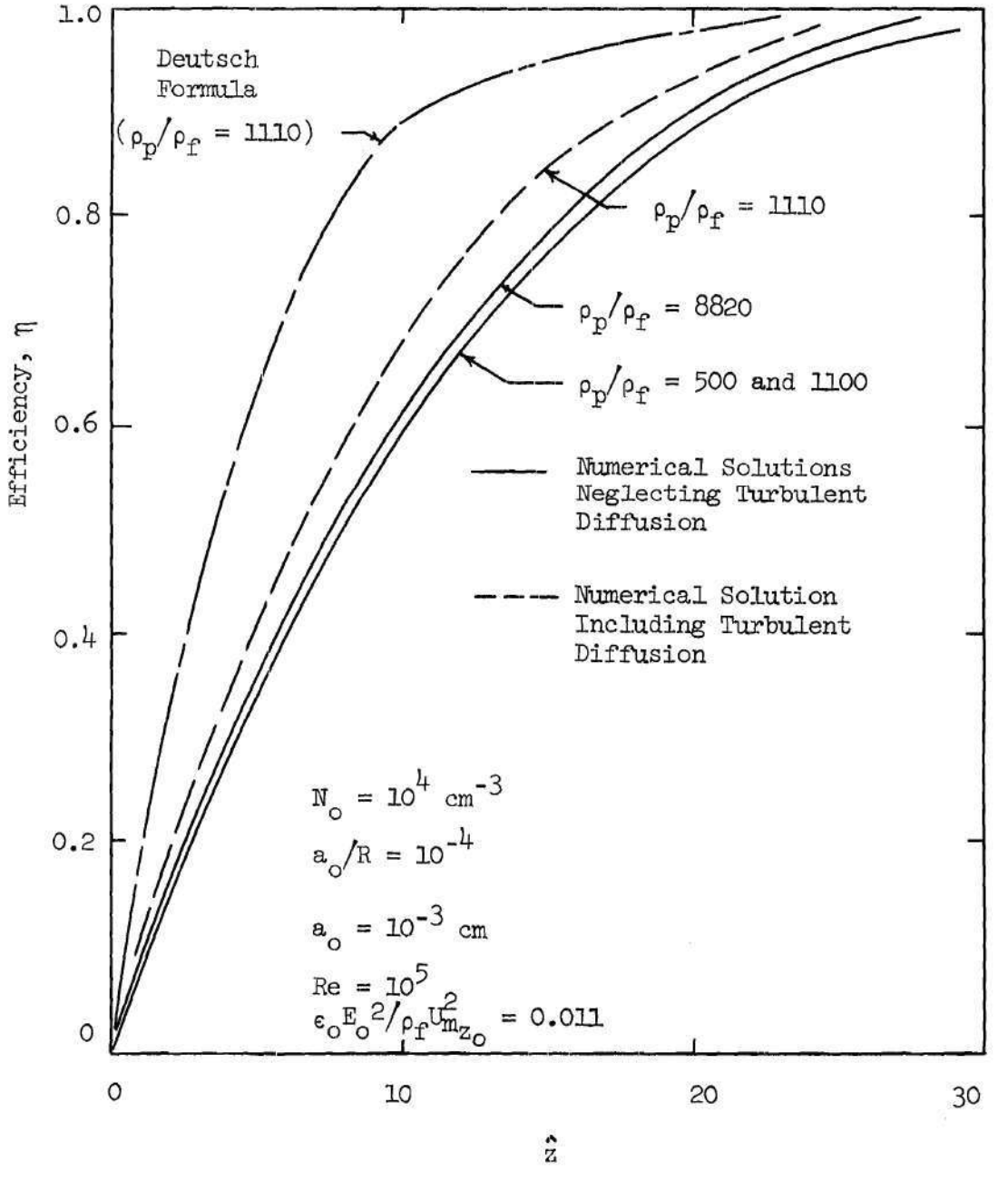

Figure 23. Particulate Removal Efficiency as a Function of Axial Location

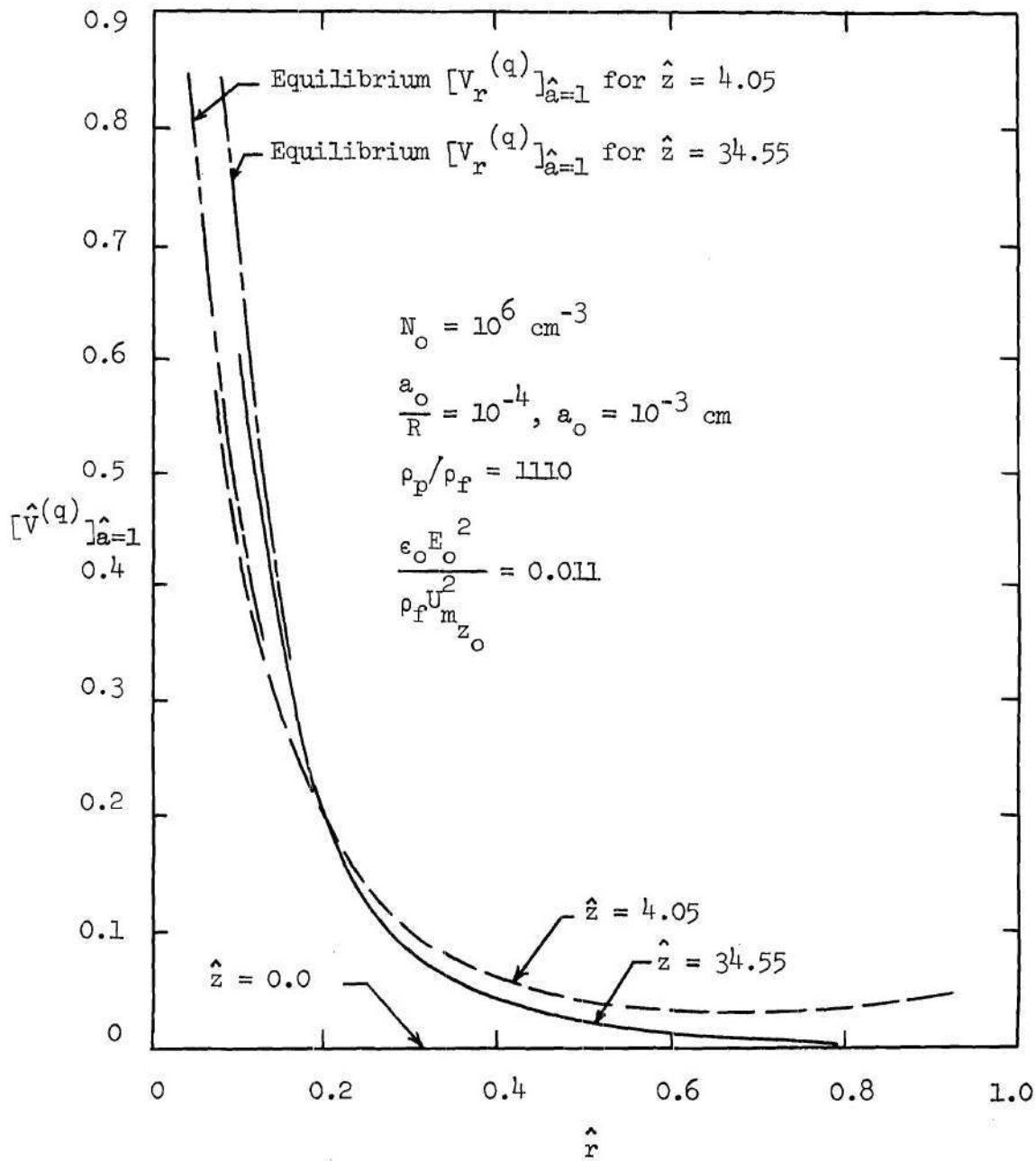

Figure 24. Particle Radial Velocity as a Function of Radial Location at Three Axial Locations

$\epsilon_o E_o^2/\rho_f U_{m_{z_o}}^2$ upon the particulate removal efficiency at several downstream locations. Comparing these results with those of Figure 18 indicates that the general trend of the curves, both including and excluding turbulent diffusion effects, are quite similar with a decrease in $\epsilon_o E_o^2/\rho_f U_{m_{z_o}}^2$ by approximately a factor of ten required for the larger particles to achieve equivalent efficiencies at given downstream locations. Otherwise, the comments made earlier with respect to Figure 18 could be repeated here.

Having examined the efficiency results presented in Figures 18 and 25, one might ask what effective drift velocity would be necessary to "fit" the Deutsch formula to the numerical solution results? The Deutsch formula may be written as

$$\eta = 1 - e^{-Aw/\bar{V}}$$

or in the form

$$\eta = 1 - e^{-2\hat{w}z/\bar{U}_{m_z}} \tag{5.48}$$

where, in the present notation,

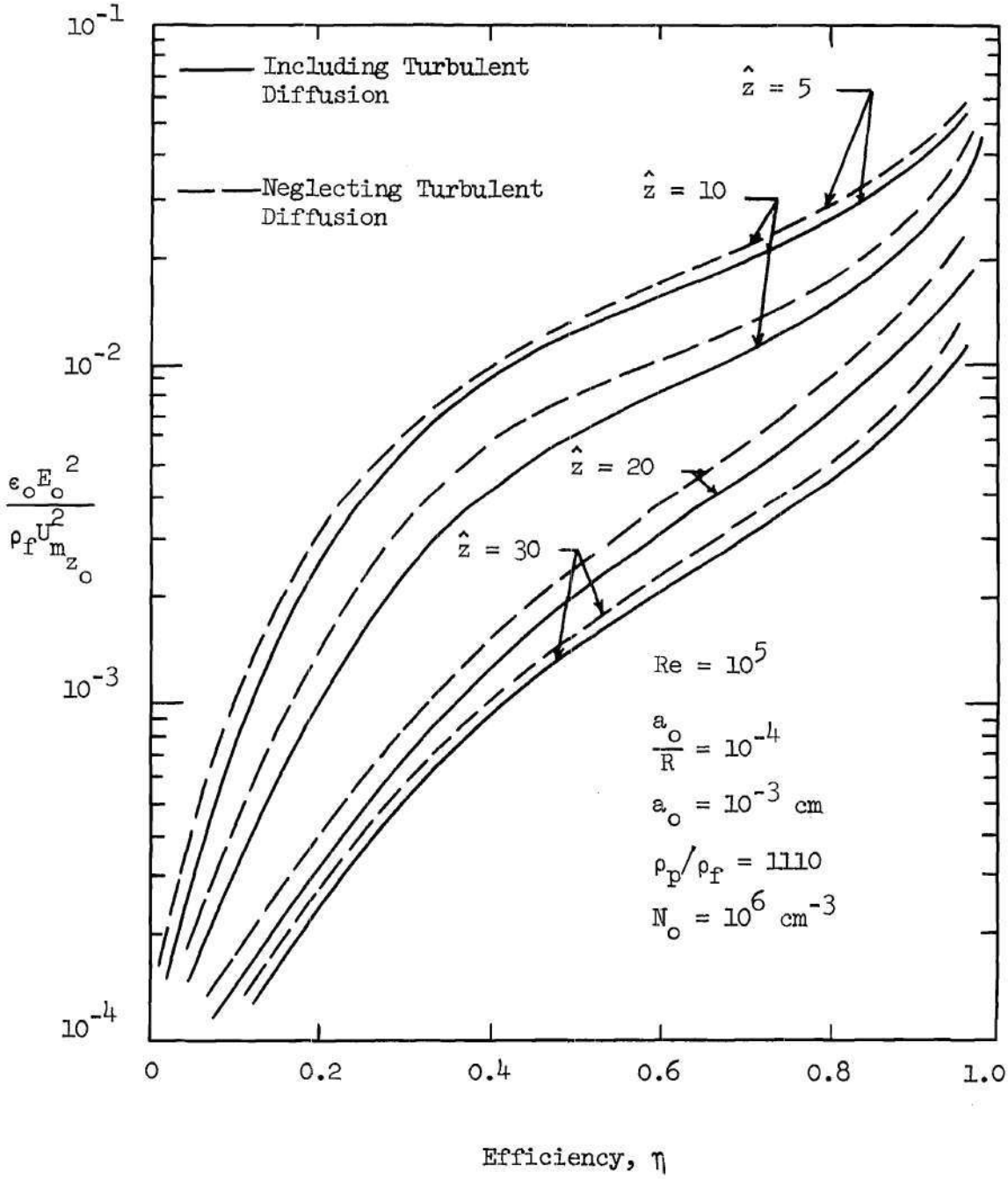

Figure 25. Particulate Removal Efficiency as a Function of $\epsilon_o E_o^2/\rho_f U^2_{m_{z_o}}$

$$\frac{w}{\bar{U}_{m_z}} \triangleq \tilde{w} = \frac{1}{3} \, Re \left(1 + 2 \, \frac{\epsilon_r - 1}{\epsilon_r + 2}\right) \left(\frac{\epsilon_o E_o^2}{\rho_f U_{m_{z_o}}^2}\right) \left(\frac{a_o}{R}\right) \left(\frac{U_{m_{z_o}}}{\bar{U}_{m_z}}\right) \qquad (5.49)$$

within the Stokes' drag regime. However, one could propose an effective drift velocity, w_{eff}, obtained by solving equation (5.48) for w, i.e.,

$$\tilde{w}_{eff} = - \frac{1}{2\hat{z}} \ln (1 - \eta) \qquad (5.50)$$

where η and $\hat{z}$ are obtained from Figure 18 or Figure 25 for given values of the parameter $\epsilon_o E_o^2 / (\rho_f U_{m_{z_o}}^2)$. Effective velocities determined in this manner, however, exhibit a slight dependence upon $\hat{z}$. By averaging with respect to $\hat{z}$, one obtain an effective drift velocity of the form

$$\tilde{w}_{eff} = \tilde{w}_{eff} \left(\frac{\epsilon_o E_o^2}{\rho_f U_{m_{z_o}}^2}\right) \qquad (5.51)$$

for given a_o/R, Re, etc. The results of this correlation are presented in Figure 26, which also indicates the corresponding drift velocity used in the conventional Deutsch formula. One notes that for $a_o/R = 10^{-5}$

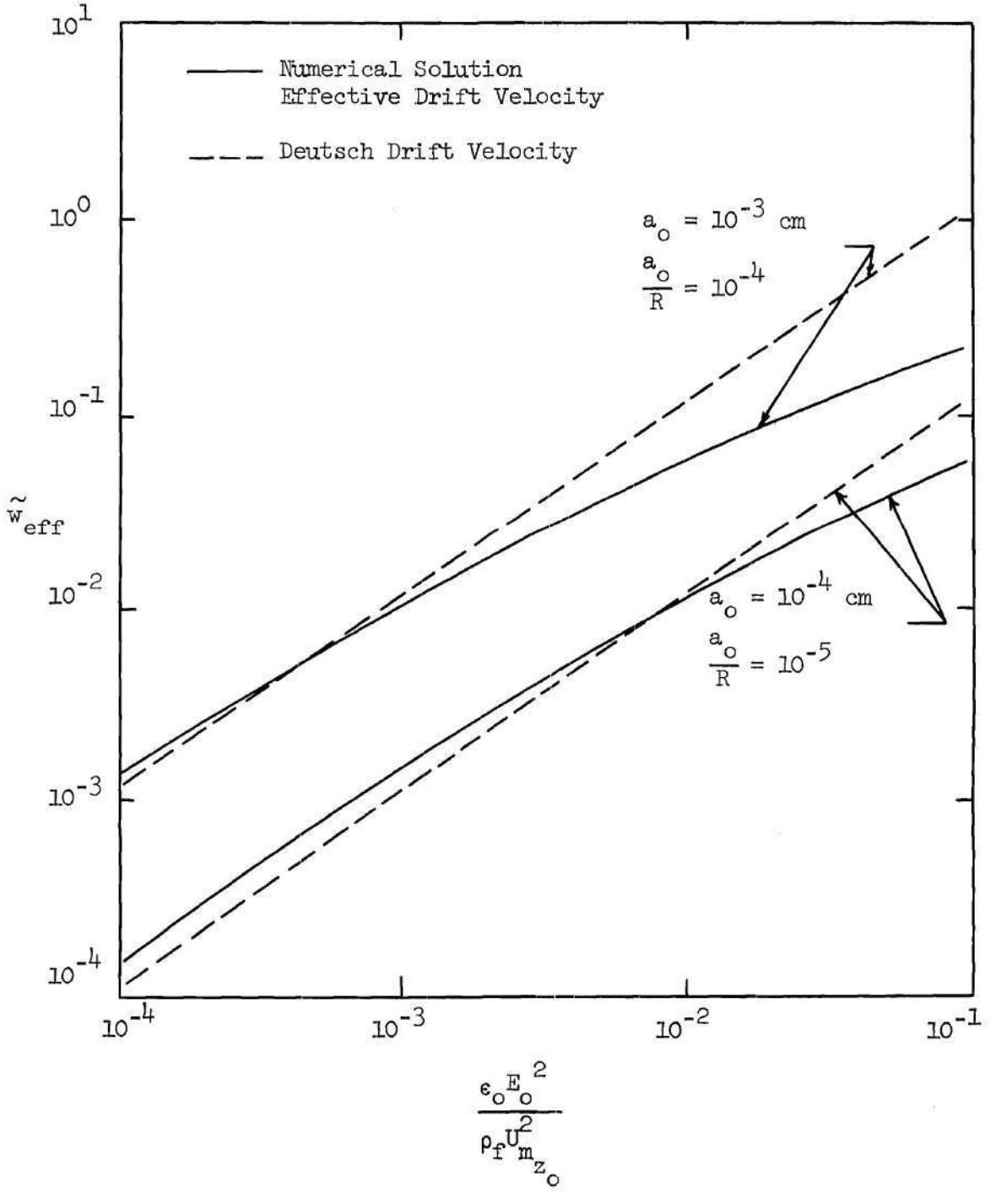

Figure 26. Effective Drift Velocity as a Function of Nondimensional Electric-Field Parameter

and $a_o = 10^{-4}$ cm, the effective drift velocity remains reasonalby close to the Deutsch drift velocity for values of $\epsilon_o E_o^2/(\rho_f U_{m_{z_o}}^2)$ less than about 10^{-2}, but that the difference between the two becomes more marked as $\epsilon_o E_o^2/(\rho_f U_{m_{z_o}}^2)$ increases beyond this value. For $a_o/R = 10^{-4}$ and $a_o = 10^{-3}$ cm, one notes a similar trend except that the difference between the Deutsch velocity and the present numerical correlation becomes marked as $\epsilon_o E_o^2/(\rho_f U_{m_{z_o}}^2)$ increases beyond 10^{-3}. The previous basic calculations discussed in some detail were generated for $\epsilon_o E_o^2/(\rho_f U_{m_{z_o}}^2) = 0.011$, a value compatible with current precipitator design. One notes from Figure 26 a confirmation of the previously discussed comparisons with the Deutsch prediction at $\epsilon_o E_o^2/(\rho_f U_{m_{z_o}}^2) = 0.011$, namely, that there is close agreement for $a_o/R = 10^{-5}$ and $a_o = 10^{-4}$ cm and rather poor agreement for $a_o/R = 10^{-4}$ and $a_o = 10^{-3}$ cm. However, the conclusion would be directly opposite this if the comparison were made at $\epsilon_o E_o^2/(\rho_f U_{m_{z_o}}^2) = 4 \times 10^{-4}$. It is important to note that the Deutsch prediction may be either below or above the numerical correlation result, depending upon the particular value of the relevant parameters, e.g., $\epsilon_o E_o^2/(\rho_f U_{m_{z_o}}^2)$, at which the comparison is being made.

Comparison with Experimental Data

It is perhaps useful here to briefly outline the available experimental work relative to the conventional pipe-wire electrostatic precipitator configuration which may be of value for comparison with present results. Although data exist for the many actual design

applications of precipitator concepts, most of these designs, through design evolution, exhibit considerable difference between their actual operating conditions and those necessarily assumed for theoretical calculations. What is of interest here are experimental data for a simple pipe-wire configuration having a smooth wall and a particulate loading which consists of spherical particles having a defined size distribution and suspended within a fully-developed turbulent flow. These requirements are most likely to be satisfied only under laboratory conditions.

Several investigations into the basic operating characteristics of pipe precipitators were made during the period 1910 and 1918. These early and rather unrefined experiments indicated that the maximum gas velocity for so-called "complete clearance" of a particulate loading is roughly proportional to precipitator length. Later, more refined experimental data indicated an exponential relationship between unprecipitated load and a parameter involving deposition surface area, gas-flow velocity, and effective particle "drift" velocity. From these results the Deutsch theoretical precipitation formula, discussed earlier, was obtained.

A program of carefully controlled experiments under laboratory conditions was performed by White [24] to check the validity of this basic precipitation formula under essentially ideal conditions. White employed pipes of 4-, 6-, 9-, and 12-inch diameters having a fixed length of 8 feet in all cases (L/D = 24, 16, 11, and 8, respectively) and a discharge electrode wire 0.014 inches in diameter. The aerosol suspension was produced by an oil-fume generator which used an electric

heater to vaporize the oil, and a controlled air blast was used to disperse and condense the vapor. Corona discharge was produced by a 100 kv direct current potential. White's purpose was to check experimentally the functional relationship between the various quantities which are involved in the Deutsch formula. Unfortunately, no information was given relative to particle size distributions, so that explicit comparison of his results with those of the present numerical solution technique cannot be made. However, with respect to precipitator efficiency as related to collecting surface area and mean gas flow rate, his results indicated good agreement with the Deutsch formula. White concludes that experimental evidence indicates a general confirmation of the validity of the exponential Deutsch precipitation formula for particles having radii less than about five microns, but for larger particles, the agreement is much less satisfactory. This is in agreement with the present numerical results for the basic precipitator parameters chosen for the earlier examples, which indicate close agreement with Deutsch efficiency predictions for one-micron radii particles but poor agreement for ten-micron size particles. White also notes that precipitator efficiency is essentially independent of inlet particle number concentration over a fairly wide range. This confirms the comment made earlier with respect to the results of the computational examples discussed previously, indicating relative insensitiveness to particle inlet concentration.

An important contribution to our understanding of the empirical behavior of the conventional pipe-wire precipitator is the work of Inyushkin and Averbukh [27]. Their tests were made under laboratory

conditions with a pipe having a diameter of 49-mm and a discharge wire electrode 0.4-mm in diameter. The electrical field strength was maintained at 2 kv/cm (at the pipe wall) by a direct current. They employed fractions of alumina dust with particle radii of two to four microns. The highest Reynolds number achieved was 2×10^4, sufficient for turbulent flow conditions, although data was presented also for Re = 2×10^3, 5×10^3, and 1×10^4. The flow at Re = 2×10^3 was laminar, and transition was noted near Re = 5×10^3.

Their efficiency data for Re = 1×10^4 and 2×10^4 are shown in Figure 27 as a function of downstream distance. For their Re = 2×10^4 data, the parameter $\epsilon_o E_o^2/(\rho_f U_{m_{z_o}}^2)$ is about 0.010, which is close to the value 0.011 chosen for the basic numerical calculations discussed previously. Also shown in Figure 27 are the efficiency curves obtained by numerical solution of the equilibrium model equations, as illustrated earlier in this chapter, and the corresponding efficiency prediction obtained from the Deutsch formula. The input parameters for the numerical solution are

$$a_o/R = 1.63 \times 10^{-4}, \qquad a_o = 4 \times 10^{-4} \text{ cm},$$

$$N_o = 1.0 \times 10^3 \text{ cm}^{-3}, \qquad \rho_p/\rho_f = 3490$$

corresponding to the Inyushkin and Averbukh data. It can be shown that, for these conditions, the equilibrium model provides an adequate

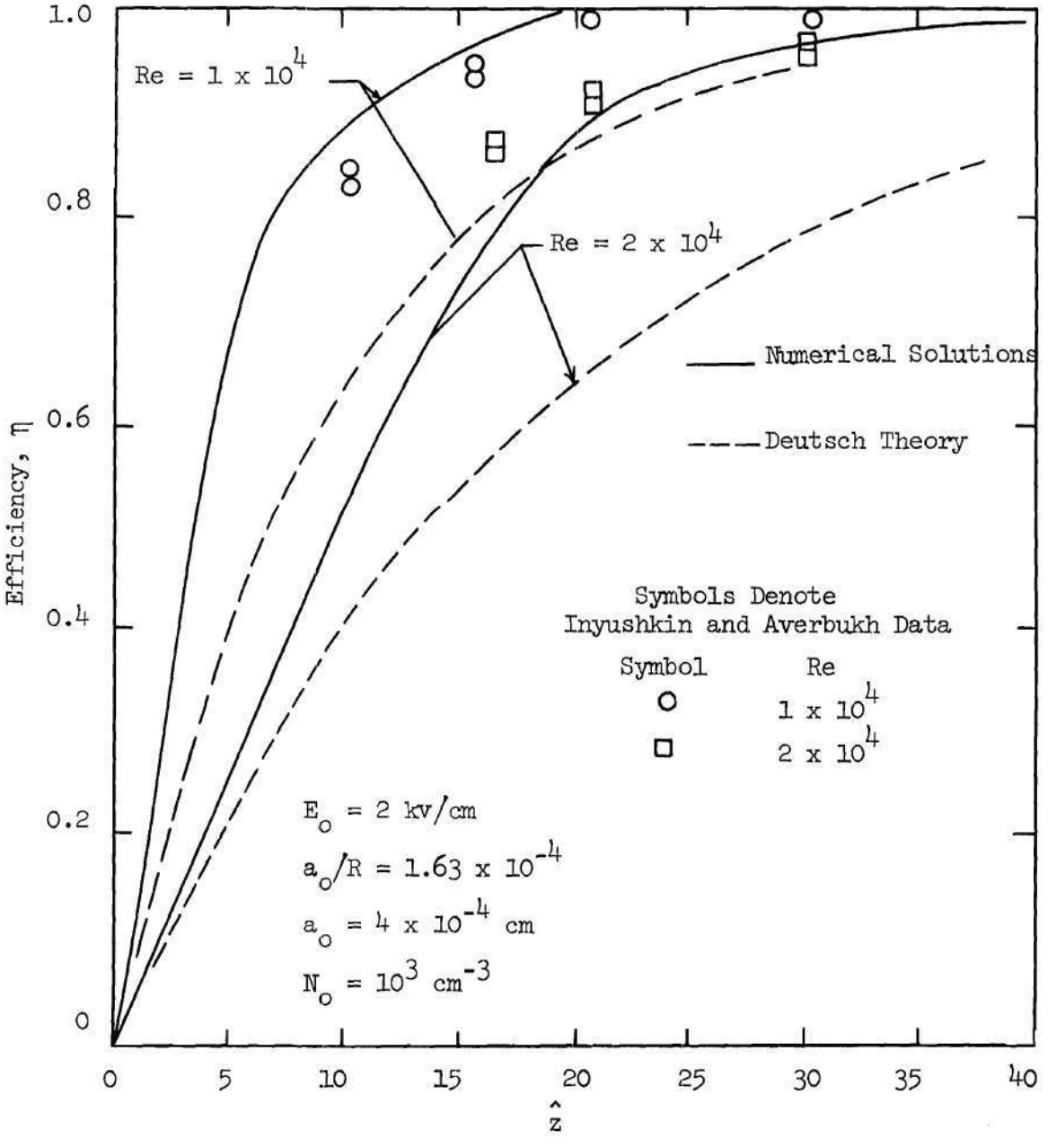

Figure 27. Particulate Removal Efficiency as a Function of Axial Location for Inyushkin and Averbukh Data

description. For these conditions, there is reasonably good agreement between the numerical solution and the experimental data, whereas the Deutsch formula significantly underpredicts the deposition. It is interesting to note that Inyushkin and Averbukh attributed their higher deposition (relative to the Deutsch prediction) to turbulent diffusion, which would be expected to result in additional deposition relative to both the Deutsch formula and the present numerical solution formulation. However, as will be shown in Chapter VI, the magnitude of this additional turbulence-induced deposition relative to that due to electrical drift is not sufficient to account for the difference, but rather that the solution to a more complete set of model equations representing the system yields a more reasonable result.

The main objective of this effort is not, however, to investigate the details of the more conventional precipitation approach, the subject of the development of this chapter, since this configuration has been the subject of a great deal of design effort during the past half century and much is known about its operational characteristics and potential from field experience. On the other hand, what is needed is a reliable theoretical prediction capability to provide the basis for evaluation of alternative design approaches and for exploring solution possibilities for problems not presently the object of attention. Therefore, several other example problems of possible interest are investigated in succeeding chapters within the framework of the theoretical model and solution techniques developed thus far.

CHAPTER VI

CHARGED PARTICLE CONCENTRATION DISTRIBUTION AND DEPOSITION WITHIN A LONG PIPE IN THE ABSENCE OF EXTERNAL ELECTRICAL FIELD

Having considered the more conventional electrostatic precipitator problem one may find useful the examination of a related problem involving a turbulent pipe flow of a charged aerosol in the absence of the dominant deposition-effecting influence of a strong radial external electric field. As indicated earlier, most naturally occurring and man-made aerosols are charged and exhibit a deposition behavior due to their own space-charge repulsion, without the influence of an external electric field. It is important to compare this deposition with that due to turbulent diffusion, as considered in Chapters II and III, since the latter deposition mechanism has been neglected in the charged-aerosol deposition problem formulation (turbulent-diffusion effects are considered in Chapter V but specific consideration of the mixing-length deposition mechanism developed in Chapters II and III is not included).

The development here closely follows that of the previous chapters, and only that portion of the analysis which need be modified for the present case is presented in order to avoid duplication. Since there exists no corona discharge to provide a particle-charging environment within the flow region of interest, particle charging must be accomplished prior to entrance into this region. For the same reason,

particles will tend to retain their charges as they proceed downstream. Therefore, two important modifications to the development of Chapter V involve the specification of the particle precharging conditions and an altered solution to Poisson's equation to account for the fact that the electric field is due only to particle charges.

In the most general case, one might expect that the particulate load would be presented at the inlet having a charge distribution as a function of particle radius and particle location. If this is the case, computationally one must be able to identify, at any given location down-stream, the origin of a given particle in order to determine its charge. This circumstance would require a significant bookkeeping effort which, although not an unsurmountable impediment, would detract from the usefulness of the technique. On the other hand, a particle charge which is a function only of particle size represents the simplest case to handle computationally and implies only that the particle charge distribution is uniform with respect to radial location at the entrance. This is not an unreasonable condition to implement in practice and is presumed to exist here. That is, particle charge throughout the flow-field is given by

$$\hat{Z}(q) = 4\pi\left(1 + 2\,\frac{\epsilon_r - 1}{\epsilon_r + 2}\right)\hat{E}_c N_o R^3 \hat{a}^2 \left(\frac{a_o}{R}\right)^2 \qquad (6.1)$$

where $\hat{E}_c$ represents a nondimensional charging electric field, taken to be constant for the entire particulate load. Thus, $\hat{E}_c$ enters as an additional parameter which may be independently varied. For this example, the other parameters appearing in equation (6.1) are assigned

values similar to those of the two basic examples of Chapter V, i.e.,

$$a_o/R = 10^{-5}, \qquad a_o = 10^{-4}\text{cm}, \qquad N_o = 10^{6}\text{cm}^{-3}$$

and

$$a_o/R = 10^{-4}, \qquad a_o = 10^{-3}\text{cm}, \qquad N_o = 10^{6}\ \text{cm}^{-3}$$

with $\epsilon_r \to \infty$ in all cases.

Approximate Solution to Poisson's Equation

Poisson's equation can be written in terms of the electric potential as

$$\frac{\partial^2 \hat{V}}{\partial \hat{r}^2} + \frac{1}{\hat{r}} \frac{\partial \hat{V}}{\partial \hat{r}} + \frac{\partial^2 \hat{V}}{\partial \hat{z}^2} = - Q(\hat{z},\hat{r}) \qquad (6.2)$$

where $Q(\hat{z},\hat{r})$ is defined by equation (5.11). In Chapter V, advantage was taken of the fact that axial derivatives of the dependent variables, e.g., $\hat{V}$, were much smaller than the equivalent radial derivatives. However, here one cannot expect that either the radial or the axial derivative of $\hat{V}$ is significantly greater than the other, and therefore the left-hand side of equation (6.2) must be considered in its complete form.

On the other hand, $Q(\hat{z},\hat{r})$ can be expected to remain relatively uniform with respect to the radial coordinate and to decrease gradually as the flow proceeds downstream. Therefore, $Q(\hat{z},\hat{r})$ can reasonably be

represented as

$$Q(\hat{z},\hat{r}) = Q_o\, e^{-\varkappa \hat{z}} \tag{6.3}$$

i.e., by an exponential decay from an initial charge, Q_o, at the inlet. The decay parameter enters as an additional unknown which must be made consistent with the computational results. In principle, one should select a reasonable value of $\varkappa$, carry out the complete numerical solution for particulate concentration as far downstream as desired, and then finally check whether the assumed value of $\varkappa$ is consistent with the determined decrease in total charge. An iterative scheme would be indicated until convergence is achieved.

Therefore, a solution is sought to the equation

$$\frac{\partial^2 \hat{V}}{\partial \hat{r}^2} + \frac{1}{\hat{r}} \frac{\partial \hat{V}}{\partial \hat{r}} + \frac{\partial^2 \hat{V}}{\partial \hat{z}^2} = - Q_o e^{-\varkappa \hat{z}} \tag{6.4}$$

subject to the boundary conditions $\hat{V} = 0$ at $\hat{r} = 1$ and V finite at $\hat{r} = 0$. A solution of the form

$$\hat{V}(\hat{z},\hat{r}) = e^{-\varkappa \hat{z}} \hat{V}_1(\hat{r}) \tag{6.5}$$

substituted into equation (6.4) yields the equation

$$\frac{d^2 \hat{V}_1}{d\hat{r}^2} + \frac{1}{\hat{r}} \frac{d\hat{V}_1}{d\hat{r}} + \varkappa^2 \hat{V}_1 = - Q_o \tag{6.6}$$

Transforming the independent variable to $\hat{r}^* = \hat{r}\varkappa$ gives

$$\frac{d^2\hat{V}_1}{d\hat{r}^{*2}} + \frac{1}{\hat{r}^*}\frac{d\hat{V}_1}{d\hat{r}^*} + \hat{V}_1 = -\frac{Q_o}{\kappa^2} \tag{6.7}$$

provided $\kappa \neq 0$. A particular solution to equation(6.7) is

$$\hat{V}_1 = -\frac{Q_o}{\kappa^2}\ , \tag{6.8}$$

and the complementary solutions are

$$\hat{V}_1 = J_o(\hat{r}^*) \text{ and } Y_o(\hat{r}^*) \tag{6.9}$$

where J_o and Y_o are the usual zero-order Bessel functions of the first and second kinds, respectively. However, since one does not expect that $\hat{V}_1$ approaches infinity as $\hat{r}^*$ approaches zero, as does $Y_o(\hat{r}^*)$, the solution $Y_o(\hat{r}^*)$ can be eliminated at the outset. Therefore, the solution to equation (6.7) can be written as

$$\hat{V}(\hat{z},\hat{r}) = [A_1 J_o(\hat{r}\kappa) - \frac{Q_o}{\kappa^2}]e^{-\kappa\hat{z}} \tag{6.10}$$

where A_1 is a constant to be determined by the boundary condition at $\hat{r} = 1$. Putting $\hat{V} = 0$ at $\hat{r} = 1$ in equation (6.10) gives

$$0 = [A_1 J_o(\kappa) - \frac{Q_o}{\kappa^2}]e^{-\kappa\hat{z}}\ ,$$

so that

$$A_1 J_o(\varkappa) - \frac{Q_o}{\varkappa^2}$$

or,

$$A_1 = \frac{Q_o}{\varkappa^2 J_o(\varkappa)} \tag{6.11}$$

Therefore, the electric potential is

$$\hat{V}(\hat{z},\hat{r}) = \frac{Q_o}{\varkappa^2}\left[\frac{J_o(\hat{r}\varkappa)}{J_o(\varkappa)} - 1\right]e^{-\varkappa\hat{z}} \tag{6.12}$$

and the electric-field components are

$$\hat{E}_r = -\frac{\partial\hat{V}}{\partial\hat{r}} = \frac{Q_o}{\varkappa}\left[\frac{J_1(\hat{r}\varkappa)}{J_o(\varkappa)}\right]e^{-\varkappa\hat{z}} \tag{6.13}$$

and

$$\hat{E}_z = -\frac{\partial\hat{V}}{\partial\hat{z}} = \frac{Q_o}{\varkappa}\left[\frac{J_o(\hat{r}\varkappa)}{J_o(\varkappa)} - 1\right] e^{-\varkappa\hat{z}}, \tag{6.14}$$

or, in view of equation (6.3)

$$\hat{E}_r = \frac{Q}{\varkappa}\ \frac{J_1(\hat{r}\varkappa)}{J_o(\varkappa)} \tag{6.15}$$

and

$$\hat{E}_z = \frac{Q}{\varkappa} \left[\frac{J_o(\hat{r}\varkappa)}{J_o(\varkappa)} - 1\right]. \tag{6.16}$$

An estimate for the decay parameter near $\hat{z} = 0$ can be obtained from a consideration of an approximate form of the continuity of mass equation. In Chapter V, this approximation was indicated by equation (5.30). This can be written as

$$\frac{d\hat{n}^{(q)}}{\hat{n}^{(q)}} \cong - \frac{2}{\hat{U}_{m_z}} \hat{V}_r^{(q)} d\hat{z}. \tag{6.17}$$

By analogy, one might assume that

$$\frac{dQ}{Q} \cong \left(\frac{d\hat{n}^{(p)}}{\hat{n}^{(p)}}\right)_{\text{average}}, \tag{6.18}$$

where p is that index corresponding to the particle size having the greatest number concentration. That is, since the charge density is related to the mass number density, it is reasonable to assume that the fractional decrease in charge density is equal to the fractional decrease in particle number density. Combining equations (6.17) and (6.18) for $\hat{r} = 1$ yields, approximately,

$$\frac{dQ}{Q} \cong - \frac{2}{\hat{U}_{m_z}} \left(\hat{V}_r^{(p)}\right)_{\text{wall}}. \tag{6.19}$$

Since $Q = Q_o e^{-\varkappa \hat{z}}$, then $dQ = -\varkappa Q_o e^{-\varkappa \hat{z}}$. Thus $dQ = -\varkappa Q d\hat{z}$ and

$$\frac{dQ}{Q} = -\varkappa d\hat{z}. \tag{6.20}$$

Combining equations (6.19) and (6.20) gives, finally

$$\varkappa \cong 2(\hat{V}_r^{(p)})_{wall}/\hat{0}_{m_z}. \tag{6.21}$$

This expression may be used to determine an approximate value for $\varkappa$ near $\hat{z} = 0$ since the quantities on the right-hand side of equation (6.21) can be calculated from the initial conditions.

Numerical Solution Procedure

The basic solution procedure is essentially the same as that developed for previous examples, and therefore only a brief summary of the technique is here given, with attention directed primarily toward those peculiar aspects of this problem which require an altered approach. As before, the continuity equation is written as equation (5.27) for $\hat{r} \neq 0$, and as equation (5.29) for $\hat{r} = 0$. The chosen flow conditions indicate that $\hat{V}_r^{(q)}$ may be assigned its equilibrium value throughout the flowfield, i.e.,

$$\hat{V}_r^{(q)} = [\hat{V}_r^{(q)}]_{eq} = \frac{1}{3} Re\left(1 + 2\,\frac{\epsilon_r - 1}{\epsilon_r + 2}\right) \frac{\epsilon_o E_o^2}{\rho_f U_{m_{z_o}}^2} \hat{E}_c \hat{E}_r \hat{a}\, \frac{a_o}{R} \tag{6.22}$$

An analogous result can be written for $V_z^{(q)}$. Note also that the term $\partial \hat{V}_z^{(q)}/\partial \hat{z}$ is neglected in equations (5.27) and (5.29). Computations

based on the electric-field equations, equations (6.15) and (6.16), indicate that this remains a reasonable assumption.

The continuity equations, equations (5.27) and (5.29), are written in finite-difference form, as before, by replacing $\hat{z}$-derivatives with simple forward-difference approximations and $\hat{r}$-derivatives with central-difference approximations. Again, an explicit numerical algorithm is generated, permitting a marching process forward from $\hat{z} = 0$. One anticipates boundary conditions for $\hat{n}^{(q)}$ identical to those indicated in Chapter V.

Discussion of Results

Figures 28 through 33 present results for total number concentration across the pipe radius for the following conditions:

$$a_o/R = 10^{-5}, \quad a_o = 10^{-4} \text{ cm}, \quad \rho_p/\rho_f = 1110, \quad Re = 10^5,$$

$$\epsilon_o E_o^2/(\rho_f U^2_{m_{z_o}}) = 0.011$$

and

$$\hat{E}_c = 1.0, 2.0, 3.0, 5.0, 7.0, \text{ and } 10.0.$$

For $\hat{E}_c = 10.0$, the number of electrons attached to a typical particle is about 8×10^5 for the conditions of this example. Under normal operating conditions, it can be shown [34, p. 150] that particles in the 0.5 micron to 10 micron size range carry an average charge per particle between 10^2 and 10^5 electronic charges in actual precipitators.

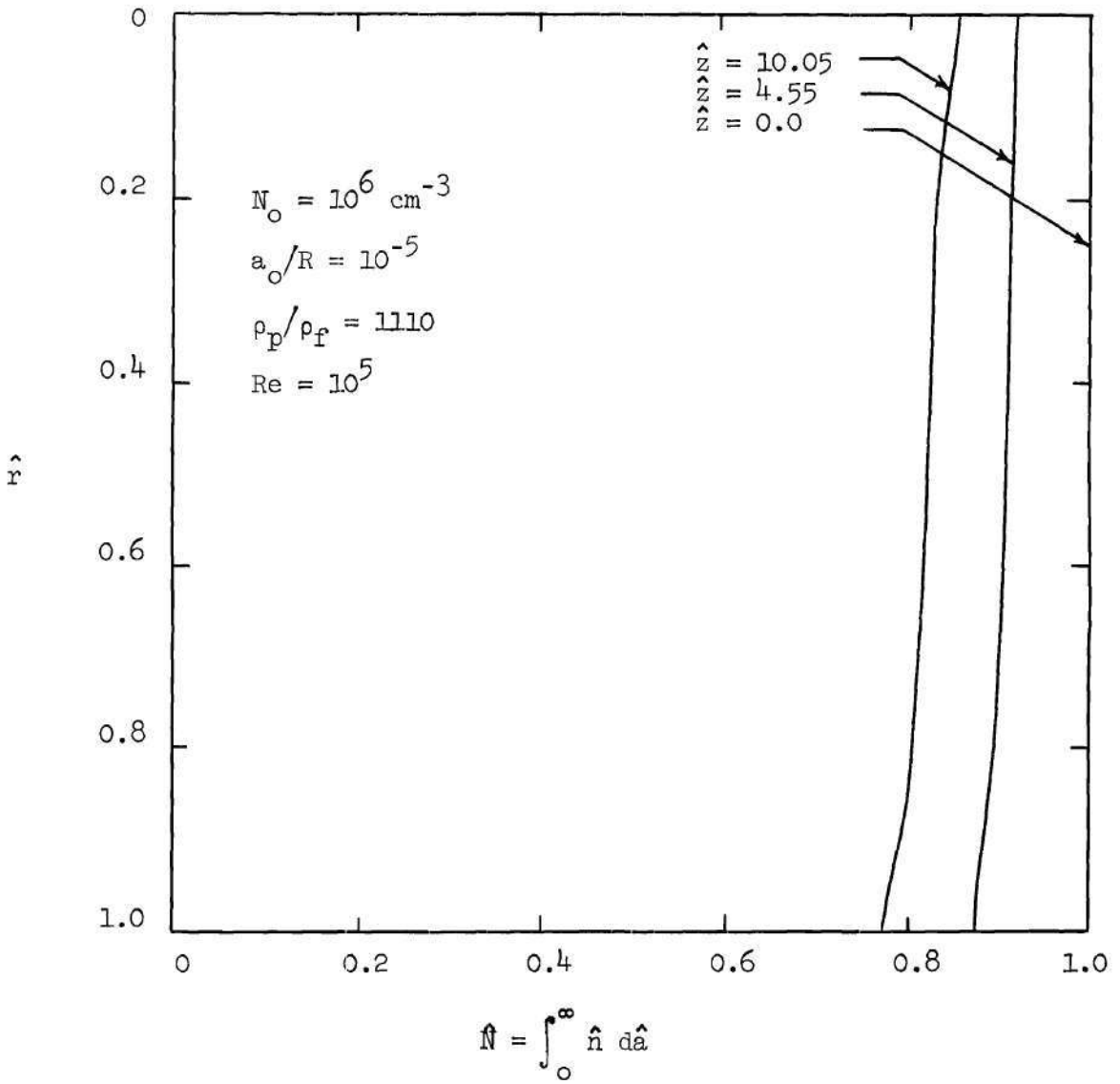

Figure 28. Total Number Concentration Across Pipe Radius at Three Axial Locations ($\hat{E}_c = 1.0$)

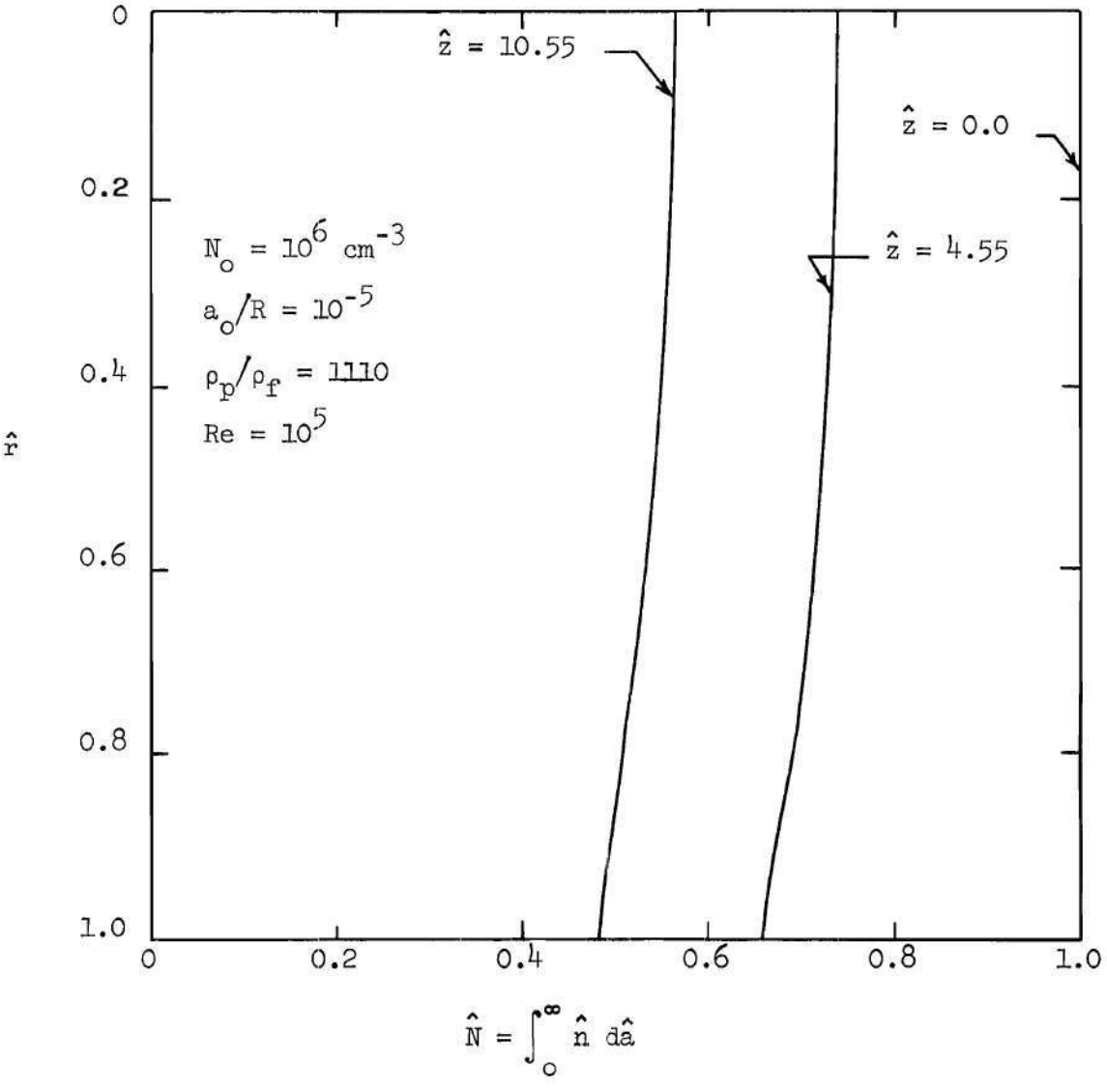

Figure 29. Total Number Concentration Across Pipe Radius at Three Axial Locations ($\hat{E}_c = 2.0$)

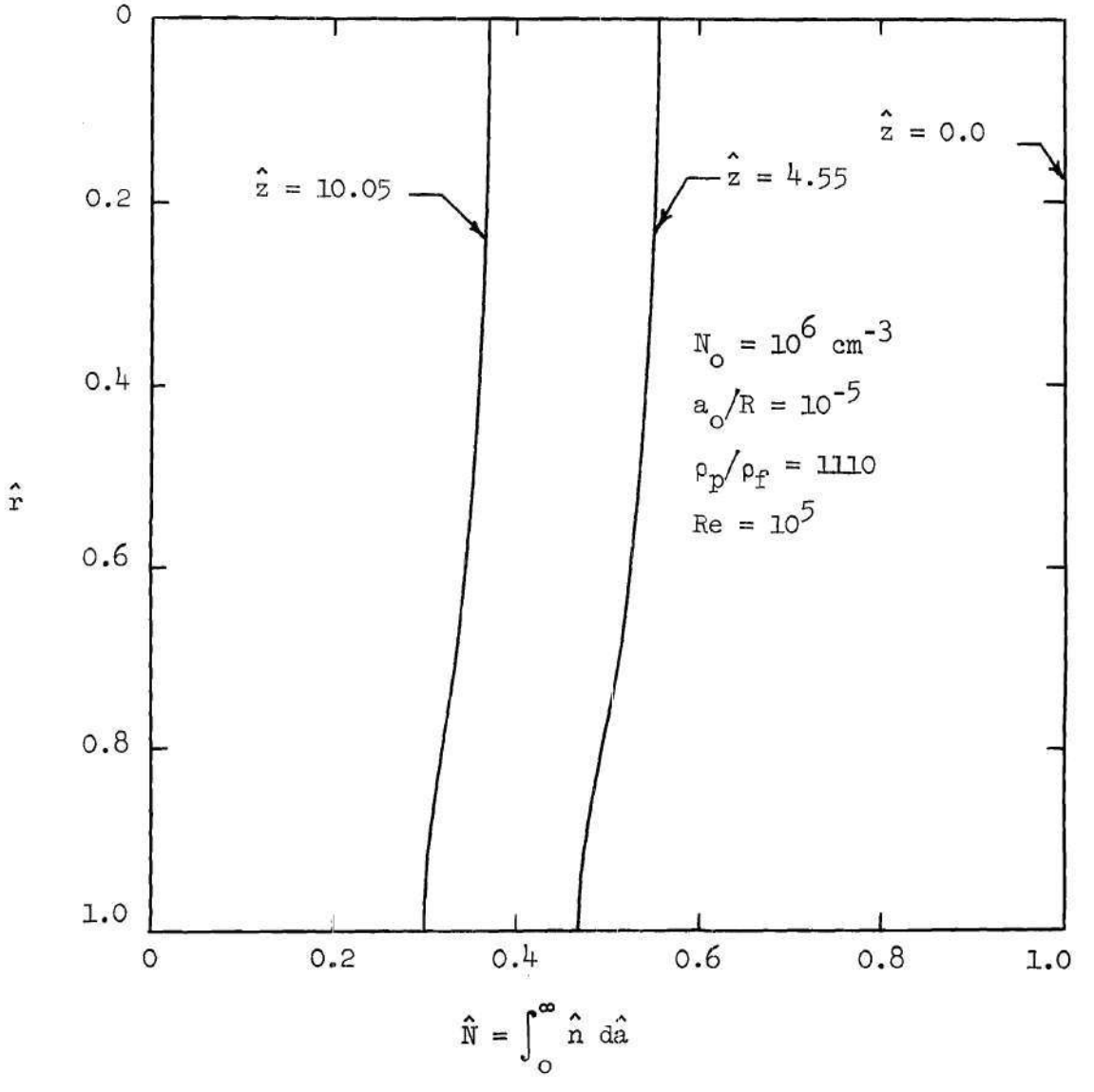

Figure 30. Total Number Concentration Across Pipe Radius at Three Axial Locations ($\hat{E}_c = 3.0$)

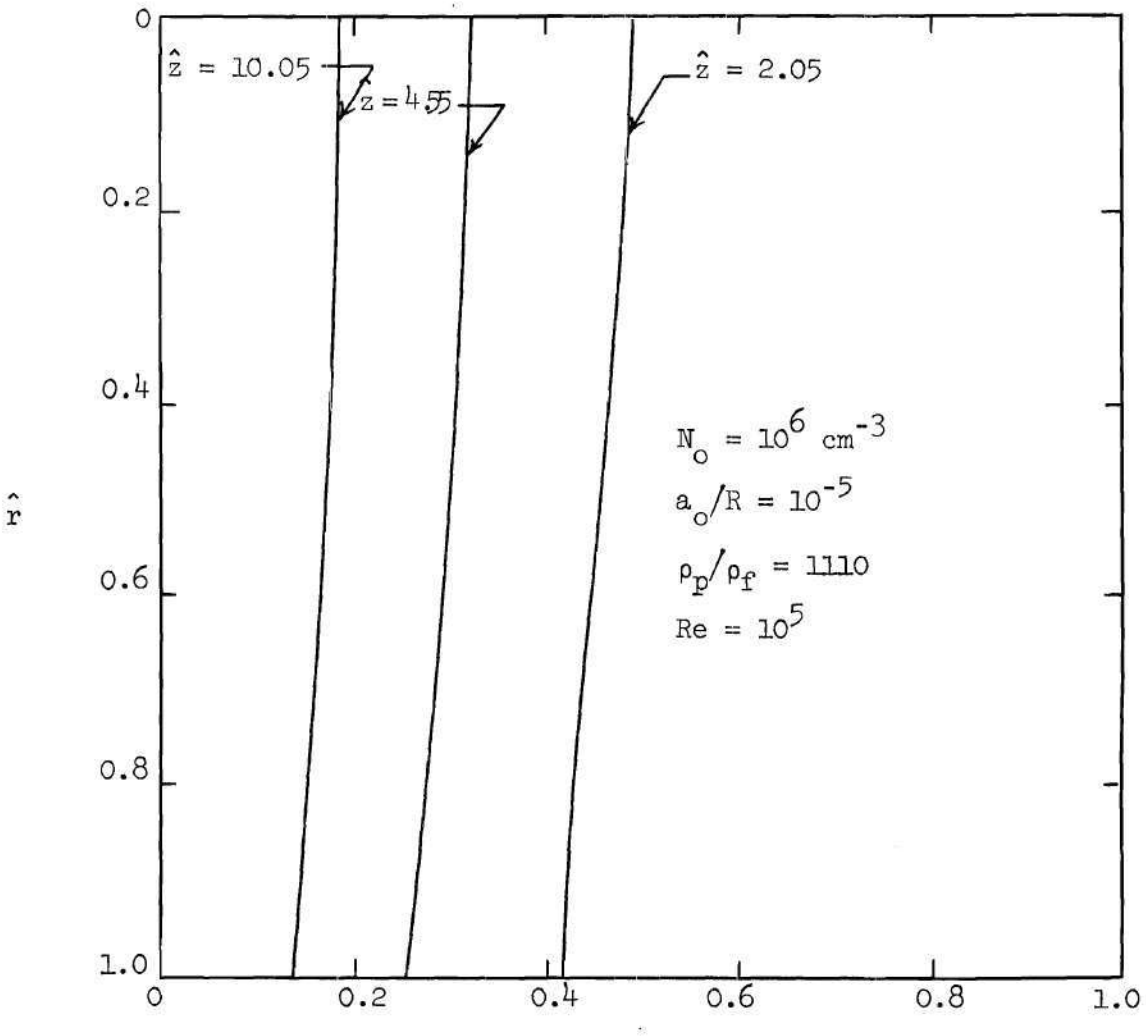

Figure 31. Total Number Concentration Across Pipe Radius at Three Axial Locations ($\hat{E}_c = 5.0$)

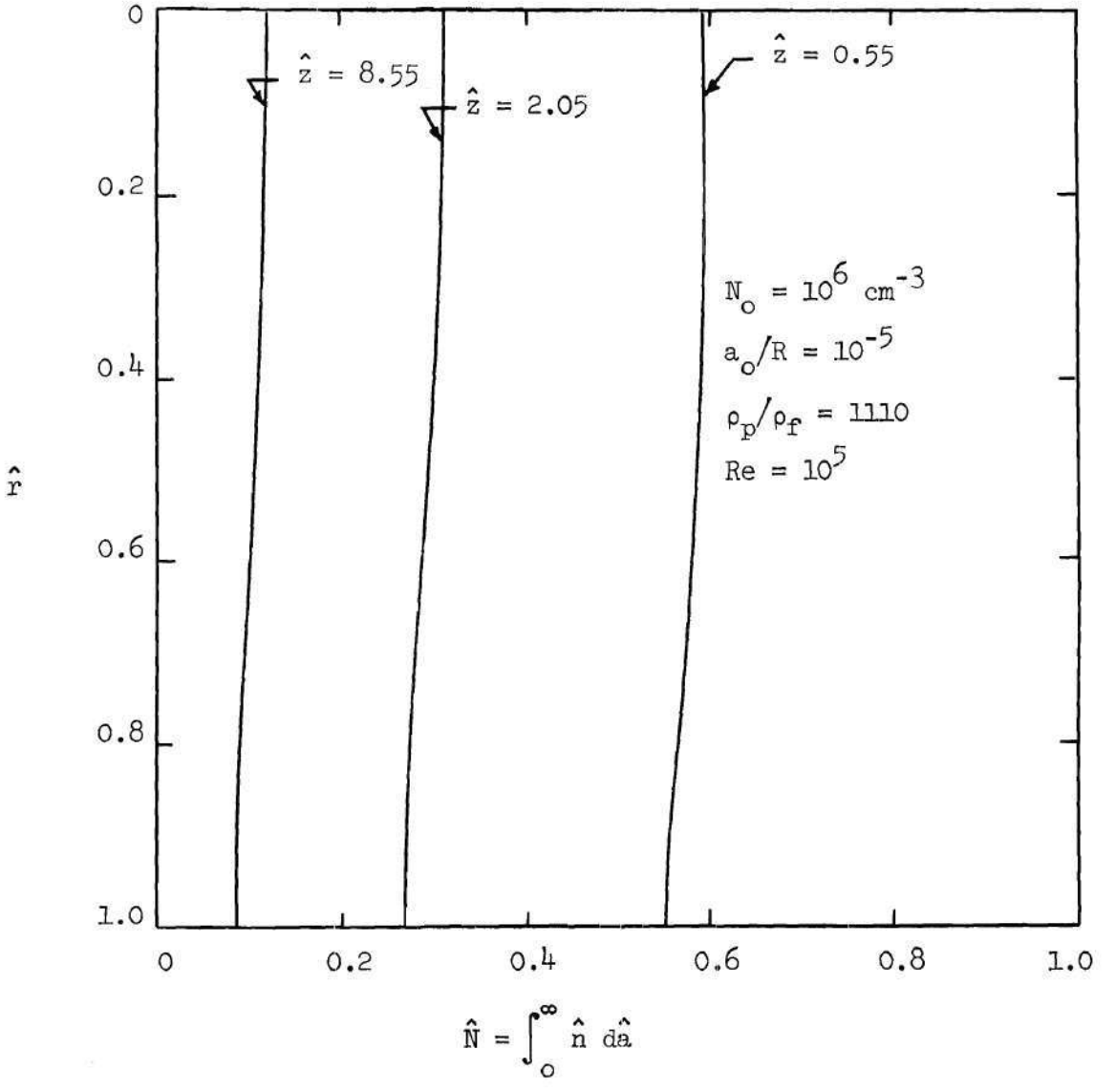

Figure 32. Total Number Concentration Across Pipe Radius at Three Axial Locations ($\hat{E}_c = 7.0$)

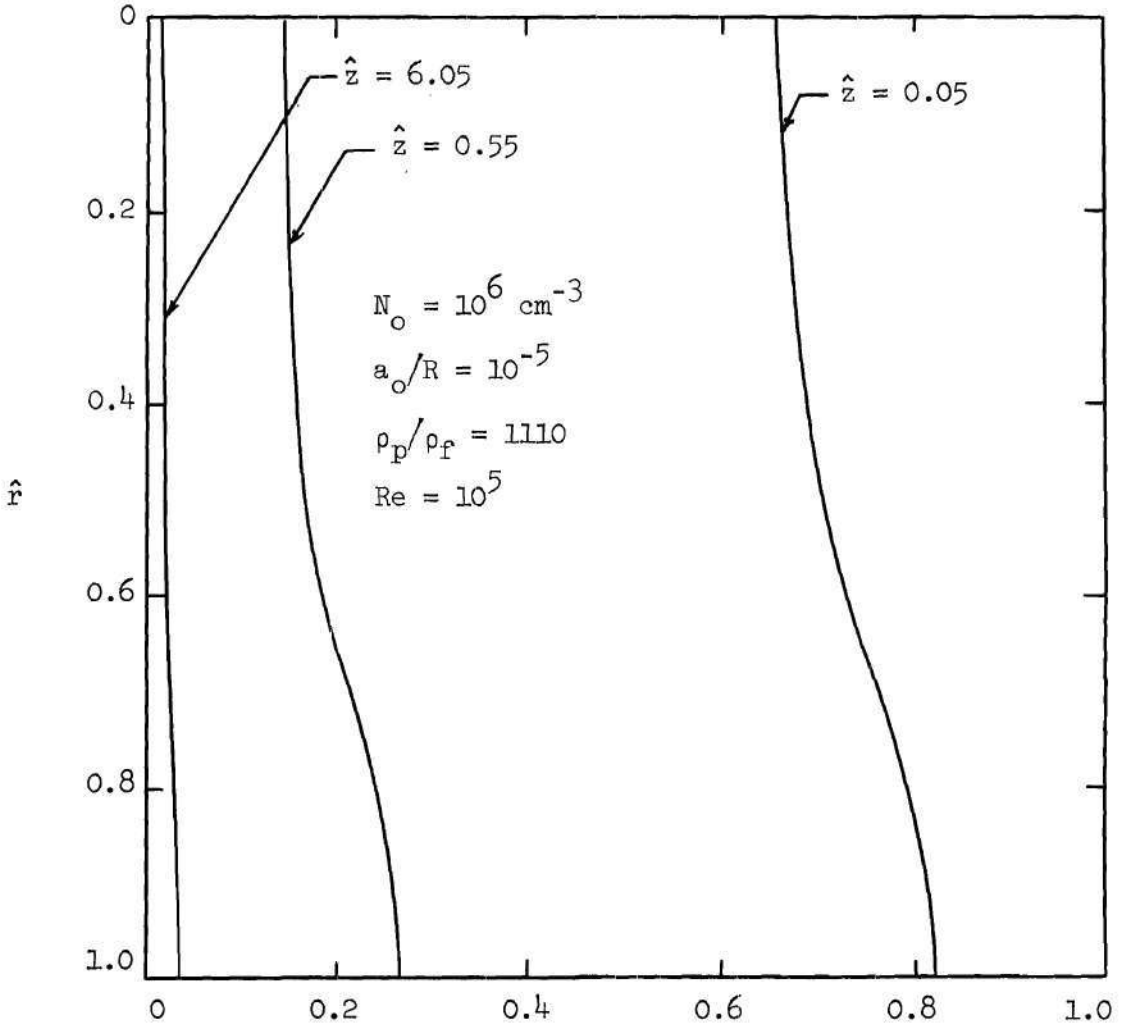

Figure 33. Total Number Concentration Across Pipe Radius at Three Axial Locations ($\hat{E}_c = 10.0$)

For the smallest precharging electric-field intensity, $\hat{E}_c = 1.0$, Figure 28 demonstrates that the decrease in total concentration is relatively uniform with respect to radial coordinate and at $\hat{z} = 10.05$ represents only about 20 percent of the initial concentration. Figures 29, 30, 31, 32, and 33 present analogous results for $\hat{E}_c = 2.0$, 3.0, 5.0, 7.0, and 10.0, respectively. As expected, increasing the initial, precharged state of the aerosol load results in increased deposition and decay of the total concentration at any given axial location. Whereas $\hat{E}_c = 1.0$ yields but a 20 percent reduction in concentration at $\hat{z} = 10$, $\hat{E}_c = 5.0$, on the other hand, results in excess of 80 percent reduction in load at $\hat{z} = 10$. An initial charging corresponding to $\hat{E}_c = 10.0$ results in almost complete clearance of the particulate load at $\hat{z} = 6.0$.

Figure 34 presents a summary of these particulate-load removal efficiencies as a function of flow distance from the inlet. It is seen that, although the efficiency curve for $\hat{E}_c = 1.0$ is reasonably linear with respect to $\hat{z}$, increasing $\hat{E}_c$ results in an increasingly nonlinear efficiency curve, with more than 80 percent removal at $\hat{z} = 1.0$ (i.e., only one radius downstream from the inlet) for $\hat{E}_c = 10.0$. Further, examination of Figure 34 also indicates that, in general, efficiency of removal at any given downstream location is a nonlinear function of the initial charging electric field, $\hat{E}_c$.

Analogous results for $a_o/R = 10^{-4}$ and $a_o = 10^{-3}$cm were also obtained and are illustrated in Figures 35 through 37. Figures 35 and 36 indicate that the total-number concentration profiles across the

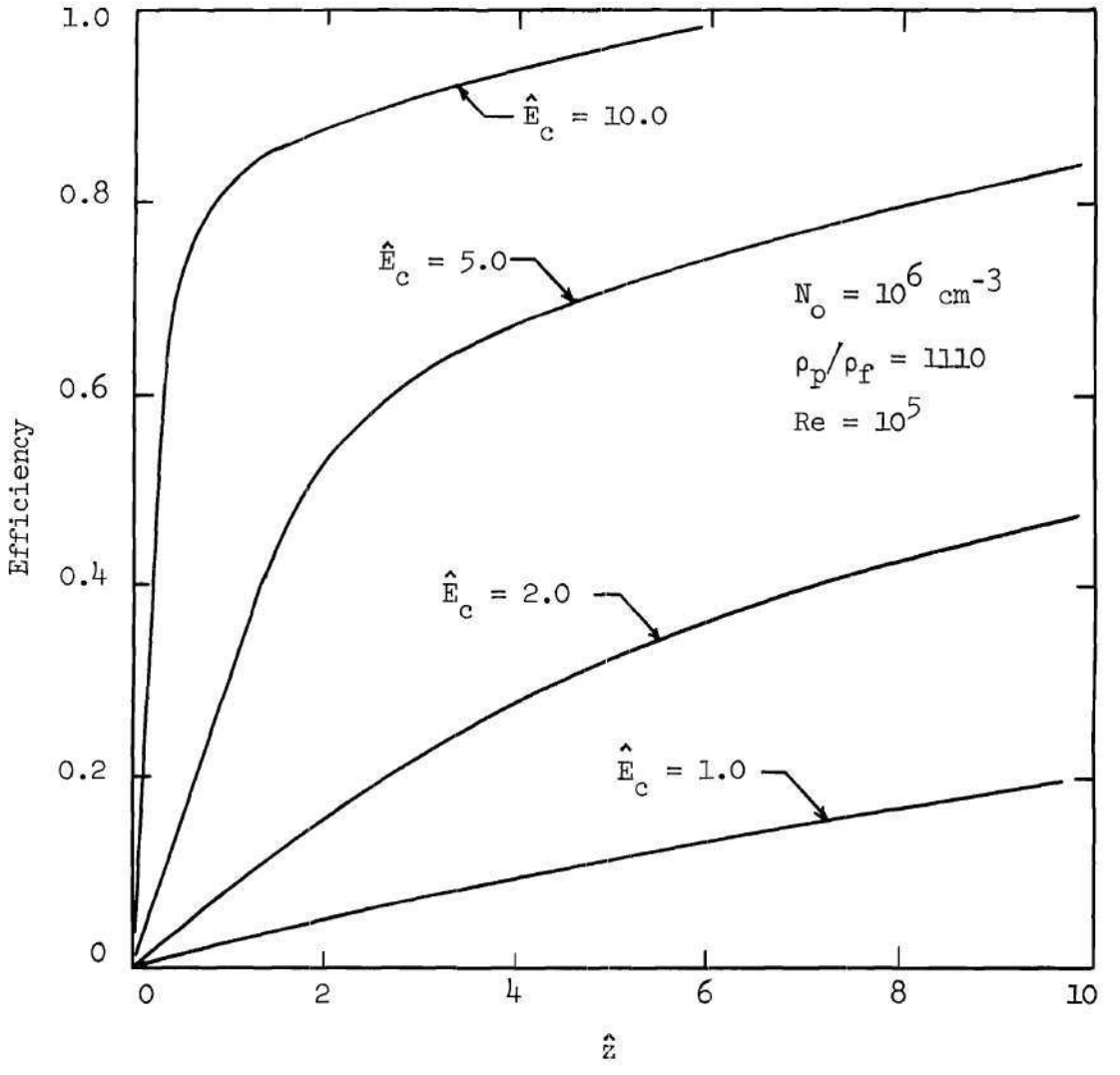

Figure 34. Particulate Removal Efficiency as a Function of Axial Location ($a_o/R = 10^{-5}$)

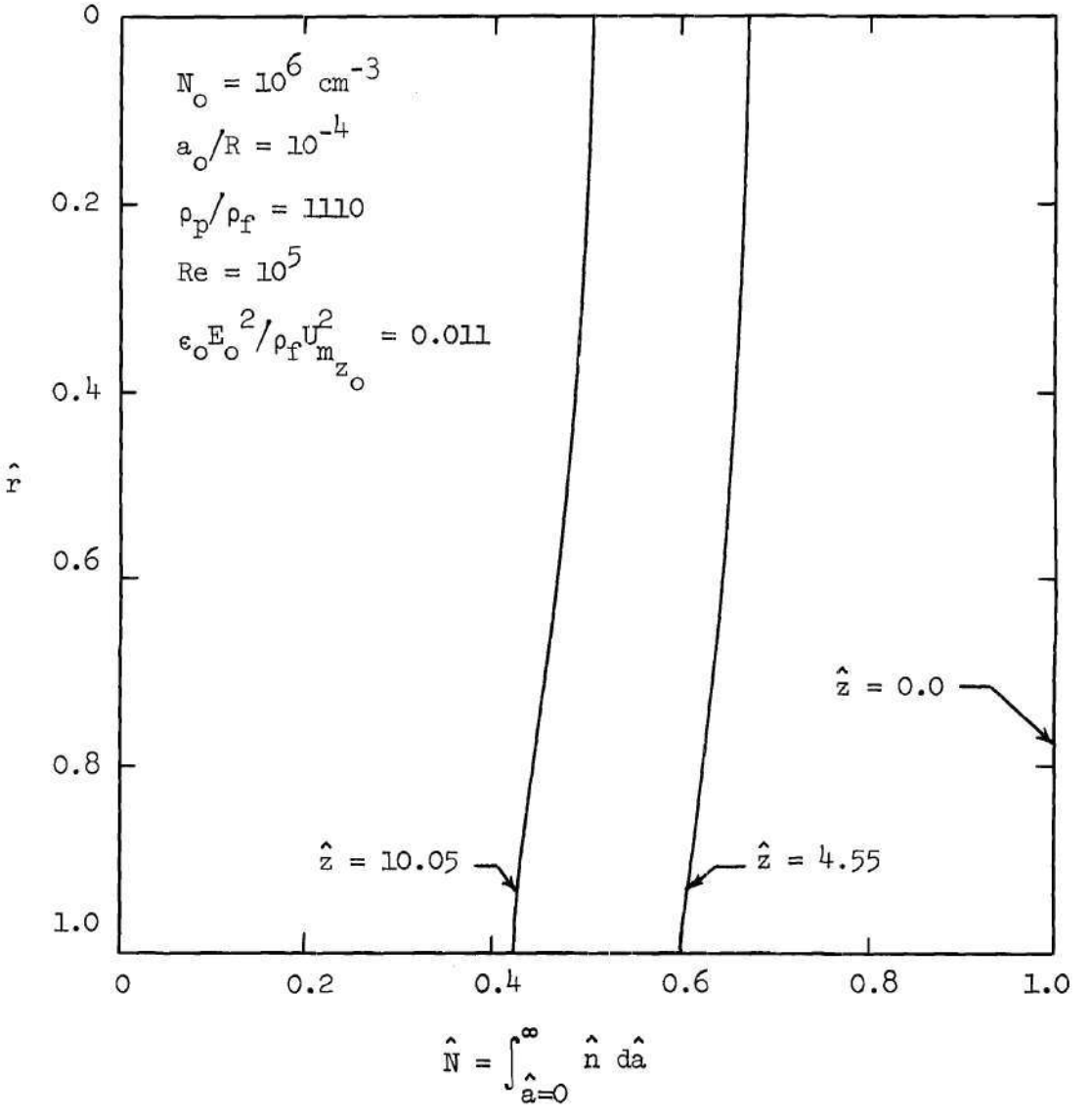

Figure 35. Total Number Concentration Across Pipe Radius at Three Axial Locations ($\hat{E}_c = 0.1$)

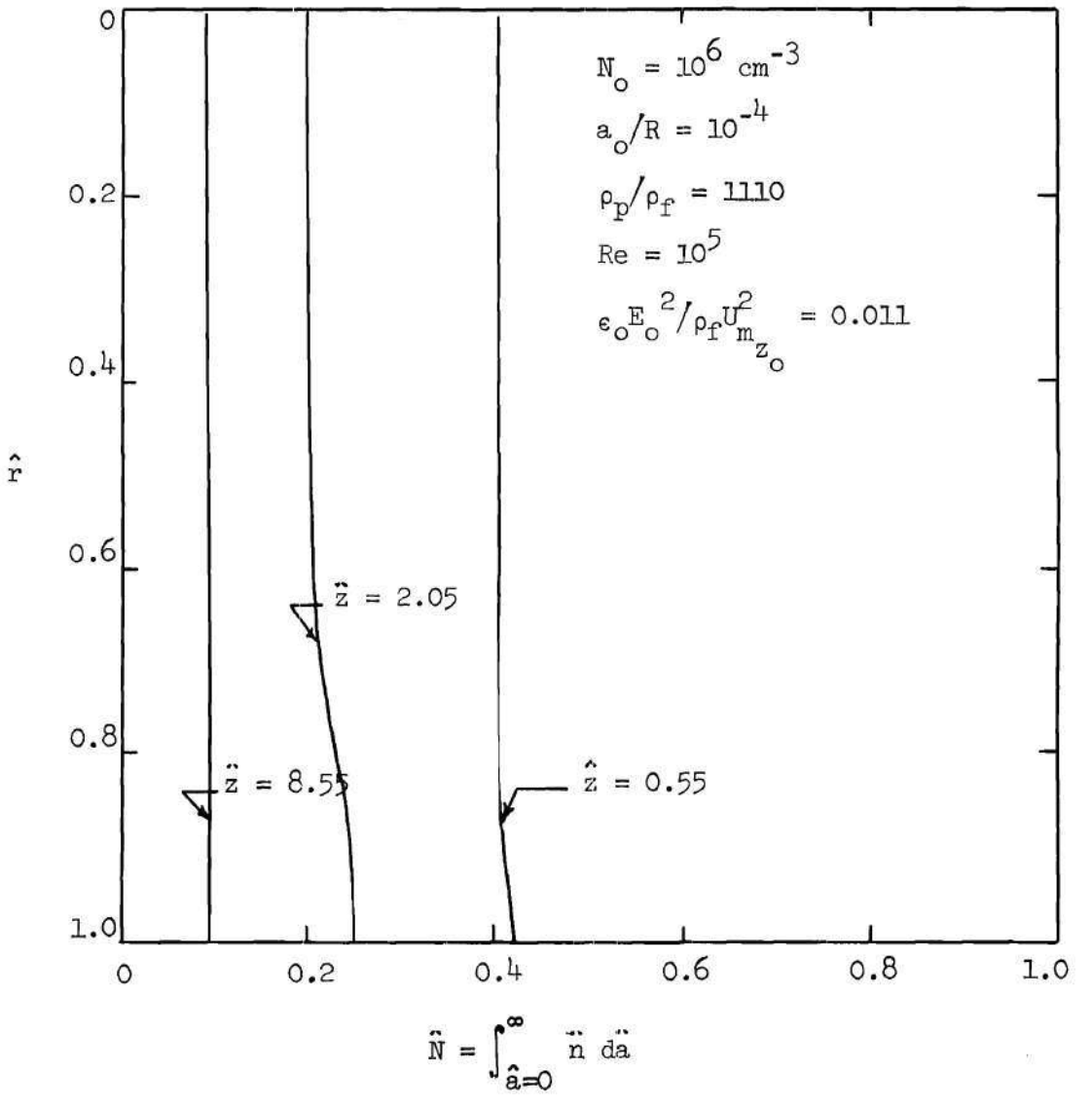

Figure 36. Total Number Concentration Across Pipe Radius at Three Axial Locations ($\hat{E}_c = 0.3$)

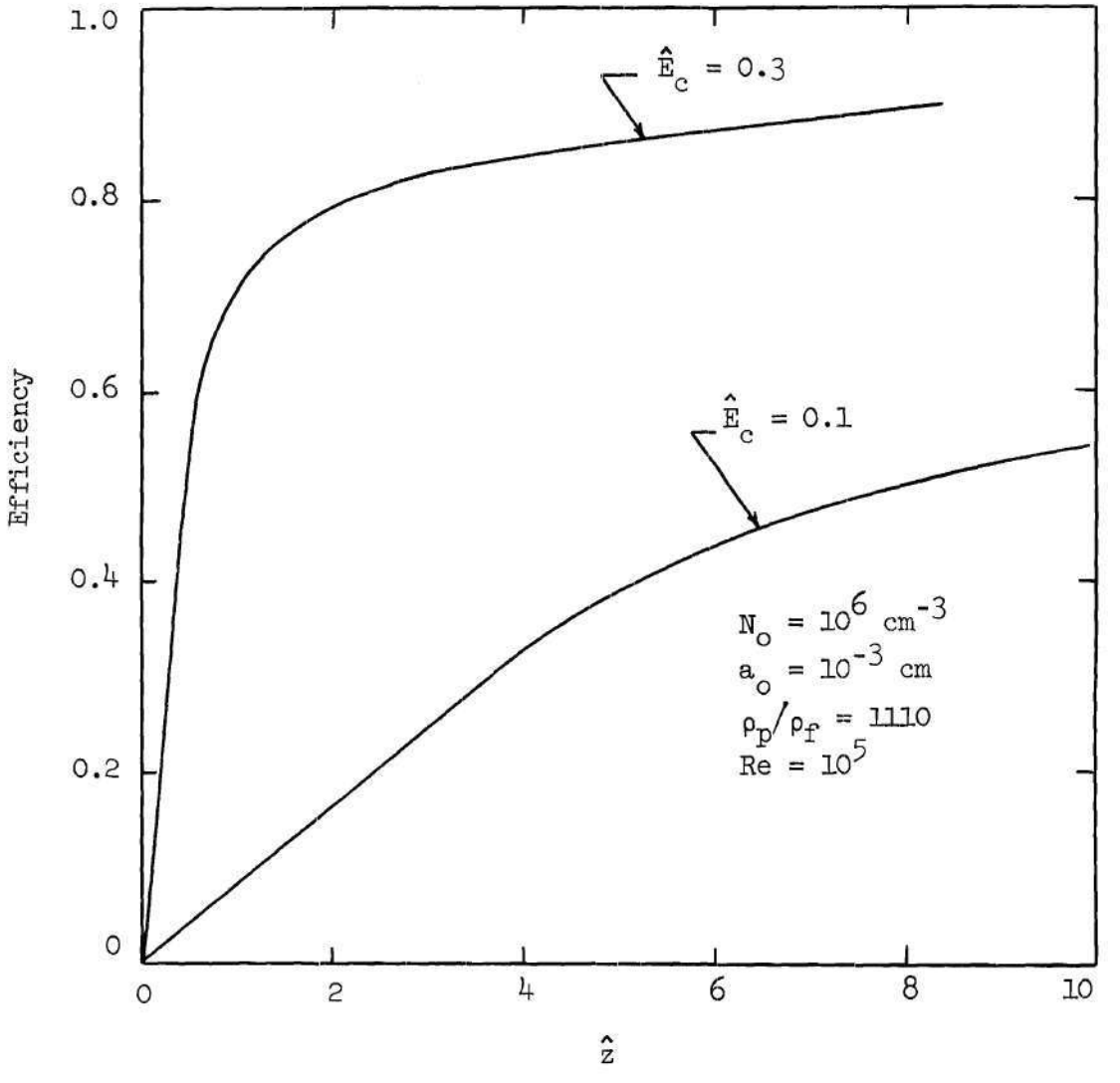

Figure 37. Particulate Removal Efficiency as a Function of Axial Location ($a_o/R = 10^{-4}$)

pipe radius are similar to those obtained for the smaller particles ($a_o = 10^{-4}$ cm), but that the required $\hat{E}_c$ values necessary for comparable efficiency are roughly a factor of 10 less. That is, for a given efficiency at a specified flow distance from the inlet, $\hat{E}_c$ appears to be approximately inversely proportional to the most probably particle size, a_o, as one might anticipate based on an examination of equation (6.25).

It is interesting to note that for both particle size ranges considered, the decrease in total concentration near the wall exceeds that near the centerline for smaller $\hat{E}_c$ values, in a relative sense, whereas the effect is reversed at larger $\hat{E}_c$ values. For larger $\hat{E}_c$, the self-repulsion effect results in a greater decrease in concentration near the pipe center than at the wall. Therefore, there is an accumulation of particles near the wall and an increase in concentration relative to that nearer the pipe centerline.

Figure 37 presents the efficiency of particulate removal for this second set of example conditions. The comments made earlier relative to the results indicated in Figure 34 also apply here and are not repeated.

As an illustration of the deposition mass flux distribution along the pipe wall, Figure 38 presents the deposition velocity as a function of downstream distance for the various values of $\hat{E}_c$ corresponding to the first set of example conditions of this chapter. One notes that the deposition velocity decreases rather rapidly, particularly for the higher $\hat{E}_c$ values. In fact, the deposition valocity for the higher $\hat{E}_c$ values actually decreases below that for lower $\hat{E}_c$ values as the flow

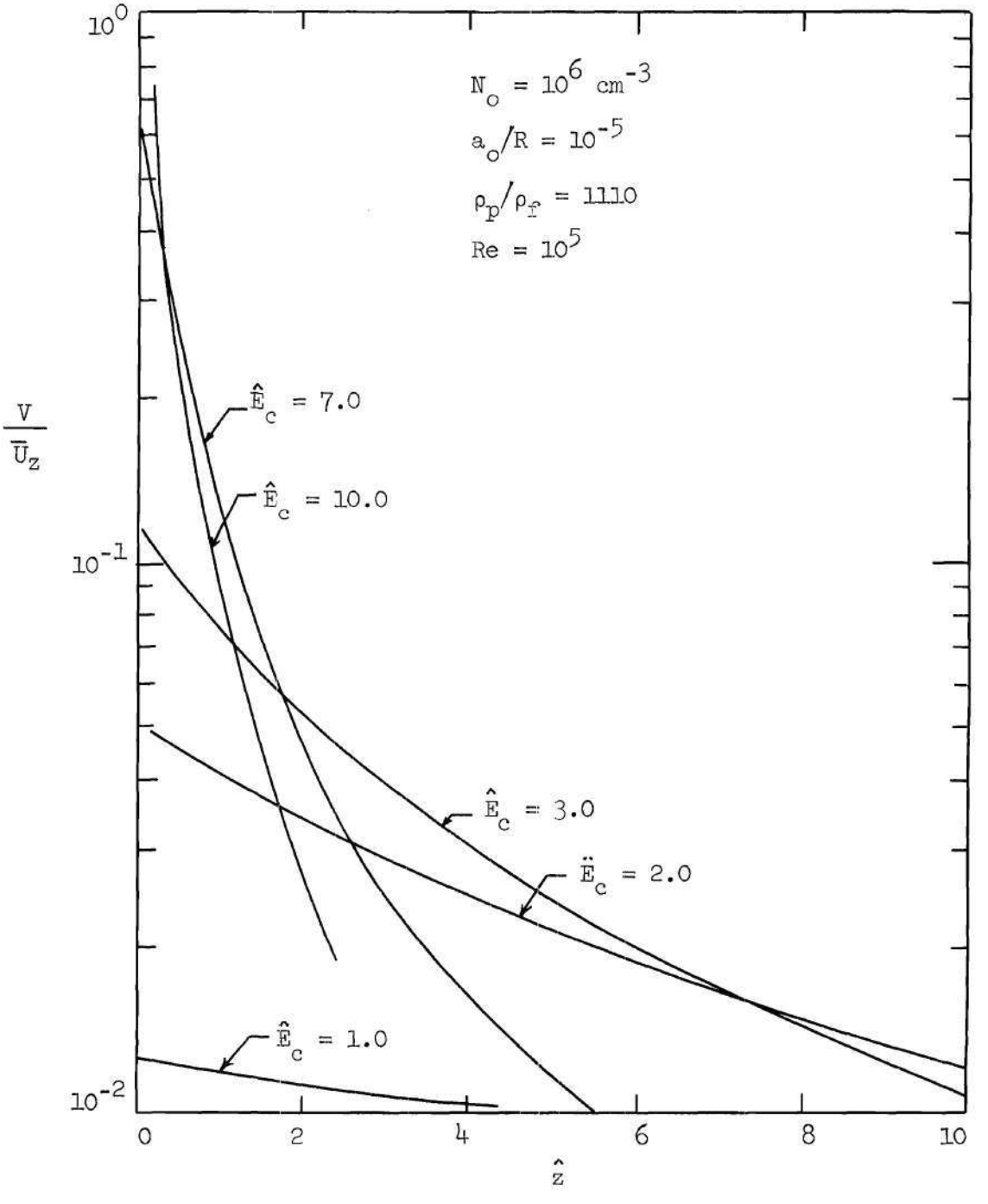

Figure 38. Nondimensional Deposition Velocity as a Function of Axial Location for Several Values of E_c

proceeds downstream. Finally, from Figure 4 of Chapter II, it can be seen that the predicted deposition velocity for only turbulent deposition is approximately 1.8×10^{-4} for these conditions and is therefore two factors of 10 less than the deposition due to the lowest precharging electric field, $\hat{E}_c$, considered here. Thus, it appears that the deposition due to turbulent convective transport is relatively small when compared to that due to electrostatic repulsion for conditions under which the latter is itself significant. Also, since there are no large concentration gradients generated by the self-repulsion space-charge field of the present examples, one does not anticipate significant turbulent transport effects, as were possible in the results of Chapter V.

Figure 39 illustrates the distribution of the radial and axial electric-field components across the pipe radius at $\hat{z} = 0.05$ and 0.55 for the first example considered ($\hat{E}_c = 10.0$). As expected, both components are of the same order of magnitude, with $\hat{E}_z$ approaching zero at the wall and $\partial\hat{E}_z/\partial\hat{r}$ becoming zero at the centerline. The radial electric field is zero at the centerline and has a vanishing radial derivative at the wall.

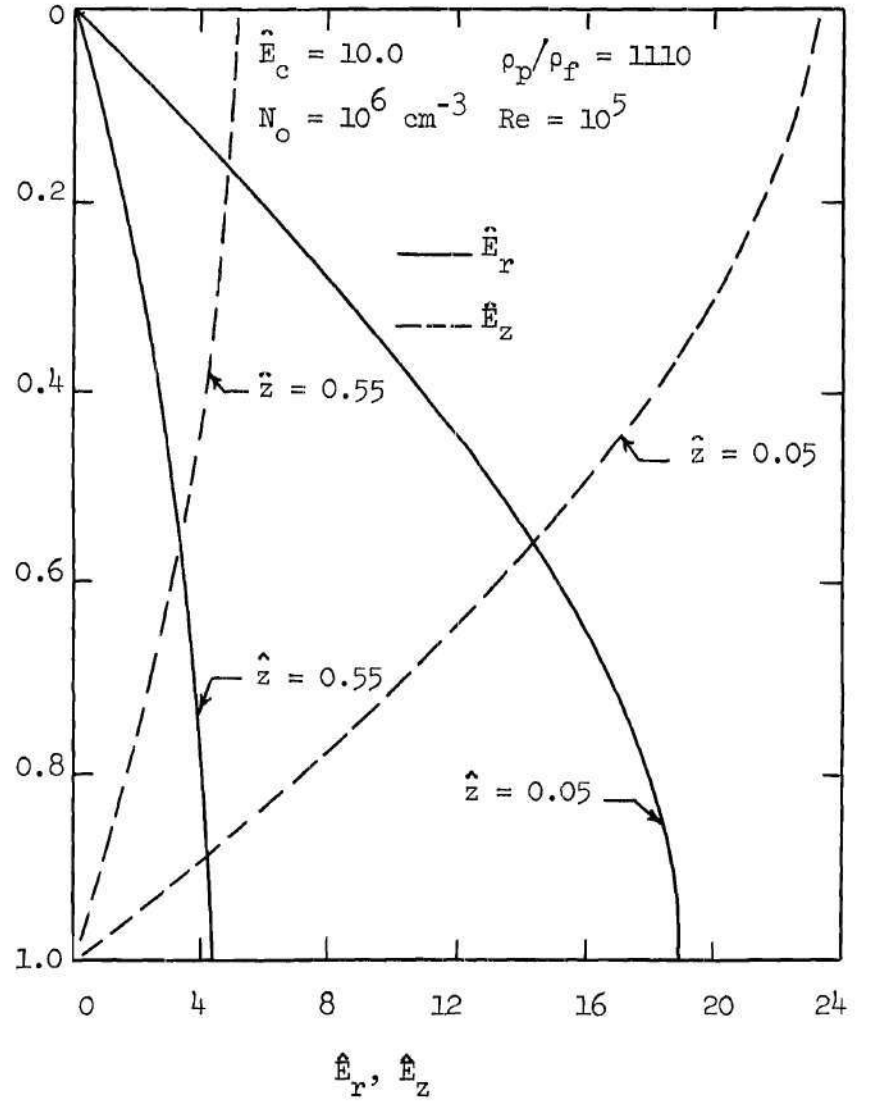

Figure 39. Electric-Field Intensity as a Function of Radial Coordinate for Two Axial Locations ($a_o/R = 10^{-5}$)

CHAPTER VII

ELECTROSTATIC DEPOSITION WITHIN A TWO-DIMENSIONAL CHANNEL

The computational examples considered thus far with respect to electrostatic deposition have been confined to axisymmetric pipe flows involving unipolar aerosols, for which particle coagulation is negligible. The purpose of this chapter is to present the results obtained by extending the previous development to examples involving bipolar aerosols within two-dimensional channel flows. The examples considered are rather idealized in nature and are presented for illustrative purposes.

Rather than devote attention to the so-called plate-wire precipitator, which has been the subject of some previous study [43], it may be of interest here to examine the electrostatic deposition of a bipolar aerosol in the presence of an electric field generated by applying voltages of different signs to the channel walls. That set of conditions results in preferential deposition of an aerosol particle onto the surface having the opposite sign of its own charge, that is, positively charged particles will be deposited on the wall having the negative polarity and negatively charged particles will be deposited on the other wall. Coagulation resulting from particle collision involving particles of either sign results in particles carrying the cummulative charge of the colliding partners. Consideration of this effect is made

later when specific reference to the coagulation model is made.

Summary of Equations

A two-dimensional coordinate system, as illustrated in Figure 40, is introduced, and the equations of Chapter IV are here specialized for this coordinate system. The continuity equation, (4.24) becomes

$$\frac{\partial}{\partial y}\left[n^{(q)}U_y^{(q)}\right] + \frac{\partial}{\partial z}\left[n^{(q)}U_z^{(q)}\right] = I^{(q)}, \quad q=1,2,\ldots \nu-1 \tag{7.1}$$

or, putting $U_z^{(q)} = U_{m_z} + V_z^{(q)}$, etc., and nondimensionalizing yields

$$\hat{n}^{(q)}\left[\frac{\partial \hat{V}_y^{(q)}}{\partial \hat{y}}\right] + \hat{V}_y^{(q)}\frac{\partial \hat{n}^{(q)}}{\partial \hat{y}} + \hat{n}^{(q)}\left[\frac{\partial \hat{U}_{m_z}}{\partial \hat{z}} + \frac{\partial \hat{V}_z^{(q)}}{\partial \hat{z}}\right] + \tag{7.2}$$

$$\left(\hat{U}_{m_z} + \hat{V}_z^{(q)}\right)\frac{\partial \hat{n}^{(q)}}{\partial \hat{z}} = \frac{N_o a_o^4 R}{U_{m_{z_o}}} I^{(q)}$$

Putting $\hat{I}^{(q)} = (N_o a_o^4 R)/(U_{m_{z_o}})I^{(q)}$ and solving equation (7.2) for $\partial \hat{n}^{(q)}/\partial \hat{z}$ yields

$$\frac{\partial \hat{n}^{(q)}}{\partial \hat{z}} = \frac{\hat{n}^{(q)}\left(\frac{\partial \hat{V}_y^{(q)}}{\partial \hat{y}} + \frac{\partial \hat{V}_z^{(q)}}{\partial \hat{z}}\right) + \hat{V}_y^{(q)}\frac{\partial \hat{n}^{(q)}}{\partial \hat{y}} - \hat{I}^{(q)}}{\hat{U}_{m_z} + \hat{V}_z^{(q)}} \tag{7.3}$$

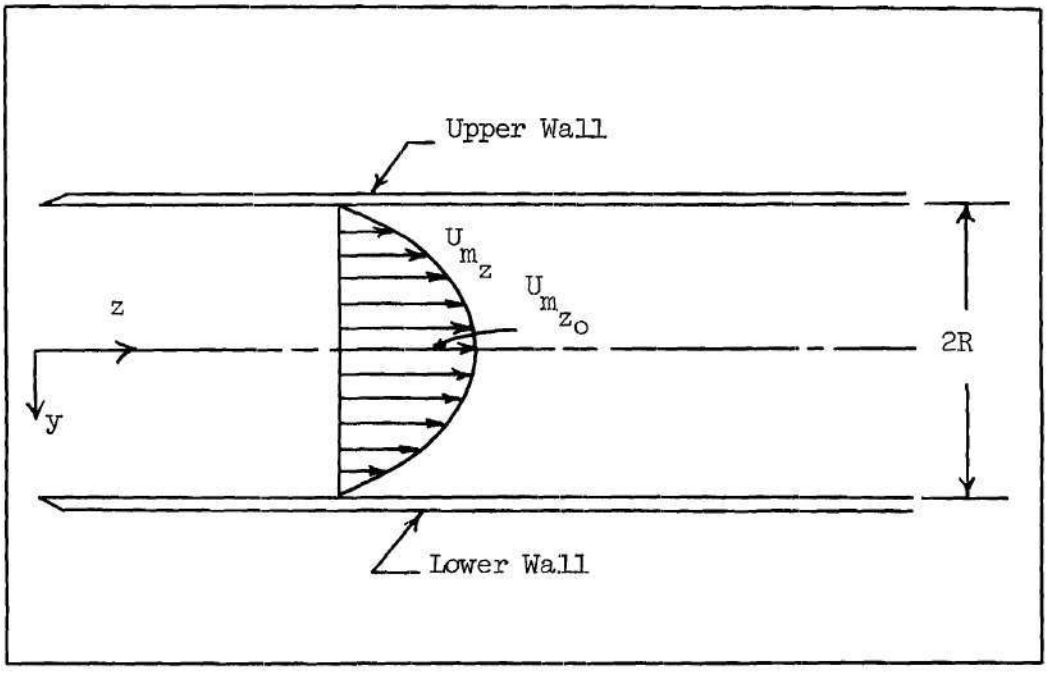

Figure 40. Two-Dimensional Channel Flow Coordinate System

since $\partial \hat{U}_{m_z} / \partial \hat{z} = 0$ for fully developed flow.

The normal momentum equation can be obtained from equation (4.23) as

$$n^{(q)}\left[U_y^{(q)} \frac{\partial U_y^{(q)}}{\partial y} + U_z^{(q)} \frac{\partial U_y^{(q)}}{\partial z}\right] = \frac{n^{(q)}}{m^{(q)}} Z^{(q)} E_y - \quad (7.4)$$

$$- V_y^{(q)} I^{(q)} S(I^{(q)}) + \frac{n^{(q)} 18 \mu_f f}{\rho_p (d^{(q)})^2} (-V_y^{(q)})$$

where the assumption has been made that

$$U_y^{(q)} - U_{I_y}^{(q)} \cong V_y^{(q)} \quad (7.5)$$

Equation (7.5) implies that $U_{I_y}^{(q)} \cong U_{m_z}$, i.e., that the velocity at which particles of type (q) are created by coagulation of smaller particles is approximately equal to the mean velocity at that point.

In nondimensional form, equation (7.4) can be shown to be

$$\hat{n}^{(q)}\left[\hat{V}_y^{(q)} \frac{\partial \hat{V}_y^{(q)}}{\partial \hat{y}} + (\hat{U}_{m_z} + \hat{V}_z^{(q)}) \frac{\partial \hat{V}_y^{(q)}}{\partial \hat{z}}\right] = \hat{n}^{(q)} A^{(q)} \hat{Z}^{(q)} \hat{E}_y - \quad (7.6)$$

$$\hat{V}_y^{(q)} \hat{I}^{(q)} S(\hat{I}^{(q)}) + \hat{n}^{(q)} \frac{18 \mu_f f}{\rho_p (d^{(q)})^2} [-\hat{V}_y^{(q)}]$$

Solving this for $\partial\hat{V}_y^{(q)}/\partial\hat{z}$ gives

$$\frac{\partial\hat{V}_y^{(q)}}{\partial\hat{z}} = \frac{A^{(q)}\hat{Z}^{(q)}\hat{E}_y - \hat{V}_y^{(q)}\left[\frac{B}{(a_o/R)^2\hat{a}^2} + \frac{\partial\hat{V}_y^{(q)}}{\partial\hat{y}}\right] - \frac{\hat{V}_y^{(q)}}{n^{(q)}}\hat{I}^{(q)}S(\hat{I}^{(q)})}{\hat{U}_{m_z} + \hat{V}_z^{(q)}} \tag{7.7}$$

Similarly, the streamwise momentum equation can be shown to give

$$\frac{\partial\hat{V}_z^{(q)}}{\partial\hat{z}} = \tag{7.8}$$

$$\frac{A^{(q)}\hat{Z}^{(q)}\hat{E}_z - \hat{V}_z^{(q)}\frac{B}{(a_o/R)^2\hat{a}^2} - \hat{V}_y^{(q)}\left[\frac{\partial\hat{U}_{m_z}}{\partial\hat{y}} + \frac{\partial\hat{V}_z^{(q)}}{\partial\hat{y}}\right] - \frac{\hat{V}_z^{(q)}\hat{I}^{(q)}S(\hat{I}^{(q)})}{\hat{n}^{(q)}}}{(\hat{U}_{m_z} + \hat{V}_z^{(q)})}$$

As earlier, particle charging is presumed to occur prior to entry into the main flow area of interest, so that, again,

$$\hat{Z}^{(q)} = 4\pi\left(1 + 2\frac{\epsilon_r - 1}{\epsilon_r + 2}\right) N_o R^3 \left(\frac{a_o}{R}\right)^2 \hat{a}^2 \hat{E}_c \tag{7.9}$$

The appropriate boundary conditions for these equations are indicated

later when specific examples are examined.

The electric-field components satisfy Poisson's equation

$$\frac{\partial \hat{E}_y}{\partial \hat{y}} + \frac{\partial \hat{E}_z}{\partial \hat{z}} = \int_{\hat{a}=0}^{\infty} \hat{n}(q)_Z(q)_{d\hat{a}} = Q(\hat{z},\hat{y}) \qquad (7.10)$$

The assumption is made that $\partial \hat{E}_z/\partial \hat{z} \ll \partial \hat{E}_y/\partial \hat{y}$ and that $Q(\hat{z},\hat{y}) \cong Q(\hat{z})$, so that equation (7.10) can be simplified to

$$\frac{\partial \hat{E}_y}{\partial \hat{y}} = Q(\hat{z}) \qquad (7.11)$$

Integrating this equation with respect to $\hat{y}$ yields

$$\hat{E}_y = \hat{y}\, Q(\hat{z}) + f(\hat{z}) \qquad (7.12)$$

where $f(\hat{z})$is an arbitrary function of $\hat{z}$. Now, $\partial \hat{V}/\partial \hat{y} = - \hat{E}_y$, so that the potential may be obtained as

$$\frac{\partial \hat{V}}{\partial \hat{y}} = - \hat{y}\, Q(\hat{z}) - f(\hat{z}) \qquad (7.13)$$

Integrating equation (7.13) with respect to $\hat{y}$ gives

$$\hat{V} = - \frac{1}{2} Q(\hat{z}) \hat{y}^2 - \hat{y} f(\hat{z}) + g(\hat{z}) \qquad (7.14)$$

As boundary conditions, put $\hat{V} = \hat{V}_w$ at $\hat{y} = -1$ and $\hat{V} = \hat{V}_w$ at $\hat{y} = 1$. These two conditions, when used with equation (7.14) yield

$$\hat{V}_w = -\frac{1}{2} Q(\hat{z}) + f(\hat{z}) + g(\hat{z}) \tag{7.15}$$

and

$$-\hat{V}_w = -\frac{1}{2} Q(\hat{z}) - f(\hat{z}) + g(\hat{z}) \tag{7.16}$$

Adding these two equations gives

$$g(\hat{z}) = \frac{1}{2} Q(\hat{z}) \tag{7.17}$$

Likewise, substracting equation (7.16) from equation (7.15) yields

$$f(\hat{z}) = \hat{V}_w \tag{7.18}$$

Therefore, equation (7.14) becomes

$$\hat{V} = -\frac{1}{2} Q(\hat{z})\hat{y}^2 - \hat{y}\hat{V}_w + \frac{1}{2} Q(\hat{z})$$

or

$$\hat{V} = \frac{Q(\hat{z})}{2} (1-\hat{y}^2) - \hat{V}_w\hat{y} \tag{7.19}$$

The electric-field components are

$$\hat{E}_y = -\frac{\partial \hat{V}}{\partial \hat{y}} = Q(\hat{z})\hat{y} + \hat{V}_w \tag{7.20}$$

$$\hat{E}_z = -\frac{\partial \hat{V}}{\partial \hat{z}} = -\frac{1}{2}(1 - \hat{y}^2)\frac{dQ}{d\hat{z}} \tag{7.21}$$

Finally, the boundary conditions for $\hat{n}^{(q)}$, $\hat{V}_y^{(q)}$, and $\hat{V}_z^{(q)}$ at the wall are as discussed before, namely, $\hat{V}_y^{(q)}$ and $\hat{V}_z^{(q)}$ approach their equilibrium values near a wall and $\partial \hat{n}^{(q)}/\partial \hat{y}$ approaches zero near a wall.

Bipolar Aerosol Deposition

If an aerosol composed of particles of both positive and negative charge is introduced into the channel of Figure 40, and if the upper and lower walls are given potentials of $\pm\hat{V}_w$, then those particles of like charge will drift under the action of electric forces toward one wall and those particles possessing opposite charge will drift toward the other wall. In addition, if the particles have a distribution in size and the number of particles of any given size possessing a negative charge is the same as the number possessing a positive charge, then the flow behavior of the charged particles is essentially symmetric with respect to particle charge. Under these conditions, one need be concerned computationally only with the behavior of particles of one charge type.

As a computational example, the following parameters are again chosen:

(i) $a_o/R = 10^{-4}$, $a_o = 10^{-3}$cm, $\hat{V}_w = 2.0$,

(ii) $a_o/R = 10^{-5}$, $a_o = 10^{-4}$cm, $\hat{V}_w = 2.0$,

with $\rho_p/\rho_f = 1110$ and $Re = 10^5$ for both cases. $\hat{E}_c$ is assigned a value which gives a reasonable and discernable deposition within the flow region of interest. The aerosol particles are presumed to be distributed log-normally with respect to size and uniformly with respect to spatial coordinate at $\hat{z} = 0$. Furthermore, there are an equal number of positively and negatively charged particles of any given size at the inlet, so that if the total particulate concentration at $\hat{z} = 0$ is 10^6 cm^{-3}, as in earlier examples, then the appropriate value for N_o for use in the analysis is $10^3 cm^{-3}$.

The mean velocity profile can be obtained, as by Schlichting [44], in nondimensional form,

$$\hat{U}_{m_z} = 1 + 2.5 \left(\frac{U_{z_*}}{U_{m_{z_o}}}\right) \ln (1-\vartheta) \tag{7.22}$$

The friction velocity is given by an appropriate friction relationship, e.g.,

$$\frac{U_{z_*}}{U_{m_{z_o}}} = \frac{(0.1267)^{7/8}}{Re^{1/8}} \tag{7.23}$$

which has been verified experimentally for particle-free flows. Thus

$$\hat{U}_{m_z} = 1 + \frac{0.410}{Re^{1/8}} \ln(1-\hat{y}) \tag{7.24}$$

The coagulation term must account for the overall collision rate among charged particles. Fuchs [1] presents some discussion relative to the thermal coagulation of aerosols having charged particles and notes that, experimentally, Fuchs and Petryanov [45] found it impossible to detect any difference between the coagulation rates of oil mists whether uncharged or charged. The analysis by Fuchs indicates that, as expected, the coagulation rate for particles of like charge is significantly reduced from its uncharged-particle rate, whereas the coagulation rate for particles of opposite charge is correspondingly increased. Overall, however, the net coagulation rate remains essentially unchanged from its uncharged-particle value. Hence, it is here assumed that the coagulation rate among the bipolar aerosol particles can be described by the turbulent coagulation model used earlier. However, the energy dissipation term appearing in the coagulation model must be specified for the present channel flow.

As earlier, the energy dissipation per unit time and volume, $\bar{\epsilon}_o$, can be shown [46] to be given approximately by

$$\bar{\epsilon}_o = \ell^2 \left| \frac{dU_{m_z}}{dy} \right|^3 \tag{7.25}$$

Relating the mixing length, ℓ, to the mean velocity profile by means of the classical von Karman similarity hypothesis gives

$$\ell = 0.378 \left| \frac{dU_{m_z}}{dy} \Big/ \frac{d^2U_{m_z}}{dy^2} \right| \tag{7.26}$$

or, with U_{m_z} given by equation (7.24) and $Re = 10^5$,

$$\ell = 0.378R\left(1 - \frac{y}{R}\right) \tag{7.27}$$

The use of equations (7.24) and (7.27) in equation (7.25) yields, after some manipulation,

$$\bar{\epsilon}_o = \frac{4.50 \times 10^{-8}}{(1-\hat{y})R^4} Re^3, \ cm^2/sec^3 \tag{7.28}$$

for standard temperature and pressure conditions.

As can be seen from the coagulation model of equation (3.4), the probability of particle collision is proportional to the difference in the squares of their radii. Hence, the most probable coagulation effects result for particles of very different size, for which the resultant charge after coalescence is approximately that given by equation (7.9). One finds, on average, that equation (7.9) can reasonably be applied to a coagulating aerosol without excessive error.

The appropriate boundary conditions for this example require

careful consideration. As before, $\hat{V}_r^{(q)}$ and $\hat{V}_z^{(q)}$ approach their equilibrium values near the upper and lower walls; however, due to the asymmetry of the behavior of each species with respect to the center plane, $\hat{y} = 0$, no statements relative to the values of $\hat{V}_r^{(q)}$ and $\hat{V}_z^{(q)}$ at $\hat{y} = 0$ can be made at the outset. The Danckwerts boundary condition, $\partial\hat{n}^{(q)}/\partial\hat{y} = 0$ is applied at the wall toward which particles are driven, i.e., at the lower wall for negatively charged particles and at the upper wall for positively charged particles. The boundary condition for $\hat{n}^{(q)}$ at the wall from which the particular set of particles is being driven is fundamentally different from that at the wall toward which they are driven. For the present example, the concentration of negatively-charged particles at the upper wall is obviously zero.

Finally, one notes that for the present formulation $Q(\hat{z})$ remains zero for all $\hat{z}$, since it is zero at $\hat{z} = 0$ and, due to the symmetry of the flow with respect to particle charge, there are an equal number of positively and negatively charged particles at any given downstream location. Note that, in reality, $Q(\hat{z},\hat{r})$ does not remain zero everywhere, since there is a charge separation as the flow progresses downstream.

Discussion of Results

Figure 41 presents negatively-charged particle number-concentration profiles at several downstream locations for $a_o/R = 10^{-4}$, $a_o = 10^{-3}$cm, and $\hat{E}_c = 2.0$, both including and excluding turbulent diffusion. When turbulent diffusion effects are considered, the approach developed in Chapter V is again followed. That is, the particle diffusion velocities

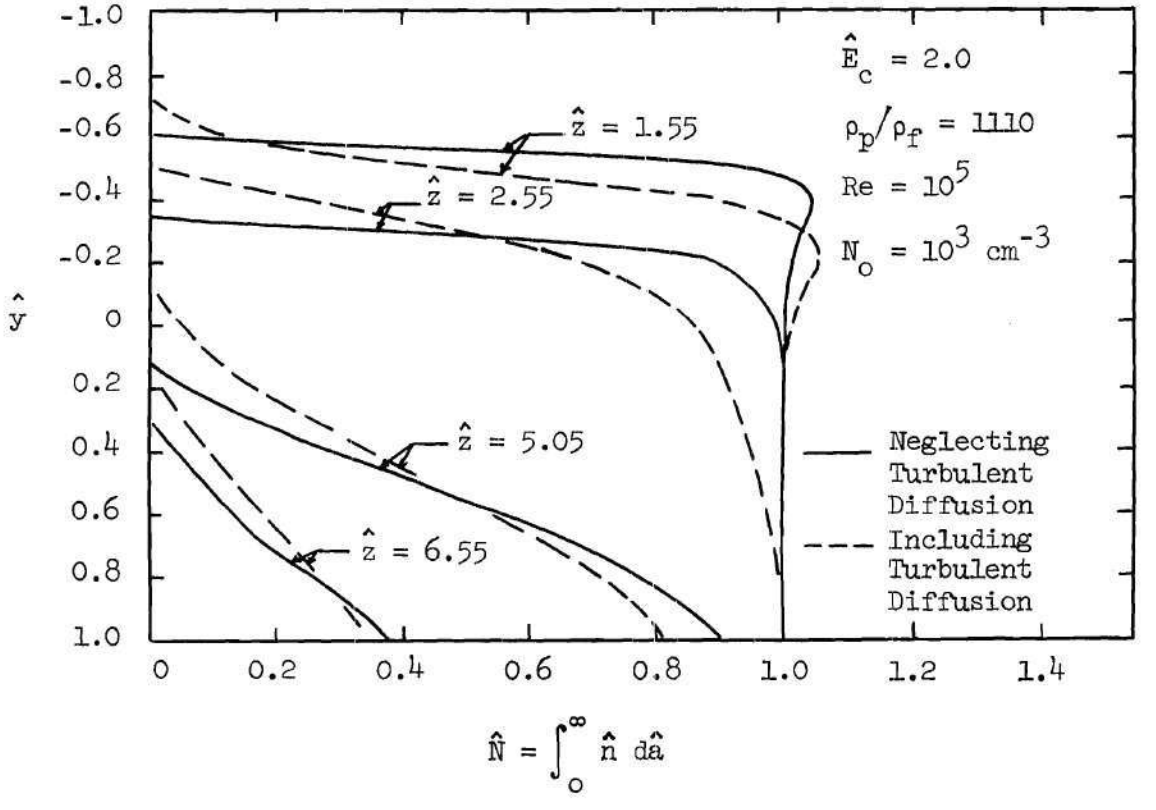

Figure 41. Number Concentration of Negatively-Charged Particles at Several Downstream Locations ($a_o/R = 10^{-4}$, $a_o = 10^{-3}$ cm

are given by

$$\hat{V}_y^{(q)} = [\hat{V}_y^{(q)}]_{\substack{\text{electrical} \\ \text{drift}}} + [\hat{V}_y^{(q)}]_{\substack{\text{turbulent} \\ \text{diffusion}}} \tag{7.29}$$

where

$$[\hat{V}_y^{(q)}]_{\substack{\text{turbulent} \\ \text{diffusion}}} = -\frac{\hat{\ell}^2}{\hat{n}^{(q)}} \left| \frac{d\hat{U}_{m_z}}{d\hat{y}} \right| \frac{d\hat{n}^{(q)}}{d\hat{y}} \tag{7.30}$$

and, with the von Karman Hypothesis,

$$\hat{\ell} = 0.378 \left| (d\hat{U}_{m_z}/d\hat{y})/(d^2\hat{U}_{m_z}/d\hat{y}^2) \right| \tag{7.31}$$

For this case, $[\hat{V}_y^{(q)}]_{\text{electrical drift}}$ can be taken as the equilibrium $\hat{V}_y^{(q)}$, as defined earlier. When turbulent diffusion effects are neglected, the full nonequilibrium momentum equations are employed.

It can be seen from Figure 41 that the concentration decreases quite rapidly near the upper wall, dropping to zero over about 20 per cent of the cross section at $\hat{z} = 1.55$. As the flow proceeds further downstream, the profiles become almost linear over much of the cross section. At $\hat{z} = 5.05$, much of the particulate load has been removed, although the concentration at the lower wall remains at almost 90 percent of its original value. Beyond $\hat{z} = 5.05$, the wall concentration decreases rapidly, dropping to about 27 percent of its entrance value

as the flow reaches $\hat{z} = 6.55$.

Figure 42 presents analogous results for $a_o/R = 10^{-5}$, $a_o = 10^{-4}$ cm, and $\hat{E}_c = 20.0$. Note that a factor of 10 increase in the precharging field is necessary for an approximately equivalent efficiency relative to that required for the larger particles. The decrease in concentration near the upper wall is similar to that observed for the larger particles, but here the concentration near the lower, collecting wall decreases more rapidly. At $\hat{z} = 5.05$, most of the particulate load has been removed, with only a small concentration remaining within about 20 percent of the cross section near the lower wall.

The effect of reducing the precharging field to $\hat{E}_c = 5.0$ for this latter example is shown in Figure 43. The number concentration profiles are similar in shape to those for $\hat{E}_c = 20.0$, but the reduction in electrical forces is seen to markedly decrease the concentration decay, with the profile at $\hat{z} = 6.55$ for $\hat{E}_c = 5.0$ being comparable to that at $\hat{z} = 2.0$ for $\hat{E}_c = 20.0$.

Figure 44 presents particulate-removal efficiency, as a function of downstream distance, resulting from several precharging fields for the two particle-size classifications examined before. Other than the three curves for $a_o/R = 10^{-5}$, $a_o = 10^{-4}$cm, $\hat{E}_c = 20.0$, and $\hat{E}_c = 5.0$, and $a_o/R = 10^{-4}$, $a_o = 10^{-3}$cm, $\hat{E}_c = 2.0$, the results represent solutions generated with coagulation effects excluded.

The results for $a_o/R = 10^{-5}$ and $a_o = 10^{-4}$ cm are cross plotted in Figure 45 in the form of particulate-removal efficiency as a function of precharging field for various downstream distances. Finally, the number-concentration distribution functions at two downstream locations

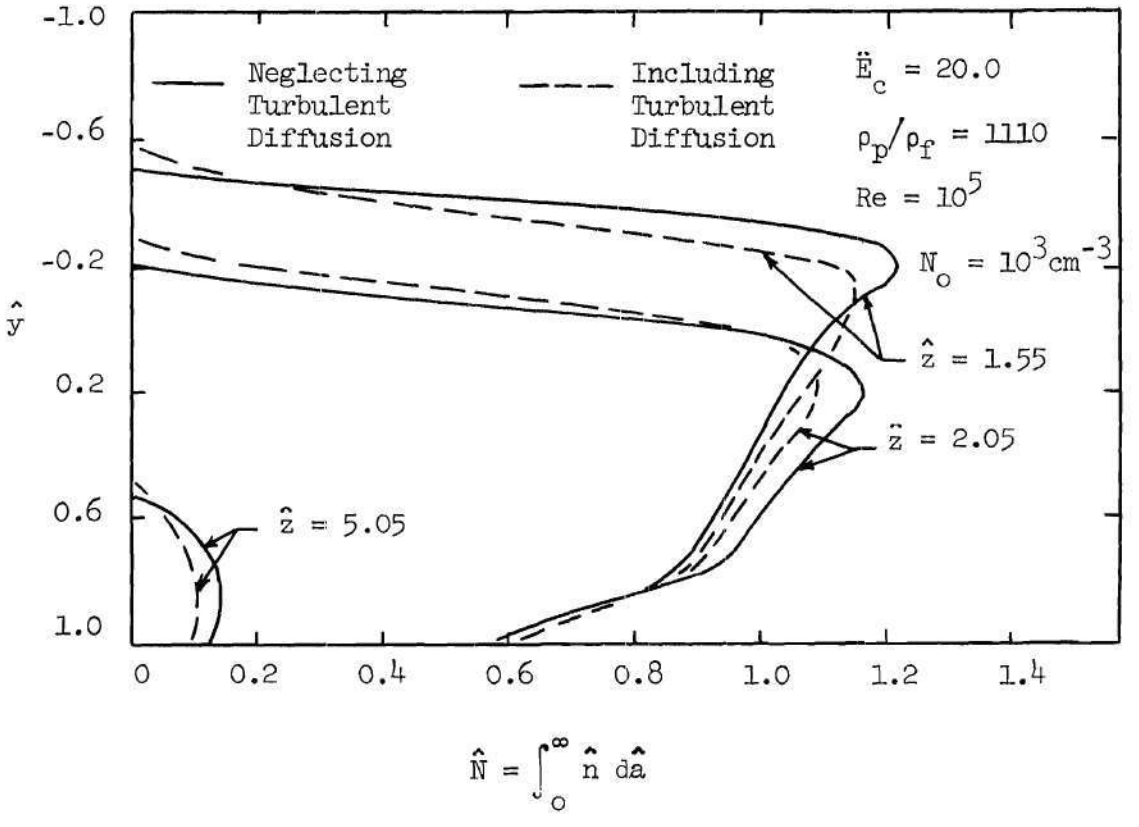

Figure 42. Number Concentration of Negatively-Charged Particles at Several Downstream Locations ($a_o/R = 10^{-5}$, $a_o = 10^{-4}$ cm)

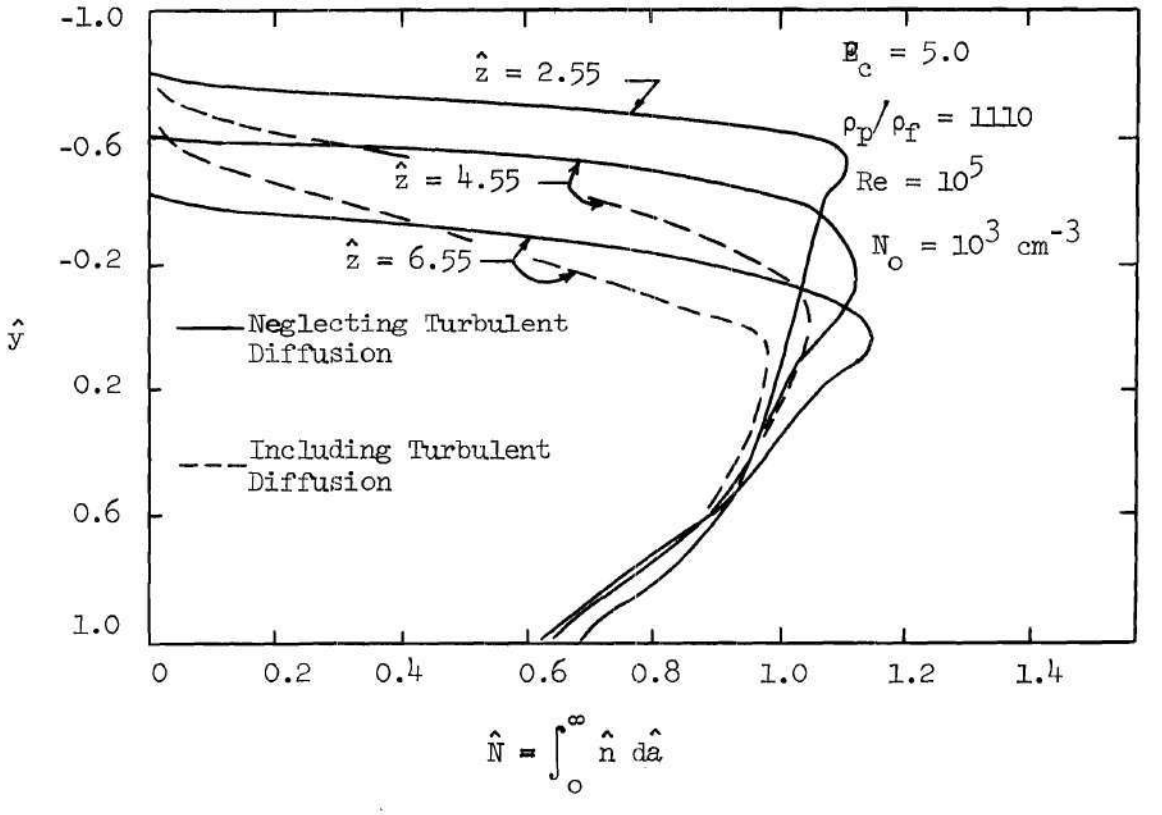

Figure 43. Number Concentration of Negatively-Charged Particles at Several Downstream Locations ($a_o/R = 10^{-5}$, $a_o = 10^{-4}$ cm

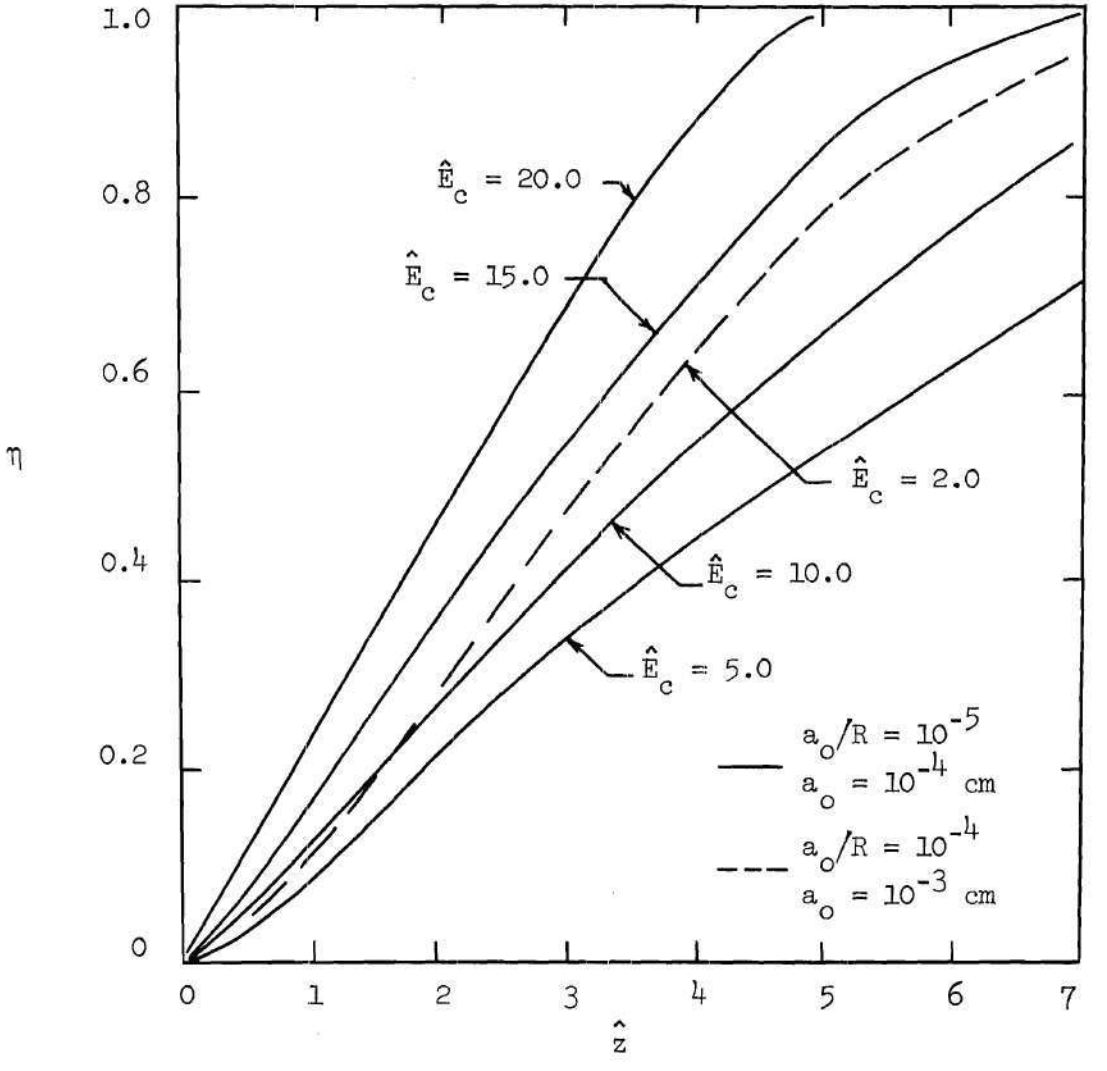

Figure 44. Particulate Removal Efficiency as a Function of Precharging Downstream Distance

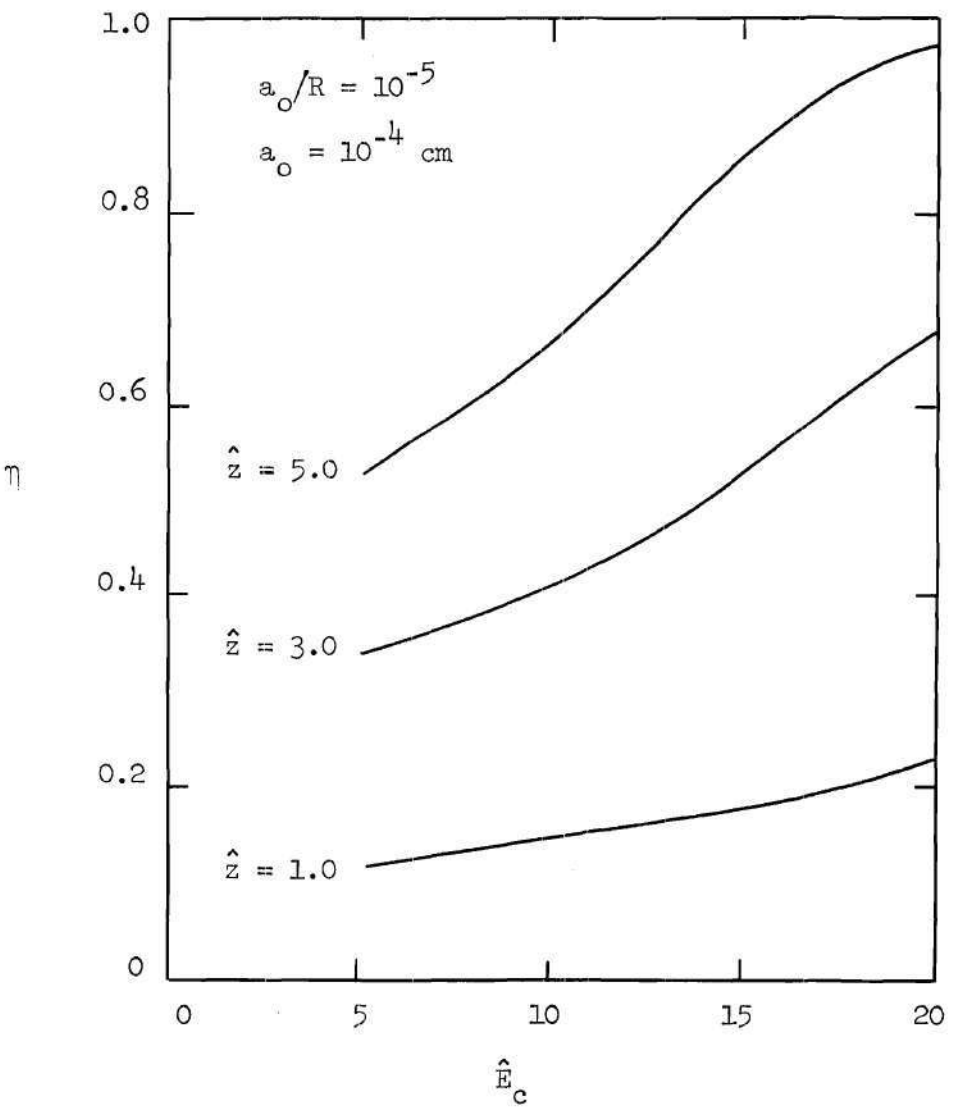

Figure 45. Particulate Removal Efficiency as a Function of Precharging Electric Field

are shown in Figure 46 for illustrative purposes. One anticipates that deposition preferentially removed the larger particles, as demonstrated earlier, whereas coagulation tends to replenish these particles, so that, on average, the two effects are compensating and tend to abrogate the individual influence of either.

Unipolar Space-Charge Induced Aerosol Deposition

Aerosol deposition due to a unipolar space charge within a two-dimensional channel represents an important problem of interest to air pollusion equipment designers and is the logical sequel to the corresponding axisymmetric problem discussed in Chapter VI. Consideration is directed toward a fully-developed turbulent gas flow supporting a particulate loading which possesses a defined distribution with respect to particle radius and uniformly distributed with respect to spatial coordinate at a given cross section. However, no external electric field is here imposed, and particles all have the same type of charge (e.g., negative) distributed with respect to particle size according to equation (7.9).

The continuity and normal and streamwise momentum equations are solved by forward-difference marching from known conditions at $\hat{z} = 0$ with specific boundary conditions at the wall taken to be as discussed before and with obvious symmetry conditions at the midplane, $\hat{y} = 0$. The electric field at any given point is described by equations (7.20) and (7.21) with $\hat{V}_w = 0$.

The specific values for various parameters are

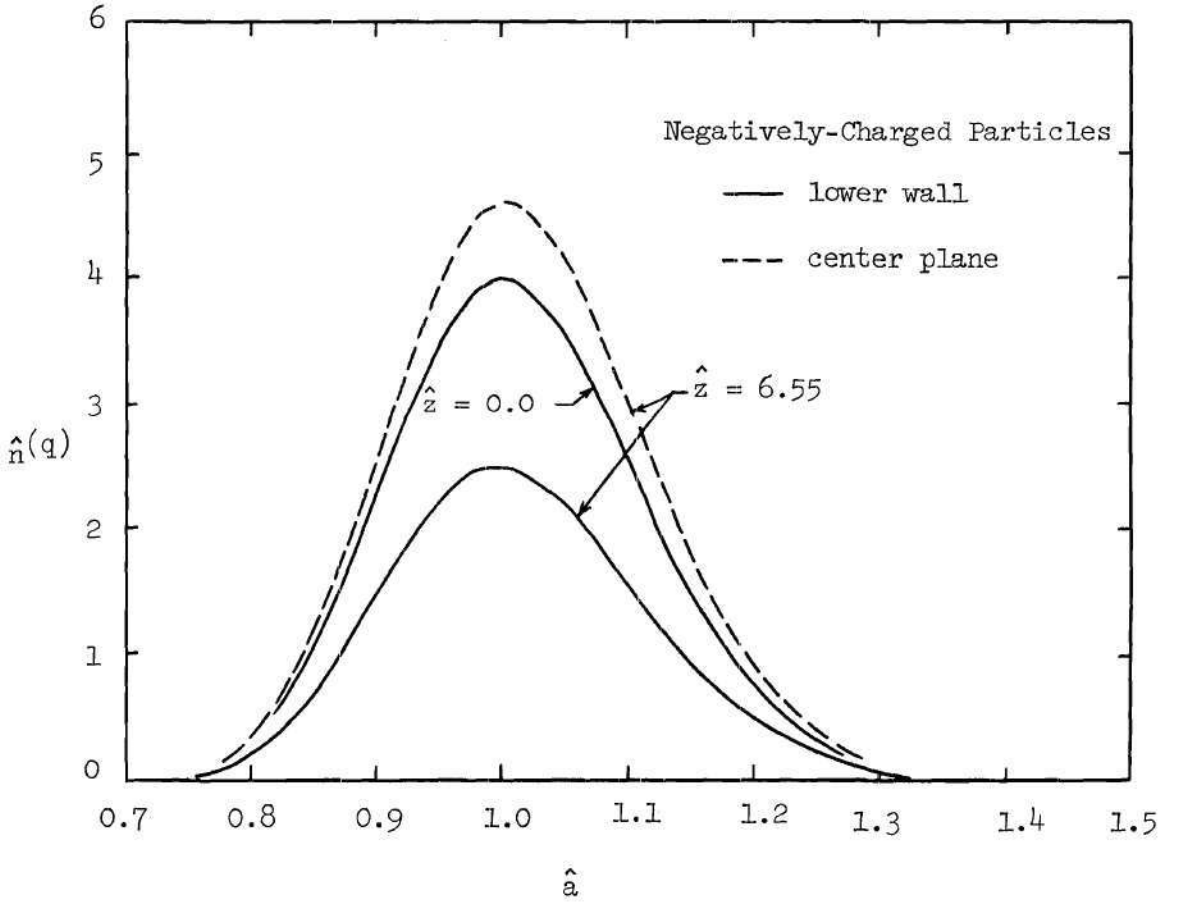

Figure 46. Particle Number-Concentration Distribution at Two Downstream Locations ($a_o/R = 10^{-5}$, $a_o = 10^{-4}$ cm, $\hat{E}_c = 5.0$)

$a_o R = 3.92 \times 10^{-4}$, $a_o = 5.0 \times 10^{-4}$ cm, $Re = 3.55 \times 10^{4}$,

$\rho_p/\rho_f = 2770$, $\sigma_o = 0.19$ (standard deviation for particle-radius distribution)

$U_{m_{z_o}} = 2040$ cm/sec, $N_o = 1.03 \times 10^{+4}$ cm^{-3}, $2.6 \times 10^{+4}$ cm^{-3},

$\epsilon_o E_o^2/\rho_f U^2_{m_{z_o}} = 0.011$, $\hat{E}_c = 0.2755$

Coagulation effects can be neglected.

Figure 47 presents results for mass deposition flux to the wall as a function of downstream distance for three values of initial particle loading density, N_o. The results indicate a zero flux at $\hat{z} = 0$, with the flux increasing rapidly as the flow proceeds downstream. As expected, the highest particulate loading yields the highest space-charge repulsion deposition rate.

Figure 48 presents a comparison of results for centerplane number concentration relative to the inlet concentration for z = 0 to $\hat{z} = 10$. The curves appear to be rather linear over most of the distance for which computation were made, although in no case did the decrease in concentration exceed 9 percent of the initial value.

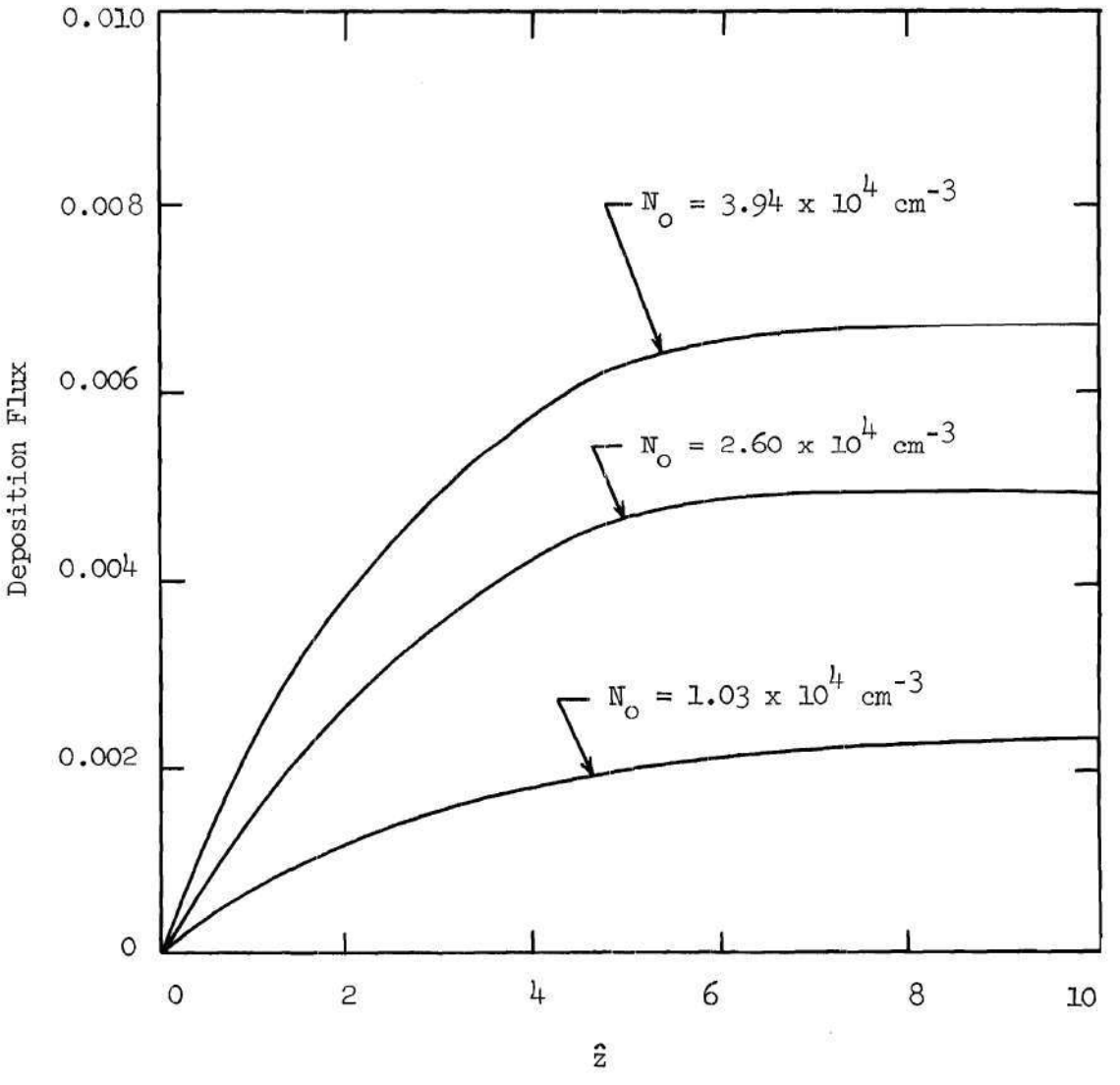

Figure 47. Wall Deposition Flux as a Function of Downstream Distance for Several Particulate Loadings

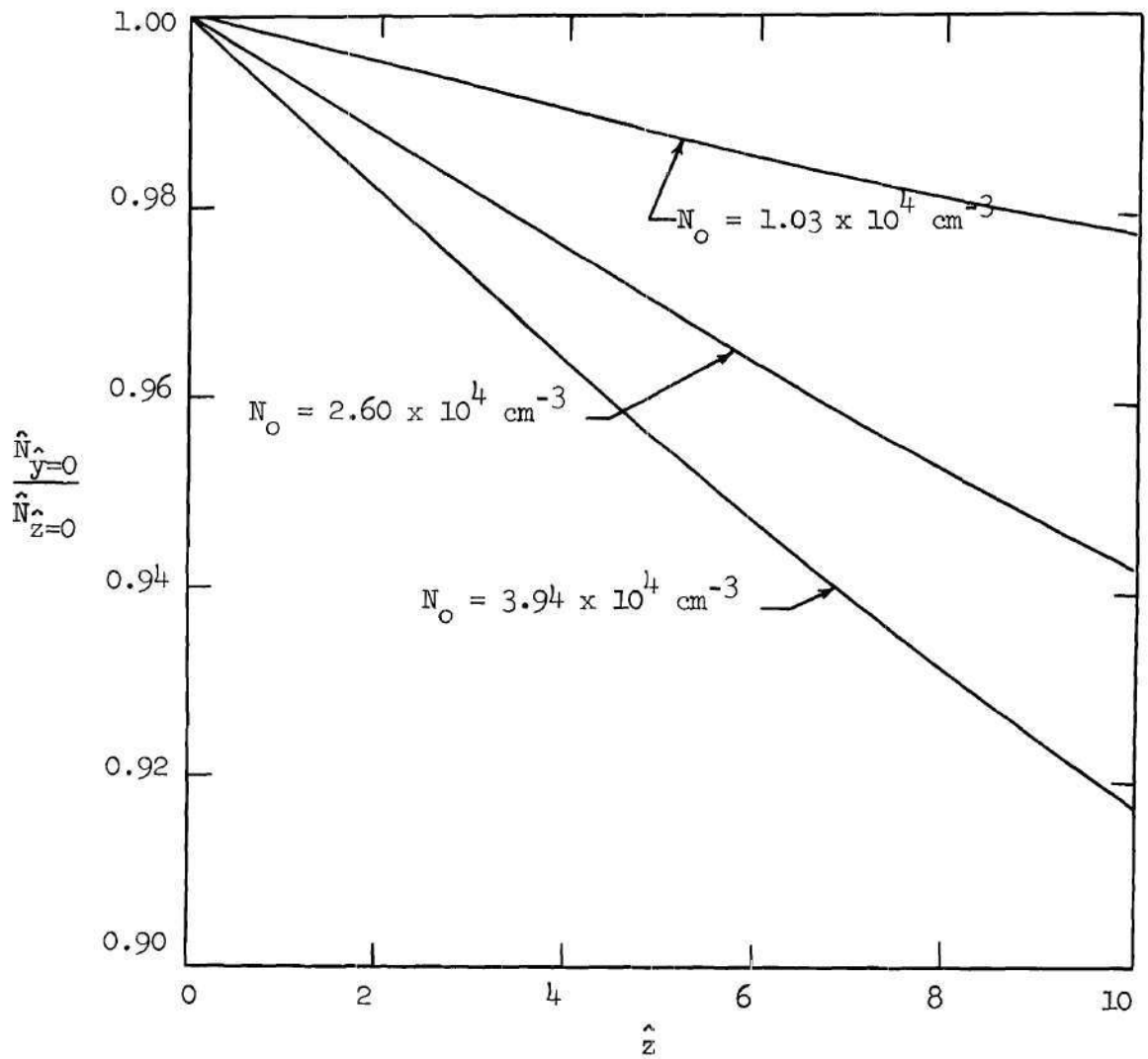

Figure 48. Centerplane Particle Concentration as a Function of Downstream Distance

CHAPTER VIII

DISCUSSION AND CONCLUSIONS

An examination has been made of some basic aspects of aerosol deposition within several configurations of practical interest. Beginning with the indication that the so-called discrete-ordinate method of recent application to rarefied-gas dynamics problems might represent a useful technique for theoretically examining the fluid-dynamic behavior of a coagulating aerosol suspension, a research effort was undertaken to develop appropriate and serviceable analytical and numerical techniques for predicting aerosol deposition, both in the presence and in the absence of electrical effects, and for revealing several other interesting aspects of aerosol behavior, e.g., concentration distributions within flow configurations of practical interest. The study is founded upon the empirical "laws" of Newton and other results of experimental observation whenever possible, and a comparison of theoretical results with available data is presented whenever appropriate. Specifically, solutions were sought to the conservation equations for multiphase systems, as specialized for fluid-particle systems having a relatively dilute particulate phase.

The results of this study may be summarized as follows:

1. Initial attention was directed toward the deposition of non-coagulating, neutral aerosols from fully-developed turbulent pipe flow and flat-plate flow. It was found that a mixing-length hypothesis

provided a basis for constructing an analytical approach for conveniently predicting, with reasonable accuracy, noncoagulating aerosol deposition from these two flow geometries when electrical forces are absent. These are equation (B.26), for axisymmetric pipe flow, and equation (B.27), for turbulent flat-plate flow. Also obtained were some associated numerical solutions for the streamwise development of aerosol concentration distributions and surface deposition characteristics for turbulent pipe flow. Comparison of results predicted by the analytical expressions with the results of the numerical solutions and with available experimental data indicates that the mixing-length hypothesis appears to offer an improvement in available theoretical prediction capability in the fully-developed turbulent flow regime. It was found that, although a significant quantity of data exists for Re less than about 10^4, the limited amount of experimental data which exists at higher Reynolds numbers indicates that extrapolations of lower Re data are probably not valid. There exists a need for additional data in this flow regime, particularly with respect to particulate diffusivity.

2. An analysis of the influence of coagulation upon overall deposition indicates that there is little effect upon overall mass transport to a bounding wall as a result of particle coagulation, at least for the conditions chosen for study. However, the application of the discrete-ordinate technique to this problem represents a convenient and accurate method for computationally processing the coagulation integrals in the particle continuity equation. This relatively straightforward method lends itself quite readily to efficient

computational algorithms for implementation via the digital computer.

3. The initial success of the present approach for investigating the deposition of neturally-charged aerosols led to the question as to whether the formulation might profitably be extended to the charged aerosol deposition problem involving significant electrical forces. It was found that a formulation based on the particle continuity and momentum equations, when combined with an approximate solution to Poisson's equation for the particular problem of interest and with several other subsidiary equations, is indeed quite susceptive to numerical solution. Several electrostatic precipitator flow problems were chosen for examination.

4. Numerical solutions for the formulation applied to the conventional pipe-wire electrostatic precipitator were obtained and compared with experimental data and with theoretical efficiencies predicted by the standard Deutsch formula for electrostatic precipitation. Particulate removal efficiences indicated by the numerical solutions were superior to those predicted by the Deutsch formula relative to the experimental data comparisons. Correlations of the numerical results were obtained for practical application. Particle diffusion velocities were found to remain very close to their equilibrium values for representative conditions. Although the problem of numerical stability for the solution procedures adopted herein represents a particularly important concern to the analyst, the rather voluminous collection of results obtained for essentially all particulate numerical solutions generated indicates a consistent lack of implicit instability with

respect to the computational procedure.

5. The influence of turbulent diffusion relative to electrically-induced drift within the conventional pipe-wire precipitator is small relative to overall efficiency, although its influence upon the concentration distribution is more significant. Computation time is essentially doubled when turbulent diffusion is accounted for in the analysis. The strong radial electric-field intensity developed within the conventional pipewire configuration tends to generate rather large concentration gradients, due to the electrically-induced particle drift, and for this configuration, turbulent diffusion does modify the concentration distribution although its effect upon overall mass deposition was found to be small.

6. Extension of the approach to space-charge induced particle deposition was successfully completed, further illustrating the flexibility of the approach. Space-charge deposition was found to be much greater than turbulent deposition for those conditions examined.

7. Finally, attention was directed toward aerosol deposition within a two-dimensional channel. Bipolar aerosol behavior in the presence of a simple, constant-strength traverse electric field and subject to coagulation effects was obtained by numerical solution. As before, coagulation effects upon total mass deposition were found to be small, although the flexibility and versatility of the technique were again demonstrated. Lastly, space-charge deposition of a unipolar aerosol within the two-dimensional channel was investigated. The

results indicate a potential for useful application to aerosol-sampler losses due to particle charge.

8. Throughout the electrical-deposition study, the so-called Danckwerts boundary condition for particle concentration at a wall was applied since it appears to represent the most reasonable assumption. However, further experimental study is indicated to illuminate additional features of the behavior of suspended particles near a bounding wall. In fact, the entire particle-surface interaction problem represents an important subject for additional study.

APPENDIX A

PARTICLE FLUCTUATION VELOCITY DISTRIBUTION

Consideration is here devoted to some analysis which roughly specifies local particle fluctuation velocities relative to the local fluid fluctuation velocities. The approach is an intuitive approximation which is based on the root-mean-square fluctuation velocities as discussed in Chapter II.

The basic problem is to determine the extent to which particles follow the turbulent fluctuations of the fluid, particularly as the particles diffuse through regions of differing turbulence. Two aspects of the problem can be identified as requiring consideration. First, consideration is devoted to the response of particles to a turbulent fluid medium of infinite extent and possessing homogeneous characteristics. Second, an approximate analysis is made of the effect on the induction period resulting from a density difference between a particle and the surrounding fluid. This induction period occurs, when, at some instant, the motion of the discrete particle is different from the equilibrium, steady-state condition.

An analysis can be made [33, p. 31] of the frequency response of a discrete particle subjected to a sinusoidal oscillation of the velocity of the surrounding fluid. It has been found [1,p. 80] that the ratio of particle-to-fluid rms velocity, $\overline{u_p^2}/\overline{u_f^2}$, can be expressed

in terms of frequency, ω, particle size and density, and fluid molecular viscosity for a Stokes drag regime. Figure 49 presents this rms velocity ratio as a function of forcing frequency for unit density particles of several radii. As expected, particles follow the motion for low frequencies, but the response begins to decrease at higher frequencies. Also important is the fraction of the turbulent motion energy which can be assigned to given frequencies. Results of Laufer's investigation [22] of turbulent pipe flow at $Re = 5 \times 10^5$ are also shown in Figure 49 and can be compared with the frequency response of the different particles. Note that the response of one-micron particles does not begin to decrease until the frequency, ω, is well above that for which any significant turbulent energy remains within the spectrum. Hence, one can expect that the one-micron particles follow the turbulent motion essentially completely and can be considered fully entrained under isotropic conditions. However, the 100-micron particles follow only the lower-frequency components of the motion and can be considered only partially entrained. The 10-micron particle frequency response drops to about 0.87 at $\omega = 10^3$ rad/sec, but the relative energy has dropped to about 20 percent of its maximum. Thus 10-micron particles can be considered to be almost completely entrained.

Therefore, if the analysis is here restricted to particle sizes less than about 10 microns, then one can assume that the particle rms fluctuation velocity and fluid rms fluctuation velocity are approximately the same in the flow region near the centerline of turbulent pipe flow. However, as particles diffuse toward the wall, their inertia tends to

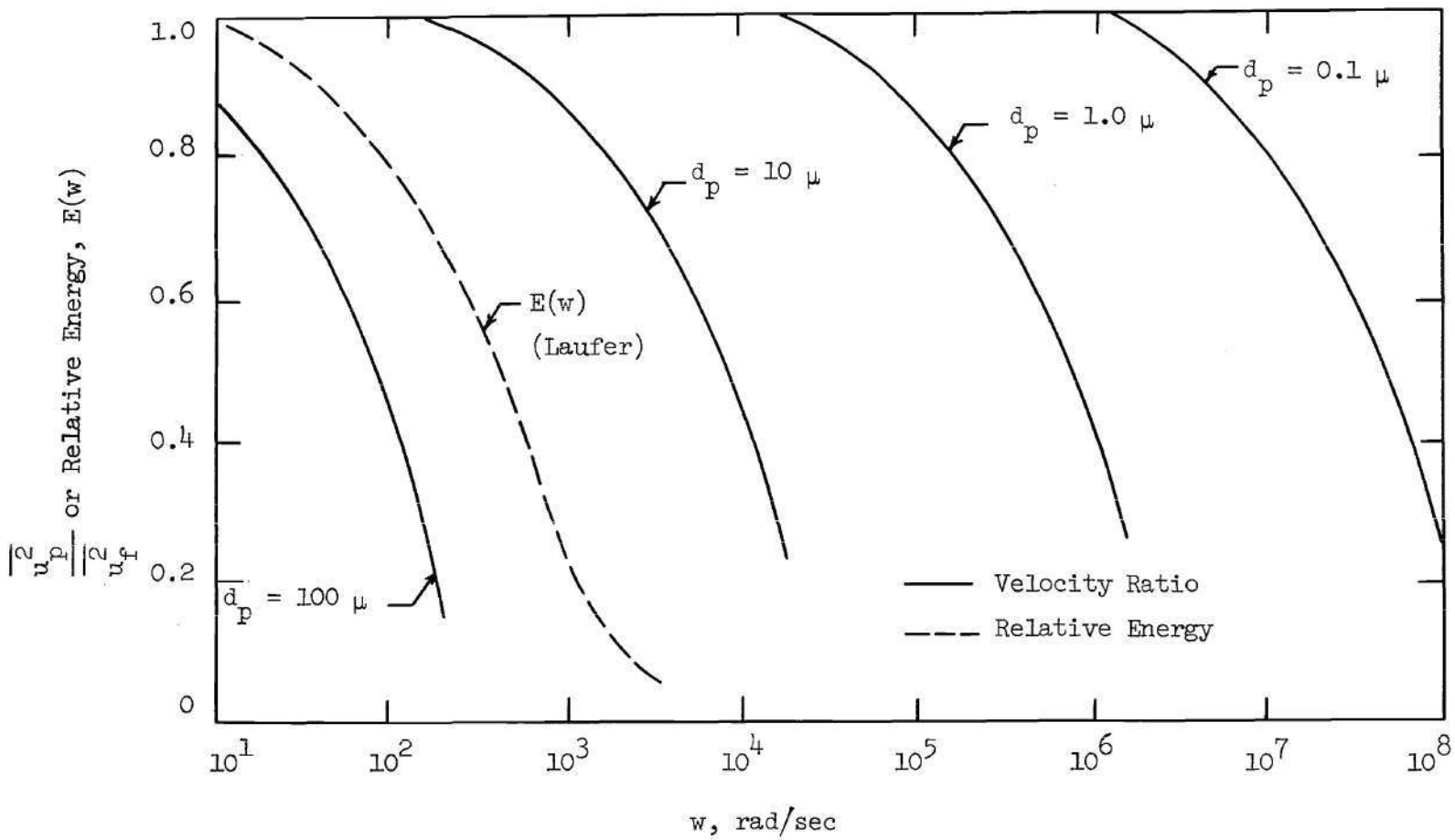

Figure 49. Relative Energy and Velocity Ratio as Functions of Frequency

retard their immediate adjustment to local fluid conditions. Hence, due to the induction period required for accommodation of particle fluctuation velocity to that of the local fluid fluctuation velocity, one expects that the particle velocity at a given point to be related to its velocity at a point further from the wall, the change being due to relaxation of particle-fluid velocity difference during the transit time between the two points. Consider a point located a distance $y_* + dy_*$ above the pipe wall. The particle rms fluctuation velocity there is $v'_{p*}(y_* + dy_*)$ and the fluid rms fluctuation velocity is $v'_{f*}(y_* + dy_*)$, so that the velocity difference is

$$v'_{p*}(y_* + dy_*) - v'_{f*}(y_* + dy_*)$$

(non-dimensional variables are used, consistent with the nondimensionalization in Appendix B).

If the particles remained at this location, the particle rms fluctuation velocity might "relax" toward the fluid rms fluctuation velocity in an exponential manner, i.e., after a time t_* the velocity difference would be

$$[v'_{p*}(y_* + dy_*) - v'_{f*}(y_* + dy_*)]\, e^{-t_*/\tau_*} \qquad (A.1)$$

where τ_* is the nondimensional Stokes relaxation time. However, during this time the particles diffuse toward the wall, so that putting

$$t_* = \frac{dy_*}{v'_{p*}(y_* + dy^*)} \qquad (A.2)$$

and noting that the particle velocity is $v'_{p*}(y_*)$ at the end of this time interval, one obtains

$$v'_{p*}(y_*) - v'_{f*}(y_* + dy_*) = [v'_{p*}(y_* + dy_*) - v'_{f*}(y_* + dy_*)]e^{-dy_*/\tau_* v'_{p*}(y_* + dy_*)} \qquad (A.3)$$

Putting

$$v'_{f*}(y_* + dy_*) \cong v'_{f*}(y_*) + \frac{dv'_{f*}}{dy_*} dy_* + \ldots$$

$$v'_{p*}(y_* + dy_*) \cong v'_{p*}(y_*) + \frac{dv'_{p*}}{dy_*} dy_* + \ldots$$

and expanding the exponential as

$$e^{-\frac{dy_*}{\tau_* v'_{p*}(y_* + dy_*)}} \cong 1 - \frac{dy_*}{\tau_* v'_{p*}(y_* + dy_*)} + \ldots \qquad (A.4)$$

$$\cong 1 - \frac{dy_*}{\tau_* v'_{p*}(y_*)},$$

one can show that equation (A.3) becomes

$$\frac{dv'_{p*}}{dy_*} = \frac{1}{\tau_*}\left(1 - \frac{v'_{f*}}{v'_{p*}}\right). \qquad (A.5)$$

Equation (A.5) may be considered the "governing" differential equation for v'_{p*}. The experimental data of Laufer [22] indicate that the fluid turbulent fluctuation velocity v'_{f*}, can be represented reasonably well by the simple expression, involving non-dimensional variables,

$$v'_{f*} = \frac{y_*}{y_* + 10} \qquad (A.6)$$

where the various non-dimensional variables are defined in Appendix B following equation (B.22). Equation (A.5) is nonlinear in the dependent variable v'_{p*}.

Asymptotic Expandion for Small τ_*

Examination of equation (A.5) indicates that in the limit as the particle relaxation time approaches zero ($\tau_* \to 0$)v'_{p*} must approach v'_{f*} in order that $(dv'_{p*})/(dy_*)$ remain finite. On the other hand, as $\tau_* \to \infty$, then $(dv'_{p*})/(dy_*) \to 0$, or $v'_{p*} \to$ constant, independent of y_*. Both of these limiting cases are as one would anticipate.

For small τ_*, one can assume an asymptotic expansion of the solution having the form

$$v'_{p*} = v'_{f*} + \tau_* g_1(y_*) + \tau_*^2 g_2(y_*) + \ldots \tag{A.7}$$

Substituting this expression into equation (A.5) and taking the limit as $\tau_* \to 0$, one finds that

$$g_1(y_*) = v'_{f*} \frac{dv'_{f*}}{dy_*} \tag{A.8}$$

Thus

$$v'_{p*} = v'_{f*} + \tau_* v'_{f*} \frac{dv'_{f*}}{dy_*} + \theta(\tau_*^2)$$

or

$$v'_{p*} = v'_{f*} \left(1 + \tau_* \frac{dv'_{f*}}{dy*}\right) + \theta(\tau_*^2) \tag{A.9}$$

Note that although this case represents a singular perturbation problem, no "inner" solution in the classical sense in necessitated since the "outer" solution, equation (A.9), satisfies the boundary condition of the problem, $v'_{p*} \to v'_{f*} = 1$ as $y_* \to \infty$ (note that $(dv'_{f*})/(dy_*) = 10/(y_* + 10)^2 \to 0$ as $y_* \to \infty$).

Numerical Solution

Numerical solutions to equation (A.5) were obtained for $\tau_* = 0.1$, 1.0, 3.0, 5.0, 10.0, and 100.0 by forward-difference marching from large values of y_* to the wall. Rather than making a transformation of

the independent variable to one having a finite range (e.g., $\hat{z} = 1 - \bar{e}^{\,y_*}$), the asymptotic expansion of the solution valid for large y_* was obtained and used to "start" the numerical solution. Since, as $y^* \to \infty$, $v'_{p^*} \to 1$ one can put

$$v'_{p^*} = 1 + \frac{1}{y_*} f_1(\tau_*) + \frac{1}{y_*^2} f_2(\tau_*) + \theta\left(\frac{1}{y_*^3}\right) \tag{A.10}$$

The known function v'_{f^*} is likewise expanded as

$$1 - v'_{f^*} = 1 - \frac{y_*}{y_*+10} = \frac{10}{y_*}\left(\frac{1}{1 + \frac{10}{y_*}}\right) \tag{A.11}$$

$$= \frac{10}{y_*} - \left(\frac{10}{y_*}\right)^2 + \ldots$$

Substituting equations (A.10) and (A.11) into equation (A.5) and taking the limit as $y_* \to \infty$, one determines that $f_1(\tau_*) = -10$ and $f_2(\tau_*) = 100 + 10\,\tau_*$. Thus

$$v'_{p^*} = 1 - \frac{10}{y_*} + \frac{100+10\tau_*}{y_*^2} + \theta\left(\frac{1}{y_*^2}\right)$$

so that

$$v'_{p^*} - v'_{f^*} = \frac{10\tau_*}{y_*^2} + \theta\left(\frac{1}{y_*^2}\right) \tag{A.12}$$

Equation (A.12) was used to compute values of v'_{p*} at some appropriate large value of y_*, e.g., $y_* = 40$, and the numerical solution was started from this point. Note however that the expansion (A.12) is nonuniform with respect to τ_*, becoming invalid as $\tau_* \to \infty$. However for this case v'_{p*} was taken equal to one at the starting location and the solution generated in the same manner as before.

Results of the numerical integration are shown in Figure 50. Comparison of the numerical solutions with the asymptotic expansion (A.9) indicates that the latter remains valid for $\tau_* = \theta(1)$. For the typical examples considered thus far, i.e., for $Re = 10^5$, $\rho_p/\rho_f = 1110$, and R= 10 cm, a 20-micron radius particle would exhibit a relaxation time, τ_*, of about 20. Likewise. a one-micron radius particle would correspond to $\tau_* \approx 0.20$. Since particles of size greater than about 10 microns cannot be considered to possess a rms fluctuation velocity approximately the same as that of the fluid near the centerline, one cannot expect the results of this simple analysis to remain reasonably valid for $\tau_* \gtrsim 20$.

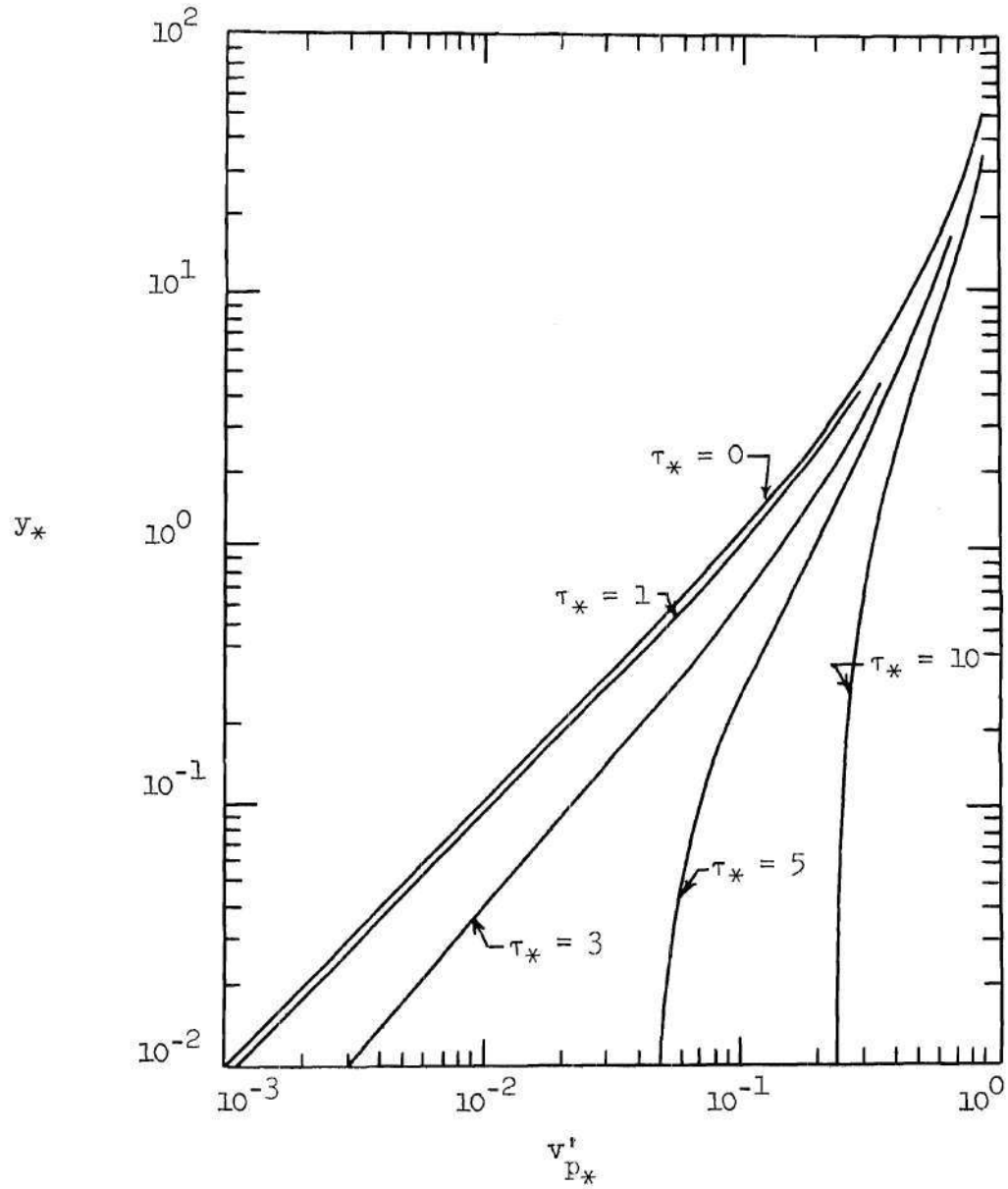

Figure 50. Particle Turbulent rms Fluctuation Velocity as a Function of Distance from Wall

APPENDIX B

ANALYTIC SOLUTIONS - NONCOAGULATING NEUTRAL AEROSOL

Turbulent Pipe Flow

Considering only convective and diffusive transport and neglecting coagulation, one can write equation (2.4) for an axisymmetric cylindrical coordinate system as

$$u_z \frac{\partial n}{\partial z} = \frac{1}{r} \frac{\partial}{\partial r} \left[r \beta \frac{\partial n}{\partial r} \right] \tag{B.1}$$

where

$$\beta = \ell^2 \left| \frac{du_z}{dr} \right| .$$

Note that here the dependence of n on particle radius can be considered parameterized and omitted from explicit consideration. Attempting a separation of variables solution, one can put

$$n(z, r) = S(z)\, T(r) \tag{B.2}$$

Thus, substituting equation (B.2) into equation (B.1) yields

$$\frac{1}{S}\frac{dS}{dz} = \frac{1}{u_z rT}\frac{d}{dr}\left[r\,\beta\,\frac{dT}{dr}\right] \tag{B.3}$$

provided $\beta = \beta(r)$. Since the left hand side of equation (B.3) is a function only of z and the right hand side a function only of r, then both must be constant, say c_1 for definiteness. Thus,

$$\frac{1}{S}\frac{dS}{dz} = c_1$$

so that upon integrating

$$\ln S = c_1 z + c_2$$

or

$$\frac{S(z)}{S(0)} = e^{c_1 z} \tag{B.4}$$

Also

$$\frac{d}{dr}\left[r\,\beta\,\frac{dT}{dr}\right] = c_1 u_z rT$$

Integrating from r' = 0 to r' = r yields

$$[r'\beta \frac{dT}{dr'}]_{r'=0}^{r} = c_1 \int_{r'=0}^{r} u_z r'Tdr' \qquad (B.5)$$

Now, numerical computations presented later indicate that T is practically constant over a large portion of the pipe radius, and u_z can be represented by a very weak power function of r. Thus, the integral on the right hand side of equation (B.5) can be approximated by

$$\int_{r'=0}^{r} u_z r'Tdr' \cong \bar{u}_z \bar{T} \int_{r'=0}^{r} r'dr' = \bar{u}_z \bar{T} \frac{r^2}{2} \qquad (B.6)$$

where $\bar{u}_z$ and $\bar{T}$ are average values of u_z and T evaluated over the pipe radius. Thus, equation (B.5) becomes

$$\beta \frac{dT}{dr} \cong \frac{c_1}{2} r\bar{u}_z \bar{T} \qquad (B.7)$$

since dT/dr is zero at r = 0 by symmetry conditions. Integrating equation (B.7) with respect to r yields

$$T(r=r) - T(r=0) \cong \frac{c_1 \bar{u}_z \bar{T}}{2} \int_{r'=0}^{r} \frac{r'}{\beta} dr' \qquad (B.8)$$

Put $y = R - r$, where R is the pipe radius. Thus, equation (B.8) becomes

$$T(y) - T(R) \cong \frac{c_1 \bar{u}_z \bar{T}}{2} \int_{y''=R-r}^{R} \frac{R-y'}{\beta} dy' \qquad (B.9)$$

where the function arguments are values of y. Now

$$\beta = \ell^2 \left| \frac{du_z}{dy} \right| ,$$

and one can approximate the mixing-length distribution for $Re \gtrsim 10^5$ by

$$\ell \cong 0.14 \, R \sqrt{y/R} \qquad (B.10)$$

from the experimental data of Nikuradse [48]. Also the velocity profile can be represented by a simple power-law expression of the form, Schlichting [44]

$$u_z = u_z(R)\left(\frac{y}{R}\right)^{1/m} \qquad (B.11)$$

where m increases slightly with the Reynolds number. For example, experimental data obtained by Nikuradse [48] for a range of Reynolds numbers extending from 4×10^3 to 3.2×10^6 would indicate that appropriate values of m would vary from about 6 to 10 over the same

range. Thus,

$$\theta = (0.14)^2 \frac{Ru_z(R)}{m} \left(\frac{y}{R}\right)^{1/m} \tag{B.12}$$

Using equation (B.12) with equation (B.9) thus yields

$$T(y) - T(R) \cong \frac{c_1 \bar{u}_z \bar{T}}{2} \frac{m}{(0.14)^2 Ru_z(R)} \int_{y'=R-r}^{R} \frac{R-y'}{(y'/R)^{1/m}} \, dy'$$

Evaluating the integral yields

$$T(y) - T(R) \cong \frac{c_1 \bar{u}_z \bar{T} m R}{(0.0392) u_z(R)} \left\{ \frac{m}{m-1} \left[1 - \left(1 - \frac{r}{R}\right)^{1-\frac{1}{m}}\right] - \right. \tag{B.13}$$

$$\left. - \frac{m}{2m-1} \left[1 - \left(1 - \frac{r}{r}\right)^{2-\frac{1}{m}}\right] \right\}$$

Near the wall, $r/R \sim 1$ so one can put $r/R = 1 - \hat{\delta}$ where $\hat{\delta} \ll 1$ near wall. Thus, equation (B.13) can be written

$$T(\delta) - T(R) \cong \frac{c_1 \bar{u}_z \bar{T} m^2 R}{(0.0392) u_z(R)} \left\{ \frac{m}{(m-1)(2m-1)} - \right. \tag{B.14}$$

$$\left. - \delta \left[\frac{\delta}{m-1}^{-1/m} - \frac{\hat{\delta}^{1-(1/m)}}{2m-1} \right] \right\}$$

For $\hat{\delta} \ll 1$, the second term in the bracketed expression is much smaller than the first and can be neglected. Thus,

$$T(\delta) - T(R) \cong \frac{c_1 \bar{u}_z \bar{T} m^2 R}{(0.0392) u_z(R)} \left\{ \frac{m}{(m-1)(2m-1)} - \frac{\hat{\delta}^{1-(1/m)}}{m-1} \right\} \qquad (B.15)$$

This equation is valid near the wall, and equation (B.13) is valid over the total pipe radius. These are the basic equations which can be used to calculate the number concentration distribution for turbulent pipe flow.

To determine the deposition for discrete particle sizes one can put $\hat{\delta} = \hat{\delta}_d$ where $\hat{\delta}_d = (\ell + a)/R$ is the distance above the wall from which deposition by inertia is assumed to take place. Recalling that $(r/R) = 1 - \hat{\delta}$, one obtains from equation (B.7)

$$\left[\beta \frac{dT}{dr}\right]_{\frac{r}{R} = 1-\hat{\delta}_d} = \frac{c_1}{2} R(1-\hat{\delta}_d) \bar{u}_z \bar{T} \qquad (B.16)$$

But by definition, the deposition flux is proportional to the left hand side of this equation. Defining the deposition velocity as

$$V_d = \frac{-\left[\beta \frac{dn}{dr}\right]_{r/R=1-\hat{\delta}_d}}{\bar{n}}$$

where $\bar{n}$ is the average value of n across the pipe radius, then

$$V_d = \frac{-\left[\beta \frac{dT}{dr}\right]_{r/R=1-\hat{\delta}_d}}{\bar{T}} \qquad (B.17)$$

and one can write equation (B.16)

$$-V_d \bar{T} = \frac{c_1}{2} R(1-\hat{\delta}_d)\bar{u}_z \bar{T} \qquad (B.18)$$

where the function argument is again a value of y. Equation (B.18) is useful because it relates the deposition velocity, V_d, to the separation of variables constant, c_1.

Recall also that the deposition flux may also be calculated by the expression, obtained from equation (2.7),

$$V_d = v'_p \, T \, (y=\delta_d)/\bar{T} \qquad (B.19)$$

where the particle fluctuation velocity, v'_p, can be obtained from Appendix A. Using equation (B.18) and (B.19) in equation (B.15) and solving this for V_d yields

$$V_d = \left[\frac{m^2}{(0.0196)(1-\hat{\delta}_d)u_z(R)} \left\{\frac{m}{(m-1)(2m-1)} - \frac{\hat{\delta}_d^{1-\frac{1}{m}}}{m-1}\right\} + \frac{1}{v'_p}\right]^{-1} \qquad (B.20)$$

Dividing both sides by $\bar{u}_z$ and noting that since $\hat{\delta}_d \ll 1$, the terms containing $\hat{\delta}_d$ can be neglected. Thus

$$\frac{V_d}{\bar{u}_z} \simeq \left[\frac{m^3}{(0.0196)(m-1)(2m-1)} \left(\frac{\bar{u}_z}{u_z(R)}\right) + \frac{\bar{u}_z}{v'_p}\right]^{-1} \tag{B.21}$$

The experimental data of Laufer [47] indicate that the fluid rms turbulent fluctuation velocity, v'_f, can be represented reasonably well by the simple expression, involving non-dimensional variables,

$$v'_{f_*} = \frac{y_*}{y_* + 10} \tag{B.22}$$

where $y_* = yu_{z*}/\nu$, $v'_{f*} = v'_f/u_{z*}$, and u_{z*} is the so-called friction velocity defined as $u_{z*} = \sqrt{\tau_w/\rho}$, where τ_w is shear stress at the wall and ρ is the mass density of the medium. Using the fundamental hypothesis of the present method, one puts $y^* = \ell_* + a_*$, where ℓ and a have been non-dimensionalized analogous to y. Recall that we must determine that value of ℓ_* for which

$$\ell_* (y_*) + a_* = y_* \tag{B.23}$$

Now for $y_* \lesssim 5$, $\ell_* = 0.378y_*$, which has been confirmed by the measurements of Nikuradse [48] and the more recent measurements of Brinkworth

and Smith [49] so that the appropriate value of $\ell_* + a_*$ is equal to $1.58a_*$ for $a_* \lesssim 3$.

One can also show that for $u_z = u_z(R)(y/R)^{1/m}$, then

$$\bar{u}_z/u_z(R) = 2m^2/[(m+1)(2m+1)] \tag{B.24}$$

Finally, the friction velocity for smooth pipes can be obtained quite accurately by the expression, Schlicting [44]

$$\frac{1}{\sqrt{\lambda}} = 0.885 \ln (R_e\sqrt{\lambda}) - 0.916 \tag{B.25}$$

where $u_{z*}/\bar{u}_z = \sqrt{\lambda/8}$. Equation (B.25) is often called "Prandtl's universal law of friction for smooth pipes." Collecting these results and combining them with equation (B.21) yields

$$\frac{V_d}{\bar{u}_z} \cong \left[\frac{2m^5}{(0.0196)(m^2-1)(4m^2-1)} + \sqrt{\frac{8}{\lambda}}\left(\frac{1}{v'_{p*}}\right)\right]^{-1} \tag{B.26}$$

Computationally, one proceeds as follows to compute the deposition velocity:

(1) Select values for R_e and a/R.

(2) Determine $m(R_e)$. (Schlichting [44], Figure 20.3).

(3) Calculate λ from equation (B.25). (Schlichting [44], Figure 20.1).

(4) Calculate $a_* \triangleq \left(\frac{a}{R}\right) \frac{R_e}{2} \sqrt{\lambda/8}$ $\left(= \frac{a u_{z^*}}{\nu}\right)$.

(5) Calculate $\tau_* \triangleq (a/R)^2 \frac{\rho_p}{\rho_f} R_e^2 \lambda \left(\frac{1}{144}\right)$.

(6) Determine, from Appendix A, v'_{p^*} at $y_* = 1.58a$, for value of τ_* computed above.

(7) Calculate $V_d / \bar{u}_z$ from equation (B.26).

Results of some sample computations are presented later and compared with the results of numerical solutions and with experimental data.

Turbulent Boundary Layer Flow

Results for this case can be obtained in a manner entirely analogous to that for turbulent pipe flow. The continuity equation is

$$u_z \frac{\partial n}{\partial z} = \frac{\partial}{\partial y} \left[\beta \frac{\partial n}{\partial y}\right] \tag{B.27}$$

where

$$\beta = \ell^2 \left| \frac{du_z}{dy} \right| .$$

Again putting

$$n(z,y) = S(z)T(y) \tag{B.28}$$

and following exactly the same procedure as that leading to equation (B.5) one obtains

$$\left[\beta \frac{dT}{dy'}\right]_{y'=y}^{\delta_D} = c_1 \int_{y'=y}^{\delta_D} u_z T dy' \qquad (B.29)$$

where δ_D is the height of the diffusion boundary layer, which is usually much smaller than the height of the velocity boundary layer. Since $dT / dy = 0$ at δ_D, then

$$\frac{dT}{dy} \cong - \frac{c_1 \bar{u}_z \bar{T} (\delta_D - y)}{\beta}$$

and employing the same approximation as that leading to equation (B.6), one can show that this becomes

$$- \beta \frac{dT}{dy} = c_1 \int_{y'=y}^{\delta_D} u_z T dy' \qquad (B.30)$$

Integration yields

$$T(\delta_D) - T(y) \cong - c_1 \bar{u}_z \bar{T} \int_{y'=y}^{\delta_D} \frac{\delta_D - y'}{\beta} dy' \qquad (B.31)$$

Now

$$\beta = \ell^2 \left| \frac{du_z}{dy} \right|,$$

and u_z can be represented by the same expression as used for pipe flow, i.e.,

$$u_z = u_z(\delta_v)\ (y/\delta_v)^{1/m} \tag{B.32}$$

where δ_v is the height of the velocity boundary layer. The data of Klebanoff [50], Townsend [51], and of Schubauer [52] indicate that the mixing-length distribution across the turbulent boundary layer differs significantly from that of the pipe flow case only near the outer edge (i.e., near the centerline for pipe flow) of the boundary layer. Since the upper integration limit in equation (B.31), δ_D, is usually much less than δ_v and since the numerator of the integrand approaches zero as y approaches δ_D, then that portion of the integral corresponding to regions where the flat-plate mixing-length expression differs from that of the pipe flow case is small and can be neglected. Thus, one can again put

$$\ell \cong 0.14\ \delta_v\sqrt{y/\delta_v} \tag{B.33}$$

Thus β becomes

$$\beta = (0.14)^2\ \frac{\delta_v u_z(\delta_v)}{m}\ \left(\frac{y}{\delta_v}\right)^{1/m} \tag{B.34}$$

Equation (B.31) becomes

$$T(\delta_D) - T(y) \simeq - c_1 \bar{u}_z \bar{T} \frac{m}{(0.14)^2 \delta_v u_z(\delta_v)} \int_{y'=y}^{\delta_D} \frac{\delta_D - y'}{(y'/\delta_v)^{1/m}} dy' \quad (B.35)$$

Integration gives

$$T(\delta_D)-T(y) \cong - \frac{c_1 \bar{u}_z \bar{T} m^2 \delta_D^{2-1/m}}{(0.14)^2 \delta_v^{1-1/m} u_z(\delta_v)} \left[\frac{m}{(m-1)(2m-1)} - \frac{\hat{y}^{1-1/m}}{m-1} \right] \quad (B.36)$$

where here $\hat{y} = y/\delta_v$. This expression can be used as before for the pipe case to determine particle deposition. The method is exactly analogous to that used before, and the manipulation is omitted here for the sake of brevity. The resulting expression for deposition velocity for a turbulent boundary layer, corresponding to equation (B.21) is

$$\frac{V_d}{\bar{u}_z} \cong \left[\frac{m^3}{(0.0196)(m-1)(2m-1)} \left(\frac{\bar{u}_z}{u_z(\delta_v)} \right) \frac{(\delta_D/\delta_v)^{1-1/m}}{1 - \delta_d/\delta_D} + \frac{\bar{u}_z}{v'_p} \right]^{-1} \quad (B.37)$$

APPENDIX C

NUMERICAL SOLUTIONS - NONCOAGULATING NEUTRAL AEROSOL

Turbulent Pipe Flow

The governing equation to be solved is equation (2.4) simplified for steady-state, axisymmetric flow conditions, with the particle mass flux given by equation (2.6) and the coagulation term neglected. The dependent function, $n(a,\vec{x})$ is a function of three variables, namely particle radius, a; and spatial coordinates r and z. However, the dependence with respect to a appears only implicity, in the boundary conditions.

Define nondimensional variables as follows:

$$\hat{r} = r/R \qquad \hat{n} = na_o/N_o \qquad \hat{a} = a/a_o$$

$$\hat{z} = z/R \qquad \hat{u}_z = u_z/u_{z_o}$$

where $u_{z_o} = u_z(r = 0)$ and $\int_{a=0}^{\infty} n_o da = N_o$, n_o being the centerline number concentration distribution function. Now using equations (2.6), (B.10), and (B.11) in equation (2.4), one can write the equation to be solved in the nondimensional form

$$u_{z_o}(1-\hat{r})^{1/m}\frac{\partial \hat{n}}{\partial \hat{z}} = \frac{u_{z_o}(0.0196)}{m}(1-\hat{r})^{1/m}\{\frac{\partial^2 \hat{n}}{\partial \hat{r}^2} + [\frac{1}{\hat{r}} - \frac{1}{m(1-\hat{r})}]\frac{\partial \hat{n}}{\partial \hat{r}}\} \qquad (C.1)$$

When aerosol coagulation is neglected, the particle number concentration varies in an exponential manner in the axial direction, as indicated by equation (B.4) obtained in Appendix B. This result may be used to eliminate the z - derivative in equation (C.1), so that for turbulent pipe flow the equation to be solved becomes

$$-u_{z_o}(1-\hat{r})^{1/m}\hat{n}\,c_1 = \frac{u_{z_o}(0.0196)}{m}(1-\hat{r})^{1/m}\{\frac{\partial^2 \hat{n}}{\partial \hat{r}^2} + \qquad (C.2)$$

$$+ [\frac{1}{\hat{r}} - \frac{1}{m(1-\hat{r})}]\frac{\partial \hat{n}}{\partial \hat{r}}\}$$

when $\hat{n} = \hat{n}(\hat{a}, \hat{r})$. The equation involves derivatives with respect to radial direction only, and upon application of the particle-radius space discretization can be solved as an ordinary differential equation. The two boundary conditions at the centerline required to "start" the numerical solution are the number concentration specification and the summetry condition which implies that $\partial\hat{n}/\partial\hat{r} = 0$ at $\hat{r} = 0$.

The radial derivatives are replaced by the following finite difference approximations:

$$\frac{\partial \hat{n}}{\partial \hat{r}} \cong \frac{1}{2(\Delta \hat{r})} [\hat{n}_{j+1} - \hat{n}_{j-1}] \tag{C.3}$$

$$\frac{\partial^2 \hat{n}}{\partial \hat{r}^2} \cong \frac{1}{(\Delta \hat{r})^2} [\hat{n}_{j+1} - 2n_j + \hat{n}_{j-1}] \tag{C.4}$$

where $\hat{r}_j = j(\Delta \hat{r})$, $\hat{n}_j = \hat{n}(\hat{r}_j)$. In so doing one obtains an explicit algorithm for "marching" the solution toward the wall. However, the value of c_1 required in the process is a function of the solution itself near the wall (i.e., the deposition is a function of the number concentration near the wall), and thus, an iterative scheme is indicated. A reasonable estimate of c_1 is made and the solution is generated across the pipe radius. The wall deposition and hence a new c_1 value is computed and the process repeated. Nor more than five iterations were found necessary during this study, and the convergence was quite definite.

BIBLIOGRAPHY

1. N. A. Fuchs, The Mechanics of Aerosols, The Macmillan Company, New York (1964).

2. L. Prandtl, "Uber die ausgebildete Turbulenz," Z. Angew. Math. u. Mech., 5, 136 (1925).

3. G. I. Taylor, "The Transport of Vorticity and Heat Through Fluids in Turbulent Motion," Proceedings of the Royal Society of London, A135, 685 (1932).

4. S. K. Friedlander and H. F. Johnstone, "Deposition of Suspended Particles from Turbulent Gas Streams," Industrial and Engineering Chemistry, 49, 1151 (1957).

5. C. N. Davies (editor), Aerosol Science, Academic Press, New York (1966).

6. S. K. Beal, "Transport of Particles in Turbulent Flow to Channel or Pipe Walls," Westinghouse Electric Corporation, Bettis Atomic Power Laboratory, Report WAPD-TM-765(1968).

7. G. A. Sehmel, "Aerosol Deposition from Turbulent Airstreams in Vertical Conduits," Pacific Northwest Laboratories, Richland, Washington, Report BNWL-578(1968).

8. L. C. Schwendiman and A. K. Postma, "Turbulent Deposition in Sampling Lines," Seventh Atomic Energy Commission Air Cleaning Conference, TIP-7627(1961).

9. T. Kneen and W. Strauss, "Deposition of Dust from Turbulent Gas Streams," Atmospheric Environment, 3, 55(1969).

10. A. C. Wells and A. C. Chamberlain, "Transport of Small Particles to Vertical Surfaces," British Journal of Applied Physics, 18, 1793 (1967).

11. G. A. Sehmel, "Particle Deposition from Turbulent Air Flow," Journal of Geophysical Research, 75, 1766 (1970).

12. J. O. Hinze, Turbulence, McGraw-Hill Book Company, New York (1959).

13. C. M. Tchen, Mean Value and Correlation Problems Connected with the Motion of Small Particles in a Turbulent Fluid, Delft, The Hague Martinus Nimhoff, Ph.D. dissertation (1947).

14. S. L. Soo and C. L. Tien, "Effect of the Wall on Two-Phase Turbulent Motion," Journal of Applied Mechanics, Transactions of the ASME, 27, 5(1960).

15. T. L. Montgomery and M. Corn, "Aerosol Deposition in a Pipe with Turbulent Airflow," Aerosol Science, 1, 185 (1970).

16. N. Stavropolous, Deposition of Particles from Turbulent Gas Streams, Columbia University, M.S. Thesis (1957).

17. P. G. Saffman and J. S. Turner, "On the Collision of Drops in Turbulent Clouds," Journal of Fluid Mechanics, 1, 16(1956).

18. S. Chandrasekhar, Radiative Transfer, Dover Publishing Company, New York (1960).

19. D. P. Giddens, Study of Rarefied Gas Flows by the Discrete Ordinate Method, Georgia Institute of Technology, Ph.D. Thesis (1967).

20. A. B. Huang and D. L. Hartley, "Nonlinear Couette Flow with Heat Transfer," Physics of Fluids, 11, 1321 (1968).

21. A. B. Huang and D. L. Hartley,"Kinetic Theory of the Sharp Leading Edge Problem in Supersonic Flow," Physics of Fluids, 12, 96 (1969).

22. J. Laufer, "The Structure of Turbulence in Fully Developed Pipe Flow," NACA Report 1174 (1954).

23. W. Deutsch, "Bewegung und Ladung der Elektricitatstrager im Zylinder Kondensator," Annals of Physics, 68, 335 (1922).

24. H. J. White, "Modern Electrical Precipitation," Industrial and Engineering Chemistry, 47, 932 (1955).

25. S. K. Friedlander, "Principles of Gas-Solid Separations in Dry Systems," Chemical Engineering Progress Symposium Series, 55, 135 (1959).

26. J. C. Williams and R. Jackson, "The Motion of Solid Particles in an Electrostatic Precipitator," in Proceedings of the Symposium on the Interaction Between Fluids and Particles (London: Institution of Chemical Engineers) (June, 1962).

27. N. V. Inyushkin and Y. D. Averbukh, "Influence of Gas Flow Pressure Conditions on Dust Collection in an Electrical Field," Soviet Journal of Nonferrous Metals, 3, 35 (1962).

28. P. Cooperman, "Turbulent Gas Flow and Electrostatic Precipitation," American Institute of Electrical Engineers, Winter General Meeting, New York (1960).

29. M. Robinson, "A Modified Deutsch Efficiency Equation for Electrostatic Precipitation," Atmospheric Environment, 1, 193 (1967).

30. M. Robinson, "Turbulent Gas Flow and Electrostatic Precipitation," Journal of the Air Pollution Control Association, 18, 235 (1968).

31. D. O. Heinrich, "Colloquium on Electrostatic Precipitation," STAUB, 25, 30 (1965).

32. M. E. Collier, M. C. Gourdine, and D. H. Malcolm, "Electrogasdynamics and Precipitation," Industrial and Engineering Chemistry, 58, 26(1966).

33. S. L. Soo, Fluid Dynamics of Multiphase Systems, Blaisdell Publishing Company, Waltham, Massachusetts (1967).

34. H. J. White, Industrial Electrostatic Precipitation, Addison-Wesley Publishing Company, Inc., Reading, Massachusetts (1963).

35. W. R. Lawrence and K. L. Goin, "Subsonic Drag of Spheres at Reynolds Numbers from 200 to 10,000," AIAA Journal, 6, 5, 961 (1968).

36. B. Gebhart, Heat Transfer, McGraw-Hill Book Company, New York (1961).

37. P. V. Danckwerts, "Continuous Flow Systems - Distribution of Residence Times," Chemical Engineering Science, 2, 1 (1953).

38. J. R. A. Pearson, "A Note on the Danckwerts Boundary Conditions for Continuous Flow Reactors," Chemical Engineering Science, 10, 281 (1959).

39. S. L. Soo, G. J. Trezek, R. C. Dimick, and G. F. Honstreiter, "Concentration and Mass Flow Distributions in a Gas-Solid Suspension," Industrial and Engineering Chemistry Fundamentals, 3, 98 (1964).

40. H. Schnitzler, "Ein neuartiger Elektroentstauber," STAUB, 23, 78 (1963).

41. H. Schnitzler, "Further Tests with a New Electrostatic Precipitator," STAUB, 25, 43 (1965).

42. H. S. Carslaw and J. C. Jaeger, Conduction of Heat in Solids, Oxford University Press, London (1959).

43. H. E. Rose and A. J. Wood, An Introduction to Electrostatic Precipitation in Theory and Practice, Constable and Company Ltd, London, Second Edition (1966).

44. H. Schlichting, Boundary Layer Theory, McGraw-Hill Book Company, Inc., New York, Fourth Edition (1960).

45. N. Fuchs and I. Petryanov, Acta Physiochim, URSS, 3, 827 (1935).

46. V. G. Levich, Physiochemical Hydrodynamics, Prentice-Hall, Inc., Englewood Cliffs, New Jersey (1962).

47. Y. V. Shupelov and S. S. Dukhin, "On the Theory of Electrical Coagulation of Spherical Aerosol Particles," Kolloidnyi Zhurnal, 24, 749 (1962).

48. J. Nikuradse, "Gesetzmabigkeit der Turbulenten Stromung in Glatten Rohren," VID-Forschungsheft, Number 356 (1932).

49. P. J. Brinkworth and P. C. Smith, "Velocity Distribution in the Core of Turbulent Pipe Flow," Chemical Engineering Science, 24, 787 (1969).

50. P. S. Klebanoff, "Characteristics of Turbulence in a Boundary Layer with Zero Pressure Gradient," NACA Report Number 1247 (1955).

51. A. A. Townsend, The Structure of Turbulent Shear Flow, Cambridge University Press (1956).

52. G. B. Schubauer, "Turbulent Processes as Observed in Boundary Layer and Pipe," Journal of Applied Physics, 25, 188 (1954).

53. W. F. Ames, Numerical Methods for Partial Differential Equations, Barnes and Noble, Inc., New York (1969).

54. D. J. Harney, An Aerodynamic Study of the Corona Wind, California Institute of Technology, M. S. Thesis (1957).

55. O. E. Ramadan, A Study of the Effects of Electric Wind in an Electrostatic Precipitator, University of Illinois, Ph.D. Thesis, (1969).

56. S. L. Soo, "Dynamics of Charged Suspension," International Reviews in Aerosol Physics and Chemistry, 61, edited by G. M. Hidy and J. Brock, Pergamon Press, New York (1971).

57. M. A. Shirazi, On the Motion of Small Particles in a Turbulent Fluid Field, University of Illinois, Ph.D. Thesis (1967).

58. A. P. Chattock, "On the Velocity and Mass of the Ions in the Electric Wind in Air," Philosophical Magazine, 48, 401(1899).

59. D. A. Kennedy, Some Measurements of the Dispersion of Spheres in a Turbulent Flow, The Johns Hopkins University, Ph.D. Thesis (1965).

60. W. F. Pickard, "Ion Drag Pumps," Journal of Applied Physics, 34, 246 (1963).

61. G. V. Jorgensen and E. Will, "Improved Drag Pump," Reviews of Scientific Instruments, 33, 55 (1962).

62. M. Robinson, "Movement of Air in the Electric Wind of the Corona Discharge," Transactions of the American Institute of Electrical Engineers, 80, 143 (1961).

63. E. Löb, "The Pressure Effects of Ion Currents in Atmospheric Air for Different Electrode Configurations," Archiv der Elektrischen Ubertragung, 8, 85 (1954).

64. O. M. Stuetzer, "Ion Drag Pumps," Journal of Applied Physics, 31, 136 (1960).

65. T. S. Yih, Ion-Neutral Interaction for Electromechanical Propulsion, University of California at Davis, Ph.D. Thesis (1966).

66. R. Ladenburg, "Untersuchungen, Uber Die Physikalischen Vorgange Bel Der Sogenannten Electrischen Gasreinigung," Annalen Der Physik, 4, 803 (1930).

67. O. E. Ramadan and S. L. Soo, "Electrohydrodynamic Secondary Flow," Physics of Fluids, 12, 1943 (1969).

68. M. Robinson, "The Effect of Polarity on Particle Concentration Profiles in Electrostatic Precipitators," Journal of the Air Pollution Control Association, 18, 688 (1968).

69. J. D. Cobine, Gaseous Conductors, Dover Publications, Inc., New York (1958).

70. S. C. Brown, Basic Data of Plasma Physics, Technology Press, John Wiley and Sons, Inc., New York (1959).

71. W. Strauss (editor), Air Pollution Control, Wiley Interscience, New York (1971).

72. D. S. Azbel and Z. G. Medvedev, "The Theory of Mass Transfer in Microheterogeneous Systems with Turbulent Flow," Theoretical Foundations of Chemical Engineering, 3, 747 (1969).

73. H. H. Chiu, "Boundary Layer Flow with Suspended Particles," Princeton University, Repost 620 (1962).

74. E. R. Corino and R. S. Brodkey, "A Visual Investigation of the Wall Region in Turbulent Flow," Journal of Fluid Mechanics, 37, 1 (1969).

75. S. Corrsin and J. L. Lumley, "On the Equation of the Motion of a Particle in Turbulent Fluid," Applied Scientific Research, 6A, 114 (1956).

76. C. N. Davies, Recent Advances in Aerosol Research, Pergamon Press, Oxford (1964).

77. M. R. Doshi and W. N. Gill, "Note on the Mixing Length Theory of Turbulent Flow," American Institute of Chemical Engineering Journal, 16, 885 (1970).

78. D. M. France and G. J. Trezek, "The Contribution of Space-Charge in Slender Channel Electrogasdynamics," Advanced Energy Conversion, 9, 135 (1969).

79. R. F. Heinrich and J. R. Anderson, "Electrostatic Precipitation," Chemical Engineering Practice, Vol. 3, Edited by H. W. Cremer and T. Davies, Academic Press, Inc., New York (1957).

80. G. M. Hidy and D. K. Lilly, "Solutions to the Equations for the Kinetics of Coagulation," Journal of Colloid Science, 20, 867 (1965).

81. A. T. Hjelmfelt, Jr., and L. F. Mockros, "Particles in a Turbulent Fluid," Applied Scientific Research, 16, 149 (1966).

82. A. Karnis, H. L. Goldsmith, and S. G. Mason, "The Flow of Suspensions Through Tubes. V. Inertia Effects," Canadian Journal of Chemical Engineering, 44, 181 (1966).

83. H. F. Kraemer and H. F. Johnstone, "Collection of Aerosol Particles in Presence of Electrostatic Fields," Industrial and Engineering Chemistry, 47, 2426 (1955).

84. A Lieberman, "Aerosol Rarefaction Studies," American Industrial Hygiene Association Journal, 29, 444 (1968).

85. J. L. Lumley, Some Problems Connected with the Motion of Small

Particles in a Turbulent Fluid, Johns Hopkins University, Ph.D. Thesis (1957).

86. M. Nagarajan and W. Murgatroyd, "A Simple Model of Turbulent Gas-Solids Flow in a Pipe," Aerosol Science, 2, 15(1971).

87. P. R. Owen, "Dust Deposition from a Turbulent Airstream," International Journal of Air-Water Pollution, 3, 8, (1960).

88. C. Orr, Particulate Technology, The Macmillan Company, New York, (1966).

89. R. Panton, "Flow Properties for the Continuum Viewpoint of a Nonequilibrium Gas-Particle Mixture," Journal of Fluid Mechanics, 31, 18 (1968).

90. R. L. Peskin, Some Effects of Particle-Particle and Particle-Fluid Interaction in Two-Phase Flow Systems, Princeton University, Ph.D. Thesis (1959).

91. R. L. Peskin, "Basic Studies in Gas-Solid Suspension," Rutgers University, Quarterly Report Number 63-2 (1963).

92. E. G. Richardson (editor), Aerodynamic Capture of Particles, Pergamon Press, New York (1960).

93. P. O. Rouhiainen, Deposition of Particles on Walls of Two-Dimensional Channels, McGill University, M. S. Thesis, (1969).

94. P. O. Rouhaininen and J. W. Stachiewicz, "On the Deposition of Small Particles from Turbulent Streams," Journal of Heat Transfer, Transactions of the ASME, 92, 169(1970).

95. G. A. Sehmel, "Complexities of Particle Deposition and Re-entrainment in Turbulent Pipe Flow," Aerosol Science, 2, 63, (1971).

96. G. A. Sehmel, "The Deposition of Aerosols by Turbulent Flow Processes within Vertical Tubes," Pacific Northwest Laboratory, Richland, Washington, BNWL-SA-1500 (1968).

97. R. E. Singleton, Fluid Mechanics of Gas-Solid Particle Flow in Boundary layers, California Institute of Technology, Ph.D. Thesis (1964).

98. J. R. Travis, H. O. Buhr, and A. Sesonske, "A Model for Velocity and Eddy Diffusivity Distributions in Fully Turbulent Pipe Flow," Canadian Journal of Chemical Engineering, 49, 14(1971).

99. G. J. Trezek and D. M. France, "One-Dimensional Particulate Electrogasdynamics," AIAA Journal, 8, 1386 (1970).

100. C. Wakstein, The Motion of Small Particles Suspended in Turbulent Air Flow in a Vertical Pipe, Queen Mary College, University of London, Ph.D. Thesis (1966).

101. C. Wakstein, "A Simple Picture of Turbulent Two-Phase Pipe Flow," Aerosol Science, 1, 69(1970).

102. J. D. Yoder and L. Silverman, "Influence of Turbulence on Aerosol Agglomeration and Deposition in a Pipe," Sixtieth Annual Air Pollution Control Association Meeting, Paper Number 67-33 (1967).

103. G. Zebel, "On the Theory of the Behavior of Electrically Charged Aerosols," Kolloid Zhurnal, 157, 37 (1958).

104. W. G. Vincenti and C. H. Kruger, Jr., Introduction to Physical Gasdynamics, John Wiley and Sons, Inc., New York (1965).

105. C. D. Donaldson, "Calculation of Turbulent Shear Flows for Atmospheric and Vortex Motions," AIAA Journal, 10, 4 (1972).

VITA

William R. Lawrence was born on November 27, 1943, in Montgomery, Alabama. After living briefly in Detroit, Michigan; Canton, Ohio; Louisville, Kentucky; St. Louis, Missouri; and Granite City, Illinois, he returned to Montgomery where, in 1961, he graduated from Sidney Lanier High School. In September of 1961, he entered the Georgia Institute of Technology as a student of Aerospace Engineering. He received the Bachelor of Science and Master of Science degrees from the University of Alabama in 1965 and 1966, respectively, in the field of Aerospace Engineering.

From June of 1966 to July of 1969, he was employed as a project engineer in aeroballistics at ARO, Inc., contract operator of the Arnold Engineering Development Center at Tullahoma, Tennessee. During this period, he also attended the University of Tennessee Space Institute at Tullahoma part time.

He returned to Georgia Institute of Technology in July of 1969 and received an NSF traineeship to study in the doctoral program.

On March 28, 1970, he married the former Bettie Ruth Johnston of Nashville, Tennessee, and they have one son, Robert.

He is employed by the United States Naval Ordnance Laboratory at Silver Spring, Maryland as an engineer in the Applied Aerodynamics Division.